Advanced Material Models
for the
Crystal Plasticity Finite Element Method

Development of a general CPFEM framework

Acknowledgments

First off all I want to thank Prof. Dierk Raabe. About ten years ago he offered me a group leader position at the Max-Planck-Institut für Eisenforschung and introduced me to the Crystal Plasticity Finite Element Method (CPFEM). Since then he gave to me all the necessary support to continue my research work in this amazingly versatile field of material science.

Second, I thank all the post-docs and PhD students with whom I had the chance to work during these last ten years. I start the list with Zisu Zhao, he was the one with whom I took my first steps in CPFEM, then there were Anxin Ma 'my' first PhD student, Jui-Chao Kuo, Yanwen Wang, Hyeon S. Jeon-Haurand, Ilja Tikhovskiy, Nader N. Zaafarani, Chung-Souk Han, Claudio Zambaldi*, Wiliam A. Counts*, Hongyang Li, Duancheng Ma, Olga Dmitrieva, Luc Hantcherli*, Eralp Demir, Christoph Kords*, Alankar Alankar*, Denny D. Tjahjanto*, and finally Philip Eienlohr*, with whom I run the joint Max-Planck–Fraunhofer group on Computational Mechanics of Polycrystals, CMC^n, and who is the main co-contributor to the general CPFEM framework presented in this thesis. Actually all people marked by '*' contributed in one or the other way to the new code. Most of the others contributed to the application examples of CPFEM included in this thesis. Besides these people mentioned by name I want to thank all my other former and present colleagues at the Max-Planck-Institut für Eisenforschung for their everlasting support and the good working atmosphere they provide.

I also especially thank my colleagues Stefanie Sandlöbes and Philip Eisenlohr for proof-reading the manuscript.

Then, there is the research world outside the Max-Planck-Institut für Eisenforschung. I also want to thank a number of collaborators, who used or use 'my' code and thereby or in some other way contributed to its improvement. These people are Kurt Helming, Martin Kraska, Maria Doig, Dmitrij Tikhomirov, Kim Kose, Victotia J. Chen, Koos van Putten, Thomas Hochrainer, Aruna Prakasch, Raphael Twardowksi, Thomas R. Bieler, and Koenraad Jansens.

Finally, I thank my family, my wife Martina, my daughter Sophia, and my son Christian. They provide the private background and support for my work. Even though they are probably not aware of it, this is the most important contributions of all!

Contents

Symbols and Abbreviations

$\mathbb{C}$	rank four elasticity matrix
$\boldsymbol{E}_\mathrm{e}$	Green Lagrange elastic strain
$\boldsymbol{F}$	total deformation gradient
$\boldsymbol{R}$	rotation tensor
$\boldsymbol{U}$	right stretch tensor
$\boldsymbol{F}_\mathrm{e}$	*elastic* deformation gradient (including rigid-body rotation)
$\boldsymbol{F}_\mathrm{p}$	plastic deformation gradient
$\boldsymbol{L}_\mathrm{p}$	plastic velocity gradient
$\boldsymbol{P}$	first Piola-Kirchhoff stress
$\boldsymbol{S}$	second Piola-Kirchhoff stress
$\boldsymbol{\sigma}$	Cauchy stress
$\boldsymbol{I}, \mathbb{I}$	rank two, rank four Identity tensor
$\boldsymbol{b}, b$	Burgers vector and its magnitude
G	shear modulus
ν	Poisson ratio
N_slip	number of slip systems
N_twin	number of twin systems
$\boldsymbol{s}^\alpha, \boldsymbol{m}^\alpha$	slip direction (of slip system α)
$\boldsymbol{n}^\alpha$	slip plane normal (of slip system α)
$\boldsymbol{t}^\alpha$	dislocation line (tangent) vector (of slip system α)
$\dot{\gamma}^\alpha$	shear rate (of slip system α)
τ^α	resolved shear stress (of slip system α)
τ_c^α	critical resolved shear stress (of slip system α)
m	rate sensitivity of slip
ρ	dislocation density
ρ_SSD	statistically stored dislocation density
ρ_GND	geometrically necessary dislocation density
ρ_m	mobile dislocation density
T	temperature
k_B	Boltzmann constant
V	volume
$\varphi_1, \phi, \varphi_2$	Euler angles (Bunge notation)

Notation

As a general scheme of notation, vectors are written as boldface lowercase letters (*e.g.* $\boldsymbol{a}$, $\boldsymbol{b}$), second-order tensors as boldface capital letters (*e.g.* $\boldsymbol{A}$, $\boldsymbol{B}$), and fourth-order tensors as blackboard-bold capital letters (*e.g.* $\mathbb{A}$, $\mathbb{B}$). For vectors and tensors, Cartesian components are denoted as, respectively, a_i, A_{ij} and A_{ijkl}. The action of a second-order tensor upon a vector is denoted as $\boldsymbol{Ab}$ (in components $A_{ij}b_j$, with implicit summation over repeated indices) and the action of a fourth-order tensor upon a second order tensor is designated as $\mathbb{A}\boldsymbol{B}$ ($A_{ijkl}B_{kl}$). The composition of two second-order tensors is denoted as $\boldsymbol{A}\,\boldsymbol{B}$ ($A_{ij}B_{jl}$). The tensor (or dyadic) product between two vectors is denoted as $\boldsymbol{a}\otimes\boldsymbol{b}$ (a_ib_j). All inner products are indicated by a single dot between the tensorial quantities of the same order, $\boldsymbol{a}\cdot\boldsymbol{b}$ (a_ib_i) for vectors and $\boldsymbol{A}\cdot\boldsymbol{B}$ ($A_{ij}B_{ij}$) for second-order tensors. The cross-product of a vector $\boldsymbol{a}$ with a second-order tensor $\boldsymbol{A}$, denoted by $\boldsymbol{a}\times\boldsymbol{A}$, is a second-order tensor defined in components as $(\boldsymbol{a}\times\boldsymbol{A})_{ij} = \epsilon_{ikl}\,a_k\,A_{lj}$, where ϵ is the Levi–Civita permutation matrix. The transpose of a tensor is denoted by a superscript "T" (*e.g.* $\boldsymbol{A}^{\mathrm{T}}$) and its inverse by a superscript "−1" (*e.g.* $\boldsymbol{A}^{-1}$). Additional notations will be introduced where required.

Chapter 1

Introduction

1.1 Crystalline anisotropy

The elastic-plastic deformation of crystalline aggregates depends on the direction of loading, *i.e.* crystals are mechanically anisotropic. This phenomenon is due to the anisotropy of the elastic tensor and to the orientation dependence of the activation of the crystallographic deformation mechanisms (dislocations, twins, martensitic transformations). A consequence of crystalline anisotropy is that the associated mechanical phenomena such as shape change, crystallographic texture, strength, strain hardening, deformation-induced surface roughening, and damage are also orientation dependent. This is not a trivial statement as it implies that mechanical parameters of crystalline matter are tensor quantities. Another major consequence of the single crystalline elastic-plastic anisotropy
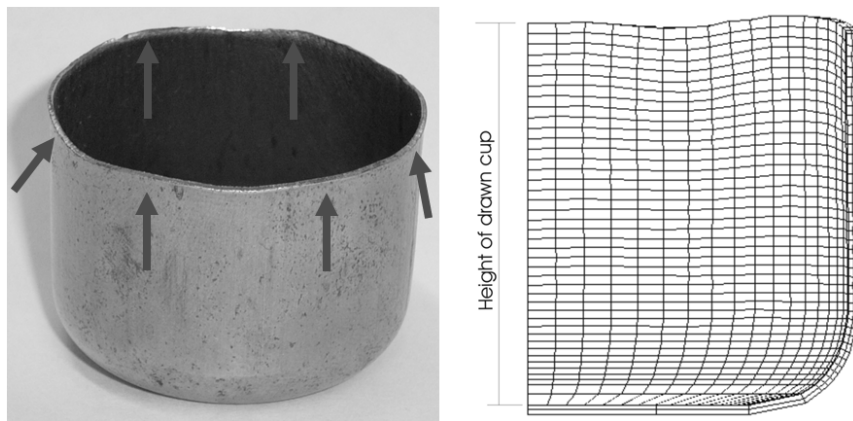
Figure 1.1: Consequence of plastic anisotropy when drawing a textured sheet into a cup. The orientation distribution before deformation exhibits a high volume fraction of grains with a crystallographic [1 1 1] axis parallel to the sheet normal. The arrows on the left mark six ears resulting from preferential material flow. On the right the corresponding crystal plasticity finite element simulation is shown.
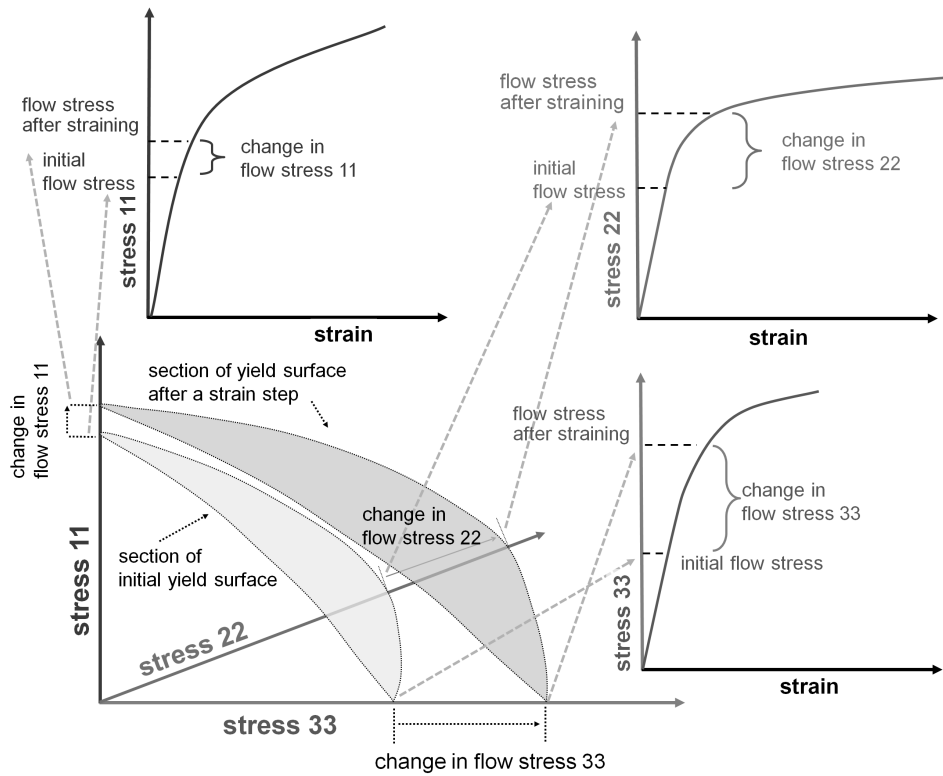
Figure 1.2: Flow stress and strain hardening of anisotropic materials are tensor quantities.

is that it adds up to produce also macroscopically directional properties when the orientation distribution (crystallographic texture) of the grains in a polycrystal is not random. Figure 1.1 shows such an example of a plain carbon steel sheet with a preferred crystal orientation (here high probability for a crystallographic {1 1 1} plane being parallel to the sheet surface) after cup drawing. Plastic anisotropy leads to the formation of an uneven rim (referred to as *ears* or *earing*) and a heterogeneous distribution of material thinning during forming. It must be emphasized in that context that a random texture is not the rule but a rare exception in real materials. In other words, practically all crystalline materials reveal macroscopic anisotropy.

A typical example of such macroscopic anisotropy is the uniaxial stress–strain curve, which is the most important mechanical measure in structural materials design. The introductory statement made above implies that uniaxial stress–strain curves represent an incomplete description of plastic deformation as they reduce a six-dimensional yield surface and its change upon loading to a one-dimensional (scalar) yield curve, see figure 1.2. Another consequence of this statement is that the crystallographic texture (orientation distribution) and its evolution during forming processes is a quantity that is inherently connected with plasticity theory, more precisely, with the anisotropy of the underlying plasticity mechanisms. Texture can, hence, be used to describe the integral anisotropy of polycrystals in terms of the individual tensorial behavior of each

grain and the orientation-dependent boundary conditions among the crystals. Formally, the connection between shear and texture evolution becomes clear from the fact that any deformation gradient can be expressed as the combination of its skew-symmetric portion, which represents a pure rotation leading to texture changes if not matched by the rotation implied by plastic shear, and a symmetric tensor that is a measure of pure stretching. Plastic shear hence creates both shape and orientation changes, except for certain highly symmetric shears. Therefore, a theory of the mechanical properties of crystals must include, first, the crystallographic and anisotropic nature of those mechanisms that create shear and, second, the orientation(s) of the crystal(s) studied relative to the applied boundary conditions (*e.g.* loading axis, rolling plane).

Early approaches to describe anisotropic plasticity under simple boundary conditions have considered these aspects, such as for instance the Sachs (1928), Taylor (1938), Bishop–Hill (Bishop and Hill, 1951a, b), or Kröner (1961) formulations. However, these approaches were neither designed for considering explicitly the mechanical interactions among the crystals in a polycrystal nor for responding to complex internal or external boundary conditions, see figure 1.3. Instead, they are built on certain simplifying assumptions of strain or stress homogeneity to cope with the intricate interactions within a polycrystal.

For that reason variational methods in the form of finite element approximations have gained enormous momentum in the field of crystal mechanical modeling. These methods, which are referred to as crystal plasticity finite element (CPFE) models, are based on the variational solution of the equilibrium of the forces and the compatibility of the displacements using a weak form of the principle of virtual work in a given finite volume element. The entire sample volume under consideration is discretized into such elements. The essential step, which renders the deformation kinematics of this approach a crystal plasticity formulation, is the fact that the velocity gradient is written in dyadic form, which reflects the tensorial crystallographic nature of the underlying defects that lead to shear and consequently, to both shape changes (symmetric part) and lattice rotations (skew-symmetric part), see section 2.2. This means that the CPFE method does not only take into account the initial mechanical anisotropy but also its evolution during deformation. In summary, the CPFE method has evolved as an attempt to employ some of the extensive knowledge gained from experimental and theoretical studies of single crystal deformation and dislocations to inform the further development of continuum field theories of deformation. The general framework supplied by variational crystal plasticity formulations provides an attractive vehicle for developing a comprehensive theory of plasticity that incorporates existing knowledge of the physics of deformation processes (Curtin and Miller, 2003; Arsenlis et al., 2004; Vitek et al., 2004) into the computational tools of continuum mechanics (Zienkiewicz, 1967; Zienkiewicz et al., 2005b; Zienkiewicz and Taylor, 2005; Zienkiewicz et al., 2005a) with the aim to develop advanced and physics-based design methods for engineering applications (Zhao et al., 2004a).

One main advantage of CPFE models lies in their capability of solving crystal mechanical
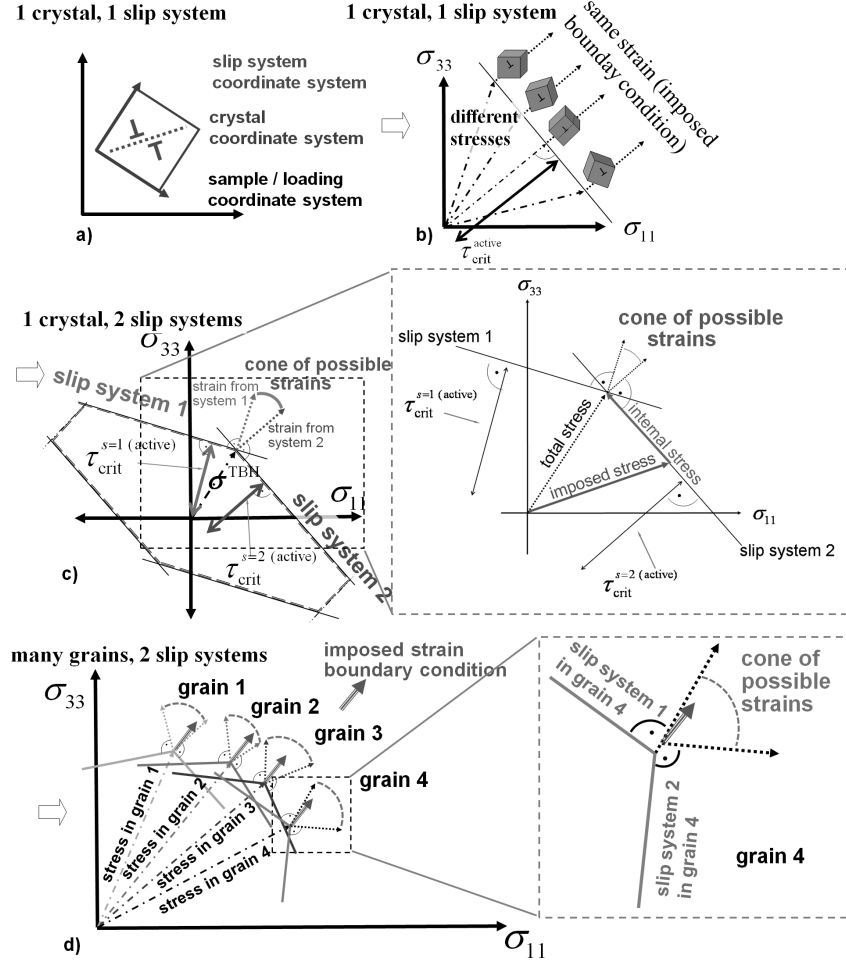
Figure 1.3: Schematical presentation of the increasing complexity of crystal-scale micro-mechanics with respect to the equilibrium of the forces and the compatibility of the displacements for different situations: a,b) Single-slip situation in a single crystal presented in stress space. c) Portion of a single crystal yield surface with three slip systems. d) Multi-slip situation in a polycrystal where all different crystals have to satisfy an assumed imposed strain in their respective yield corners. If the strain is homogeneous this situation leads to different stresses in each crystal (Raabe et al., 2002a, 2004a). τ_{crit}: critical shear stress; σ^{TBH}: Taylor–Bishop–Hill stress state (stress required to reach a yield corner).
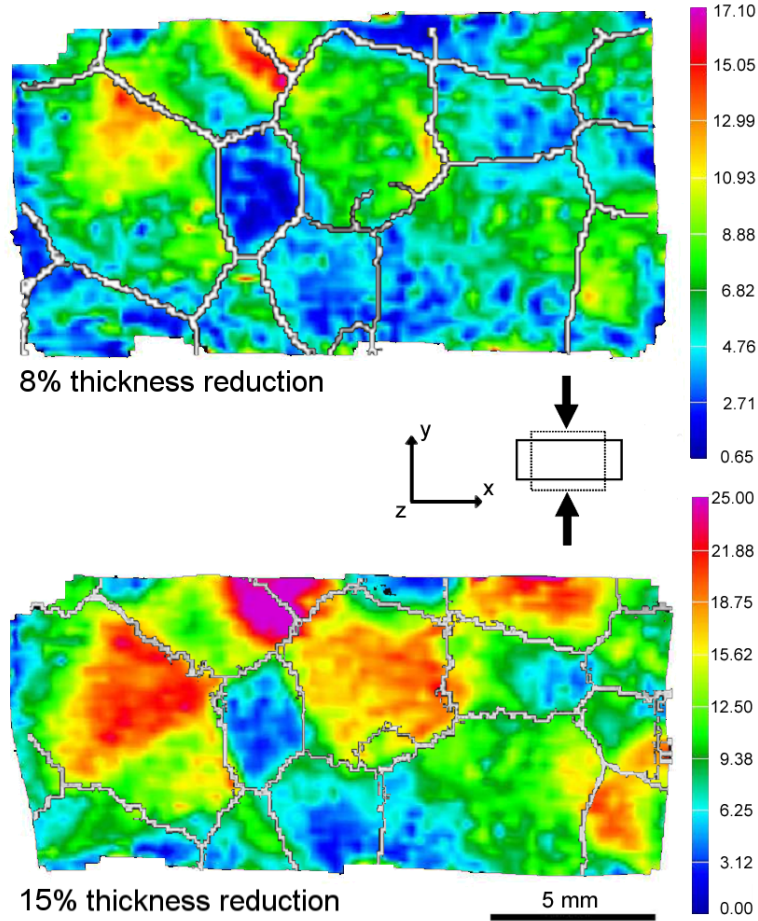
Figure 1.4: Experimental example of the heterogeneity of plastic deformation at the grain and sub-grain scale using an aluminum oligocrystal with large columnar grains (Sachtleber et al., 2002). The images show the distribution of the accumulated von Mises equivalent strain in a specimen after $\Delta y/y_0 = 8\,\%$ and $15\,\%$ thickness reduction in plane strain (y_0: initial sample height). The experiment was conducted in a lubricated channel-die setup. White lines indicate high-angle grain boundaries derived from EBSD microtexture measurements. The equivalent strains (determined using digital image correlation) differ across some of the grain boundaries by a factor of 4–5 giving evidence of the enormous orientation-dependent heterogeneity of plasticity even in pure metals.

problems under complicated internal and/or external boundary conditions. This aspect is not a mere computational advantage but it is an inherent part of the physics of crystal mechanics since it enables one to tackle those boundary conditions that are imposed by inter- and intra-grain micro-mechanical interactions, figure 1.4 (Sachtleber et al., 2002). This is not only essential to study in-grain or grain cluster mechanical problems but also to better understand the often quite abrupt mechanical transitions at interfaces (Raabe et al., 2003).

However, the success of CPFE methods is not only built on their efficiency in dealing with complicated boundary conditions. They also offer high flexibility with respect to including various constitutive formulations for plastic flow and hardening at the elementary shear system level. The constitutive flow laws that were suggested during the last decades have gradually developed from empirical viscoplastic formulations (Rice, 1971; Asaro and Rice, 1977) into microstructure-based multiscale models of plasticity including a variety of size-dependent effects and interface mechanisms (Arsenlis and Parks, 1999, 2002; Arsenlis et al., 2004; Evers et al., 2002, 2004a, b; Cheong and Busso, 2004; Ma and Roters, 2004; Ma et al., 2006a, b). In this context it should be emphasized that the finite element method itself is not the actual model but the variational solver for the underlying constitutive equations. Since its first introduction by Peirce et al. (1982) the CPFE method has matured into a whole family of constitutive and numerical formulations, which has been applied to a broad variety of crystal mechanical problems, see Roters et al. (2010) for a recent review. In parts I and II of this thesis some of these constitutive models including newly developed ones will be discussed.

1.2   CPFEM as a multi-physics framework

A main conceptual advantage of the CPFE approach for tackling anisotropic micro-mechanical problems in materials science and engineering is that it can combine a variety of mechanical effects, which are direction-dependent due to the underlying crystalline structure. Figure 1.5 shows an example where only elastic anisotropy is considered.

When considering elasto-plastic problems, CPFE models may not only include dislocations as the main carriers of plastic deformation in metals but also other mechanisms that follow dyadic kinematics, see figures 1.6 and 1.7. Some of these mechanisms were implemented in CPFE models in earlier works such as for instance martensite formation (Thamburaja and Anand, 2001; Lan et al., 2005; Tjahjanto et al., 2008), shear band formation (*e.g.* in glassy matter) (Anand and Su, 2005, 2007), mechanical twinning (Kalidindi, 1998; Staroselsky and Anand, 1998; Marketz et al., 2002; Salem et al., 2005), and even superplastic grain boundary shear (Wei and Anand, 2004; Wei et al., 2006).

The CPFE method allows the user to incorporate these mechanisms including their interactions. But it also adds complexity to the model: The use of different competing crystallographic deformation mechanisms within a CPFE model requires to formulate
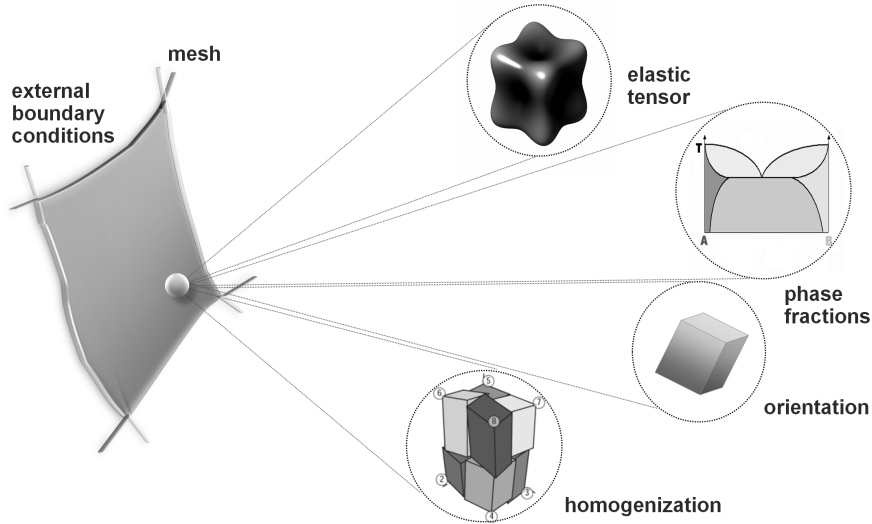
Figure 1.5: FE example where only elastic anisotropy is considered. The phase fractions and homogenization approaches are indicated as well for the case that more than one phase and multiple crystals must be considered at one integration point.
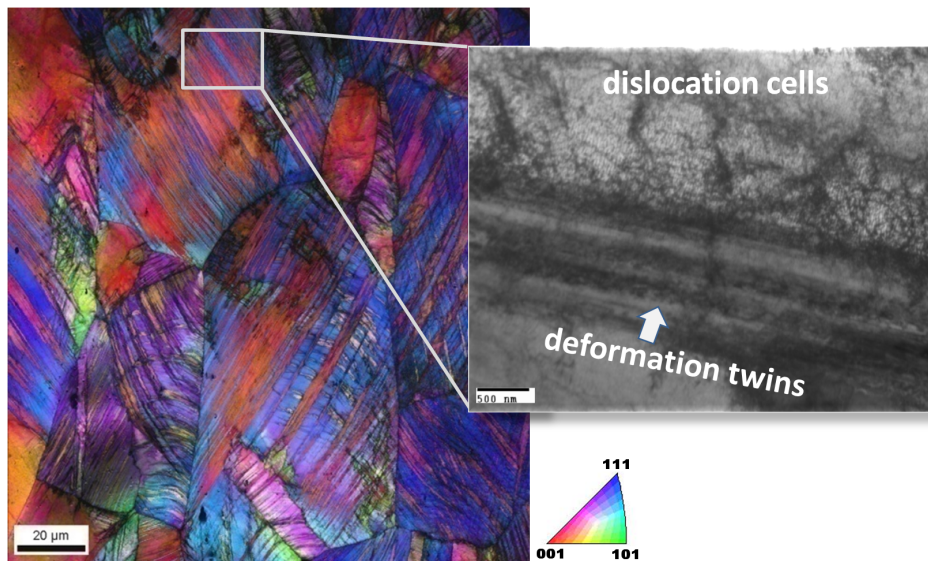
Figure 1.6: Micrograph showing the complexity of deformation microstructures in cases where more than one lattice defect type is involved. On the left hand side an electron back scatter diffraction (EBSD) map shows the orientation contrast of a deformed TWIP steel (TWIP: twinning induced plasticity). On the right hand side a transmission electron microscopy (TEM) image reveals details of the local interaction between dislocation cells and deformation twins.

local homogenization rules (Raabe et al., 2002a; Raabe and Roters, 2004; Tjahjanto et al., 2010). This means that at some material points only one type of deformation mechanism (*e.g.* dislocation slip) may occur while in others a mix (*e.g.* dislocations and twins) must be considered within the same material volume, figure 1.6. The latter situation requires appropriate sub-models that describe the evolving fractions (*e.g.* of the twinned volume) and the interactions of coexisting and competing deformation mechanisms at the same material point, see figure 1.7 and section 7.3. Another aspect that increases complexity in such cases is the possibility that deformation martensite or twins may, after their formation, undergo further plastic deformation or create accommodation strains related to volume changes.

The CPFE approach can and has been used to devise models for size-dependent mechanical behavior. For this, the equivalence between a gradient of the plastic deformation and an excess content of dislocations is exploited. Since excess dislocation content is associated with a lattice orientation change (Nye, 1953; Kröner, 1958, 1981, figure 1.8), the nowadays accessible high-resolution measurements of crystal orientation in 2-D and 3-D allow for thorough validation of such type of models (Larson et al., 2002; Zaefferer et al., 2003; Kuo et al., 2003; Roters et al., 2004; Zaafarani et al., 2006; Zaefferer et al., 2008; Demir et al., 2009).

Typically, the dislocation density in those models is divided into dislocations connected to gradients in plastic strain (then termed *geometrically necessary* (Ashby, 1970)) and ordinary (termed *statistically stored*) dislocation content. It should be noted, however, that an individual dislocation cannot distinguish whether it belongs to the geometrically necessary fraction. This distinction follows only as a consequence of excess dislocation *content* within a particular observation volume, determined by the closure failure of a corresponding Burgers circuit. Even then geometrical necessity does not render those dislocations distinct from statistically stored ones, but both their evolutions must be embedded in a unified kinetic framework, *i.e.* they can assume either state depending on the local lattice defect configuration. This arbitrary distinction is overcome by the non-local model introduced in section 4.2.

CPFE simulations can be used both at microscopic and macroscopic scales (Raabe et al., 2002a; Roters, 2005; Roters et al., 2010). Examples for small-scale applications are inter- and intra-grain mechanics, damage initiation, mechanics at interfaces, simulation of micro-mechanical experiments (*e.g.* indentation (Zaafarani et al., 2006, 2008, section 5.4), pillar compression (Maaß et al., 2007, 2009, section 5.3), beam bending (Demir et al., 2010), or the prediction of local lattice curvatures and mechanical size effects). Consequently, CPFE methods gain momentum in the field of small-scale material testing where the experimental boundary conditions are difficult to control and/or monitor. In such cases the experimental results may sometimes be hard to interpret without corresponding CPFE simulations, which allow an experimentalist to simulate the effects of details in the contact and boundary conditions (Maaß et al., 2009). Miniaturization also occurs in engineering design. Many products nowadays have dimensions in the range of the grain scale such as for instance micro-electro-mechanical systems
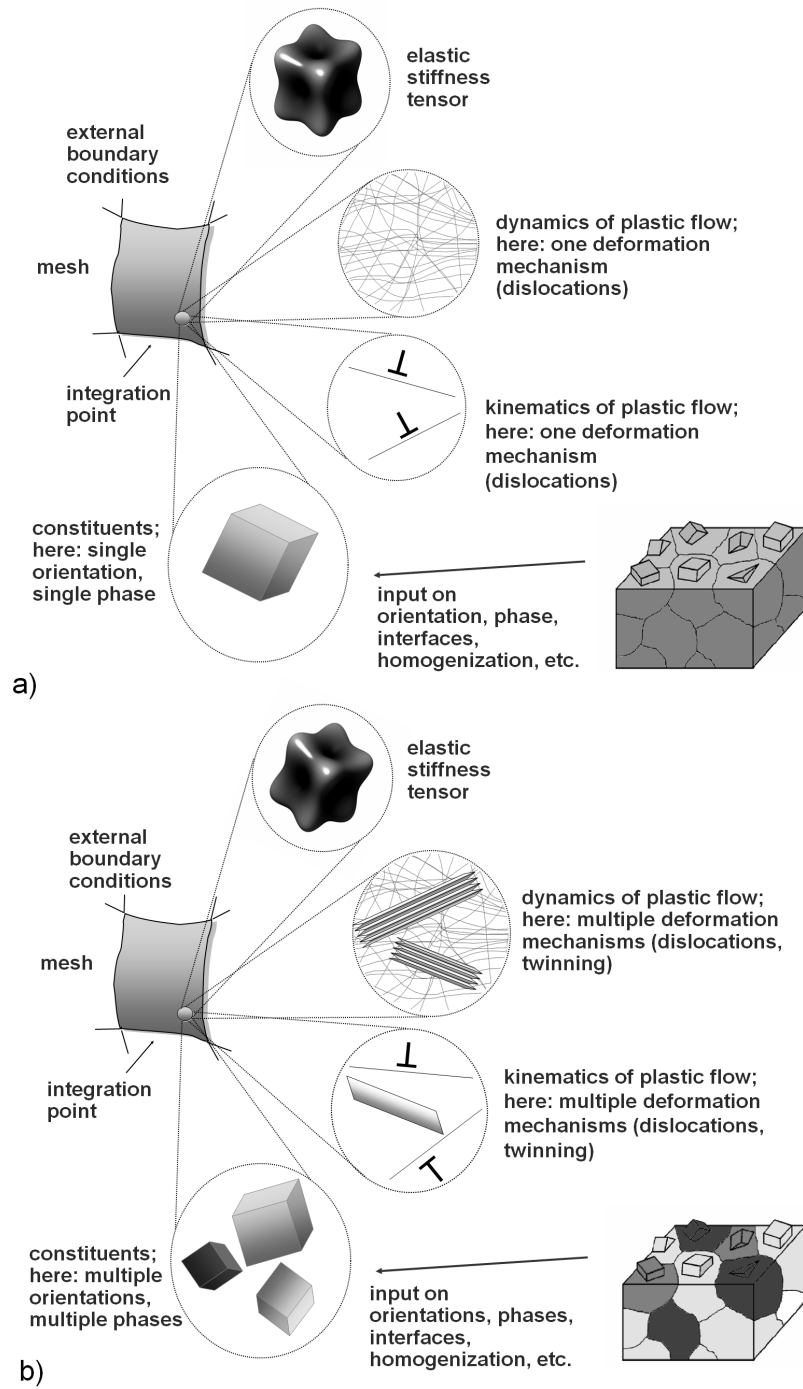
Figure 1.7: Schematic presentation of the conceptual ingredients in CPFE simulations for elasto-plastic micro-mechanical problems. a) Example of a case with one type of deformation mechanism (lattice dislocations) and one phase. b) Example of a case with different deformation mechanisms, phases, orientations, and homogenization schemes at the same integration point.
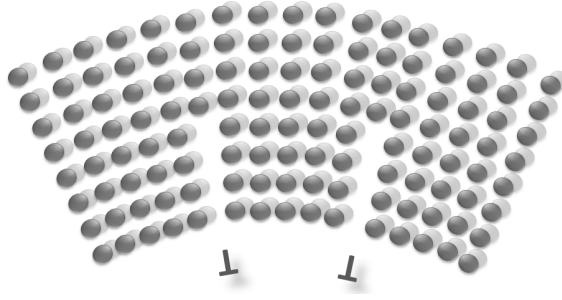
Figure 1.8: Relationship between single dislocations and curvature.

(MEMS), bonding wires and pillars, stents, and practically all materials in electronic components. Design of such parts increasingly requires consideration of grain-scale crystalline anisotropy. Some applications along these lines are discussed in the first part of this thesis.

Macroscopic applications of the CPFE method occur particularly in the fields of large-scale forming and texture simulations. These problems require appropriate homogenization schemes within a CPFE model since a large number of crystals and/or phases is usually considered in each volume element linked with a finite element integration point. Primary engineering objectives of CPFE applications in macroscopic forming simulations are the prediction of the precise material shape after forming, thickness distribution, material failure, optimization of material flow, elastic springback, forming limits, texture evolution, and the mechanical properties of the formed part (Nakamachi et al., 2001; Zhao et al., 2001; Xie and Nakamachi, 2002; Zhao et al., 2004a; Raabe et al., 2005; Kraska et al., 2009). Further related applications include tool design, press layout, and surface properties. The latter aspect involves both macroscopic (*e.g.* wrinkling) as well as microstructural mechanisms (*e.g.* roping, ridging, orange peel) that influence the surface topography (Becker, 1998; Raabe et al., 2003; Zhao et al., 2004b). A recent development is the use of the CPFE method as a virtual mechanical laboratory. This approach substitutes crystal plasticity simulations for rather involved mechanical tests required for fitting yield surface coefficients (Kraska et al., 2009, section 8.4).

A further advantage of CPFE predictions is that they can be compared to experiments in a very detailed fashion probing a variety of quantities. Corresponding studies compared shape changes, forces, strains, strain path and rate effects, texture evolution, interface response, local stresses, and size effects one-to-one at different scales, table 1.1. Examples for applications and experimental validation procedures are given in both parts I and II of this thesis.

Table 1.1: Examples of measurable quantities that can be predicted by CPFE models

Prediction by CPFE methods	Experimental access
Surface roughening	Speckle interferometry, digital image correlation (photogrammetry), atomic force microscopy, white-light confocal microscopy
Elasticity, interface mechanics, grain size effects, grain interaction, size effects	Indentation testing, tensile and compression testing, mechanical tests at different sample sizes, digital image correlation, electron backscatter diffraction, scanning electron microscopy, ultrasonic testing, X-ray and synchrotron Bragg peak broadening and shifting
Creep, high temperature deformation, superplasticity	Tensile testing, texture measurement, *in situ* electron microscopy
Dislocation-based constitutive modeling	Flow stress measurement, transmission electron microscopy, lattice orientation measurements, electron channeling contrast imaging in the scanning electron microscope
Martensite mechanics, phase transformation, shape memory	Magnetic measurements, multiphase electron backscatter diffraction, X-ray and synchrotron Bragg diffraction
In-grain texture, grain-scale mechanics, non-uniform deformation, multiphase mechanics	Digital image correlation, indentation hardness testing, orientation determination (Kikuchi, SAD, CBED diffraction in the transmission or scanning electron microscope; X-ray Bragg diffraction), mechanical testing
Texture evolution, texture stability, in-grain texture formation, anisotropy	Texture measurements using electron (Kikuchi, SAD, CBED) diffraction in the transmission and scanning electron microscope or X-ray Bragg diffraction
Forming, deep drawing, process modeling, cup drawing, springback, earing, wire drawing, extrusion, anisotropy, design, fretting	Shape analysis, cup drawing experiments, springback measurements, ultrasonic measurement of elastic polycrystal constants

Table 1.1: Examples ... (continued)

Prediction by CPFE methods	Experimental access
Crystal plasticity and recrystallization	Hardness testing, metallography, electrical resistivity, X-ray and synchrotron diffraction, electron backscatter diffraction, transmission electron microscopy, grain size determination, kernel average orientation determination, calorimetry
Deformation twinning	Metallography, X-ray and synchrotron diffraction, electron backscatter diffraction, transmission electron microscopy, electron channeling contrast imaging in the scanning electron microscope
Nanoindentation, micro-scale deformation, miniaturized mechanical testing	Hardness and stiffness analysis using nanoindenter or nano-manipulator tests, surface shape analysis using atomic force microscopy, electron microscopy

1.3   Scope of this thesis

Beyond the metallurgical and mechanical considerations discussed in the two preceding sections numerical aspects also deserve attention. While CPFEM is an extremely versatile tool, this is up to now not reflected in its numerical implementation. For almost all of the many applications mentioned above and in the extensive list presented in Roters et al. (2010) dedicated codes have been used, *i.e.* today there exists a large number of CPFE implementations but each of them is more or less tailored to a certain application involving a distinct constitutive model. Moreover, CPFE formulations can be either fully integrated into finite element codes or implemented as user-defined subroutines into commercially available solvers. The latter point is important because engineering applications are often tackled using commercial platforms. The use of standard solvers helps to make CPFE methods accessible to a broader community.

Part III of this thesis, therefore, introduces the CPFEM implementation developed in my research group at the Max-Planck-Institut für Eisenforschung in Düsseldorf, Germany, during the last decade. This implementation uses a modularization of the code to achieve a strict disjunction of numerics and physics. This means, that while the numerical part of the code needs to know some value for the plastic deformation gradient, L_p, it does not need to know the physical assumptions made to calculate L_p. This is completely left to the underlying constitutive model, *i.e.* the physics part of the code.

Due to this modularization new constitutive models and homogenization schemes can be easily integrated into the code. This allows to systematically improve the constitutive models used without the need to readjust the numerical part of the code. Moreover, the incorporation of several constitutive models in one code will allow for the first time to combine them in a single FE model. At the same time the formulation as general user-defined subroutine allows the integration into various FE solvers by providing a dedicated interface module.

In summary this thesis intends to demonstrate the versatility of the CPFE method by presenting example applications at the micro- (part I) and macroscale (part II). All application examples are taken from the work of my group and are chosen to demonstrate certain special aspects of the application of the CPFE method. Finally, part III introduces the new CPFEM implementation accounting for this versatility by its modularized code structure.

Chapter 2

The Crystal Plasticity Finite Element Method

2.1   Concise Historical Review

The first finite element (FE) simulation was performed by Courant in 1943 (Courant, 1943). The breakthrough of the method came with the publication of the monograph "The Finite Element Method in Structural and Continuum Mechanics" by O. C. Zienkiewicz in 1967 (Zienkiewicz, 1967). The three succeeding volumes (Zienkiewicz et al., 2005b; Zienkiewicz and Taylor, 2005; Zienkiewicz et al., 2005a) are considered the most important monographs in the field to date.

The Finite Element Method (FEM) is today the most used simulation technique in the field of continuum mechanics. This is mainly due to its great flexibility in the treatment of (mechanical) boundary conditions. However, the FEM can be used to solve almost any kind of boundary value problem, of which mainly the simulation of thermal fields is of interest also in conjunction with mechanical simulations. While state of the art continuum simulations are in many cases coupled thermo-mechanical calculations, as plastic deformation is always producing some heat, in Crystal Plasticity FEM most simulations are purely mechanical and ignore any temperature effects, *i.e.* assume constant temperature.

Even though it has been known since 1934 (Taylor, 1934a, b; Orowan, 1934; Polanyi, 1934) that crystalline materials deform plastically by the slip of dislocations on discrete slip systems, for a long time continuum mechanical FE simulations used isotropic material models that were based on empirical equations. The first CPFE simulations were performed by Peirce, Asaro and Needleman in 1982 (Peirce et al., 1982). Due to computational restrictions they used a simplified setup of two symmetric slip systems in order to study the tensile behavior of a single crystal. These simulations were later extended to a polycrystalline arrangement by Harren et al. (Harren et al., 1988; Harren and Asaro, 1989) using a 2-D setup with two or three slip systems. In 1991 R. Becker

was the first to perform simulations on the basis of the 12 slip systems of a face-centered cubic (fcc) crystal. Using a 3-D model for the crystallographic degrees of freedom he simulated channel-die deformation of a single crystal (Becker et al., 1991) and of a columnar polycrystal aggregate (Becker, 1991).

Since that time an ever-increasing number of CPFE simulations has been performed owing to the increase in computational power. In the field of direct or one-to-one crystal plasticity models numerous grain- and sub-grain scale problems have been tackled using meshes with sub-grain resolutions and, in part, complex 2-D and 3-D grain arrangements (Beaudoin et al., 1996; Sarma and Dawson, 1996a; Sarma et al., 1998; Mika and Dawson, 1998; Bachu and Kalidindi, 1998; Sachtleber et al., 2002; Zhao et al., 2007, 2008). On the other hand advanced homogenization schemes were developed for the application of the CPFE method to large-scale problems (see section 7.2). In this case one main problem was the correct representation of the (statistical) crystallographic texture of the material in the CPFE mesh. This can be achieved in different ways using *e.g.* texture components (Zhao et al., 2001; Raabe and Roters, 2004) or direct sampling of single orientations from the Orientation Distribution Function (ODF) (Tóth and Van Houtte, 1992; Melchior and Delannay, 2006; Eisenlohr and Roters, 2008, and sections 7.1.1 and 7.1.2).

All CPFE models mentioned so far used phenomenological constitutive equations (see section 2.3) and considered dislocation slip as the only deformation mechanism. When applying the CPFE method in new areas such as small-scale deformation or interface mechanics existing phenomenological constitutive laws are often insufficient. Also, new classes of materials such as TWIP and TRIP steels (TWIP: twinning-induced plasticity, TRIP: transformation-induced plasticity) or shape memory alloys show additional deformation and hardening mechanisms, *i.e.* twinning and/or deformation-induced phase transformations.

Size effects can be introduced into CPFE frameworks by using phenomenological strain gradient theories, which were developed by Fleck et al. (1994); Fleck and Hutchinson (1997); Nix and Gao (1998); Gao et al. (1999). However, as strain gradients can be associated with geometrically necessary dislocations (GNDs), new internal-variable constitutive formulations were developed that incorporate dislocation densities as physically-based state variables instead of strain measures that were often used in phenomenological formulations (Arsenlis and Parks, 1999, 2002; Arsenlis et al., 2004; Gao and Huang, 2003; Ma et al., 2006a, b, also see chapter 4). This most recent class of constitutive models also allows one to incorporate additional metallurgical mechanisms such as grain boundary mechanics (section 4.1.4) or damage initiation into the constitutive description. Concerning additional deformation mechanisms, such as occurring in TWIP or TRIP steels, extended CPFE formulations have been suggested by Kalidindi (1998, 2001); Salem et al. (2005); Staroselskya and Anand (2003); Suiker and Turteltaub (2005) (also see section 7.3).
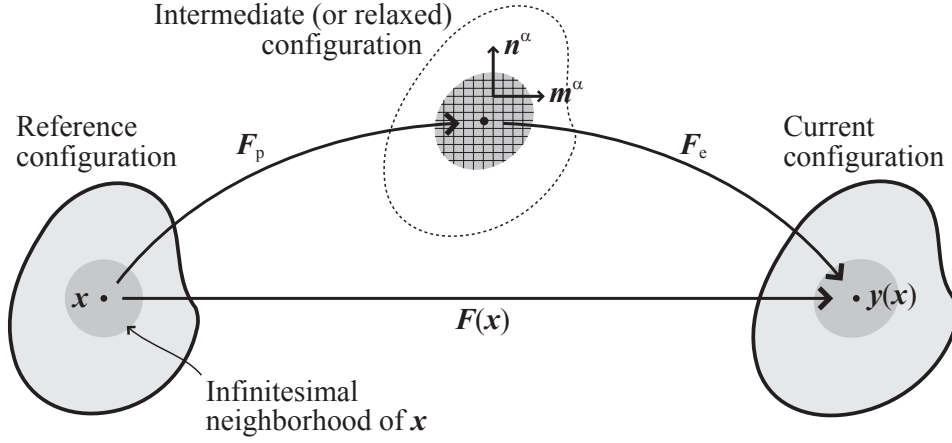
Figure 2.1: Schematic representation of the decomposition of deformation gradient $\boldsymbol{F} = \frac{\mathrm{d}y}{\mathrm{d}x}$. Vectors $\boldsymbol{m}^\alpha$ and $\boldsymbol{n}^\alpha$ are, respectively, the slip direction and the slip plane normal of the crystallographic lattice in the intermediate (relaxed) configuration.

2.2 Continuum Mechanical Framework

All crystal plasticity FEM models discussed in this work are formulated in a finite strain framework. The total deformation gradient, $\boldsymbol{F} = \frac{\mathrm{d}y}{\mathrm{d}x}$, can therefore be multiplicatively decomposed (Lee, 1969, figure 2.1)

$$\boldsymbol{F} = \boldsymbol{F}_\mathrm{e} \boldsymbol{F}_\mathrm{p}. \tag{2.1}$$

Here $\boldsymbol{F}_\mathrm{e}$ is the elastic part of the deformation gradient that describes both the elastic distortion and the rigid-body rotation. $\boldsymbol{F}_\mathrm{p}$ is the plastic part of the total deformation that is due to crystallographic slip. It is noteworthy that crystallographic slip does not change the orientation of the crystal lattice even though $\boldsymbol{F}_\mathrm{p}$ in general does include a rotational part, *i.e.* can be decomposed as $\boldsymbol{F}_\mathrm{p} = \boldsymbol{R}_\mathrm{p} \boldsymbol{U}_\mathrm{p}$.

As shown in figure 2.1, the decomposition of the total deformation gradient can be illustrated by introducing a reference configuration, an intermediate (relaxed) configuration and a current configuration. The plastic deformation gradient $\boldsymbol{F}_\mathrm{p}$ maps a material point from the reference configuration to the intermediate configuration. Respectively, the elastic deformation gradient $\boldsymbol{F}_\mathrm{e}$ projects the point from the intermediate configuration to the current configuration. It is, however, important to realize that, in general, the order of the decomposition does not correspond to the actual deformation sequence.

The velocity gradient in the current configuration, denoted as $\tilde{\boldsymbol{L}}$, can be written as

$$\tilde{\boldsymbol{L}} := \dot{\boldsymbol{F}} \boldsymbol{F}^{-1} = \dot{\boldsymbol{F}}_\mathrm{e} \boldsymbol{F}_\mathrm{e}^{-1} + \boldsymbol{F}_\mathrm{e} \dot{\boldsymbol{F}}_\mathrm{p} \boldsymbol{F}_\mathrm{p} \boldsymbol{F}_\mathrm{e}^{-1} = \tilde{\boldsymbol{L}}_\mathrm{e} + \tilde{\boldsymbol{L}}_\mathrm{p} . \tag{2.2}$$

In the CPFEM the plastic velocity gradient $\boldsymbol{L}_\mathrm{p}$ (in the intermediate (relaxed) configu-

ration) is determined by the slip rates $\dot{\gamma}^\alpha$ on all active slip systems α

$$\boldsymbol{L}_\text{p} := \dot{\boldsymbol{F}}_\text{p}\boldsymbol{F}_\text{p}^{-1} = \sum_{\alpha=1}^{N_\text{slip}} \dot{\gamma}^\alpha \boldsymbol{m}^\alpha \otimes \boldsymbol{n}^\alpha, \tag{2.3}$$

where $\boldsymbol{m}^\alpha$ is the slip direction and $\boldsymbol{n}^\alpha$ the slip plane normal of slip system α. The magnitude of the shear rates $\dot{\gamma}^\alpha$ is determined by the constitutive model used, see sections 2.3, 4.1, and 4.2.

2.3   Phenomenological Constitutive Equations

Phenomenological constitutive models mostly use a critical resolved shear stress, τ_c^α, as state variable for each slip system α. Therefore, the shear rate, $\dot{\gamma}^\alpha$, is formulated as a function of the resolved shear stress, $\tau^\alpha = 0.5\, \mathbb{C} \left[\boldsymbol{F}_\text{e}^\text{T}\boldsymbol{F}_\text{e} - \boldsymbol{I} \right] : \boldsymbol{m}^\alpha \otimes \boldsymbol{n}^\alpha$, and that critical resolved shear stress

$$\dot{\gamma}^\alpha = f\left(\tau^\alpha, \tau_\text{c}^\alpha\right) \tag{2.4}$$

and the evolution of the material state is formulated as function of the total shear, γ, and the shear rate, $\dot{\gamma}^\alpha$

$$\tau_\text{c}^\alpha = g\left(\gamma, \dot{\gamma}\right). \tag{2.5}$$

One prominent group of examples for such a formulation is the one suggested by Rice (1971); Hutchinson (1976); Peirce et al. (1982) and Peirce et al. (1983) for face-centered cubic (fcc) metallic crystals. In this framework the kinetic law on a slip system is

$$\dot{\gamma}^\alpha = \dot{\gamma}_0 \left| \frac{\tau^\alpha}{\tau_\text{c}^\alpha} \right|^n \operatorname{sgn}\left(\tau^\alpha\right) , \tag{2.6}$$

where $\dot{\gamma}^\alpha$ is the shear rate on slip system α subjected to the resolved shear stress τ^α at a slip resistance τ_c^α; $\dot{\gamma}_0$ and n are material parameters that determine the reference shear rate and the rate sensitivity of slip, respectively. The influence of any slip system, index β, on the hardening behavior of a (fixed) slip system α is given by

$$\dot{\tau}_\text{c}^\alpha = h_{\alpha\beta} \left| \dot{\gamma}^\beta \right| , \tag{2.7}$$

where $h_{\alpha\beta}$ is referred to as hardening matrix

$$h_{\alpha\beta} = q_{\alpha\beta} \left[h_0 \left(1 - \frac{\tau_\text{c}^\beta}{\tau_\text{s}} \right)^a \right] , \tag{2.8}$$

which empirically captures the micro-mechanical interactions among different slip systems. In this formulation h_0, a, and τ_s are slip hardening parameters, which are assumed to be identical for all fcc slip systems owing to the underlying characteristic dislocation reactions. The parameter $q_{\alpha\beta}$ is a measure for latent hardening; its value is usually taken as 1.0 for coplanar slip systems α and β, and 1.4 otherwise, which renders the hardening model anisotropic.

In the literature a number of variations of equations (2.6) and (2.7) can be found. Some authors (Becker, 1991) use the hyperbolic sine function instead of a power law in equation (2.6), while others (Sarma et al., 1998) use modified hardening laws like a generalized Voce equation (Voce, 1948; Kocks, 1976) instead of equation (2.7).

These types of kinetic formulations are currently the most frequently used ones in CPFE models although they suffer from the drawback that the material state is only described in terms of the critical resolved shear stress, τ_c, and not in terms of lattice defect populations (Kocks, 1966; Mecking and Kocks, 1986). The latter approach, however, is required to render crystal plasticity models path- and size-dependent, as will be discussed later.

Part I

Crystal Plasticity at Small Microstructural Scales

Chapter 3

Special Aspects of Small Scale Plasticity Simulations

In the context of this work small scale simulation denotes all kinds of simulations, where the element size of the finite element mesh is smaller than the grain size, *i.e.* each grain is represented by several elements. This kind of simulation is often also called direct crystal plasticity simulation.

Due to its anisotropic nature plastic deformation is never homogeneous on a subgrain scale. First, grains of different orientation are of different stiffness, which leads to strain differences between grains (Sachtleber et al., 2002), *i.e.* long range strain gradients, second grain boundaries as well as free surfaces also lead to in-grain (short range) strain gradients (see *e.g.* Kuo et al., 2003). Therefore, constitutive models for direct CPFEM should be able to take strain gradients as well as the influence of grain boundaries and free surfaces into account. As strain gradients are associated with so called geometrically necessary dislocations (GNDs), dislocation density based models have been developed (Arsenlis and Parks, 1999, 2002; Arsenlis et al., 2004). However, also phenomenological models as presented in section 2.3 have been extended to incorporate strain gradients as well as the influence of grain boundaries (Evers et al., 2002, 2004a, b; Svendsen, 2002).

Grain boundaries act as obstacles to dislocation motion. At the onset of plastic deformation of polycrystals, mobile dislocations are first created on the slip system with the largest *local* resolved shear stress in the grain with the most favorable orientation. When encountering a grain boundary these mobile dislocations accumulate in front of that interface. Such events lead to stress concentrations at the interface that add to the external stress field at this material point. These micro-plastic effects, where the local arrangement of dislocations determines the local stress, cannot be treated one-to-one in a crystal plasticity continuum mechanical framework because such models map the underlying dislocation mechanics in a phenomenological statistical or even empirical form. However, homogenization is admissible at larger plastic strains where most of the slip activation processes can be captured by long-range stresses rather than by local ones

(Clark et al., 1992). This means that the dislocation mechanics can, beyond the micro-plastic regime, be homogenized in the form of statistical dislocation populations, which in turn can be embedded in state evolution constitutive equations in a crystal plasticity theory (Evers et al., 2004a, b; Arsenlis and Parks, 2002; Arsenlis et al., 2004; Ma et al., 2006b).

Phenomenological treatment of GNDs by the Geers group (Evers et al., 2002)   In their polycrystal model Evers, Parks, Brekelmans, and Geers treat the situation where more than one grain is present at each integration point. This situation will be discussed in detail in part II of this thesis. However, they introduce a kind of strain gradient on the single grain scale to be discussed here. In the model the grains are divided into a core region and a surrounding composed out of several bicrystal regions shared with the neighboring grains. Boundary conditions are formulated for the compatibility and stresses of the bicrystals to calculate the deformation gradients $\boldsymbol{F}_{\mathrm{p}}^{b}$. Due to this the plastic deformation gradient of the core $\boldsymbol{F}_{\mathrm{p}}^{c}$ of each grain will deviate from the plastic deformation gradient in the surrounding bicrystals. Using the approach of Arsenlis and Parks (1999) this jump in $\boldsymbol{F}_{\mathrm{p}}$ can be translated into densities of geometrically necessary dislocations using Nye's dislocation tensor $\boldsymbol{\Lambda}$ (Nye, 1953):

$$\boldsymbol{\Lambda} = -\left(\boldsymbol{n}_0^b \times \frac{\Delta \boldsymbol{F}_{\mathrm{p}}^{\mathrm{T}}}{l}\right)^T , \ \Delta \boldsymbol{F}_{\mathrm{p}} = \boldsymbol{F}_{\mathrm{p}}^c - \boldsymbol{F}_{\mathrm{p}}^b , \tag{3.1}$$

here $\boldsymbol{n}_0^b$ is the normal of the boundary between core and bicrystal region and l a length parameter representing the width of the transition zone. $\boldsymbol{\Lambda}$ can also be calculated as function of the GND densities

$$\boldsymbol{\Lambda} = \sum_\xi \rho_{\mathrm{GND}}^\xi \boldsymbol{b}_0^\xi \boldsymbol{t}_0^\xi , \tag{3.2}$$

where $\boldsymbol{b}_0^\xi$ and $\boldsymbol{t}_0^\xi$ are the initial Burgers and tangent vector of dislocation type ξ. However, equating equations (3.1) and (3.2) does not lead to a unique solution, therefore, minimizing the sum of the squares of the dislocation densities is used to calculate ρ_{GND}^ξ.

In the constitutive model finally a set of interaction parameters $A^{\alpha\xi}$ is used to calculate an additional strength contribution due to these GNDs:

$$s_{\mathrm{GND}}^\alpha = cGb\sqrt{\sum_\xi A^{\alpha\xi} \left|\rho_{\mathrm{GND}}^\xi\right|} \tag{3.3}$$

with c a constant and G the shear modulus.

Dislocation density based treatment of GNDs by Arsenlis and Parks (Arsenlis and Parks, 2002; Arsenlis et al., 2004)   In 2002, Arsenlis and Parks introduced a

constitutive model based on signed dislocation densities, *i.e.* positive and negative edge and screw dislocations. The usual evolution equations derived for the four dislocation populations do not alter the polarity of the dislocation network. However, *additional density evolution equations that do modify the polarity can be considered, based on (i) the divergence of dislocation density flux and (ii) plastic flow in the presence of non-vanishing net dislocation tensor (i.e., non-vanishing dislocation polarity)* (cited from Arsenlis and Parks (2002)). While these processes were neglected in the 2002 publication a follow-up paper (Arsenlis et al., 2004) was published that includes these terms in the evolution equations for the dislocation densities. In the corresponding 2-D implementation the dislocation densities and their gradients are implemented as additional (nodal) degrees of freedom in the element formulation. Therefore, dislocation density/density-flux boundary conditions need to be specified to solve the dislocation evolution equations. This formulation does not only allow the calculation of geometrically necessary dislocation densities, *i.e.* differences between positive and negative densities of edges and screws respectively, but at the same time grain boundaries and free surfaces can be described by means of adequate boundary conditions.

Phenomenological treatment of grain boundaries by the Geers group (Evers et al., 2004b)   In this type of models grain boundaries appear as perfect obstacles that do not allow dislocation penetration events. This can be implemented in FE simulations as an additional set of boundary conditions, namely, as a zero shear condition perpendicular to the interfaces. While the approach appears to be relatively straightforward at first view it can be rather intricate when meshing complicated grain aggregates. As shown in Evers et al. (2004b) these additional boundary conditions result in an increased hardening of the material, however, they do not result in an increase of the initial yield stress, *i.e.* the Hall–Petch effect is not captured. In order to overcome this drawback Evers et al. suggested grain boundary dislocations (GBDs) as an initial content of GNDs at the position of the grain boundaries. These GBDs are calculated from the crystallographic misorientation across the interface in the following way (Evers et al., 2004b): Consider two crystals of orientation $\boldsymbol{Q}_\mathrm{I}$ and $\boldsymbol{Q}_\mathrm{II}$ with slip systems $\left(\boldsymbol{m}^{\alpha,\beta}, \boldsymbol{t}^{\alpha,\beta}, \boldsymbol{n}^{\alpha,\beta}\right)$ and $\alpha, \beta = 1, 2, \ldots, 12$,[1] separated by a grain boundary with normal vector $\boldsymbol{n}_\mathrm{GB}$. The density of the GBDs is then obtained as

$$\rho^{\alpha}_\mathrm{GBD} = \mathrm{sgn}\left(\boldsymbol{n}^\alpha \cdot \boldsymbol{n}_\mathrm{GB}\right) \frac{\left(\left|\boldsymbol{n}^\alpha \cdot \boldsymbol{n}_\mathrm{GB}\right| - \left|\boldsymbol{n}^\beta \cdot \boldsymbol{n}_\mathrm{GB}\right|\right)^2}{b^2} \, , \qquad (3.4)$$

where the slip system β has to be chosen such as to minimize the magnitude of $\rho^{\alpha}_\mathrm{GBD}$.

In the following the two dislocation density based models developed at the Max-Planck-Institut für Eisenforschung are presented.

---

[1]The indices α and β always refer to crystals I and II respectively.

Chapter 4

Constitutive Models for Small Scale Simulations

Both constitutive models presented in this section are based on dislocation densities. The main difference is that the first model treats unsigned dislocation densities, while the second one is based on signed dislocation densities and fluxes thereof. This gives a more direct access to geometrically necessary dislocations and the associated long range stress fields. Moreover the incorporation of grain and phase boundaries is easier as it does not require special grain boundary elements. As a consequence, meshing complex microstructures is straightforward using the second model while it was almost impossible using the first one.

Apart from these differences both models have a similar structure as they are build on the same general constitutive framework. As kinetic equation of state they use the Orowan equation (Orowan, 1934), however, with some small differences in the respective implementations. The second part of the models is in both cases formed by a set of state evolution equations, which are, however, rather different as both models use different sets of state variables.

4.1 A Constitutive Model Based on Unsigned Dislocation Densities

This model was systematically derived from the three internal variable model (3IVM) introduced by Roters et al. (2000). To achieve this goal the 3IVM was first extended to take individual slip systems into account (Ma and Roters, 2004). In a second step the model was adopted for the implementation into a finite element framework (Ma et al., 2006a). In this process also non-local effects, *i.e.* strain gradients, where incorporated. Finally, the effect of grain boundaries was added (Ma et al., 2006b) to complete the model.

As state variables the model uses one density of statistically stored dislocations, $\rho_{\mathrm{SSD}}^{\alpha}$, for each slip system α. For the description of the slip system interaction two additional sets of dislocations are derived for each slip system by means of simple geometric projections:

$$\rho_{\mathrm{F}}^{\alpha} = \sum_{\beta=1}^{N_{\mathrm{slip}}} \chi^{\alpha\beta} \rho_{\mathrm{SSD}}^{\beta} \left| \cos\left(\boldsymbol{n}^{\alpha}, \boldsymbol{t}^{\beta}\right) \right| \tag{4.1}$$

$$\rho_{\mathrm{P}}^{\alpha} = \sum_{\beta=1}^{N_{\mathrm{slip}}} \chi^{\alpha\beta} \rho_{\mathrm{SSD}}^{\beta} \left| \sin\left(\boldsymbol{n}^{\alpha}, \boldsymbol{t}^{\beta}\right) \right| . \tag{4.2}$$

The forest dislocations, $\rho_{\mathrm{F}}^{\alpha}$, are those dislocations perpendicular to slip system α. These have to be cut by the moving mobile dislocations, $\rho_{\mathrm{m}}^{\alpha}$, of slip system α. The dislocations parallel to slip system α, $\rho_{\mathrm{P}}^{\alpha}$, have to be passed by the mobile dislocations, $i.e.$ their long range stress field forms the critical stress of slip system α. In above equations, $\boldsymbol{n}^{\alpha}$ are the slip plane normals and $\boldsymbol{t}^{\beta}$ the dislocation line directions of the respective slip systems. The interaction strength between different slip systems, $\chi^{\alpha\beta}$, distinguishes self interaction strength, coplanar interaction strength, cross slip strength, glissile junction strength, Hirth lock strength, and Lomer–Cottrell lock strength depending on the reaction products formed between the two slip systems α and β (Arsenlis and Parks, 2002).

4.1.1   The Kinetic Equation of State

In a dislocation-based model the Orowan equation typically serves as kinetic equation of state instead of equation (2.6) introduced in section 2.3 as it couples shear rates to mobile dislocations, $i.e.$ it translates a continuum mechanical term into the physics of dislocations:

$$\dot{\gamma}^{\alpha} = \rho_{\mathrm{m}}^{\alpha} b v^{\alpha} , \tag{4.3}$$

where $\rho_{\mathrm{m}}^{\alpha}$ is the density of mobile dislocations, b the magnitude of the Burgers vector and v^{α} the average velocity of the mobile dislocations. According to Ma and Roters (2004), the mobile dislocation density can be calculated from the statistically stored dislocation density by a simple scaling law

$$\rho_{\mathrm{m}}^{\alpha} = \frac{2 k_{\mathrm{B}} T}{c_1 c_2 c_3 G b^3} \sqrt{\rho_{\mathrm{P}}^{\alpha} \rho_{\mathrm{F}}^{\alpha}} , \tag{4.4}$$

where T is the absolute temperature and k_{B} the Boltzmann constant, while c_1 to c_3 are constants introduced in the dislocation density evolution laws described below.

Under the assumption of forest cutting as the rate determining process, the velocity of the mobile dislocations can be calculated as

$$v^{\alpha} = \lambda^{\alpha} \nu_{\mathrm{attack}} \exp\left(-\frac{Q_{\mathrm{slip}}}{k_{\mathrm{B}} T}\right) \sinh\left(\frac{\tau_{\mathrm{eff}}^{\alpha} V^{\alpha}}{k_{\mathrm{B}} T}\right) \mathrm{sgn}\left(\tau^{\alpha}\right) , \tag{4.5}$$

where λ^α is the jump width, which is inversely proportional to the forest dislocation spacing, ν_{attack} is the attack frequency, Q_{slip} is the effective activation energy for dislocation glide, and V^α the activation volume, which can be calculated as

$$V^\alpha = c_3 \lambda^\alpha b^2 \tag{4.6}$$

with c_3 being a fitting constant of order unity.

Finally, the effective shear stress τ_{eff}^α can be calculated from the resolved shear stress and the passing stress as

$$\tau_{\text{eff}}^\alpha = \begin{cases} |\tau^\alpha| - \tau_{\text{pass}}^\alpha = |\tau^\alpha| - c_1 G b \sqrt{\rho_{\text{P}}^\alpha + \rho_{\text{m}}^\alpha} & \text{for} \quad |\tau^\alpha| > \tau_{\text{pass}}^\alpha \\ 0 & \text{for} \quad |\tau^\alpha| \leq \tau_{\text{pass}}^\alpha \end{cases} . \tag{4.7}$$

4.1.2 The State Evolution

The phenomenological description of hardening (equation (2.7) in section 2.3) is substituted by the evolution of the dislocation densities. For this purpose rate equations are formulated based on individual dislocation reactions. In Ma and Roters (2004) four such processes are taken into account, namely, lock and dipole formation as processes increasing the dislocation density and both, athermal and thermally activated annihilation as recovery processes. Detailed derivations of these rate equations can be found in Ma and Roters (2004). In the following we summarize the results:

- Lock formation

$$\dot{\rho}_{\text{SSD}}^{\alpha+} = \frac{c_4}{b} \sqrt{\rho_{\text{F}}^\alpha} \, |\dot{\gamma}^\alpha| \tag{4.8}$$

- Dipole formation

$$\dot{\rho}_{\text{SSD}}^{\alpha+} = \frac{c_5}{b} d_{\text{dipole}}^\alpha \rho_{\text{m}}^\alpha \, |\dot{\gamma}^\alpha| \tag{4.9}$$

$$d_{\text{dipole}} = \frac{\sqrt{3} G b}{16\pi(1-\nu)} \left(|\tau^\alpha| - \tau_{\text{pass}}^\alpha \right)^{-1} \tag{4.10}$$

- Athermal annihilation

$$\dot{\rho}_{\text{SSD}}^{\alpha-} = -c_6 \rho_{\text{SSD}}^\alpha \, |\dot{\gamma}^\alpha| \tag{4.11}$$

- Thermal annihilation due to climb of edge dislocations

$$\dot{\rho}_{\text{SSD}}^{\alpha-} = -c_7 \frac{D_0 b^3}{k_{\text{B}} T} \exp\left(-\frac{Q_{\text{bulk}}}{k_{\text{B}} T} \right) \rho_{\text{SSD}}^{\alpha}{}^2 |\tau^\alpha| \left| \frac{\dot{\gamma}^\alpha}{\dot{\gamma}_{\text{ref}}} \right|^{c_8} \tag{4.12}$$

$c_4, ..., c_8$ are fitting constants, d_{dipole} is the critical distance for dipole formation, D_0 is the diffusion coefficient, Q_{bulk} is the activation energy for dislocation climb, and $\dot{\gamma}_{\text{ref}}$ is a reference shear rate.

4.1.3 Geometrically Necessary Dislocations – Strain Gradients

This section shows how geometrically necessary dislocations (GNDs) can be introduced in the dislocation model presented above. Nye's dislocation tensor (Nye, 1953) can be used to translate the strain gradient into GNDs:

$$\mathbf{\Lambda} = -\frac{1}{b}\left(\boldsymbol{\nabla}_{\boldsymbol{x}} \times \boldsymbol{F}_{\mathrm{p}}{}^{\mathrm{T}}\right)^{\mathrm{T}}, \tag{4.13}$$

where the nabla operator $\boldsymbol{\nabla}_{\boldsymbol{x}}$ is defined as the derivative with respect to the reference coordinate $\boldsymbol{\nabla}_{\boldsymbol{x}} = \partial/\partial\boldsymbol{x}$. Using equation (4.13) the resultant Burgers vector for an arbitrary oriented surface can be calculated. In general this tensor is non-symmetric with nine independent values. Although there are 12 slip systems for the fcc crystal structure, the calculation of the exact GND content for every slip system requires additional assumptions, as only 6 of them are geometrically independent (Nemat-Nasser et al., 1998).

Using the material time derivative of equation (4.13) in conjunction with equation (2.3), the change of the geometrically necessary dislocation density can be derived (Ma et al., 2006a)

$$\dot{\rho}_{\mathrm{GND}}^{\alpha} = \frac{1}{b}\left|\left|\boldsymbol{\nabla}_{\boldsymbol{x}} \times \left(\dot{\gamma}^{\alpha}\boldsymbol{F}_{\mathrm{p}}{}^{\mathrm{T}}\boldsymbol{n}^{\alpha}\right)\right|\right|. \tag{4.14}$$

The integration of the GNDs into the constitutive model is now simply a matter of extending the projection into forest and parallel dislocations (equations (4.1) and (4.2)). To render this projection more convenient, $\dot{\rho}_{\mathrm{GND}}^{\alpha}$ is first decomposed into three groups of dislocations: one group of screw dislocations with its tangent vector parallel to the slip direction $\boldsymbol{m}^{\alpha}$, the other two groups of edge dislocations with their tangent vectors parallel to $\boldsymbol{n}^{\alpha}$ and $\boldsymbol{t}^{\alpha} = \boldsymbol{n}^{\alpha} \times \boldsymbol{m}^{\alpha}$

$$\dot{\rho}_{\mathrm{GNDs}}^{\alpha} = \frac{1}{b}\left[\boldsymbol{\nabla}_{\boldsymbol{x}} \times \left(\dot{\gamma}^{\alpha}\boldsymbol{F}_{\mathrm{p}}{}^{\mathrm{T}}\boldsymbol{n}^{\alpha}\right)\right] \cdot \boldsymbol{m}^{\alpha} \tag{4.15}$$

$$\dot{\rho}_{\mathrm{GNDet}}^{\alpha} = \frac{1}{b}\left[\boldsymbol{\nabla}_{\boldsymbol{x}} \times \left(\dot{\gamma}^{\alpha}\boldsymbol{F}_{\mathrm{p}}{}^{\mathrm{T}}\boldsymbol{n}^{\alpha}\right)\right] \cdot \boldsymbol{t}^{\alpha} \tag{4.16}$$

$$\dot{\rho}_{\mathrm{GNDen}}^{\alpha} = \frac{1}{b}\left[\boldsymbol{\nabla}_{\boldsymbol{x}} \times \left(\dot{\gamma}^{\alpha}\boldsymbol{F}_{\mathrm{p}}{}^{\mathrm{T}}\boldsymbol{n}^{\alpha}\right)\right] \cdot \boldsymbol{n}^{\alpha}, \tag{4.17}$$

which satisfy

$$\left(\dot{\rho}_{\mathrm{GND}}^{\alpha}\right)^2 = \left(\dot{\rho}_{\mathrm{GNDs}}^{\alpha}\right)^2 + \left(\dot{\rho}_{\mathrm{GNDet}}^{\alpha}\right)^2 + \left(\dot{\rho}_{\mathrm{GNDen}}^{\alpha}\right)^2. \tag{4.18}$$

Equations (4.15) to (4.17) are a set of evolution equations for ρ_{GND}, just like those for ρ_{SSD} derived in the previous section. Finally, the extended projection reads

$$\begin{aligned}
\rho_{\mathrm{F}}^{\alpha} = \sum_{\beta=1}^{N}\chi^{\alpha\beta}\Bigg[&\rho_{\mathrm{SSD}}^{\beta}\left|\cos(\boldsymbol{n}^{\alpha},\boldsymbol{t}^{\beta})\right| + \left|\rho_{\mathrm{GNDs}}^{\beta}\cos(\boldsymbol{n}^{\alpha},\boldsymbol{m}^{\beta})\right| \\
&+ \left|\rho_{\mathrm{GNDet}}^{\beta}\cos(\boldsymbol{n}^{\alpha},\boldsymbol{t}^{\beta})\right| + \left|\rho_{\mathrm{GNDen}}^{\beta}\cos(\boldsymbol{n}^{\alpha},\boldsymbol{n}^{\beta})\right|\Bigg]
\end{aligned} \tag{4.19}$$
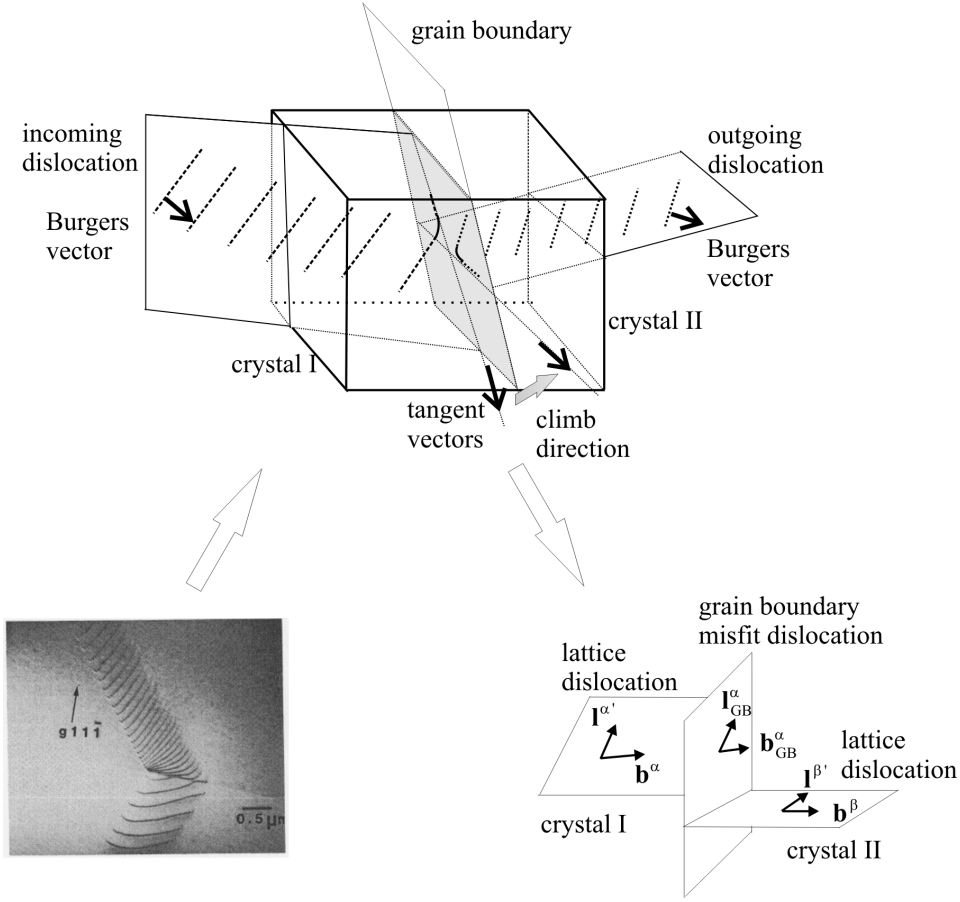
Figure 4.1: Schematic drawing of penetration events for mobile dislocations through a grain boundary. The experimentally obtained micrograph is taken from the work of Shen, Wagoner, and Clark (1986) on steel. Here $\boldsymbol{l}^{\alpha\prime}$, $\boldsymbol{l}^{\beta\prime}$, and $\boldsymbol{l}^{\alpha}_{\mathrm{GB}}$ are the tangent vectors of the dislocations, and $\boldsymbol{b}^{\alpha}$, $\boldsymbol{b}^{\beta}$, and $\boldsymbol{b}^{\alpha}_{\mathrm{GB}}$ are their Burgers vectors.

$$
\begin{aligned}
\rho^{\alpha}_{\mathrm{P}} \;=\; & \sum_{\beta=1}^{N} \chi^{\alpha\beta} \left[\rho^{\beta}_{\mathrm{SSD}} \left| \sin(\boldsymbol{n}^{\alpha}, \boldsymbol{t}^{\beta}) \right| + \left| \rho^{\beta}_{\mathrm{GNDs}} \sin(\boldsymbol{n}^{\alpha}, \boldsymbol{m}^{\beta}) \right| \right. \\
& \left. + \left| \rho^{\beta}_{\mathrm{GNDet}} \sin(\boldsymbol{n}^{\alpha}, \boldsymbol{t}^{\beta}) \right| + \left| \rho^{\beta}_{\mathrm{GNDen}} \sin(\boldsymbol{n}^{\alpha}, \boldsymbol{n}^{\beta}) \right| \right] \;,
\end{aligned}
\tag{4.20}
$$

where absolute values of GNDs are used, so that the signs of their Burgers vectors are neglected. A direct result of this treatment is that no kinematic hardening can be predicted, which is acceptable for single phase material and unidirectional loading. This shortcoming is overcome by the second MPIE model including dislocation fluxes presented in section 4.2.

4.1.4 Grain Boundaries

In this model partial transparency of the interface to dislocations is assumed (Ma et al., 2006b). The transmission probability of incoming mobile dislocations to penetrate a grain boundary can be treated in terms of an activation concept (see figure 4.1). The enthalpy for this activation process stems from the elastic energy that is required for the formation of misfit dislocations, which remain as debris in the interface upon slip penetration. This activation enthalpy enters as an additional contribution into the activation term for the slip of mobile dislocations (equation (4.5)). It is likely that each transmission event will occur at the smallest possible energy consumption. This condition provides a selection criterion for the slip systems involved. The main task in this model, therefore, consists in identifying the outbound slip system on the other side of the boundary, which provides the closest geometrical match to the inbound slip system. The smallest misalignment between the active inbound and the expected outbound slip systems leads to the smallest possible energy barrier[1]. For an arbitrary transmission event, it is obvious that any incoming slip system does not, as a rule, match a corresponding one on the outbound side exactly, *i.e.* the shear is usually not coherent on the two sides of a grain boundary. Therefore, in order to meet the conservation of the lattice defect vector sum when crossing an interface, misfit dislocations will be created in the grain boundary. The additional energy required to produce such an extra misfit dislocation acts as an energy barrier for the thermally activated slip transmission event. This barrier, hence, acts as a penalty energy for such a situation. However, it should be interpreted in a somewhat more statistical manner. This means that it is not required to yield a strict one-to-one correlation between incoming and outgoing dislocations rather than a match in the overall shear on either side. Moreover, it is conceivable that the transmission event only rarely takes place owing to the local stiffening effect that it introduces. Along with this grain boundary hardening effect the accumulation of geometrically necessary dislocations in front of the interfaces acts as an additional stiffness effect. The mathematical treatment of this dislocation-based approach to grain boundary effects in the CPFE framework shown in Ma et al. (2006b) leads to the following equation for the penalty energy

$$E_{\mathrm{GB}}^{\alpha} = \min_{\beta} \left\{ c_9' \frac{1}{2} G b^2 l^{\alpha} R^{\alpha} \right\}, \tag{4.21}$$

where c_9' is a fitting constant, l^{α} is the length of the incoming dislocation and R^{α} is a geometrical factor describing the correlation of the incoming system α and the outgoing system β that minimizes the activation energy.

It is worth to mention, that while the absolute magnitude of E_{GB}^{α} can be changed by the choice of c_9', the ratio of the activation energies for different boundaries is not affected by this value. A detailed study on the effect of the magnitude of parameter c_9' can be found in Ma et al. (2006c).

---

[1]It is not actually checked whether or not this slip system can be activated by the local stress but it is anticipated as a likely situation as the outbound slip system orientation is close to the inbound one.

Figure 4.2: Normalized activation energy for a twist grain boundary with rotations about the $[1\,1\,1]$ direction using $c_9' = 1$ in equation (4.21).

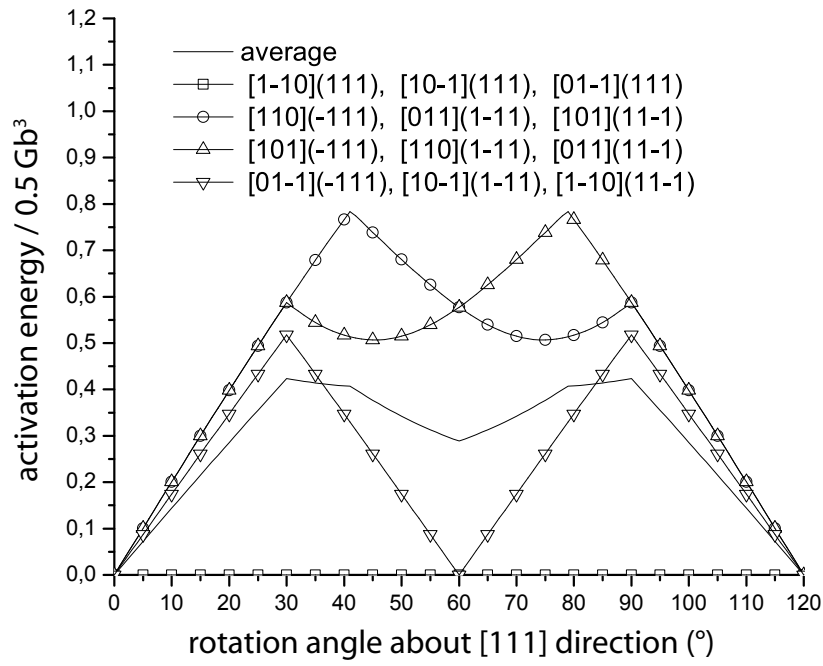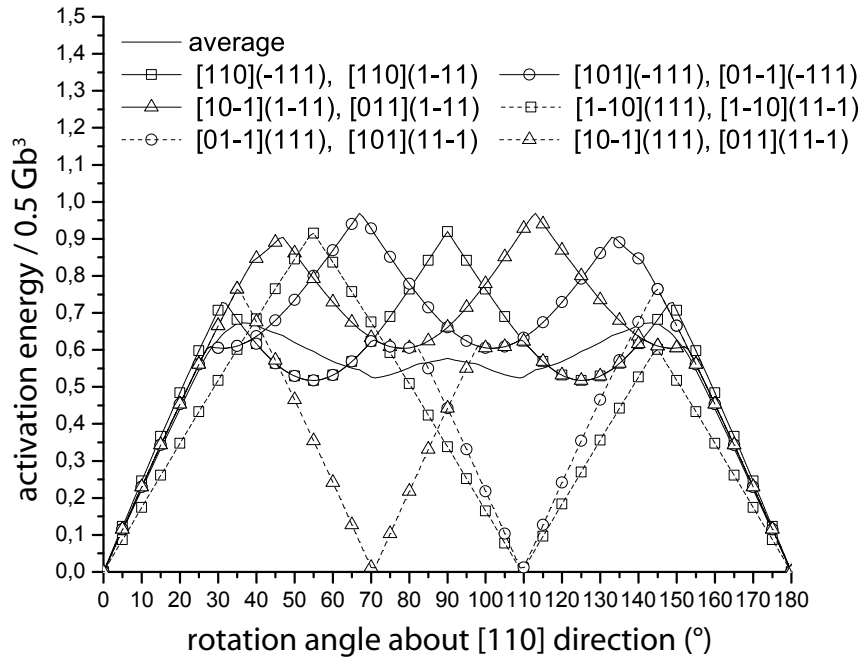

Figure 4.3: Normalized activation energy for a twist grain boundary with rotations about the $[1\,1\,0]$ direction using $c_9' = 1$ in equation (4.21).

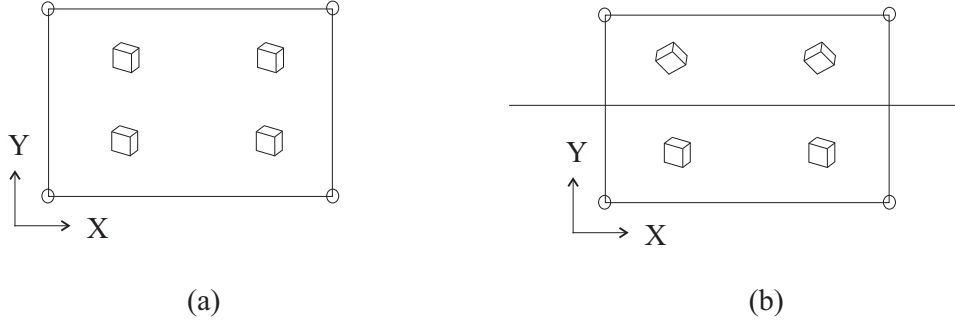(a)   (b)

Figure 4.4: 2-D schematic drawing of the bulk element (a) and of the grain boundary element (b) for the initial case. During the deformation, for the bulk element GNDs should keep the continuity of the lattice in X and Y directions, while for the grain boundary element the lattice continuity is only kept in X direction. In Y direction the penetration energy is introduced.

As an example, the activation energies of an incoming dislocation with a length b are calculated for twist boundaries that are characterized by rotations about the $[1\,1\,1]$ and $[1\,1\,0]$ crystal directions, respectively, under the additional constraint, that the grain boundary plane is perpendicular to the rotation axes. The calculations apply for the fcc crystal structure. The results are shown in figures 4.2 and 4.3, where the activation energy has been normalized by the factor $\frac{1}{2}Gb^3$ and the constant c_9' was chosen to be equal to one. Both figures show also the average of the energy barrier for better comparison. From these curves it is clear that a grain boundary is a strong obstacle to dislocation motion, as the average activation energies for the formation of the misfit dislocations easily reach the order of magnitude of the activation energy for cutting forest lattice dislocations.

It is observed that the energies for slip penetration are periodic. This effect arises from the octahedral symmetry of the slip systems in the crystal. The activation energy for the penetration shows a complex relationship with the misorientation especially when the rotation angle is larger than about 20°. One can see that the energy barrier strongly depends on the misorientation of the two crystals. However, the average activation energies show a much more constant behavior, which implies that the strong effects for single slip systems will be averaged out to some extend in macroscopic experiments.

In most CPFE implementations grain boundaries coincide with element boundaries. In the dislocation-based approach discussed above a special type of bi-material element across the grain boundary is introduced. In this element one half of the Gauss points belongs to one crystal, while the other one belongs to the other crystal (see figure 4.4). In this new type of element one can use a modified version of equation (4.5), namely

$$v^\alpha = \lambda^\alpha \nu_{\text{attack}} \exp\left(-\frac{Q_{\text{eff}}^\alpha}{k_{\text{B}}T}\right) \sinh\left(\frac{\tau_{\text{eff}}^\alpha V^\alpha}{k_{\text{B}}T}\right) \text{sgn}\left(\tau^\alpha\right) \ , \qquad (4.22)$$

where Q_{eff}^{α} is the modified effective activation energy

$$Q_{\text{eff}}^{\alpha} = Q_{\text{slip}} + Q_{\text{GB}}^{\alpha} . \tag{4.23}$$

When comparing this equation with the one specified in section 4.1.1, the only difference is the use of Q_{eff}^{α} instead of Q_{slip}. According to equation (4.21) the energy Q_{GB}^{α} is calculated by finding the outgoing slip system β that minimizes it:

$$Q_{\text{GB}}^{\alpha} = (E_{\text{GB}}^{\alpha})_{l^{\alpha}=b} = \min_{\beta} c_9 \frac{1}{2} Gb^3 R^{\alpha}, \tag{4.24}$$

where c_9 is a dimensionless fitting parameter, which is a function of c_9' and the grain boundary element thickness L_{GB}.

4.2 A Constitutive Model Based on Signed Dislocation Densities Including Dislocation Fluxes

In this section a second constitutive model based on dislocation densities is introduced. Based on the experiences with the model presented in the previous section two aspects were in the focus of the development. First, a more intuitive way of calculating the geometrically necessary dislocation density, and second, to avoid the need of a special element for the grain boundaries. Both points are achieved by introducing signed dislocation densities and their fluxes.

4.2.1 Microstructural State Variables

4.2.1.1 Signed Densities of Single Dislocations

The dislocation structure at the material point is characterized by densities of signed edge and screw dislocations, $\rho_{\text{e}+}^{\alpha}$, $\rho_{\text{e}-}^{\alpha}$ and $\rho_{\text{s}+}^{\alpha}$, $\rho_{\text{s}-}^{\alpha}$, where $\alpha = 1, \ldots, N_{\text{slip}}$ indicates the slip system. The signed nature of those densities allows to discriminate between the total dislocation densities

$$\rho^{\alpha} = \rho_{\text{e}}^{\alpha} + \rho_{\text{s}}^{\alpha} \tag{4.25a}$$
$$\rho_{\text{e}}^{\alpha} = \rho_{\text{e}+}^{\alpha} + \rho_{\text{e}-}^{\alpha} \tag{4.25b}$$
$$\rho_{\text{s}}^{\alpha} = \rho_{\text{s}+}^{\alpha} + \rho_{\text{s}-}^{\alpha} \tag{4.25c}$$

and the (either positive or negative) excess densities of edge and screw character

$$\Delta\rho_{\text{e}}^{\alpha} = \rho_{\text{e}+}^{\alpha} - \rho_{\text{e}-}^{\alpha} \tag{4.26a}$$
$$\Delta\rho_{\text{s}}^{\alpha} = \rho_{\text{s}+}^{\alpha} - \rho_{\text{s}-}^{\alpha} . \tag{4.26b}$$
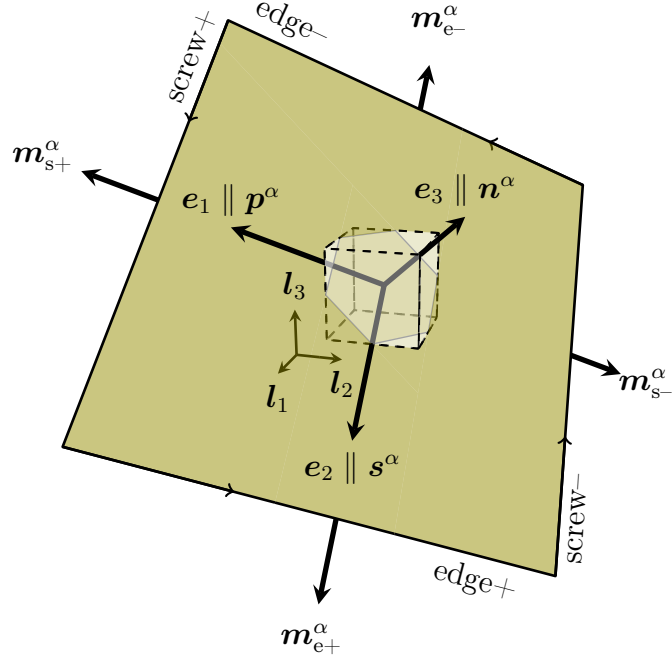
Figure 4.5: Schematic dislocation loop (dark shade) on its slip plane with normal $\boldsymbol{n}^\alpha$ and slip direction $\boldsymbol{s}^\alpha$ defining slip system triad $\boldsymbol{e}_1$, $\boldsymbol{e}_2$, $\boldsymbol{e}_3$ (thick lines). Arrows along the loop periphery indicate positive line direction giving rise to the convention for signed dislocation characters as shown. The small (dashed) interior cube illustrates the crystal unit cell orientation with the basis triad $\boldsymbol{l}_1$, $\boldsymbol{l}_2$, $\boldsymbol{l}_3$.

Figure 4.5 illustrates the convention adopted in this chapter for the sign of edge and screw dislocations with respect to the direction of slip, $\boldsymbol{s}^\alpha$, and the corresponding slip plane normal, $\boldsymbol{n}^\alpha$.

The signed character of single dislocations entails a directionality of their motion under a given resolved shear stress. For a positive shear increment, *i.e.* increase in the slipped area by loop *expansion*, those directions of motion follow as (see figures 4.5 and 4.7):

$$\boldsymbol{m}_{\text{e}+}^\alpha = \boldsymbol{s}^\alpha \tag{4.27a}$$

$$\boldsymbol{m}_{\text{e}-}^\alpha = -\boldsymbol{s}^\alpha \tag{4.27b}$$

$$\boldsymbol{m}_{\text{s}+}^\alpha = \boldsymbol{p}^\alpha \tag{4.27c}$$

$$\boldsymbol{m}_{\text{s}-}^\alpha = -\boldsymbol{p}^\alpha \ . \tag{4.27d}$$

Obstacles in the microstructure, especially grain boundaries in polycrystals may impede the motion of dislocations. In this case, they only partly cross the obstacle, the rest gets stuck and is left immobile in front of it. This immobile dislocation density does not contribute to crystallographic shear and dislocation flux anymore. For that reason it is necessary to distinguish between the single mobile dislocation density $\rho_{p,\text{mob}}^\alpha$ and

the immobile counterpart $\rho_{p,\mathrm{imm}}^{\alpha}$ with $p \in \{\mathrm{e+}, \mathrm{e-}, \mathrm{s+}, \mathrm{s-}\}$ denoting the dislocation type. Since immobile dislocations are only immobile in one of the two possible glide directions on the slip system, it is necessary to discriminate between immobility in direction of positive and negative shear. Thus, the value of the immobile dislocation density gets the same sign as the shear that it created. In contrast, the mobile dislocation density is always positive. The total density of single dislocations of type p becomes:

$$\rho_p^{\alpha} = \rho_{p,\mathrm{mob}}^{\alpha} + \left| \rho_{p,\mathrm{imm}}^{\alpha} \right| \ . \tag{4.28}$$

With v_p^{α} denoting the dislocation velocity, the flux density $\boldsymbol{f}_p^{\alpha}$ of dislocations of type p on slip system α finally follows as

$$\boldsymbol{f}_p^{\alpha} = \rho_{p,\mathrm{mob}}^{\alpha} \, v_p^{\alpha} \, \boldsymbol{m}_p^{\alpha} \ . \tag{4.29}$$

4.2.1.2   Density of Dislocations in Dipole Configuration

The presence of stable dipoles is a necessary prerequisite to dislocation annihilation and is hence explicitly accounted for in the present parameterization. Stable dipoles contain two single dislocations of the same character but opposite sign, hence two dipole densities, $\rho_{\mathrm{e,dip}}^{\alpha}$ and $\rho_{\mathrm{s,dip}}^{\alpha}$, per slip system are recorded and sum up to the overall dipole density of system α:

$$\rho_{\mathrm{dip}}^{\alpha} = \rho_{\mathrm{e,dip}}^{\alpha} + \rho_{\mathrm{s,dip}}^{\alpha} \ . \tag{4.30}$$

These densities quantify the length per volume contributed by *both* constituents, *i.e.* the overall dislocation density value of signed (single) dislocations plus dislocations in dipole configuration remains constant when dislocations change between the two states.

Dipoles are stable against dissociation by the resolved shear stress τ^{α} if the mutual elastic interaction between the two constituents is strong enough, *i.e.* if the distance between the glide planes of the two dislocations does not exceed

$$\hat{d}_{\mathrm{e}}^{\alpha} \;\; = \;\; \frac{1}{8\pi} \frac{G\,b}{|\tau^{\alpha}|} \frac{1}{1-\nu} \quad \text{for edge dislocations} \tag{4.31a}$$

$$\hat{d}_{\mathrm{s}}^{\alpha} \;\; = \;\; \frac{1}{8\pi} \frac{G\,b}{|\tau^{\alpha}|} \quad\quad\;\; \text{for screw dislocations,} \tag{4.31b}$$

with G being the shear modulus, b the length of the Burgers vector, and ν the Poisson ratio. On the other hand, there exists a minimum glide plane separation, $\check{d}_{\mathrm{e,s}}^{\alpha}$, below which the dipole spontaneously disintegrates by either producing point defects (edge dipoles) or immediate cross-slip (screw dipoles).

4.2.1.3   Forest dislocation density

Following Ma and Roters (2004), the density on any particular system β can be projected with respect to system α into a corresponding forest density. By summation of the

contribution of each slip system β the overall forest density on system α results as:

$$\rho_{\mathrm{f}}^{\alpha} = \sum_{\beta=1}^{N_{\mathrm{slip}}} \left[\left(\rho_{\mathrm{e}}^{\beta} + \rho_{\mathrm{e,dip}}^{\beta} \right) \left| \boldsymbol{n}^{\alpha} \cdot \boldsymbol{p}^{\beta} \right| + \left(\rho_{\mathrm{s}}^{\beta} + \rho_{\mathrm{s,dip}}^{\beta} \right) \left| \boldsymbol{n}^{\alpha} \cdot \boldsymbol{s}^{\beta} \right| \right] \tag{4.32}$$

with $\boldsymbol{n}^{\alpha}$ and $\boldsymbol{s}^{\alpha}$ unit vectors normal to the plane and along the slip direction of system α.

4.2.2 Microstructure Evolution

4.2.2.1 Dislocation Multiplication / Athermal Storage

New dislocation density is generated through growth of mobile dislocation loops (figure 4.5), whereas the dipole density remains unchanged.

$$\dot{\rho}_{c+}^{\alpha} + \dot{\rho}_{c-}^{\alpha} \geq 0 \quad , \quad \dot{\rho}_{c,\mathrm{dip}}^{\alpha} = 0 \tag{4.33}$$

Following Arsenlis and Parks (2002) we define the generation of new dislocation density as

$$\mathrm{d}\rho_{\mathrm{e+,mob}}^{\alpha} = \mathrm{d}\rho_{\mathrm{e-,mob}}^{\alpha} = \frac{\rho_{\mathrm{s+,mob}}^{\alpha} \left| v_{\mathrm{s+}}^{\alpha} \right|}{\bar{l}_{\mathrm{s+}}^{\alpha}} + \frac{\rho_{\mathrm{s-,mob}}^{\alpha} \left| v_{\mathrm{s-}}^{\alpha} \right|}{\bar{l}_{\mathrm{s-}}^{\alpha}} \tag{4.34a}$$

$$\mathrm{d}\rho_{\mathrm{s+,mob}}^{\alpha} = \mathrm{d}\rho_{\mathrm{s-,mob}}^{\alpha} = \frac{\rho_{\mathrm{e+,mob}}^{\alpha} \left| v_{\mathrm{e+}}^{\alpha} \right|}{\bar{l}_{\mathrm{e+}}^{\alpha}} + \frac{\rho^{\alpha}\mathrm{e-,mob} \left| v_{\mathrm{e-}}^{\alpha} \right|}{\bar{l}_{\mathrm{e-}}^{\alpha}} \tag{4.34b}$$

with $\bar{l}_{p}^{\alpha}$ being the average segment length in a given population of dislocations of type p. In contrast to the work of Arsenlis and Parks (2002), where the segment length is treated as an additional microstructural parameter, we assume the segment length to be equal for all types of dislocations and directly relate it to the internal length scale of the dislocation structure governed by the forest dislocation spacing $1/\sqrt{\rho_{\mathrm{f}}^{\alpha}}$. With equation (4.48) we reformulate the rate equations for the density evolution as

$$\mathrm{d}\rho_{\mathrm{e+,mob}}^{\alpha} = \mathrm{d}\rho_{\mathrm{e-,mob}}^{\alpha} = \frac{\left| \mathrm{d}\gamma_{\mathrm{s+}}^{\alpha} \right| + \left| \mathrm{d}\gamma_{\mathrm{s-}}^{\alpha} \right|}{2\, b\, \Lambda_0\, \sqrt{\rho_{\mathrm{f}}^{\alpha}}} \tag{4.35a}$$

$$\mathrm{d}\rho_{\mathrm{s+,mob}}^{\alpha} = \mathrm{d}\rho_{\mathrm{s-,mob}}^{\alpha} = \frac{\left| \mathrm{d}\gamma_{\mathrm{e+}}^{\alpha} \right| + \left| \mathrm{d}\gamma_{\mathrm{e-}}^{\alpha} \right|}{2\, b\, \Lambda_0\, \sqrt{\rho_{\mathrm{f}}^{\alpha}}} \tag{4.35b}$$

with Λ_0 being a fitting parameter.

The resulting equations indeed also reflect the phenomenological description of the athermal storage rate by the concept of a "mean free path" of dislocations commonly denoted Λ (Kocks, 1976; Mecking and Kocks, 1986). Setting the mean free path proportional to the mean forest dislocation spacing we recover the relationship of equation (4.35).

4.2.2.2 Dislocation Transformation

The term dislocation transformation comprises all mechanisms that lead to a change in the class of dislocation, be it between single and dipole or between mobile and immobile dislocations, without altering the overall dislocation density. Thus, the sum over the transformation rates of all types of single and dipole dislocations with same character $c \in \{e, s\}$ equals to zero:

$$\dot{\rho}_{c+}^{\alpha} + \dot{\rho}_{c-}^{\alpha} + \dot{\rho}_{c,\mathrm{dip}}^{\alpha} = 0 \ . \tag{4.36}$$

Dipole formation by glide The total volume fraction, V_c^{α}, sampled by gliding dislocations of character c for potential dipole partners depends on the stability limit (equation (4.31)) and follows as:

$$\mathrm{d}\ln V_c^{\alpha} = 2\,\hat{d}_c^{\alpha}\,\frac{|\mathrm{d}\gamma_c^{\alpha}|}{b} \ . \tag{4.37}$$

Within this volume fraction gliding single dislocations can form a new dipole with either a mobile or an immobile single dislocation of opposite sign. Since immobile dislocations do not contribute to the shear rate, but only serve as a passive partner for the creation of a dipole, and under the presumption that dislocations are distributed homogeneously in the volume, the transfer rate from single dislocations to dipoles due to gliding can be expressed as:

$$\dot{\rho}_{c+,\mathrm{mob}}^{\alpha} = -\frac{2\,\hat{d}_c^{\alpha}}{b}\left(\rho_{c+,\mathrm{mob}}^{\alpha}\left|\dot{\gamma}_{c-}^{\alpha}\right| + \rho_{c-}^{\alpha}\left|\dot{\gamma}_{c+}^{\alpha}\right|\right) \tag{4.38a}$$

$$\dot{\rho}_{c-,\mathrm{mob}}^{\alpha} = -\frac{2\,\hat{d}_c^{\alpha}}{b}\left(\rho_{c+}^{\alpha}\left|\dot{\gamma}_{c-}^{\alpha}\right| + \rho_{c-,\mathrm{mob}}^{\alpha}\left|\dot{\gamma}_{c+}^{\alpha}\right|\right) \tag{4.38b}$$

$$\dot{\rho}_{c+,\mathrm{imm}}^{\alpha} = -\frac{2\,\hat{d}_c^{\alpha}}{b}\,\rho_{c+,\mathrm{imm}}^{\alpha}\left|\dot{\gamma}_{c-}^{\alpha}\right| \tag{4.38c}$$

$$\dot{\rho}_{c-,\mathrm{imm}}^{\alpha} = -\frac{2\,\hat{d}_c^{\alpha}}{b}\,\rho_{c-,\mathrm{imm}}^{\alpha}\left|\dot{\gamma}_{c+}^{\alpha}\right| \tag{4.38d}$$

$$\dot{\rho}_{c,\mathrm{dip}}^{\alpha} = -\dot{\rho}_{c+,\mathrm{mob}}^{\alpha} - \dot{\rho}_{c-,\mathrm{mob}}^{\alpha} + \left|\dot{\rho}_{c+,\mathrm{imm}}^{\alpha}\right| + \left|\dot{\rho}_{c-,\mathrm{imm}}^{\alpha}\right| \ . \tag{4.38e}$$

Dipole dissociation by stress increase The distribution of dipole heights is assumed to be uniform within the stability range, *i.e.* between $\check{d}_c^{\alpha}$ and $\hat{d}_c^{\alpha}$. Then, a reduction in the upper stability limit due to increasing resolved shear stress will lead to a (symmetric) dissociation of dipoles back into signed dislocation density:

$$\dot{\rho}_{c,\mathrm{dip}}^{\alpha} = \rho_{c,\mathrm{dip}}^{\alpha}\,\frac{1}{\hat{d}_c^{\alpha} - \check{d}_c^{\alpha}}\,\frac{\mathrm{d}\hat{d}_c^{\alpha}}{\mathrm{d}t} \tag{4.39a}$$

$$\dot{\rho}_{c+,\mathrm{mob}}^{\alpha} = \dot{\rho}_{c-,\mathrm{mob}}^{\alpha} = -\dot{\rho}_{c,\mathrm{dip}}^{\alpha}/2 \tag{4.39b}$$

Dislocation remobilization by stress reversal The immobile dislocation density can be remobilized if the resolved shear stress changes its sign. Then, the direction of dislocation motion is reversed and the formerly immobile dislocations can freely move again. If we assume that all immobile dislocations instantaneously remobilize, the entire immobile dislocation density is converted to mobile dislocation density:

$$\left| \rho_{p,\text{imm}}^{\alpha} \right| \rightarrow \rho_{p,\text{mob}}^{\alpha} \ . \tag{4.40}$$

Since the remobilized dislocations again contribute to the shear rate, they give rise to a kind of Bauschinger effect. This has to be taken into account prior to all other dislocation reactions, as it directly influences the rate equations.

4.2.2.3 Dislocation Annihilation

The model considers athermal and thermally activated annihilation of dipoles, both leading to a decrease in the overall dislocation density.

Athermal annihilation Out of all dipoles newly formed by glide (equation (4.38)), those that happen to have a glide plane separation below $\check{d}_c^{\alpha}$, annihilate instantaneously:

$$\dot{\rho}_{c,\text{dip}}^{\alpha} = -2 \frac{2\,\check{d}_c^{\alpha}}{b} \left(\rho_{c+}^{\alpha} \left| \dot{\gamma}_{c-}^{\alpha} \right| + \rho_{c-}^{\alpha} \left| \dot{\gamma}_{c+}^{\alpha} \right| \right) \ . \tag{4.41}$$

In addition to these close encounters among single dislocations, a second athermal annihilation opportunity is due to moving single dislocations knocking out a compatible constituent from an already existing dipole:

$$\dot{\rho}_{c,\text{dip}}^{\alpha} = -\frac{2\,\check{d}_c^{\alpha}}{b}\, \rho_{c,\text{dip}}^{\alpha} \left(\left| \dot{\gamma}_{c-}^{\alpha} \right| + \left| \dot{\gamma}_{c+}^{\alpha} \right| \right) \ . \tag{4.42}$$

The latter process does not alter the overall density of single dislocations since the remaining dipole constituent substitutes the annihilated single dislocation.

Thermally activated annihilation The mutual elastic interaction between dipole constituents provides the driving force for their out-of-glide-plane motion.

In the case of edge dipoles this leads to climb at an average velocity

$$v_{\text{climb}}^{\alpha} = \frac{D\,\Omega}{b\,k_{\text{B}}T} \frac{G\,b}{2\pi(1-\nu)} \frac{2}{\hat{d}_{\text{e}}^{\alpha} + \check{d}_{\text{e}}^{\alpha}} \ . \tag{4.43}$$

The resulting annihilation rate then reads

$$\dot{\rho}_{\text{e,dip}}^{\alpha} = -\rho_{\text{e,dip}}^{\alpha} \frac{2\,v_{\text{climb}}^{\alpha}}{\left(\hat{d}_{\text{e}}^{\alpha} - \check{d}_{\text{e}}^{\alpha} \right)/2} \ , \tag{4.44}$$

since all dipoles would be annihilated if half the average dipole separation is overcome by climb.

4.2.3 Dislocation Kinetics

Having in mind a pure single crystal, we adopt the mechanism of thermally activated dislocation glide through an obstacle population posed by forest dislocations to be rate-controlling. The velocity is assumed equal for all four types of dislocations and is formulated as:

$$v^{\alpha} = v_0 \, \exp\left[-\frac{Q_0}{k_{\mathrm{B}}T} \left(1 - \frac{|\tau^{\alpha}|}{\hat{\tau}^{\alpha}} \right) \right] \, \mathrm{sgn}\,(\tau^{\alpha}) \tag{4.45}$$

The resolved shear stress τ^{α}, which acts as mechanical driving force, is composed out of the projected externally applied stress on the one hand and the internal dislocation stress on the other hand:

$$\tau^{\alpha} = (\boldsymbol{S}_{\mathrm{ext}} + \boldsymbol{S}_{\mathrm{int}}(\mathrm{grad}\,\Delta\rho)) \cdot (\boldsymbol{s}^{\alpha} \otimes \boldsymbol{n}^{\alpha}) \; . \tag{4.46}$$

The latter is a long-range stress field caused by a gradient in the excess dislocation density (see section 4.2.4.3). Each dislocation induces an elastic distortion of the crystal and, hence, creates a stress field around it. As long as the difference between positive and negative dislocation density, *i.e.* the excess dislocation density, is homogeneously distributed these stress fields are balanced. For a spatial gradient in the excess dislocation density, however, these do not level out anymore, but contribute to the overall stress field.

The mechanical threshold stress $\hat{\tau}^{\alpha}$ depends on the local dislocation densities and reads

$$\hat{\tau}^{\alpha} = G\,b \left(\sum_{\alpha'=1}^{N_{\mathrm{slip}}} \xi_{\alpha\alpha'} \left(\rho^{\alpha'} + \rho_{\mathrm{dip}}^{\alpha'} \right) \right)^{0.5} \tag{4.47}$$

where $\xi_{\alpha\alpha'}$ characterizes the interaction strength between different slip systems α and α' as a result of the possible interaction types self, coplanar, collinear, orthogonal, glissile and sessile Kubin et al. (2008).

Finally, the rate of crystallographic shear carried by the motion of dislocations follows from Orowan's equation:

$$\dot{\gamma}^{\alpha} = \sum_p \dot{\gamma}_p^{\alpha} = \sum_p \rho_{p,\mathrm{mob}}^{\alpha} \, b \, v^{\alpha} . \tag{4.48}$$

4.2.4 Finite Volume Discretization

In order to make the spatial gradients of dislocation densities and flux densities numerically available and considering a subsequent implementation in a mechanical Finite Element solver we reformulate the above introduced constitutive laws on the basis of a Finite Volume discretization.
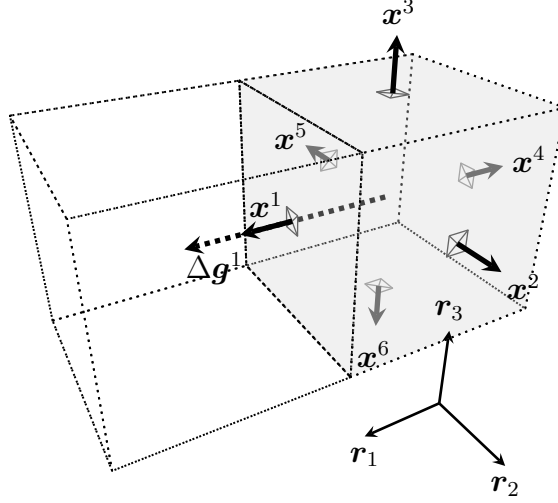
Figure 4.6: Control volume with basis triad $\boldsymbol{r}_1$, $\boldsymbol{r}_2$, $\boldsymbol{r}_3$. Interfaces between neighboring material points are characterized by their outward pointing unit normals $\boldsymbol{x}^n$ and have the area A^n. The vector $\Delta\boldsymbol{g}^n$ connects from the center of gravity of the central material point (dark shade) to that of all of its neighbors (shown only along $\boldsymbol{r}_1$ as example).

4.2.4.1 Material Point Grid and Associated Control Volumes

Having in mind the typically irregular grid of integration points in a Finite Element discretization we define arbitrarily distorted eight-node hexahedral finite control volumes anchored each at one integration point (also called "material point"). The center of gravity $\boldsymbol{g}$ of these control volumes of magnitude V is identical to the position of the integration point. The neighborhood of a particular material point p is identified by a set of vectors, $\Delta\boldsymbol{g}^n$, which connect from p to its nearest neighbors $n = 1, \ldots, 6$ (see figure 4.6). A shared interface with area A^n is situated between both points and is characterized by its outward pointing unit normal $\boldsymbol{x}^n$.

The discretization of the spatial domain into finite control volumes entails an upper bound for the propagation speed of dislocations. Within a time step Δt on average all dislocations that exceed a velocity $\hat{v}$ will have crossed the entire control volume.

$$\hat{v} = \frac{\sqrt[3]{V}}{\Delta t} \tag{4.49}$$

To ensure that no dislocation can move further than the next neighboring control volume the dislocation velocity should be limited to $\hat{v}$. In the integration scheme though this will be guaranteed by choosing an appropriate time step.

4.2.4.2 First Order Approximation of the Microstructure Evolution Rates

In a Finite Volume scheme the subdivision of the spatial domain into finite volumes leads to an integral over the control volume of a material point for the dislocation evolution rates (index r represents all dislocation reactions introduced in section 4.2.2)

$$\int_V \frac{\partial \rho}{\partial t}\, \mathrm{d}V + \int_V \operatorname{div} \boldsymbol{f}\, \mathrm{d}V = \sum_r \int_V \dot{\rho}_r\, \mathrm{d}V \ . \tag{4.50}$$

By integrating the first term and applying the divergence theorem on the flux term a description for the volume average evolution rate of the microstructure for a particular control volume V is derived

$$\frac{\mathrm{d}\bar{\rho}}{\mathrm{d}t} = \frac{1}{V} \sum_r \int_V \dot{\rho}_r\, \mathrm{d}V - \underbrace{\frac{1}{V} \oint_{\partial V} \boldsymbol{f} \cdot \boldsymbol{x}\, \mathrm{d}A}_{\dot{\rho}_{\text{flux}}} \ . \tag{4.51}$$

The first integral on the right hand site of equation (4.51) comprises the reactions of dislocations amongst each other. These rates depend on the dislocation density ρ and the crystallographic shear rate $\dot{\gamma}$, which is proportional to the dislocation density and velocity via the Orowan equation (4.48). For the dislocation reactions we assume a constant dislocation density *within* the control volume. Then, we may approximate ρ by its volume average

$$\frac{1}{V} \sum_r \int_V \dot{\rho}_r(\rho)\, \mathrm{d}V \approx \sum_r \dot{\rho}_r(\bar{\rho}) \ . \tag{4.52}$$

The flux term in equation (4.51), denoted by $\dot{\rho}_{\text{flux}}$, describes the balance for all incoming and outgoing fluxes of dislocation line length through the surface of a given control volume. The special geometry of a hexahedral control volume with six flat surfaces as described above allows to distinguish between surfaces with outgoing and incoming flux (see figure 4.7). Outgoing fluxes are defined by the flux density vector having the same orientation as the surface normal, incoming fluxes the opposite. For a specific dislocation type p moving on slip system α the set of interfaces with outgoing flux is defined as

$$S_{\text{out}}^{\alpha,p} = \left\{ n \ \middle| \ \boldsymbol{f}_p^\alpha \cdot \boldsymbol{x}^n > 0 \right\} \tag{4.53}$$

and the interfaces with incoming flux as

$$S_{\text{in}}^{\alpha,p} = \left\{ n \ \middle| \ \boldsymbol{f}_p^\alpha \cdot \boldsymbol{x}^n < 0 \right\} \ . \tag{4.54}$$

Further on we define $\tilde{\boldsymbol{f}}_p^{\alpha,n}$ as the average flux density through the interface n. It must be equal on both sides of the interface to ensure a conservation of the dislocation line length.
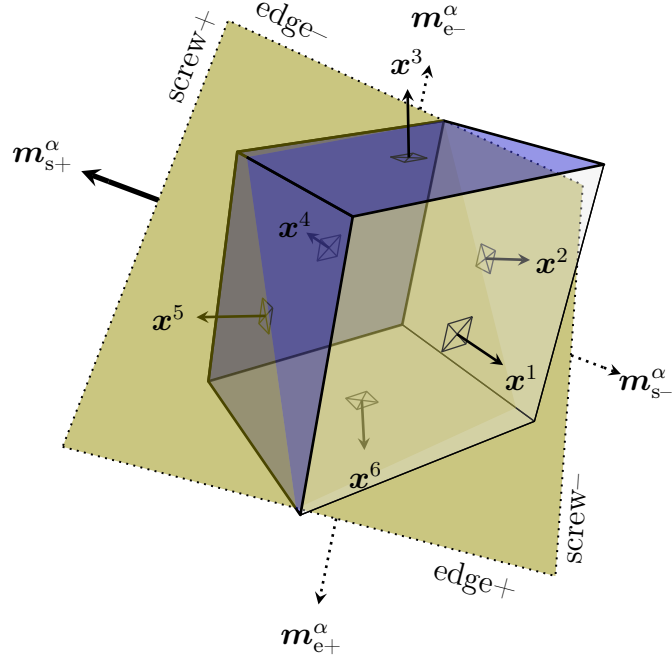
Figure 4.7: Deformed material point with exemplary slip plane α (inclined, dark shade) in intermediate configuration. Interface normals correspond to those of figure 4.6. Dotted vectors on the slip plane periphery indicate directions $\boldsymbol{m}_p^\alpha$ of dislocation motion for a positive shear increment (loop expansion). Blue shaded interfaces on left, back, and upper material point side represent the exemplary set $S_{\text{out}}^{\alpha,s+}$, *i.e.* those interfaces through which positive screw dislocations traveling along $\boldsymbol{m}_{s+}^\alpha$ (thick peripheral vector) leave the material point volume (and enter the neighboring volume, if existent).

(Despite the conservation of dislocation line length the absolute change in dislocation *density* differs for two neighboring material points of unequal volume). We then may reformulate the flux integral on the right hand side of equation (4.51) in a discrete form

$$\oint_{\partial V} \boldsymbol{f} \cdot \boldsymbol{x} \, \mathrm{d}A = \sum_{n \in S_{\text{out}}^{\alpha,p}} \tilde{\boldsymbol{f}}_p^{\alpha,n} \cdot \boldsymbol{x}^n A^n + \sum_{n \in S_{\text{in}}^{\alpha,p}} \tilde{\boldsymbol{f}}_p^{\alpha,n} \cdot \boldsymbol{x}^n A^n \ . \tag{4.55}$$

The average flux density at the interface, $\tilde{\boldsymbol{f}}_p^{\alpha,n}$, that determines the amount of interchanging dislocation line length is unknown and must be approximated. Since second-order approximation schemes like central differences are known to produce spurious oscillation for convective terms, an upwind differencing scheme is chosen, which is only first-order accurate, but unconditionally bounded and highly stable

$$\tilde{\boldsymbol{f}}_p^{\alpha,n} = \begin{cases} \tilde{\boldsymbol{f}}_p^\alpha & \text{if } n \in S_{\text{out}}^{\alpha,p} \ , \\ \tilde{\boldsymbol{f}}_p^{\alpha,n} & \text{if } n \in S_{\text{in}}^{\alpha,p} \ . \end{cases} \tag{4.56}$$

For material points with a free surface, the neighboring dislocation density is assumed zero. Hence, there is no incoming flux of dislocation density from a free surface.

For the case of a grain boundary we consider the flux between neighboring control volumes to be impeded. Therefore, the dislocation flux density at the interface is decreased by a factor χ, the so called "transmissivity factor". This factor reflects the lattice compatibility of two neighboring material points for interchanging dislocations on a specific system and is equal to one in the single crystal case. For a grain boundary we define a transmissivity factor $0 \leq \chi < 1$, so that just a fraction of the dislocation density can enter the neighboring control volume. The rest, *i.e.* the flux multiplied by $(1 - \chi)$, piles up at the grain boundary and is left there as immobile dislocation density.

With equation (4.55) we can finally formulate the rate equations for the flux of dislocation densities of type p on system α as follows

$$\dot{\rho}^{\alpha}_{p,\mathrm{mob}} = -\frac{1}{V} \sum_{n \in S^{\alpha,p}_{\mathrm{in}}} \chi^n \, \tilde{\boldsymbol{f}}^{\alpha,n}_p \cdot \boldsymbol{x}^n A^n - \frac{1}{V} \sum_{n \in S^{\alpha,p}_{\mathrm{out}}} \tilde{\boldsymbol{f}}^{\alpha,n}_p \cdot \boldsymbol{x}^n A^n \tag{4.57a}$$

$$\dot{\rho}^{\alpha}_{p,\mathrm{imm}} = \frac{1}{V} \sum_{n \in S^{\alpha,p}_{\mathrm{out}}} (1 - \chi^n) \, \tilde{\boldsymbol{f}}^{\alpha,n}_p \cdot \boldsymbol{x}^n A^n \, \mathrm{sgn}(v^{\alpha}_p) \, . \tag{4.57b}$$

The sgn operator in equation (4.57b) is used to define the direction of immobility of the single immobile dislocation density.

4.2.4.3   First Order Approximation of Gradients in Dislocation Stress

An inhomogeneous distribution of excess dislocation density leads to a significant contribution of the internal dislocation stresses to the overall stress. The present model captures this to first-order by considering only the excess density of the immediate neighborhood of any particular material point p. In the context of finite volumes this means that only the six neighboring control volumes sharing an interface with p contribute to its internal stress field.

The spatial arrangement of the dislocations in the neighboring control volumes is unknown. With the help of elasticity theory, though, it is possible to analytically investigate the stress field for some characteristic spatial arrangements. The elastic distortion of the lattice around a straight dislocation induces a tensorial stress field with five non-zero components for a straight edge dislocation (σ_{e}) and four non-zero components for a straight screw dislocation (σ_{s}). At some distance from the core the stresses are given

by (Hirth and Lothe, 1982)

$$\sigma_{e,xx} = -G^* \frac{y\left(3x^2 + y^2\right)}{(x^2 + y^2)^2} \tag{4.58a}$$

$$\sigma_{e,yy} = G^* \frac{y\left(x^2 - y^2\right)}{(x^2 + y^2)^2} \tag{4.58b}$$

$$\sigma_{e,zz} = -2\nu G^* \frac{y}{x^2 + y^2} \tag{4.58c}$$

$$\sigma_{e,xy} = \sigma_{e,yx} = G^* \frac{x\left(x^2 - y^2\right)}{(x^2 + y^2)^2} \tag{4.58d}$$

$$\sigma_{e,xz} = \sigma_{e,zx} = \sigma_{e,yz} = \sigma_{e,zy} = 0 \tag{4.58e}$$

$$\sigma_{s,xz} = \sigma_{s,zx} = -G^*(1 - \nu)\frac{y}{x^2 + y^2} \tag{4.58f}$$

$$\sigma_{s,yz} = \sigma_{s,zy} = G^*(1 - \nu)\frac{x}{x^2 + y^2} \tag{4.58g}$$

$$\sigma_{s,xx} = \sigma_{s,yy} = \sigma_{s,zz} = 0 \tag{4.58h}$$

$$\sigma_{s,xy} = \sigma_{s,yx} = 0 \;, \tag{4.58i}$$

where $G^* = Gb/(2\pi\left(1 - \nu\right))$. It should be noticed that the coordinate frames for the stresses of an edge and screw dislocation are not identical. In both cases the z axis is oriented in the line direction of the respective dislocation.

To analyze the influence of the spatial arrangements of dislocations we consider a simple 2-D case with a circular area of unit length diameter. The stresses are evaluated in unit length distance around this area according to equation (4.58). For a single dislocation in the center of the circular area the stress at point P (see figure 4.8) yields

$$\bar{\boldsymbol{\sigma}}_{\text{single dislocation}} = \boldsymbol{\sigma}(\cos\phi, -\sin\phi) \tag{4.59}$$

If the circular area contains more than one dislocation the stress field is given by the superposition of the stresses of the single dislocations. Assuming a homogeneous distribution of N dislocations inside the circular area the mean stress of a single dislocation for $N \to \infty$ converges to

$$\bar{\boldsymbol{\sigma}}_{\text{dislocation array}} = \frac{4}{\pi} \int_{\chi^-}^{\chi^+} \int_{\psi^-(x)}^{\psi^+(x)} \boldsymbol{\sigma}(x, y)\, \mathrm{d}y\, \mathrm{d}x \;, \tag{4.60}$$

where

$$\chi^{\pm} = \pm\frac{1}{2} + \cos\phi \tag{4.61a}$$

$$\psi^{\pm}(x) = \pm\frac{1}{2}\sqrt{1 - 4(\cos\phi - x)^2} - \sin\phi \;. \tag{4.61b}$$

(a) Super dislocation

(b) Dislocation array

(c) Dislocation wall
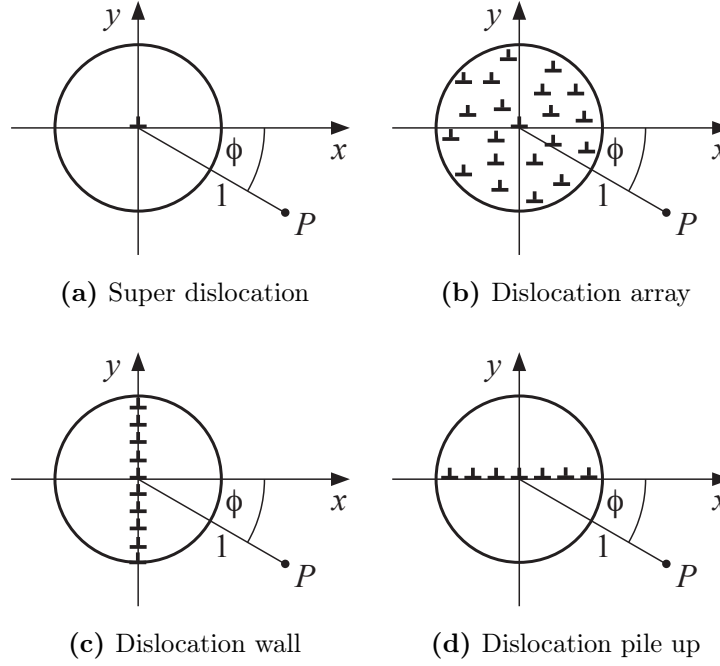
(d) Dislocation pile up

Figure 4.8: Circular area with unit length diameter containing dislocations in various spatial arrangements; for each case the internal dislocation stress is evaluated at P.

The mean stress for a single dislocation in a dislocation wall (limiting case $N \to \infty$) is then easily deduced from equation (4.60)

$$\bar{\boldsymbol{\sigma}}_{\text{dislocation wall}} = \int\limits_{-\frac{1}{2}-\sin\phi}^{\frac{1}{2}-\sin\phi} \boldsymbol{\sigma}\left(\cos\phi, y\right) \mathrm{d}y \; . \tag{4.62}$$

Similarly, the mean value for the stress of a single dislocation in a dislocation pile up becomes

$$\bar{\boldsymbol{\sigma}}_{\text{dislocation pile up}} = \int\limits_{-\frac{1}{2}+\cos\phi}^{\frac{1}{2}+\cos\phi} \boldsymbol{\sigma}\left(x, -\sin\phi\right) \mathrm{d}x \; . \tag{4.63}$$

Figure 4.9 shows the normalized mean stress components for a super dislocation, a random dislocation array, a dislocation wall, and a dislocation pile up in a range of $0° \leq \phi \leq 90°$. It can be seen that the stress field exerted by a cluster of dislocations — at some distance from it — is rather independent of the spatial arrangements within that cluster. Deviations are highest for the extreme cases of a pile up and a wall configuration. The stress for a super dislocation and a dislocation array lies in between those cases.

As a result it may be valid to approximate the unknown spatial arrangement by a homogeneous density distribution of straight dislocations — independent of local inhomogeneities that may be present on a smaller scale. The local dislocation density
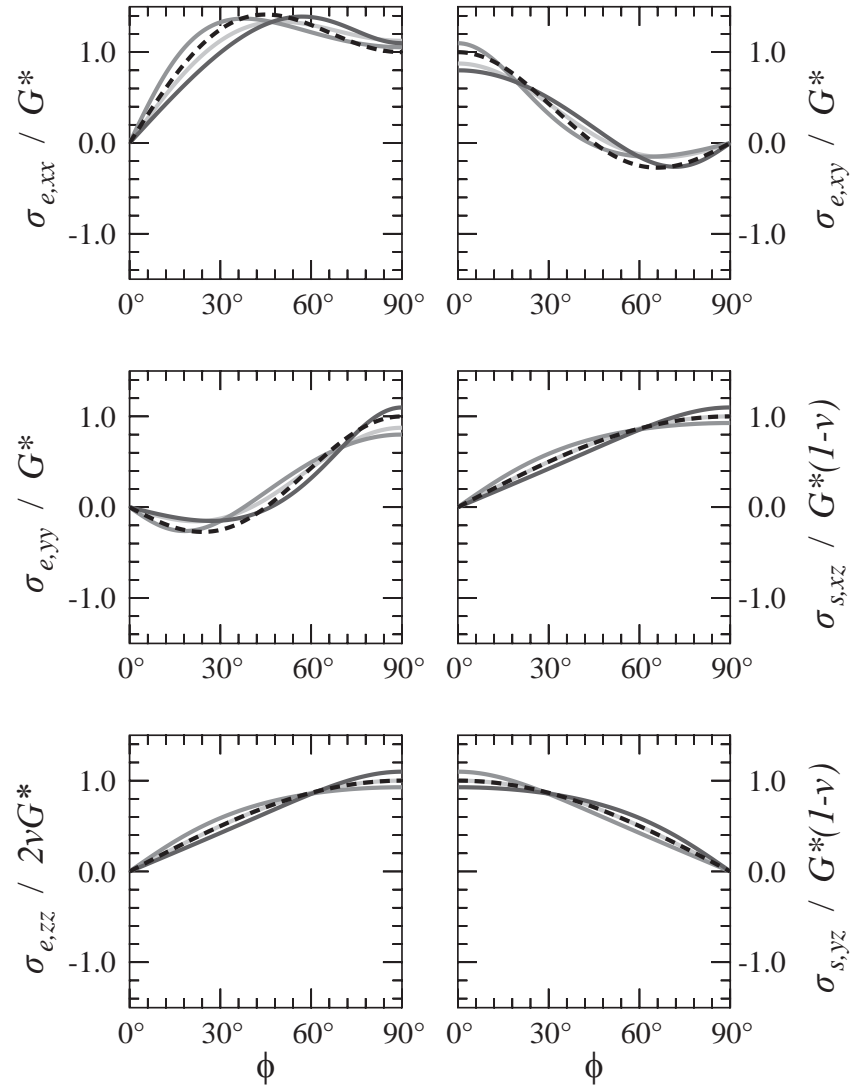
Figure 4.9: Normalized integral over the stress field of a straight edge or screw dislocation for a circular area of unit size; from light to dark: super dislocation, wall of dislocations, pile up of dislocations, homogeneously distributed dislocation array (dashed).

around a central material point might then be expressed as a first-order Taylor series approximation in space

$$\tilde{\rho}_c^\alpha(x,y,z) = \rho_c^\alpha + \operatorname{grad}\tilde{\rho}_c^\alpha \cdot \begin{pmatrix} x \\ y \\ z \end{pmatrix} \ . \tag{4.64}$$

We assume that only dislocations within a finite volume around a material point contribute to its stress field. This volume is defined by a circular region with radius R around the line direction of the regarded dislocation type, *i.e.* around $\boldsymbol{p}^\alpha$ for edge dislocations and around $\boldsymbol{s}^\alpha$ for screw dislocations. Within this volume we assume a homogeneous distribution of single straight dislocation segments of length $2R$ according to equation (4.64). The effective overall stress field at the central material point can then be given as

$$\boldsymbol{\sigma}^\alpha = -\int\limits_0^{2\pi}\int\limits_0^R \sum_{c\in\{e,s\}} \boldsymbol{\sigma}_c^\alpha \Delta\tilde{\rho}_c^\alpha r \mathrm{d}r\,\mathrm{d}\varphi \ , \tag{4.65}$$

with

$$\Delta\tilde{\rho}_c^\alpha = \tilde{\rho}_{c+}^\alpha - \tilde{\rho}_{c-}^\alpha \tag{4.66}$$

being the interpolated excess density at point (x,y,z). Following Hirth and Lothe (1982) we use the more general expressions for the stress field around a straight dislocation of finite length. Using an orthonormal coordinate frame $\boldsymbol{e}_1$, $\boldsymbol{e}_2$, $\boldsymbol{e}_3$ that is attached to each slip system of the central material point as shown in figure 4.5, and considering dislocation density gradients only orthogonal to the dislocation line the integral in equation (4.65) solves to

$$\sigma_{\mathrm{xx}}^\alpha = \frac{1 - \frac{3}{4}\sqrt{2} + \nu\left(\sqrt{2}-1\right)}{1-\nu} GbR^2 \frac{\partial\Delta\rho_e^\alpha}{\partial z} \tag{4.67a}$$

$$\sigma_{\mathrm{yy}}^\alpha = \frac{\frac{15}{16}\sqrt{2} - 1}{1-\nu} GbR^2 \frac{\partial\Delta\rho_e^\alpha}{\partial z} \tag{4.67b}$$

$$\sigma_{\mathrm{zz}}^\alpha = \frac{\frac{13}{16}\sqrt{2} - 1}{1-\nu} GbR^2 \frac{\partial\Delta\rho_e^\alpha}{\partial z} \tag{4.67c}$$

$$\sigma_{\mathrm{xy}}^\alpha = \frac{1}{2}\left(\sqrt{2}-1\right) GbR^2 \frac{\partial\Delta\rho_s^\alpha}{\partial z} \tag{4.67d}$$

$$\sigma_{\mathrm{yz}}^\alpha = -\frac{\frac{1}{16}\sqrt{2}}{1-\nu} GbR^2 \frac{\partial\Delta\rho_e^\alpha}{\partial y} - \frac{1}{2}\left(\sqrt{2}-1\right) GbR^2 \frac{\partial\Delta\rho_s^\alpha}{\partial x} \tag{4.67e}$$

$$\sigma_{\mathrm{xz}}^\alpha = 0 \ . \tag{4.67f}$$

Note that the dislocation stress depends on the spatial *gradient* rather than the total amount of excess density.

The dislocation density gradients in equation (4.67) can be approximated by a first-order interpolation of the neighboring densities. Neighboring material points are located at

$\Delta \boldsymbol{g}^n$ when seen from the central material point. The proper orthonormal matrix

$$\boldsymbol{Q}^\alpha = \begin{bmatrix} \boldsymbol{p}^\alpha \\ \boldsymbol{s}^\alpha \\ \boldsymbol{n}^\alpha \end{bmatrix}_l \quad . \tag{4.68}$$

with $\boldsymbol{p}^{\alpha,n}$, $\boldsymbol{s}^{\alpha,n}$, and $\boldsymbol{n}^{\alpha,n}$ expressed in the basis $\boldsymbol{l}_1$, $\boldsymbol{l}_2$, $\boldsymbol{l}_3$ transforms these coordinates, which are defined in the lattice frame, into the slip system frame. Using equation (4.64) we may now describe the difference in the excess density of two opposite neighbors $n = 1$ and $n = 2$ in terms of the local excess dislocation gradient defined in the slip system frame of the central material point:

$$\Delta \rho_c^{\alpha,n=1} - \Delta \rho_c^{\alpha,n=2} = \left(\boldsymbol{Q}^\alpha \Delta \boldsymbol{g}^{n=1} - \boldsymbol{Q}^\alpha \Delta \boldsymbol{g}^{n=2} \right) \cdot \operatorname{grad} \Delta \rho_c^\alpha \tag{4.69}$$

(disregarding higher order gradients). With the complete neighborhood of six adjacent material points one gets three linearly independent equations with three unknowns: $\frac{\partial \Delta \rho_c^\alpha}{\partial x}$, $\frac{\partial \Delta \rho_c^\alpha}{\partial y}$ and $\frac{\partial \Delta \rho_c^\alpha}{\partial z}$. This can be easily solved by a (3×3)-matrix inversion:

$$\begin{pmatrix} \frac{\partial \Delta \rho_c^\alpha}{\partial x} \\ \frac{\partial \Delta \rho_c^\alpha}{\partial y} \\ \frac{\partial \Delta \rho_c^\alpha}{\partial z} \end{pmatrix} = \boldsymbol{Q}^\alpha \begin{bmatrix} \Delta \boldsymbol{g}^{n=1} - \Delta \boldsymbol{g}^{n=2} \\ \Delta \boldsymbol{g}^{n=3} - \Delta \boldsymbol{g}^{n=4} \\ \Delta \boldsymbol{g}^{n=5} - \Delta \boldsymbol{g}^{n=6} \end{bmatrix}^{-1} \begin{pmatrix} \Delta \rho_c^{\alpha,n=1} - \Delta \rho_c^{\alpha,n=2} \\ \Delta \rho_c^{\alpha,n=3} - \Delta \rho_c^{\alpha,n=4} \\ \Delta \rho_c^{\alpha,n=5} - \Delta \rho_c^{\alpha,n=6} \end{pmatrix} \quad . \tag{4.70}$$

Equation (4.70) can also be applied when the central material point has less than six neighbors (*e.g.* at the surface of the material). As long as there is one neighboring material point in each direction missing neighbors in the finite differences are replaced by the central material points' values. For element types other than eight-node hexahedra similar schemes can be found.

With equation (4.67) and equation (4.70) the dislocation stress exerted by a spatial gradient of the excess dislocation density on slip system α is given in the slip system frame of the central material point. Orthogonal transformation of this stress by $\boldsymbol{Q}^{\alpha \mathrm{T}}$ yields a corresponding (second Piola–Kirchhoff) stress. The overall influence of the excess dislocation density around the central material point finally results from summation over all slip systems:

$$\boldsymbol{S}_{\mathrm{int}} = \sum_{\alpha=1}^N \boldsymbol{Q}^{\alpha \mathrm{T}} \boldsymbol{\sigma}^\alpha \boldsymbol{Q}^\alpha \quad . \tag{4.71}$$

4.2.4.4   The Control Volume and its Associated Measures in a Continuum Mechanical Framework

Each control volume undergoes a deformation that is defined by the deformation gradient associated with its material point. This has to be taken into account for the connecting vectors $\Delta \boldsymbol{g}^n$, the unit normals $\boldsymbol{x}^n$ and the interface area A^n. As these measures are always shared among two neighboring material points (see figure 4.6), their values in the

deformed configuration result, to a first-order approximation, from averaging the two deformation gradients, $\boldsymbol{F}$ and $\boldsymbol{F}^n$, valid at the central and neighboring material point:

$$\bar{\boldsymbol{F}}^n = \frac{\boldsymbol{F} + \boldsymbol{F}^n}{2} \, . \tag{4.72}$$

Using the average deformation gradient to define a common deformed configuration, we can thus write:

$$\boldsymbol{x}_{\mathrm{d}}^n = \frac{\bar{\boldsymbol{F}}^{n^{-\mathrm{T}}} \boldsymbol{x}_0^n}{\left|\left| \bar{\boldsymbol{F}}^{n^{-\mathrm{T}}} \boldsymbol{x}_0^n \right|\right|} \tag{4.73a}$$

$$\boldsymbol{x}^n = \frac{\boldsymbol{F}_{\mathrm{e}}^{\mathrm{T}} \boldsymbol{x}_{\mathrm{d}}^n}{\left|\left| \boldsymbol{F}_{\mathrm{e}}^{\mathrm{T}} \boldsymbol{x}_{\mathrm{d}}^n \right|\right|} \tag{4.73b}$$

$$\Delta \boldsymbol{g}_{\mathrm{d}}^n = \bar{\boldsymbol{F}}^n \Delta \boldsymbol{g}_0^n \tag{4.74a}$$

$$\Delta \boldsymbol{g}^n = (\boldsymbol{F}_{\mathrm{e}}^n)^{-1} \Delta \boldsymbol{g}_{\mathrm{d}}^n \tag{4.74b}$$

$$A_{\mathrm{d}}^n = A_0^n \, \det \bar{\boldsymbol{F}}^n \, \left|\left| \bar{\boldsymbol{F}}^{n^{-\mathrm{T}}} \boldsymbol{x}_0^n \right|\right| \tag{4.75a}$$

$$A^n \approx A_{\mathrm{d}}^n \, . \tag{4.75b}$$

A subscript "d" refers to quantities defined in the common deformed configuration. Observe that the interface normal $\boldsymbol{x}^n$ is valid in the lattice configuration of the *central* material point, while the connection vector $\Delta \boldsymbol{g}^n$ refers to the lattice configuration of the *neighboring* material point. Note that both $\boldsymbol{x}_{\mathrm{d}}^n$ and $\boldsymbol{x}^n$ remain at unit length due to the normalizing denominator in equation (4.73). The interface area in the lattice configuration of p, A^n, does not differ significantly from that in the common deformed configuration, A_{d}^n, since $\det \boldsymbol{F}_{\mathrm{e}} \approx 1$, *i.e.* the elastic deformation gradient contains mainly a rotation with only negligible stretches.

4.2.5 Test Cases Using Simplified Geometries

In this section some results obtained by applying the new model to simplified geometries are presented.

4.2.5.1 Single Crystal Beam

Figure 4.10 shows an Al single crystalline beam oriented for single slip under simple shear. It consists out of $4 \times 40 \times 4$ reduced integration linear elements and is oriented in
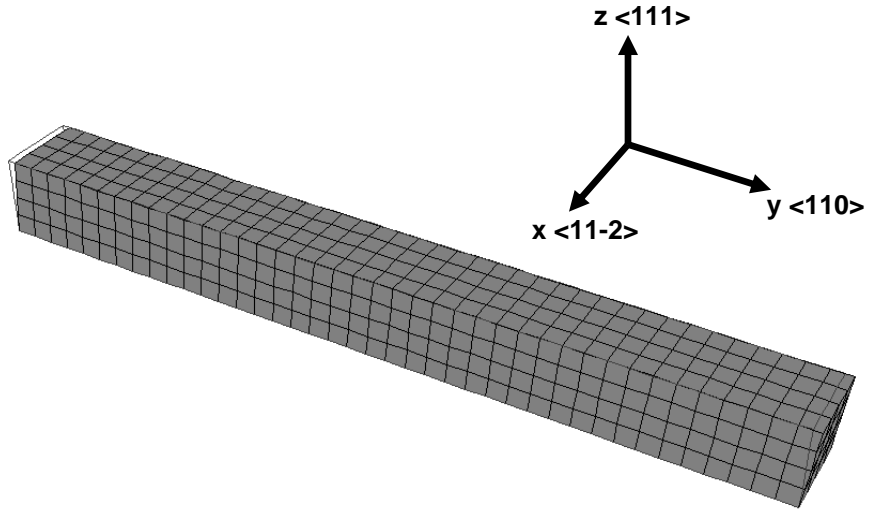
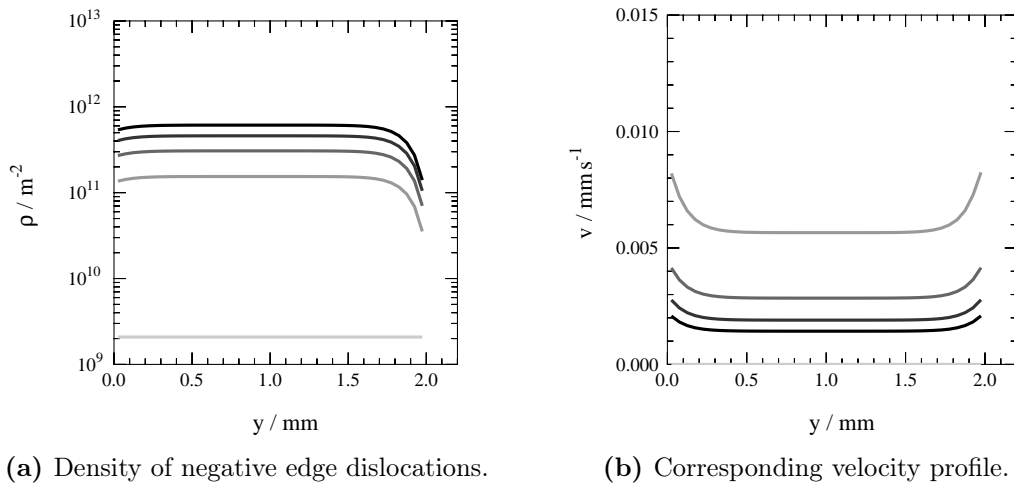**Figure 4.10:** Al single crystal beam oriented for single slip under simple shear.

(a) Density of negative edge dislocations.

(b) Corresponding velocity profile.

Figure 4.11: Results for the single crystal beam (increasing shear from $0\,\%$ (light gray) to $10\,\%$ (black)).

such way that the edge dislocations of slip system $(1\,1\,1)[1\,1\,0]$ flow along the y direction. Accordingly, the corresponding screw dislocations flow into the x direction. However, the dislocation flux boundary conditions on the x surfaces are chosen such that no dislocation gradients develop, *i.e.* the magnitude of the in and out fluxes is always identical. Therefore, dislocation gradients are expected to develop in the y direction only, *i.e.* for the edge dislocations.

The profile of the distribution of the negative edge dislocations along the y direction is shown in figure 4.11a for different shears. The negative edge dislocations flow from right to left. There is a distinct gradient on the right side as no dislocation enter from the free surface and this area looses dislocations due to the outflow to the left. The less distinct reduction of dislocations on the left side is due to the fact that due to a lower total number of dislocations[2] the dislocations in this area have to flow faster to achieve the prescribed fixed shear rate (see figure 4.11b).

4.2.5.2   Artificial Bicrystal Beam

Now an artificial grain boundary is introduced in the single crystal model of the previous section. That is, the left and the right half of the beam are defined as different crystals even though both still have the same crystal orientation. The grain boundary with a transmissivity of 0.5 poses an obstacle to the dislocation flux, *i.e.* dislocation pile up in front of the boundary (figure 4.12). Looking at the dislocation density distribution, we again get mirrored profiles for negative and positive edges (figure 4.13), which results in an antisymmetric distribution of excess dislocations (figure 4.14) and finally an increased shear stress in the boundary area (figure 4.15).

---

[2]The positive edge dislocations show an exactly mirrored profile.
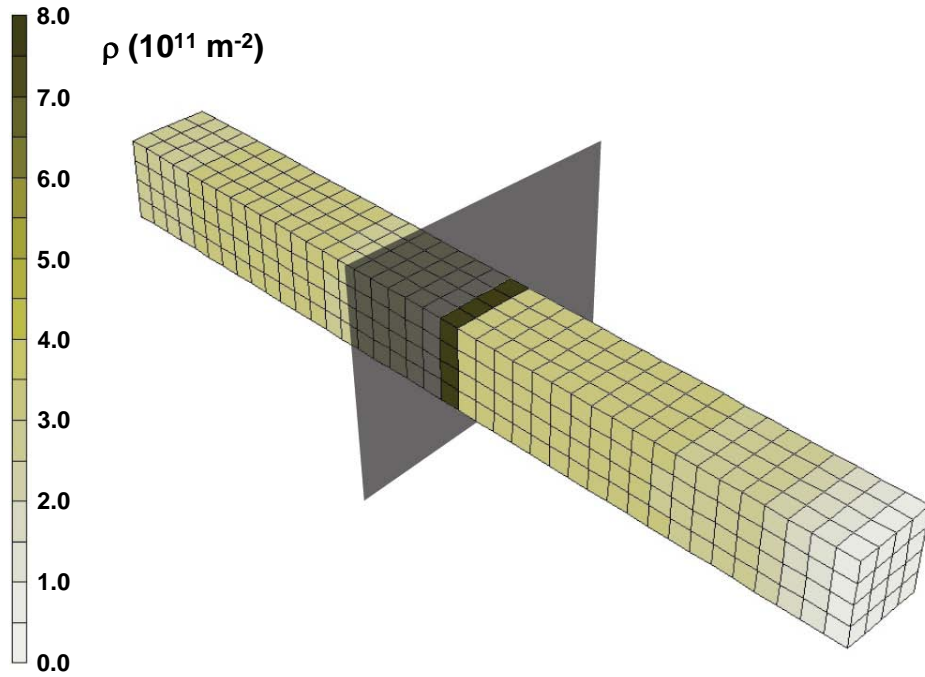
Figure 4.12: Distribution of negative edge dislocations in a bicrystal beam oriented for single slip containing an artificial grain boundary.
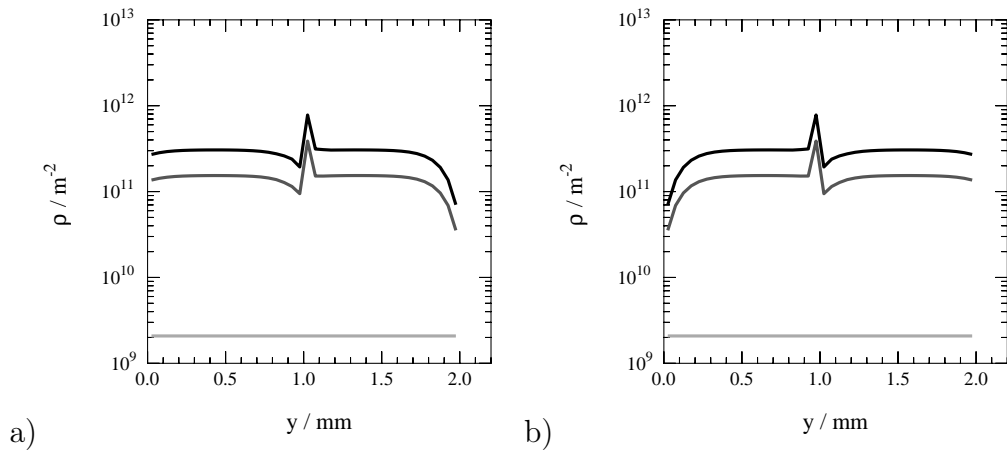

Figure 4.13: Negative(a) and positive (b) edge dislocation density for increasing shear from $0\,\%$ (light gray) to $5\,\%$ (black).
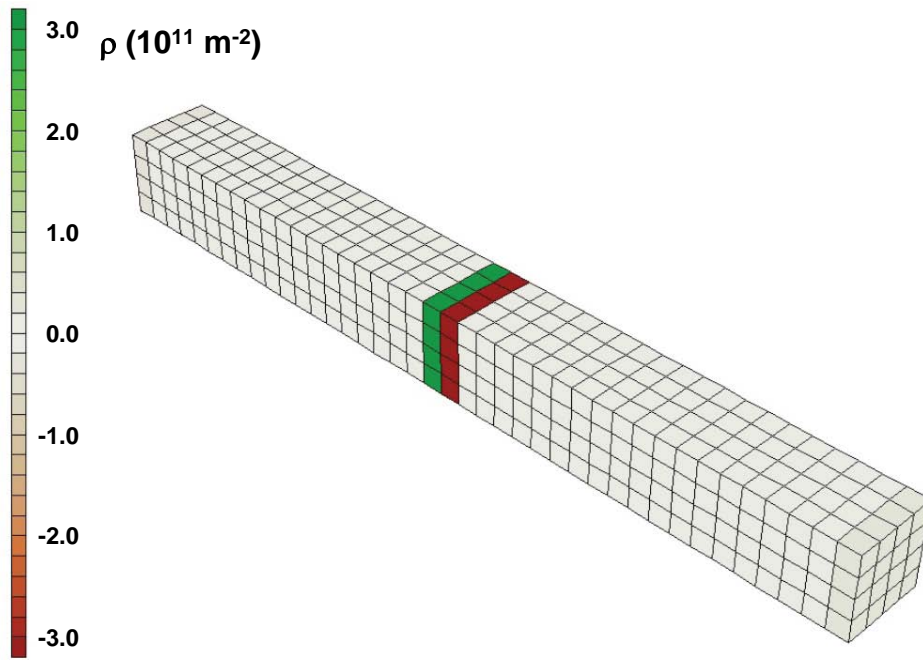
Figure 4.14: Distribution of excess dislocations in a bicrystal beam oriented for single slip containing an artificial grain boundary.
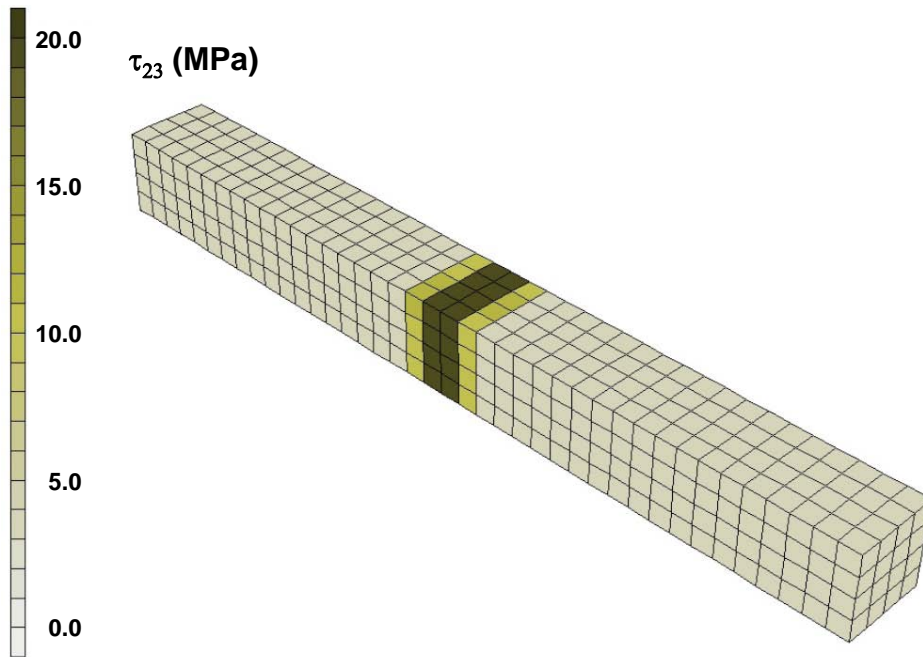

Figure 4.15: Distribution of shear stress τ_{23} in a bicrystal beam oriented for single slip containing an artificial grain boundary.

Chapter 5

Small Scale Application Examples

In this chapter three different examples for the application of CPFEM at small scales, *i.e.* with a subgrain mesh resolution, are presented. This kind of simulation is often referred to as direct CPFEM.

Each experiment is chosen to demonstrate a different aspect of CPFEM and the models presented in the previous chapter.

The simple shear experiments demonstrate that the correct reproduction of macroscopic behavior does not imply correct simulation on the microscale. While the phenomenological model is well capable of reproducing the shear stress–shear strain curves for both the single and the bicrystal, it is clearly not capable of predicting the correct distribution of local strain in the bicrystals. This is only achievable with physics-based models taking the effect of the grain boundary into account.

The experiments on microcompression clearly highlight the importance of computer simulation in the interpretation of experiments with complex boundary conditions. Especially in the micro regime experimental boundary conditions are hard to control. Here computer simulation can help to judge what the boundary conditions most likely have been. This is actually a benefit from the incorporation of crystal plasticity into the FEM with its strength in handling complex boundary conditions. However, as shown for the examples on simple shear experiments, this also strongly depends on a sufficient constitutive model. First, a theoretical study on the influence of boundary conditions is presented. The second part of this section presents an experiment that could not be understood without the knowledge on the correct boundary conditions. Here the CPFEM simulation was able to identify the possible reason for the experimentally observed behavior.

Nanoindentation became a very popular testing method to probe material properties at a local scale. However, due to the very complex loading conditions, again experimental findings are hard to interpret. As shown here, advanced simulation models can improve the understanding of the underlying physical processes.
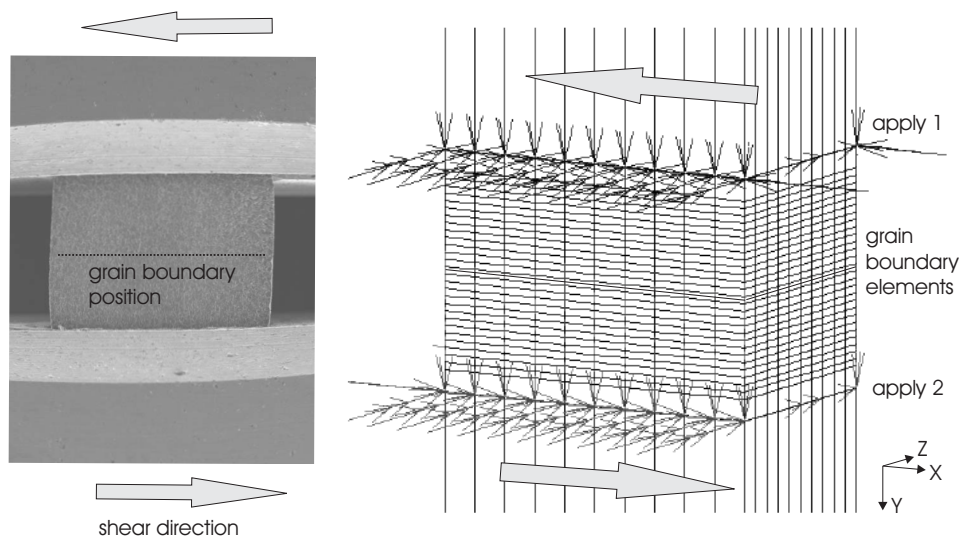
Figure 5.1: Experimental setup and the FE mesh used in the simulations showing also
the boundary conditions applied. The (approximate) grain boundary position is
also indicated for the bicrystal case.

5.1   Simulation of Single and Bicrystal Shear

5.1.1   Experimental and Simulation Setup

The experimental setup and the FE mesh using eight-noded, isoparametric, three-
dimensional brick elements with trilinear interpolation together with the boundary con-
ditions are shown in figure 5.1.

In the FE calculations, the displacements in X, Y, and Z direction were set to zero
for the nodes at the front and back surfaces in the lower part of the mesh. This set
of boundary conditions is referred to as apply 1 in figure 5.1. In the upper part of
the mesh the displacements in Y and Z direction of the nodes at the front and back
surfaces were also set to zero while a constantly increasing value was assigned to the
X displacements. This set of boundary conditions is referred to as apply 2. In the
case of the bicrystals the central element layer (indicated in figure 5.1) was build out
of grain boundary elements as introduced in section 4.1.4. The average orientation
obtained from micro-texture measurements was assigned to each crystal. During the
shear experiments (shear rate $2.6 \times 10^{-4}\,\mathrm{s}^{-1}$) digital images were recorded from the
decorated sample surface for photogrammetric analysis providing the von Mises strain
distribution for an area of $3.1\,\mathrm{mm} \times 2.2\,\mathrm{mm}$. Details of this method were reported in
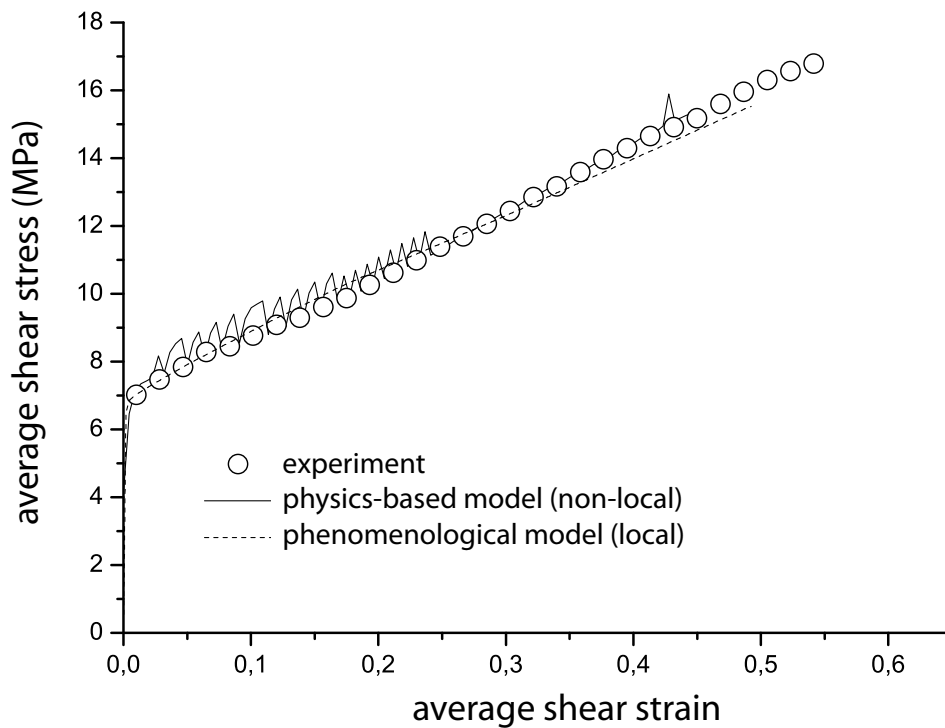Sachtleber et al. (2002); Zaefferer et al. (2003); Roters et al. (2004) and Kuo (2004).

Figure 5.2: Parameter determination by a simple shear test of an aluminum single crystal.

Table 5.1: The parameters of the physics-based non-local model for pure aluminum crystals.

symbol	value	meaning
Q_{slip}	3.0×10^{-19} J	activation energy for slip
Q_{bulk}	2.4×10^{-19} J	activation energy for climb
c_1	0.1	constant for passing stress
c_2	2.0	constant for jump width
c_3	1.0	constant for obstacle width
c_4	$1.5 \times 10^7 \, \text{m}^{-1}$	constant for lock forming rate
c_5	10.0	constant for athermal annihilation rate
c_6	$1.0 \times 10^{-30} \, \text{m}^{-1}$	constant for thermal annihilation rate
c_7	$1.07 \, \text{m}^5 \text{s}^{c_8}$	constant for dipole forming rate
c_8	0.3	constant for nonlinear climb of edge dislocations

Table 5.2: The values used for the interaction strength, $\chi^{\alpha\beta}$, as given in Arsenlis and Parks (2002).

interaction / reaction product	$\chi^{\alpha\beta}$
self interaction	1.0
coplanar	2.2
cross slip	3.0
glissile junction	3.8
Hirth lock	1.6
Lomer–Cottrell lock	4.5

5.1.2　Model Calibration

The average shear stress–shear strain curve of a simple shear test of an aluminum single crystal with 99.999 wt % purity (figure 5.2) was used to fit the constitutive parameters of the physics-based model introduced in section 4.1 (table 5.1). In this process we used the values for the interaction strength, $\chi^{\alpha\beta}$, as given in Arsenlis and Parks (2002) (see table 5.2). The initial orientation of the single crystal was $\varphi_1 = 3.4°$, $\phi = 37.6°$, $\varphi_2 = 36.5°$ and the shear rate amounted to $2.6 \times 10^{-4}\,\mathrm{s}^{-1}$.

5.1.3　Size Dependence of the Non-local Model

The introduction of the geometrically necessary dislocations (GNDs) renders the non-local model size sensitive. To demonstrate this simulations were performed on a set of three virtual specimens of different height-to-length ratios. For this purpose the height of the sheared sample was changed to one half and one tenth of the original height, respectively. The resulting shear stress–shear strain curves are shown in figure 5.3.

Equations (4.7), (4.8), (4.19) and (4.20) reveal that the GNDs contribute to the passing and the cutting stress in the flow rule, and to the multiplication term of the immobile dislocation density. For this reason one would expect higher predicted stresses for the thinnest sample owing to the relative increase of zones, which are mechanically affected by the presence of interfaces. This is indeed confirmed by figure 5.3. From figures 5.4b,e,h it becomes obvious how the relative size of the zone influenced by the GNDs increases with the decreasing sample height. The increased GND density entails also an increase of the SSDs as expected and shown in figures 5.4a,d,g. Additionally figures 5.4c,f,i also show that the texture evolution of the crystal is changed. This results in an intersection of the stress–strain curves for $H = H_0$ and $H = H_0/2$ in figure 5.3.

The strong influence of incorporating GNDs into the crystal plasticity FE framework on the predicted reorientation rates is due to the penalty function they impose. This means
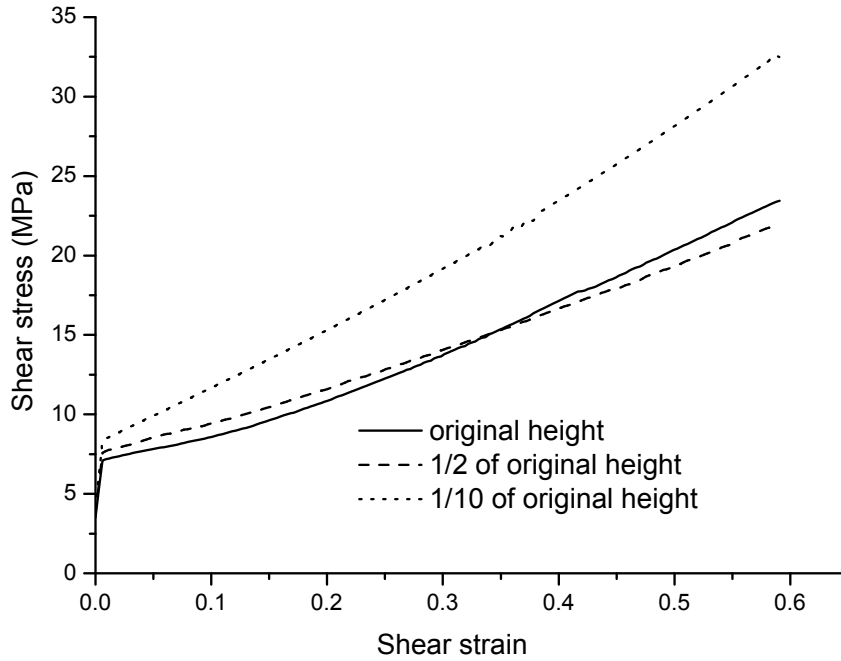
Figure 5.3: Simulated shear stress–shear strain curves for samples with different height-to-length ratios demonstrating the size sensitivity of the physics-bases non-local model.

that each reorientation step that introduces an orientation divergence with respect to the neighborhood is impeded owing the corresponding introduction of GNDs (Raabe et al., 2002b).

Figure 5.5 shows profiles of the two immobile dislocation densities (SSDs and GNDs) across the specimen near the sample center for a shear deformation of about 30 %. While both dislocation densities are always of the same order of magnitude, their ratio is clearly influenced by the relative sample height. For $H = H_0$ the SSD density is always higher than the GND density. However, this situation is gradually changed with decreasing relative sample heigth. Finally, for $H = H_0/10$ the GND density surpasses the SSD density near the edges of the heavily sheared zone of the sample.

5.1.4 Comparisons of von Mises Strain Distributions and Crystal Orientation

The experimental results are compared to simulations achieved using the phenomenological viscoplastic local model as presented in section 2.3 and the non-local model presented in section 4.1.

In the single crystal experiments the maximum deformation is always found in the lower left corner of the crystal and extends diagonally across the crystal surface (figure 5.6).
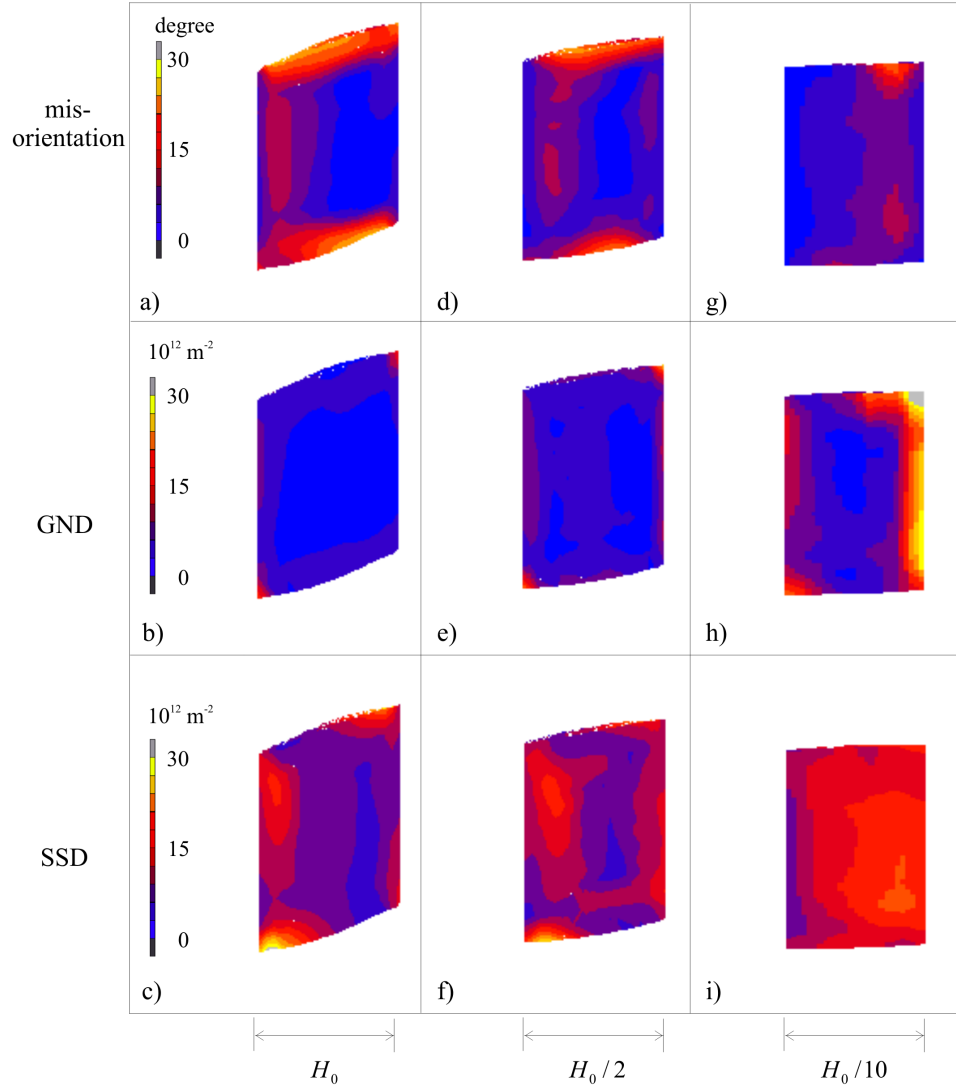
Figure 5.4: Comparisons of dislocation densities and misorientation for different samples after 30% shear deformation. Heights of samples are $H = H_0$, $H = H_0/2$ and $H = H_0/10$ (all plots are scaled to the same heigth for a better comparison), respectively. GND: geometrically necessary dislocation density, SSD: statistically stored dislocation density.
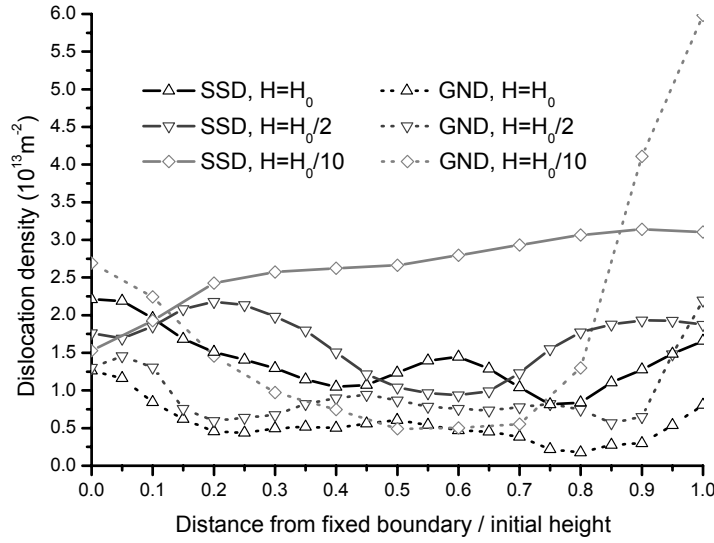
Figure 5.5: Comparison of statistically stored dislocation density (SSD) and geometrically necessary dislocation density (GND) for simulated shear tests of samples with different heights after 30 % shear deformation (line scan near the sample center).

While this behavior is correctly reproduced by the non-local model, the phenomenological viscoplastic model predicts the highest strains in the upper left corner of the specimen. One can assume that the better prediction yielded by the non-local model is mainly a consequence of the physically based latent hardening law and the introduction of the GNDs. This assumption is supported by the data presented in figure 5.4b, which reveals that substantial densities of GNDs are generated near the sample borders. For better comparison of the relative contributions of the two types of dislocations, figures 5.4a and b show both, the SSD and the GND distributions on the ND-surface.

The calibrated model is then applied to the case of 50 % (frictionless) simple shear deformation of three aluminum bicrystals with a low-, intermediate-, and high-angle grain boundary, respectively, parallel to the shear plane (figure 5.1). Figures 5.7–5.9 show the comparison of the von Mises strain distributions obtained from the experiment (left column), from the simulation with the phenomenological viscoplastic local constitutive law without an interface model (middle column), and from the simulation series that is based on the new set of constitutive laws including dislocation rate formulations on each slip system, geometrically necessary dislocations on each slip system, and a geometrical model for the grain boundary resistance against slip transmission events as introduced in section 4.1 (right column). The figures show the von Mises equivalent strain distributions for five subsequent stages of shear with a constant increase of 10 % per load step.

The experimental data clearly reveal for all three bicrystals the strong micro-mechanical effect imposed by the presence of the respective grain boundary. Even for the low-angle grain boundary (7.4° misorientation) the shear experiment clearly shows an effect of strain separation among the two abutting crystals. With increasing grain boundary
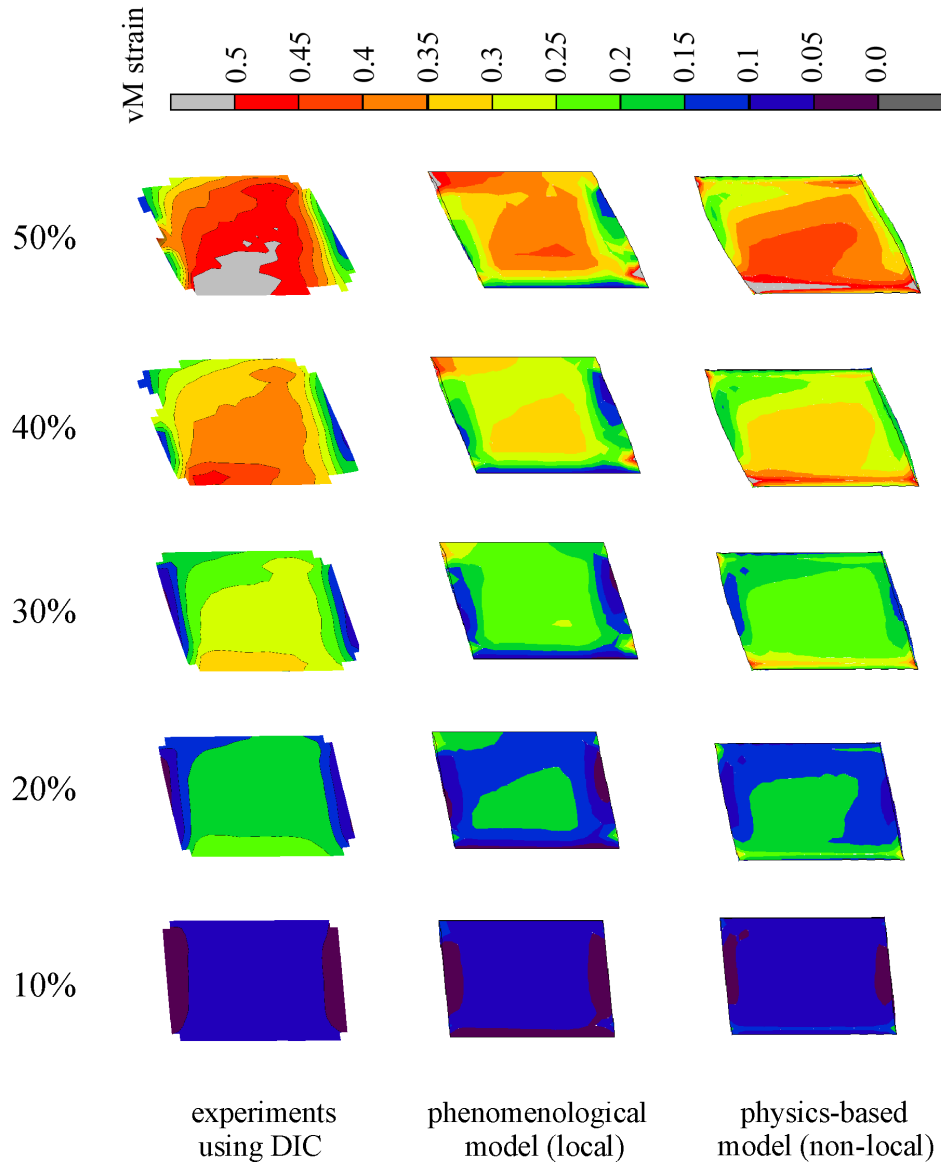
Figure 5.6: Comparison of the von Mises equivalent strain on the surface of an aluminum single crystal (3.1 mm long, 2.0 mm thick and 2.2 mm high) for a simple shear test. The left column shows experimental results obtained by strain measurements via digital image correlation (DIC). The central column shows results obtained by using the phenomenological viscoplastic local formulation (section 2.3). The right column shows results obtained by using the physics-based non-local model (section 4.1), which considers geometrically necessary dislocations.

Figure 5.7: Simple shear test of a bicrystal (3.1 mm long, 2.0 mm thick and 2.2 mm high) with a low-angle grain boundary (7.4°). Comparison of the von Mises strain patterns of the experiment obtained by digital image correlation (DIC, left column), from the simulation with a phenomenological viscoplastic local constitutive law (middle column), and from the simulation that uses the physics-based non-local model (right column).
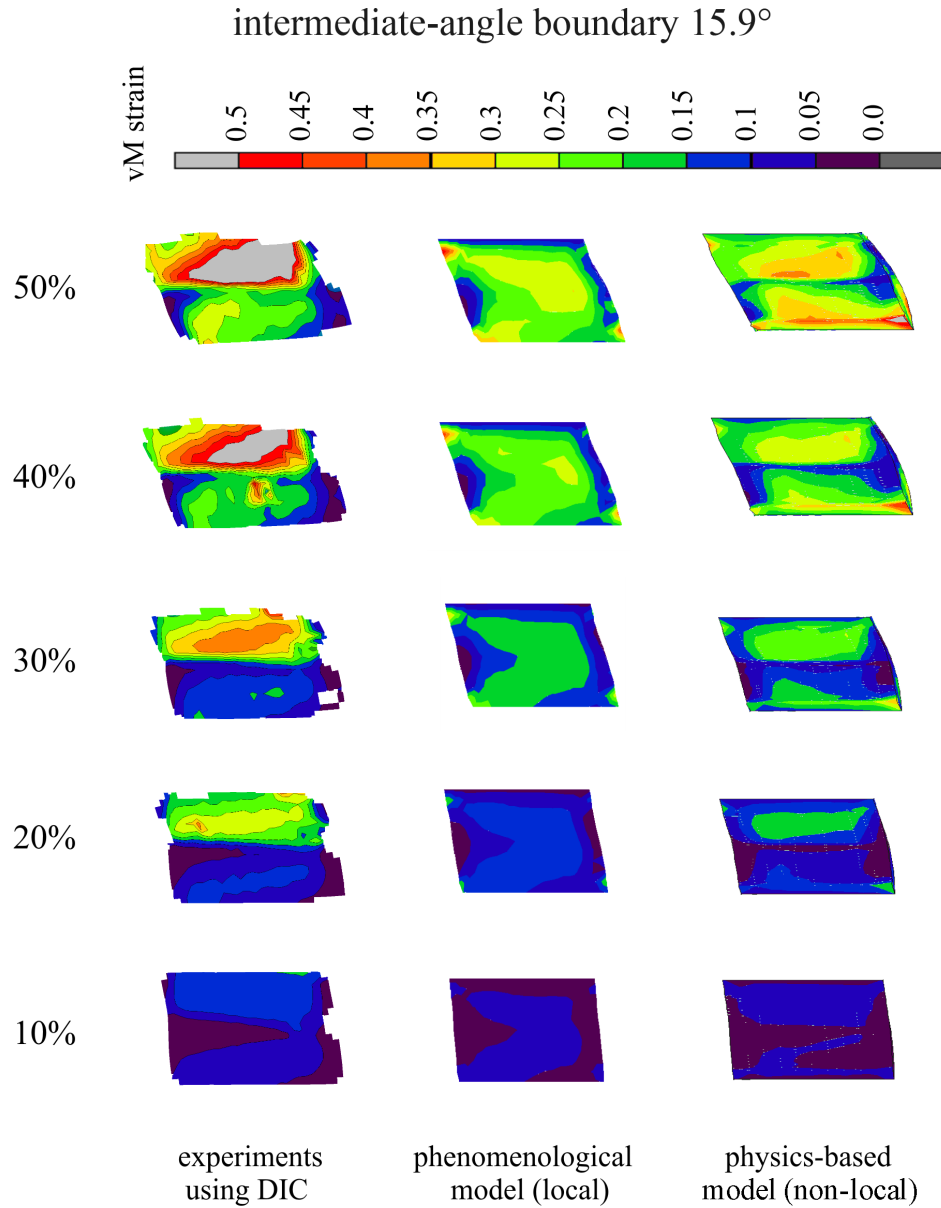
Figure 5.8: Simple shear test of a bicrystal (3.1 mm long, 2.0 mm thick and 2.2 mm high) with an itermediate-angle grain boundary (15.9°). Comparison of the von Mises strain patterns of the experiment obtained by digital image correlation (DIC, left column), from the simulation with a phenomenological viscoplastic local constitutive law (middle column), and from the simulation that uses the physics-based non-local model (right column).
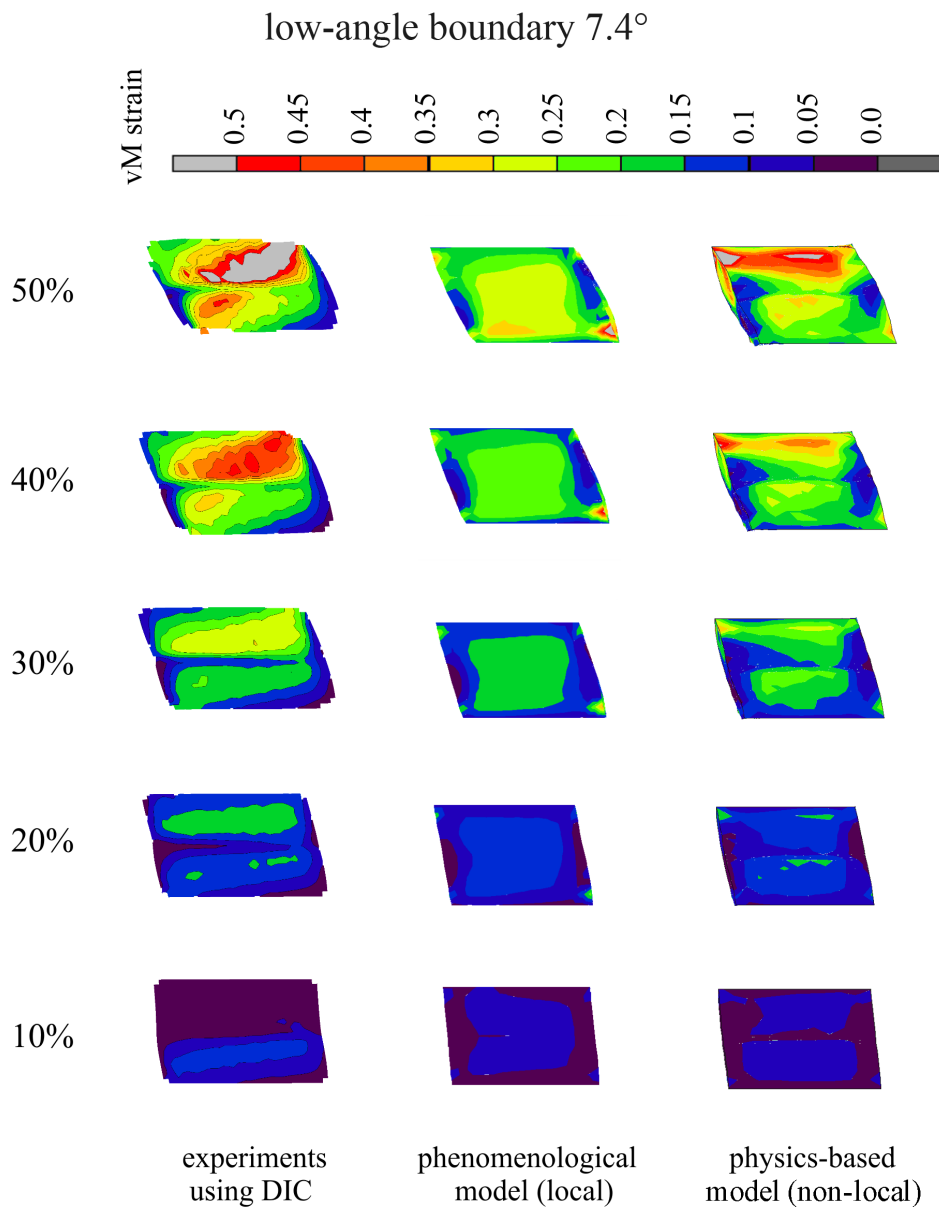
Figure 5.9: Simple shear test of a bicrystal (3.1 mm long, 2.0 mm thick and 2.2 mm high) with a high-angle grain boundary (33.2°). Comparison of the von Mises strain patterns of the experiment obtained by digital image correlation (DIC, left column), from the simulation with a phenomenological viscoplastic local constitutive law (middle column), and from the simulation that uses the physics-based non-local model (right column).
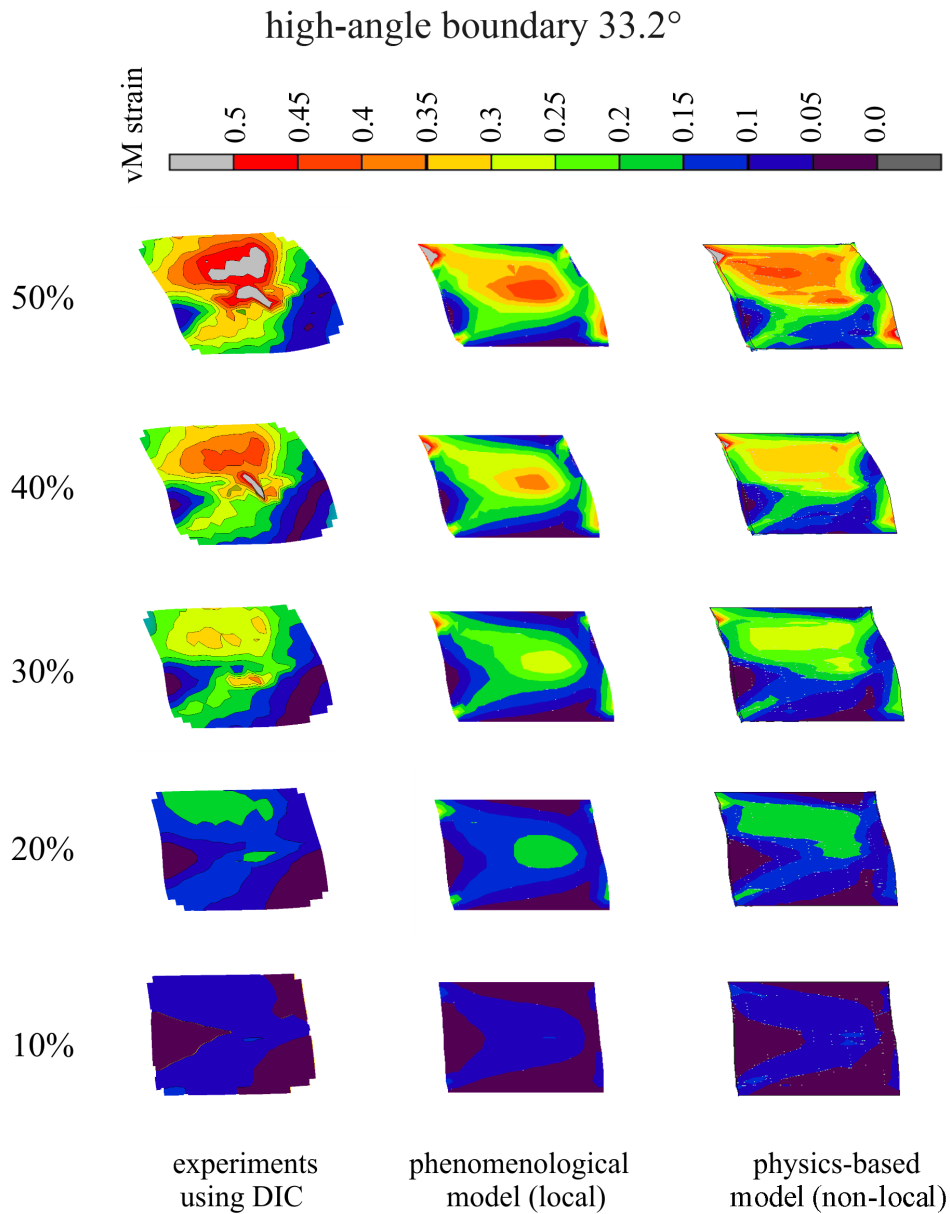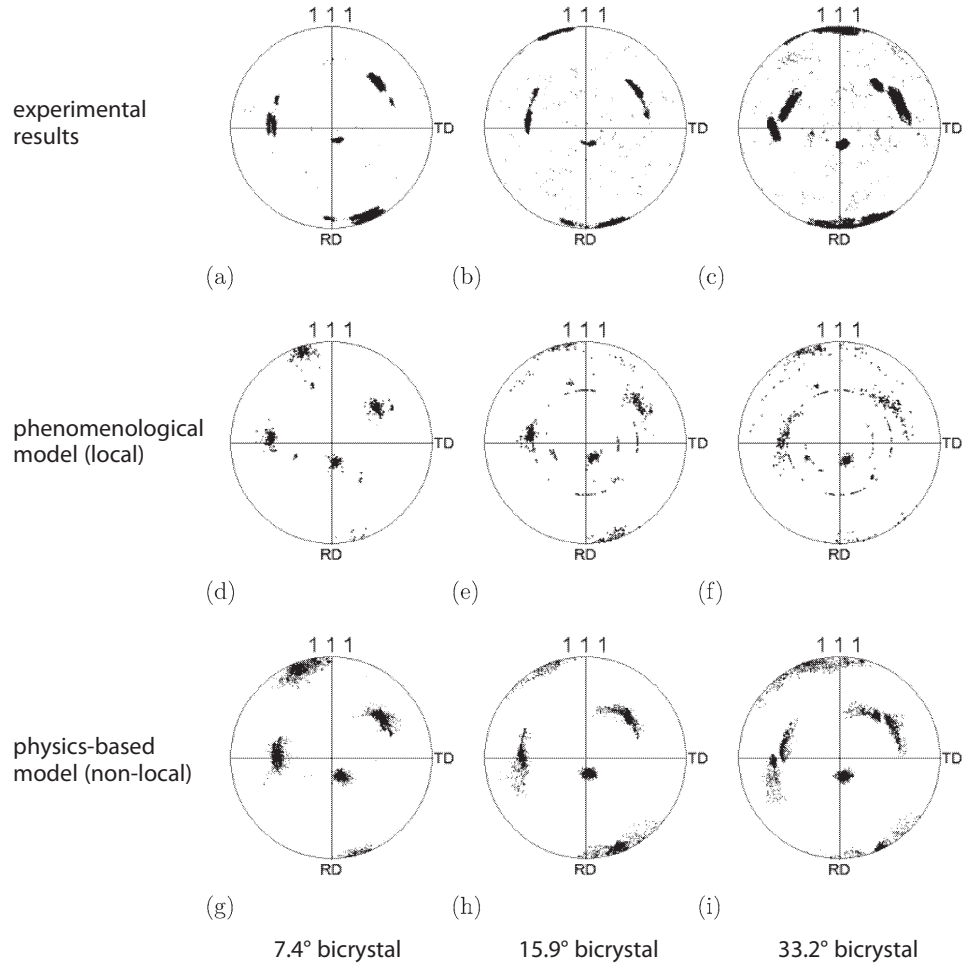
Figure 5.10: Texture comparison for the simple shear tests (50 %) conducted with the three bicrystals. (a,b,c) experimental textures; (d,e,f) phenomenological local model; (g,h,i) physics-based non-local model; (a,d,g) bicrystal with low-angle grain boundary (7.4°); (b,e,h) bicrystal with intermediate-angle grain boundary (15.9°); (c,f,i) bicrystal with high-angle grain boundary (33.2°).

misorientation the heterogeneous distribution of the von Mises strain between the two grains becomes more pronounced.

Concerning the corresponding simulation results it is essential to note that the use of the phenomenological viscoplastic local law (middle column of figures 5.7–5.9) does not adequately reproduce the influence of the grain boundaries on the distribution of the accumulated von Mises strain. This applies in particular for the two bicrystals that have a small- and intermediate-angle grain boundary, respectively. For the bicrystal with the high-angle grain boundary, figure 5.9, the phenomenological local model is capable of predicting some, although not all, characteristics of the strain separation between the two crystals. The partial success of the simulation with the phenomenological viscoplastic hardening law in case of the high-angle grain boundary is attributed to the strong effect

of the change in the Schmid factor across the interface. This means that the kinematical effect that arises from distinct differences in the slip system selection on either side of a grain boundary plays an essential role in this case. We refer to this effect as *kinematical hardening* imposed by grain boundaries.

Figure 5.10 shows the {1 1 1} pole figures for the three bicrystals as obtained from the experiments and simulations using both, the phenomenological local model and the non-local model (50 % shear deformation). The experimental pole figures show reorientation zones with a strong Z (ND) rotation, which is common to both crystals for all three bicrystal specimens. The scatter of the texture is in all samples rather weak, *i.e.* the reorientation took place rather homogeneously throughout the crystal when considering that the two orientations were not stable in all three cases under the imposed load. The scatter is due to minor differences in the reorientation rates (similar rotation direction), which originate from local differences in the accumulated strain as is evident from von Mises strain diagrams shown before. The texture predictions, which were obtained by using the local viscoplastic constitutive model (figures 5.10d–f), show a rather large orientation scatter in all three cases. The texture spread substantially exceeds the scatter observed in the experiments. The texture evolution in the two crystals is similar, *i.e.* the character of a bicrystal pole figure is lost. This observation matches the strain distributions predicted by the viscoplastic constitutive model. The viscoplastic simulations do not show any influence of the grain boundary on the micromechanical behavior except for the case of the high-angle grain boundary with 33.2° misorientation where the kinematics of the interface prevailed in terms of the change in the Schmid factor across the boundary.

The texture predictions obtained by the use of the physics-based non-local constitutive model (figures 5.10g–i) reveal much smaller orientation scatter and smaller reorientation rates when compared to the simulations obtained by the local phenomenological model (figures 5.10d–f). The simulated textures are in excellent agreement with the experimental pole figures. We explain this *smoothing* effect on the texture evolution mainly in terms of the influence of the geometrically necessary dislocations, which act twofold: First, their accumulation in conjunction with the generation of orientation gradients introduces a direct mechanical resistance to the further deformation of the material points affected by such gradients in terms of an increase in the overall local dislocation density. The second aspect (coupled to the first one) is the resulting constitutive tendency of the non-local model to reduce the difference in lattice rotation between neighboring material points. This means that the implicit introduction of the geometrically necessary dislocations imposes a strong penalty or respectively drag force against lateral gradients in the reorientation rates. The {1 1 1} pole figures shown in figures 5.10c and i reveal that the projected orientation points cluster in the form of two groups, while in subfigure f this effect is less pronounced. This is attributed to the influence of the grain boundary on the texture evolution, in particular to the *anisotropy* of the modeled resistance of the grain boundaries to different slip systems. The overall reduction in the rate at which the deformation textures evolve, as achieved by the physics-based non-local model, is a long standing problem in texture research since many classical texture models (including the

crystal plasticity finite element approach) suffer from the drawback that the predicted textures are often too sharp and the predicted evolution rates are often too high when compared to experiments.

5.1.5   Conclusion

A simple shear experiment of an aluminum single crystal was used to calibrate the physics-based non-local model introduced in section 4.1. The predicted distribution of the local deformation was found to be in better accordance with the experiment than for a phenomenological viscoplastic local model. One can assume that the better prediction yielded by the new model is mainly a consequence of the introduction of the GNDs and the physically based latent hardening law into the constitutive framework.

The size sensitivity of the physics-based non-local model has been clearly demonstrated numerically for samples of different heights. Besides the Hall–Petch hardening effect, also the texture evolution is found be size sensitive.

The simulations and experiments using bicrystals clearly show that the classical kinematical treatment of grain boundaries, which is automatically included in all CPFE models owing to the change in the Schmid factor across the interfaces, is not sufficient to adequately reproduce the micro-mechanics associated with the presence of grain boundaries.

5.2   Bicrystal Shear Revisited

As a first test for the new dislocation flux-based non-local model presented in section 4.2 it is applied to once more simulate the bicrystal shear experiment with the low-angle boundary[1] discussed in the previous section. The simulation used a somewhat simplified FE mesh (800 elements with reduced integration) that represents the sheared area only (see figure 5.11). The boundary conditions are also modified by applying the shear to the full top and bottom faces. The transmissivity factor χ was set to 0.5 and no parameter fitting was performed but standard values for aluminum were used.

Figure 5.12 compares the local strain distribution after 30 % shear predicted by the new dislocation flux-based model with the experiment and the prediction of the non-local physical model used in section 5.1 As can be seen the qualitative agreement with the experiment is even better for the flux-based model. However, the average strain level is lower. This is probably due to the modified boundary conditions, which lead to a more homogeneous deformation. The improved qualitative agreement becomes even more

---

[1]As in the current implementation it is assumed that the dislocations transmitted through a grain boundary stay on the same slip system, it can be applied to small-angle boundaries only, where this assumption is reasonable.
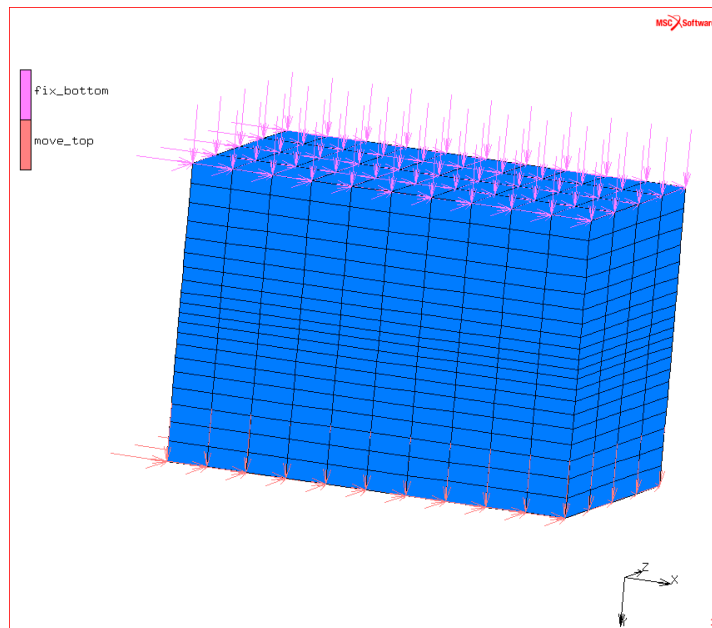
Figure 5.11: A biased mesh consisting of 800 3-D-hexahedral elements with reduced integration was used to model the sheared area of the small-angle bicrystal.
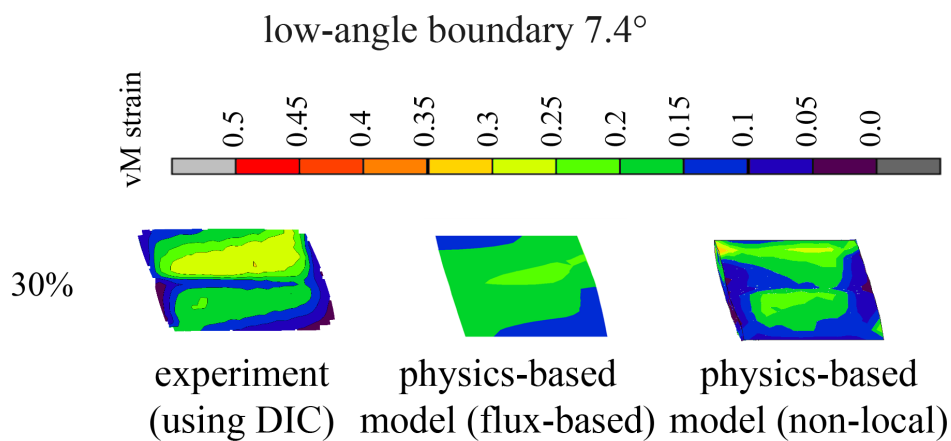
Figure 5.12: Simple shear test of a bicrystal (3.1 mm long, 2.0 mm thick and 2.2 mm high) with a low-angle grain boundary (7.4°). Comparison of the von Mises strain patterns of the experiment obtained by digital image correlation (DIC, left column), from the simulation with the dislocation flux-based constitutive law (middle column), and from the simulation that uses the physics-based non-local model (right column).

low-angle boundary 7.4°

Figure 5.13: Same as figure 5.12 but all images auto-scaled using different minimum and maximum values!

obvious looking at figure 5.13. Here each image is individually scaled according to its minimum and maximum values.

In summary the new dislocation-flux based constitutive model introduced in section 4.2 further increases the prediction quality regarding the local distribution of deformation. This is an important prereq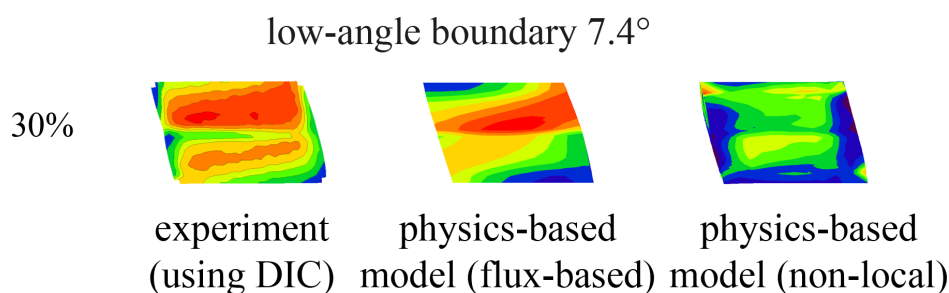uisite for using local CPFEM results in connection with other local microstructural processes such as damage and recrystallization nucleation.

5.3 Single Crystal Micro-Compression

5.3.1 Introduction and Motivation

Mechanical size effects discovered recently during microscale compression tests of crystalline metallic single crystals (Uchic et al., 2004) currently attract great attention. The main experimental observation is that the mechanical properties observed in such tests become remarkably different compared with bulk specimens when the sample dimensions of the pillars approach the micrometer regime. Uchic et al. (2004) tested three different materials, namely, Ni, Ni_3Al-1%Ta, and a Ni-based superalloy. By recording the engineering stress–strain curves during microscale compression the authors observed that the yield stresses dramatically increased as the diameters of the test pillars decreased. The group of Nix and Greer (Greer et al., 2005; Nix et al., 2007) did similar tests but using two different sample fabrication methods on gold pillars. The authors found a similarly significant flow stress increase as in Uchic et al. (2004), and suggested as a possible explanation a dislocation starvation effect. This hypothesis suggests that dislocations that are present at the onset of plastic deformation leave the tiny specimens owing to their small dimensions before the dislocations can multiply. This effect is suggested to entail a dislocation starvation. The authors propose that if this state is reached, very high stresses would be required to nucleate new dislocations, either at the sample surface or in the bulk of the crystal, leading to the observed near-theoretical–strengths. Similar observations were reported by Dimiduk et al. (2005) and Volkert and Lilleodden (2006).

Afrin and Ngan (2006) performed similar micro-compression experiments using a nanoindenter at room temperature on Ni_3Al specimens. Their columns, which were also produced via focused ion-beam milling, had a diameter of $2\,\mu m$.

By using finite element simulations with an isotropic constitutive law Zhang et al. (2005) proposed some guidelines from a continuum mechanics point of view in terms of geometry and system setup to design accurate micro-compression tests. This investigation is sensible since finite element simulations are well suited to study details of the influence of the external boundary conditions and their possible changes during compression encountered in such tests. Points of particular interest in the paper were the effects of the strain hardening behavior, the initial height, and of the Coulomb friction coefficient.

The motivation for the presented theoretical study consists in merging some aspects of the different investigations quoted above into one simulation procedure. This means that we combine the advantages of an anisotropic crystallographic law for the constitutive description of the material in conjunction with the full consideration of crystallographic orientation effects and orientation evolution with proper boundary condition treatment via a crystal plasticity finite element simulation.

The aim of this approach is to address the compression deformation of cylindrical single crystal micro-pillars with respect to the role of the initial crystal orientation, evolution of deformation-induced orientation changes, sample geometry (diameter-to-length ratio), crystalline anisotropy, and Coulomb friction on the course of such tests. The results are used to investigate our hypothesis that even in the case of a homogeneous initial crystallographic orientation and homogeneous initial boundary conditions at the beginning of a compression test, gradual formation of orientation gradients can take place within the specimen during loading.

The second part shows the application of the same formalism to explain the unexpected shift of the peak positions of Laue diffraction patterns observed *in situ* during pillar compression in the group of Van Swygenhofen (Maaß et al., 2009).

5.3.2 Simulation Procedure

5.3.2.1 Constitutive Law and Material Parameters

All the simulations shown in this section use the phenomenological constitutive model as presented in section 2.3.

The hardening parameters in equations (2.6) – (2.8) for Cu were taken from Wang et al. (2004) and Zaafarani et al. (2006), namely, $h_0 = 180\,MPa$, $a = 2.25$, $\tau_s = 148\,MPa$, and $m = 0.012$. The initial value of the slip resistance was chosen as $16\,MPa$ and $\dot{\gamma}_0$ was taken to be $0.001\,s^{-1}$. The elastic constants were those for pure Cu, *i.e.* $C_{11} = 168\,GPa$, $C_{12} = 121.4\,GPa$, and $C_{44} = 75.4\,GPa$.
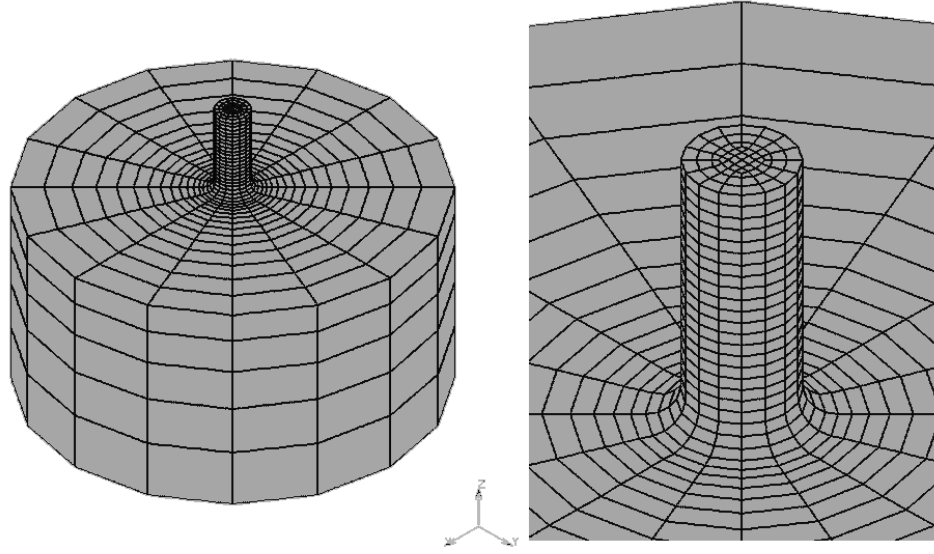
Figure 5.14: Finite element mesh as used for the case of an initial diameter-to-length ratio of 0.4. Right hand side: closer view of the pillar. The chosen geometry is typical for some of the current experimental work being conducted in that field. Characteristic for such tests, when prepared via cutting the sample in a focused ion beam (FIB) microscope, is the fact that the sample is connected with some curvature to the substrate bulk sample from which the pillar was cut.

5.3.2.2 Finite Element Model and Boundary Conditions

The pillar-shaped compression samples for the simulations were modeled as perfect cylinders placed on a large substrate that has the same crystal orientation and hardening parameters as the pillar itself. Typical of all such pillar compression tests is the fact that the sample is connected with some curvature to the substrate bulk sample from which the pillar was cut. The radius where the pillar connects to the substrate amounts in all cases to $0.5\,\mu m$ (figure 5.14). The compression tool was treated as a rigid surface. The mesh consisted of 3376, 3952, 4528 elements (3-D-quadrilateral, 8 integration points), respectively, and 3767, 4424, 5081 nodes, respectively, for specimens with different initial diameter-to-length ratios 0.68, 0.4, and 0.29. The geometry is typical for some of the experimental work being conducted in that field.

In the formulation of the boundary condition, the nodes on the bottom of the substrate are not allowed to undergo displacements along the loading axis (z axis) and the nodes among the bottom nodes on the lines that are parallel to x or y axis could not be displaced along the y or x axis, respectively. The crystal plasticity finite element constitutive model used in this study does not include mechanical size effects and, therefore, takes into account only the relative variation in the diameter-to-length ratio but not the fact that the original sample geometries reported in the literature are actually in the micrometer regime.

5.3.3 Theoretical Study on Pillar Stability

The study aimed towards a better understanding of the influence of the initial orientation, deformation-induced orientation changes including orientation gradient formation, sample geometry, anisotropy, and friction in micro-pillar compression tests. In order to cover these aspects the simulations were divided in 4 groups:

Group 1 (effect of sample height): Different initial diameter-to-length ratios of 0.68, 0.4, and 0.29; same initial crystallographic orientation for all 3 tests ($[1\,1\,12]$ compression axis); same Coulomb friction coefficient for all 3 tests ($\mu = 0.0$).

Group 2 (effect of friction in case of unstable orientation): Same initial diameter-to-length ratio of 0.4 for all 3 tests; same initial crystallographic orientation for all 3 tests ($[1\,1\,12]$ compression axis); different Coulomb friction coefficients ($\mu = 0, 0.05, 0.1$).

Group 3 (effect of friction in case of stable orientation): Same initial diameter-to-length ratio of 0.4 for all 3 tests; same initial crystallographic orientation (exact $[0\,0\,1]$ compression axis) for all 3 tests; different Coulomb friction coefficients ($\mu = 0.0, 0.005, 0.05, 0.1$).

Group 4 (effect of friction in case of nearly stable orientation): Same initial diameter-to-length ratio of 0.4 for all 3 tests; same initial crystallographic orientation (near Cube orientation with a compression axis close to the $[0\,0\,1]$ axis); different Coulomb friction coefficients ($\mu = 0.0, 0.05, 0.1$).

The reasoning behind this choice of the model parameters is the following: First, we wanted to study the influence of the stability of the initial orientation of the single crystal on the course of the compression tests. For this purpose we selected 3 different initial crystallographic orientations, namely, a $[1\,1\,12]$ compression axis, exact $[0\,0\,1]$ compression axis, and a compression axis near the $[0\,0\,1]$ direction. The first orientation is known as a very unstable one upon compression (Raabe et al., 2002c). We used it in order to probe a situation where the sample has a small crystallographic stability. It may be expected from such a start condition that strong deformation-induced orientation changes including orientation gradient formation may take place during the simulated compression test. This situation is simulated in order to study the relationship between the *crystallographic* stability and the *geometric* stability of the pillar.

Extreme opposite cases for *crystallographic* stability are examples with pronounced orientation changes upon loading versus cases where the orientation is stable during loading (no deformation-induced orientation scatter upon straining). Extreme opposite cases for *geometric* stability are examples with a strong shape change versus situations with shape stability during testing.

The crystallographic stability criterion that we used for the selection of an unstable starting orientation uses the approach suggested in Raabe et al. (2002c). It is based on

the divergence of the reorientation field for a given orientation under an imposed loading state. An orientation with a high reorientation divergence in orientation space means that tiny changes either in the external boundary conditions or in the internal state (*e.g.* very small initial orientation spread) may entail drastic changes in the reorientation path upon plastic deformation. It must be underlined that a large value in the reorientation divergence (indicating high instability) is not due to a non-linear effect but simply due to a certain variety in the sets of potential slip systems with similar Schmid factors, which, when activated, would entail a highly divergent rotation field in orientation space. In contrast to this unstable initial orientation we have chosen as a second variant the more stable Cube orientation with a [0 0 1] compression axis, the stability of which was investigated in detail in Raabe et al. (2002c, 2004b). Owing to the high symmetry of this orientation under compressive load (8 slip systems have identical Schmid factor) we have studied the same orientation again but with a slight orientation deviation of 0.1° from the exact [0 0 1] compression axis. This non-perfect [0 0 1] orientation was originally used as one of the starting orientations in order to mimic the effect of a slight asymmetry at the beginning of an experiment.[2] We assumed that an initial situation with a tiny deviation from the desired exact orientation relative to the compression tool is not too unrealistic given the complexity associated with the focused ion beam (FIB) sample preparation and the subsequent compression technique. This selection, hence, opens the orientation spectrum from the most unstable to a rather stable orientation.

The other variations are obvious, *i.e.* the diameter-to-length ratio is relevant for modifying the buckling tendency of the pillar and the friction imposes loads that deviate from the pure compressive state introducing a shear component in the deformation.

5.3.3.1   Simulation Results

Group 1 effect of sample height (different height, same initial unstable orientation, no friction):   This group evaluates the geometrical shape stability or, respectively, buckling tendency during single crystal compression along the [1 1 12] axis. Figure 5.15 shows the predicted evolution of the pillar shapes and of the deformation-induced orientation changes for the 3 cases (diameter-to-length ratios 0.68, 0.4, 0.29). A pronounced shape instability was observed for the slim pillars with diameter-to-length ratios of 0.4 and 0.29. The shape of the thick pillar with a diameter-to-length ratio of 0.68 remained stable during compression even up to large strains. The color code in figure 5.15 shows the magnitude of the accumulated crystallographic plastic shear. It is revealed that in both cases where geometrical instability occurs (diameter-to-length ratios 0.4 and 0.29) the accumulated shear is localized close to the bottom of the pillar and close to the (friction-free) contact zone between the pillar and the compression tool. The strong shape changes observed for the slim pillars lead to a strong reduction of the

---

[2]The relevance of this choice was impressively shown by the experiments shown in the second part of the section were a very similar setup was used to explain peak shifts in Laue diffraction patterns observed *in situ* during micro-pillar compression (Maaß et al., 2009).
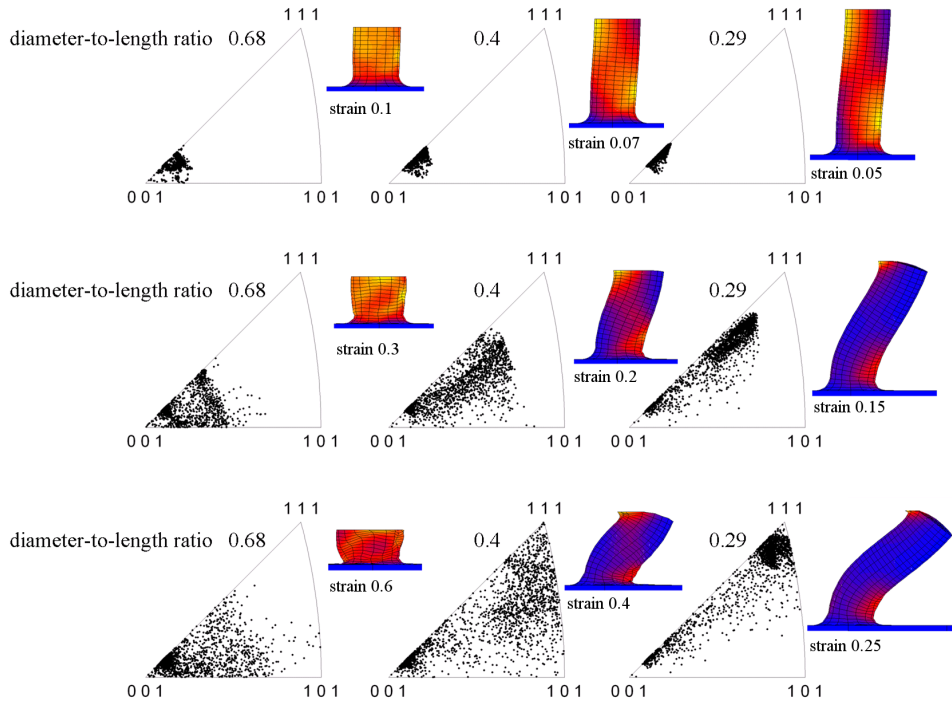
Figure 5.15: Crystallographic orientation changes and shapes of three pillars with different initial dimensions (diameter-to-length ratios: 0.68 (left column), 0.4 (middle column), 0.29 (right column)) after different displacements (color code: accumulated plastic shear from blue (low) to yellow (large)). Starting compression axis: $[1\,1\,12]$ (unstable in compression). The strain is given as engineering thickness reduction.

contact zone between pillar and tool, and, hence, to corresponding strain localization and shear effects at the top of the pillars.

The model with an initial diameter-to-length ratio of 0.4 was chosen for the ensuing simulations below (groups 2–4), because it reveals some shape instability and at the same time relatively small localization effects. This is of advantage when studying crystallographic orientation changes and boundary condition effects in greater detail. In addition this value of the diameter-to-length ratio is close to some typical pillar shapes reported in the literature.

The shape instabilities observed in figure 5.15 (middle and left columns) differ from classical elastic-plastic buckling, which would be predicted for pillars that are at least about a factor of 20 longer than in the current case (assuming the same diameter), *i.e.* classical isotropic solutions to predict buckling of such pillars do not apply. It is rather an unidirectional bulk shear process of the entire specimen with two main localization zones that is observed. The first zone is close to the bottom of the pillar and the second one is located near the contact zone to the tool. This behavior may be attributed to the discreteness of the plastic slip in the case of the crystal plasticity finite element simulations.

The analysis of the active slip systems reveals that during the early stage of plastic deformation the activation of the slip systems is still homogeneously distributed throughout the volume of the compressed samples. In the slim pillars this early stage was followed by pronounced shear localization phenomena in the region close to the bottom of the pillars and in the contact region, which becomes smaller during the simulated test owing to the strong shape change and bending of the slim pillars.

The difference in the orientation evolution between the three different types of originally single crystalline samples is quite remarkable. The shortest and geometrically most stable sample (largest diameter-to-length ratio of 0.68, left hand side in figure 5.15) reveals a strong spread of the initial orientation after deformation into an orientation distribution that is characterized by rotations towards the $[1\,1\,1]$ direction and particularly towards the $[1\,0\,1]$ direction. The $[1\,0\,1]$ compression axis would be the most stable final crystal orientation for the case of conventional frictionless uniaxial compression of face-centered cubic single crystals according to a simple Schmid factor calculation. Although the other orientations with high symmetry are also mathematically stable, already small deviations from the exact orientation would entail irreversible orientation changes. In contrast to that small changes away from an exact $[1\,0\,1]$ compression axis would always entail a back-rotation into that orientation.

The other two compression samples (diameter-to-length ratio of 0.4 and 0.29) are geometrically less stable and, hence, undergo a pronounced shape distortion entailing complete sample inclination. This phenomenon strongly affects the resulting orientation spread observed in the two simulation series. In both cases the orientation distribution evolves towards the $[1\,1\,1]$ direction. This effect is particularly pronounced in case of the geometrically most unstable sample (diameter-to-length ratio 0.29) where a very strong $[1\,1\,1]$ orientation distribution is formed after 25 % engineering thickness reduction.

Group 2 effect of friction in the case of an unstable orientation (all pillars with same initial thickness and same initial unstable orientation, different friction coefficients): The results on the change in the stress distribution together with the pillar shapes and the crystallographic orientation distributions are shown in figures 5.16a and b for different strains. Figure 5.16a uses individual color spread for each image to reveal patterning phenomena.

The deformation-induced orientation changes in the sample that was deformed with zero friction (left columns in figures 5.16a and b reveal a very strong tendency for reorientation with particular preference towards the evolution of a crystallographic $[1\,1\,1]$ orientation distribution (figure 5.16b).

The other two specimens that were deformed under non-zero friction conditions reveal slower orientation changes. In these two samples the initial orientation evolves towards the $[1\,1\,1]$ and the $[1\,0\,1]$ axis (middle and right columns of figures 5.16a and b. Also, the overall spread in the deformation-induced orientation distribution is in both cases with non-zero friction much smaller than in the case with zero friction. The latter
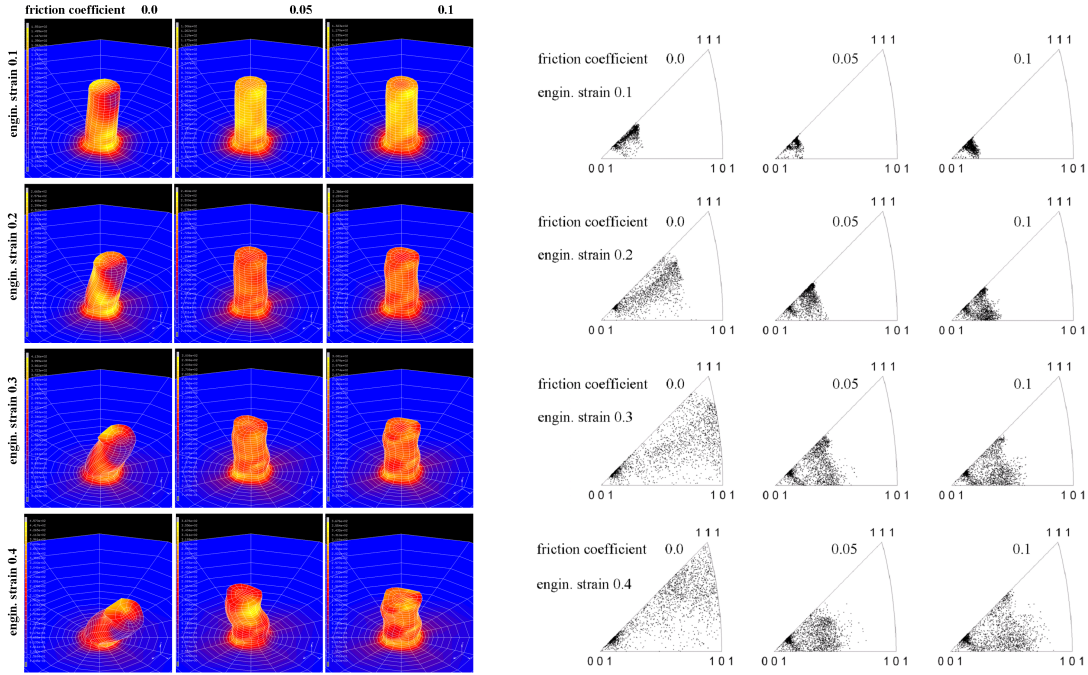
(a) Presentation of the pillar shapes. Color code: equivalent von Mises stress from blue (low) to yellow (large). Individually chosen color spread for each image to reveal patterning phenomena.

(b) Orientation scatter in inverse pole figures.
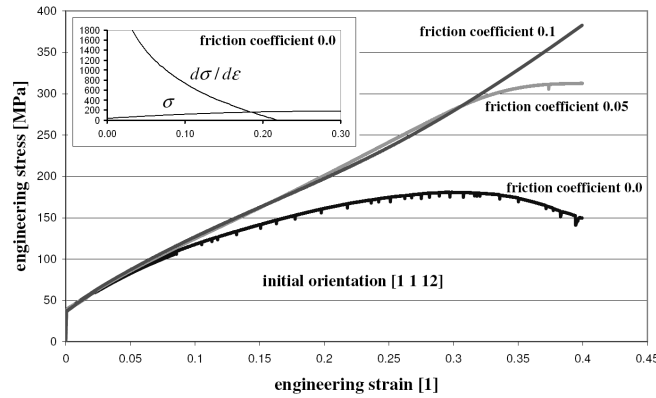
(c) Engineering stress vs. engineering strain curves for the three cases with different friction coefficients (σ = stress, $d\sigma/d\epsilon$ = hardening).

Figure 5.16: Crystallographic orientation distribution and shapes of pillars with identical initial diameter-to-length ratio of 0.4, which were deformed assuming different Coulomb friction coefficients (0.0 (left column), 0.05 (middle column), 0.1 (right column)). Starting single crystal orientation: $[1\,1\,12]$ compression axis (unstable in compression).

Figure 5.17: Shear distribution on the four most active slip systems for the pillar with an initial diameter-to-length ratio of 0.4; Coulomb friction coefficient 0.05. (color code: accumulated crystallographic shear on the slip systems indicated above the images from blue (low) to yellow (large)). Initial single crystal orientation: [1 1 12] compression axis (unstable in compression). Individually chosen color spread for each image to reveal the shear patterning.

Figure 5.18: Shear distribution on the four most active slip systems for the pillar with an initial diameter-to-length ratio of 0.4; Coulomb friction coefficient 0.1. (color code: accumulated crystallographic shear on the slip systems indicated above the images from blue (low) to yellow (large)). Initial single crystal orientation: [1 1 12] compression axis (unstable in compression). Individually chosen color spread for each image to reveal the shear patterning.

simulation (zero friction, left column) reveals a large deformation-induced orientation spread covering nearly the entire standard triangle. The results clearly confirm that the chosen initial crystal orientation is in all three cases very unstable against compression. This observation matches earlier results on the kinematical origin of the instability of this orientation (Raabe et al., 2002c).

The shape changes of the pillars also reveal clear differences among the 3 samples (figure 5.16a). The sample that was deformed under zero-friction shows a very strong instability, while the two specimens that were deformed with non-zero friction reveal a more stable evolution of the shape. This observation is also reflected by the corresponding flow curves. In the case of zero friction the stress–strain curve shows that the simulated test becomes unstable at an early stage of deformation, figure 5.16c. This observation matches the shape change presented in figure 5.16a. The stability of the flow curve is analyzed in terms of the Considère criterion, *i.e.* in terms of the point of intersection between the stress–strain curve and its derivative (upper left diagram in figure 5.16c). The point of intersection between the two curves occurs at an engineering strain of 0.185. The two stress–strain curves for non-zero friction (friction coefficients 0.05, 0.1) are much more stable and do not experience geometrical softening. Such behavior is typical for conventional bulk compression tests, which as a rule do not undergo geometrical softening but instead shape stabilization in cases when the diameter-to-length ratio is much larger than the critical ratio at which buckling occurs. It should be mentioned here that shape instability may for anisotropic (single crystalline) constitutive elastic-plastic behavior occur at much lower strains than for isotropic behavior, *i.e.* conventional isotropic buckling theory does not apply. The two samples with friction coefficients 0.05 and 0.1 reveal practically identical hardening behavior. At large strains above 0.35 the sample with a friction coefficient of 0.05 shows some softening, which can be attributed to shape instability.
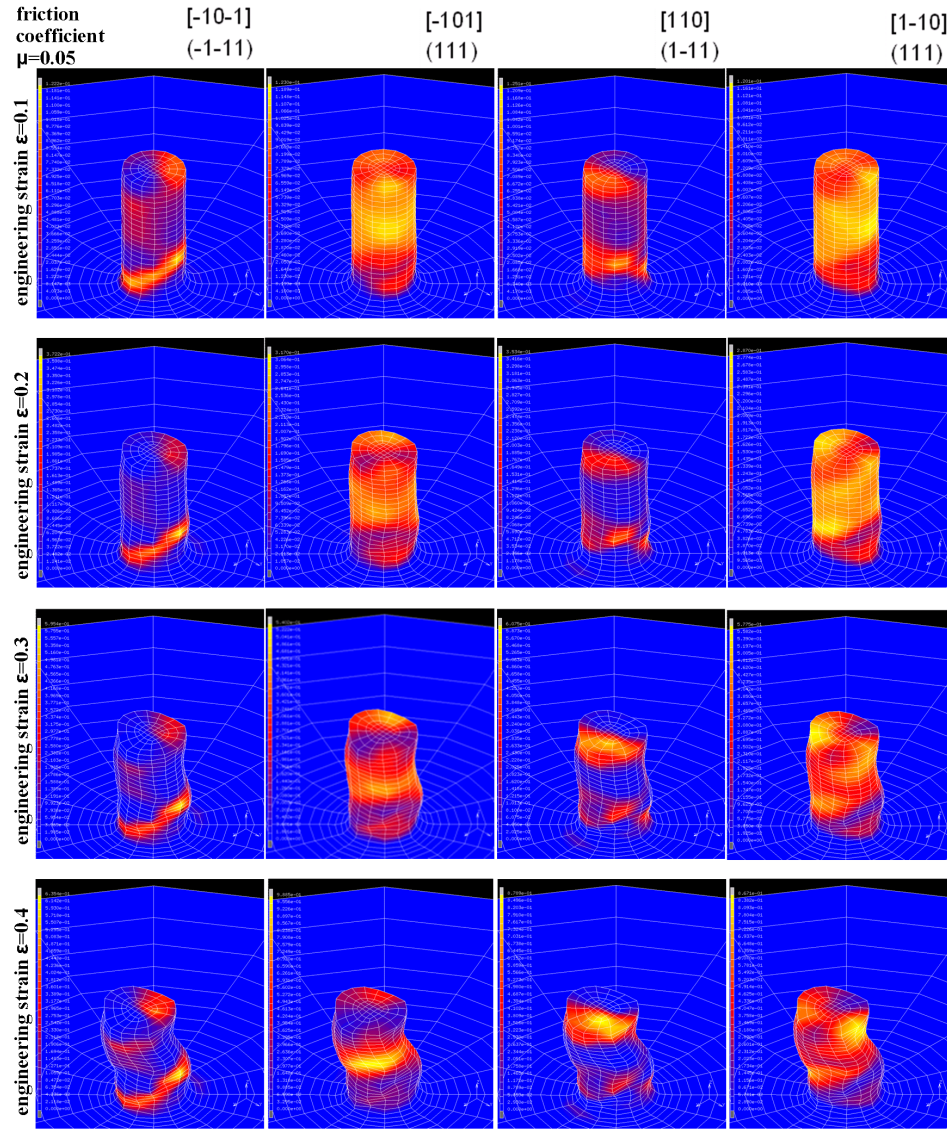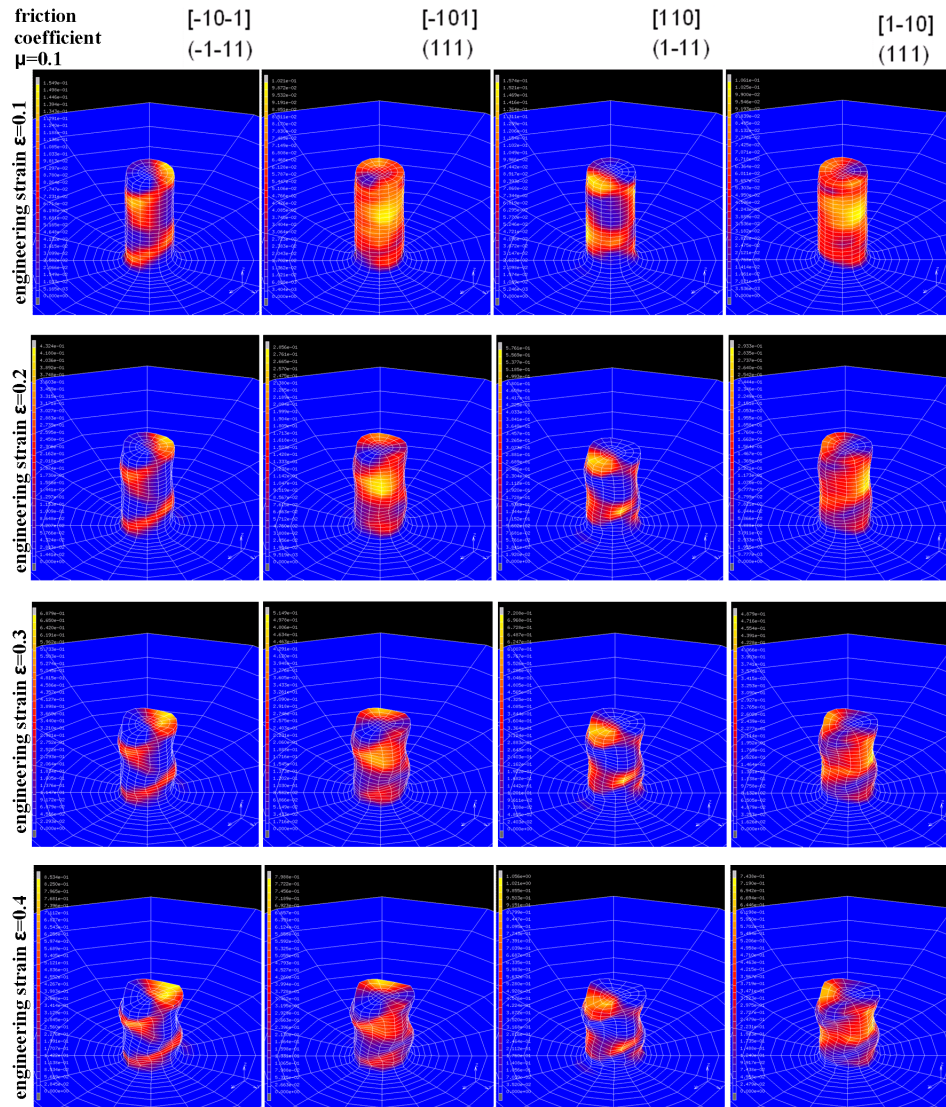
Figures 5.17 and 5.18 show the shear distribution on the four most active slip systems for the pillar with an initial diameter-to-length ratio of 0.4 at a Coulomb friction coefficient of 0.05 (figure 5.17) and 0.1 (figure 5.18), respectively (sample with $[1\,1\,12]$ compression axis, see figures 5.16a and b). The color code refers to the magnitude of accumulated crystallographic shear on the slip systems. Yellow color indicates the largest and blue the smallest amount of crystallographic shear. Note that the color spread has been individually chosen for each image to better reveal the shear patterning at all strains.

In both cases the shear on slip system $[\bar{1}\,0\,\bar{1}](\bar{1}\,\bar{1}\,1)$ is highly localized in an oblique shear band that crosses the pillar close to the bottom (left column in both figures). This zone of concentrated slip occurs already at an early stage of the simulated compression test. The shear on slip system $[\bar{1}\,0\,1](1\,1\,1)$ is more equally distributed in the pillar (second column in both figures). At larger strains it is particularly concentrated in the zone where buckling occurs first. The shear distribution on slip system $[1\,1\,0](1\,\bar{1}\,1)$ reveals in both cases a concentration of crystallographic shear at the top of the pillar where tool contact occurs and at the bottom close to the transition zone between the pillar and the bulk material below it (third column in both figures). Shear on slip system $[1\,\bar{1}\,0](1\,1\,1)$

is more equally distributed throughout the pillar with dominance in those zones where buckling occurs.

The strong localization of slip on the systems $[\bar{1}\,0\,\bar{1}](\bar{1}\,\bar{1}\,1)$ and $[1\,1\,0](1\,\bar{1}\,1)$ in the form of oblique shear zones coincides with the occurrence of strong shape instabilities in the pillars. The fact that the shape changes observed in the present examples cannot be interpreted in terms of classical analytical solutions of Euler or plastic buckling theory suggests that it is the crystalline anisotropy that promotes early shape instability owing to its directional discreteness of the shear distribution. This effect can obviously not be captured by isotropic buckling theory.

Another important observation is that the simulation with the higher friction coefficient (0.1, figure 5.18) does not show a more homogeneous distribution of the crystallographic shear than the simulation with the smaller friction coefficient (0.05, figure 5.17).

Group 3 effect of friction in the case of a stable orientation (all pillars with same initial thickness and same initial stable orientation, different friction coefficients): The exact Cube orientation with a $[0\,0\,1]$ compression axis is for face-centered cubic single crystals known to be kinematically relatively stable under compressive loads as was investigated in detail in Raabe et al. (2002c, 2004b). Owing to the high symmetry of the exact Cube orientation under compression (8 slip systems have identical Schmid factor) we have selected a modified set of friction coefficients since it has been observed in earlier works that even minor changes in friction can have a substantial influence on the stability of this orientation when subjected to a compressive load.

The Cube-oriented single crystals ($[0\,0\,1]$ compression axis) reveal under compressive loads pronounced differences in shape change and orientation evolution as a function of the friction coefficient (figures 5.19 and 5.20). Slight differences in the apparent pillar height in figure 5.19a are due to perspective and differences in buckling. One should note that the color spread has been individually chosen for each image to better reveal the individual stress patterns for the subsequent loading stages. Figure 5.19b shows the deformation-induced orientation scatter in terms of inverse pole figures. The (homogeneous) shape changes of the pillars are similar for all three cases (non-zero friction coefficients 0.005, 0.05, 0.1, figure 5.19a). Similar as observed for the preceding case with a less stable starting orientation (figure 5.16a and b) the $[0\,0\,1]$ oriented samples develop in part a large orientation spread (figure 5.19b) during deformation. In the case of the zero friction compression test the gradual formation of a very strong orientation spread out of an originally single crystal orientation is by far strongest owing to the distorted and inclined shape of the sample after straining. However, as above, this strong orientation change (see left column in figure 5.19a) is caused in part by the pillar inclination and not only by crystallographic reorientation (figure 5.20).

In contrast to the cases discussed above with a less stable orientation the present results on the $[0\,0\,1]$ compression axis suggest that crystallographically symmetric orientations
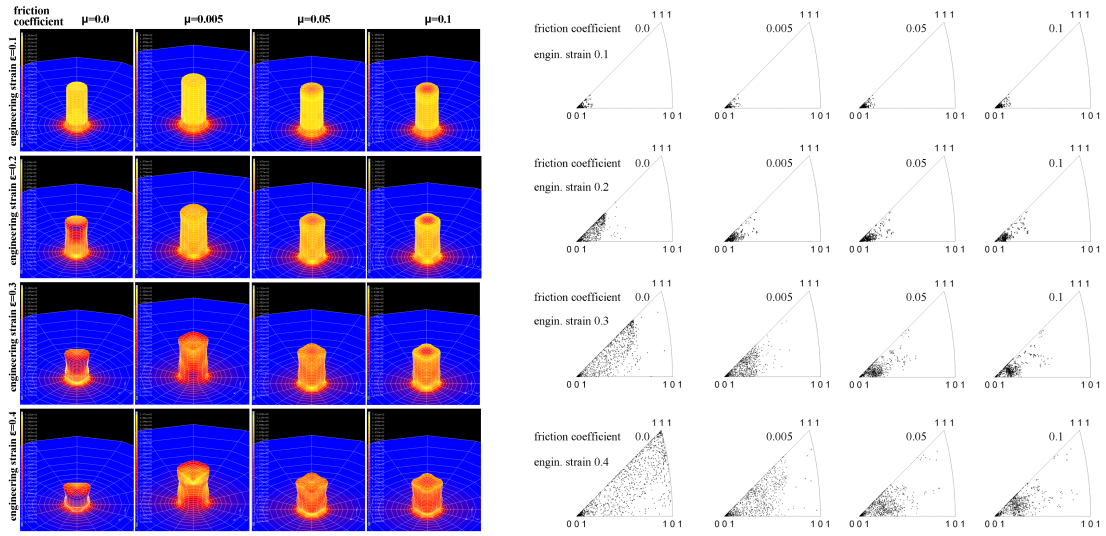
(a) Presentation of the pillar shapes. Color code: equivalent von Mises stress from blue (low) to yellow (large). Individually chosen color spread for each image to reveal patterning phenomena.

(b) Orientation scatter in inverse pole figures.
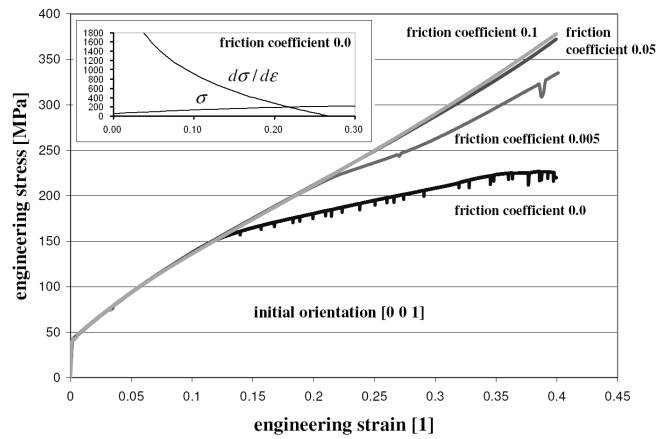
(c) Engineering stress vs. engineering strain curves for the three cases with different friction coefficients (σ = stress, $\mathrm{d}\sigma/\mathrm{d}\epsilon$ = hardening).

Figure 5.19: Crystallographic orientation distribution and shapes of pillars with identical initial diameter-to-length ratio of 0.4, which were deformed assuming different Coulomb friction coefficients (0.0 (left column), 0.05 (middle column), 0.1 (right column)). Starting single crystal orientation: [0 0 1] compression axis (stable in compression).
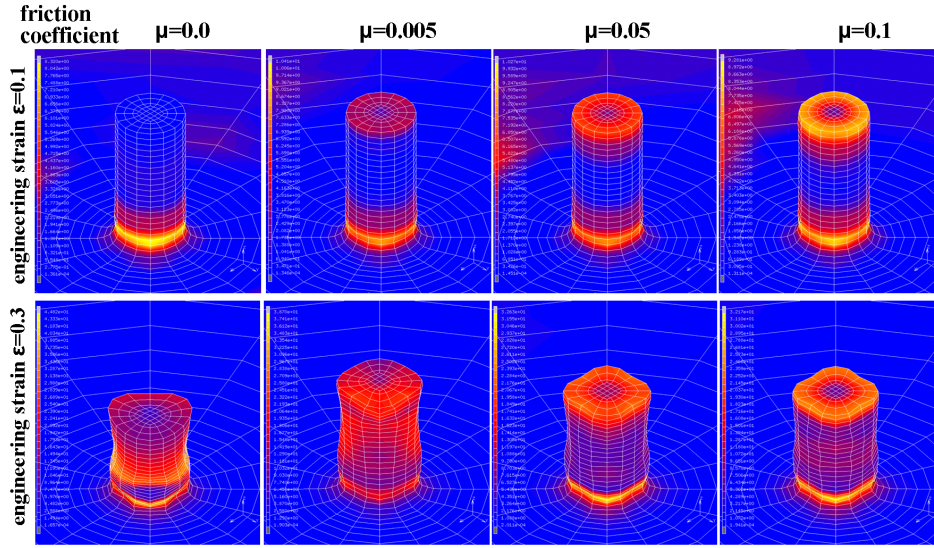
Figure 5.20: Crystallographic orientation distribution within pillars with respect to the
initial orientation for two deformation stages. Pillars with identical initial diameter-
to-length ratio of 0.4, which were deformed assuming different Coulomb coefficients
(0.0 (left column) , 0.005 (left middle column), 0.05 (right middle column), 0.1
(right column)). Starting single crystal orientation: Cube orientation, [0 0 1] com-
pression axis (stable in compression). Color code: misorientation (angle only, axis
not indicated) with respect to the original Cube orientation from blue (low orienta-
tion deviation to the original orientation) to yellow (large orientation deviation to
the original orientation). Individually chosen color spread for each image to reveal
patterning phenomena.
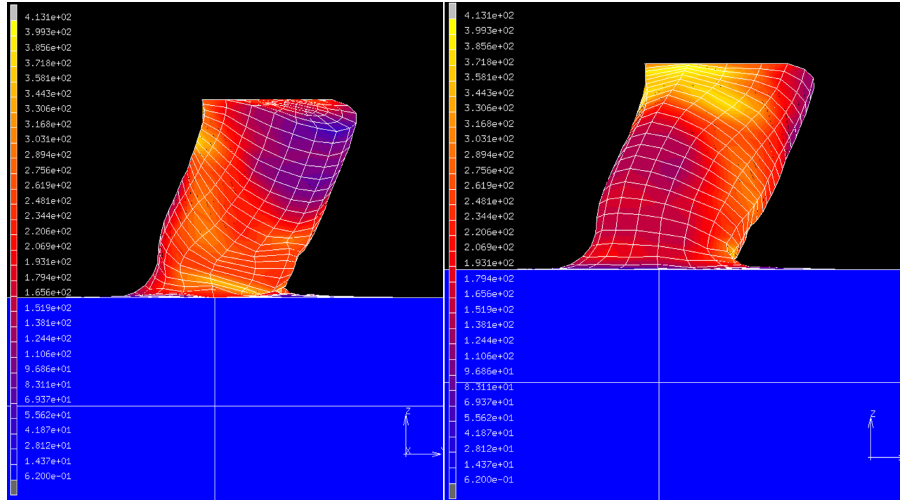
Figure 5.21: Front and back view on the shape change of the pillar with an initial [0 0
1] axis compressed at zero friction to 40 % engineering thickness reduction. Pillar
with initial diameter-to-length ratio of 0.4. Color code: von Mises stress from blue
(low) to yellow (large).

reveal a slightly better shape stability during compression than less symmetric orientations.

Although the shapes of the [0 0 1] oriented pillars show a strong four-fold anisotropy in the cross section after straining under non-zero friction (see *e.g.* bottom row in figure 5.20) the specimens do not undergo any buckling during compression. Buckling only occurred for the case with zero friction (figures 5.19a and 5.21). This observation indicates the important role of crystallographic symmetry on the one hand and of friction on the other hand for a successful buckling-free compression experiment. The observation of the stabilizing influence of friction is rather essential since in real experiments it is very difficult to prepare a sample with an exact desired orientation. An important point that deserves attention in that context is the possible influence of numerical aspects on the buckling behavior predicted. For instance for the zero-friction boundary conditions the high symmetry of the [0 0 1] compression load case and the absence of any shear forces at the beginning of the simulation would suggest higher shape stability than observed in the present case (figure 5.21). We, hence, attribute the early shape instability observed even for highly symmetric situations also to some extent to numerical aspects associated with the integration of the crystal plasticity constitutive law. The simulation results observed for slightly off-cube situations, which are no longer perfectly symmetric, indeed indicate that even minor deviations (be they of a crystallographic or of a numerical nature) induce strong strain localization and shape change effects.

These observations on the shape changes for the different simulated single crystal compression tests correspond to the flow curves, figure 5.19c. For the relatively unstable case with zero friction the stress–strain curve shows that the test becomes unstable at an early stage of deformation. This observation matches the observed shape change, figure 5.21. The Considère analysis (upper left diagram in figure 5.19c) shows that instability starts at an engineering strain of 0.22. This value is small compared to the excellent stability of the simulated tests conducted with non-zero friction conditions but it is high compared to the small value of 0.185 that was observed for the crystallographically less stable sample [1 1 12], figure 5.16c. This means that the geometrical stability of single crystal compression tests can be improved by choosing stable orientations. The three stress–strain curves for non-zero friction conditions (friction coefficients 0.005, 0.05, 0.1) are much more stable and do not experience substantial geometrical softening.

Another important characteristic of the simulations with [0 0 1] compression axis as starting single crystal orientation is the pronounced localization of the misorientation in a narrow band at the bottom of the compression samples close to the transition into the bulk material (figure 5.20). This observation holds for samples with all friction conditions. Those samples that were deformed with a non-zero friction coefficient also show a thin layer with strong misorientations at the contact area to the tool.

While the localization at the bottom of the sample can be attributed to the change in the boundary conditions owing to the curved transition into the bulk material the misorientation localization at the contact zone for samples deformed under friction is due to the shear created in this thin contact zone. Both aspects deserve close attention for

the design of optimal compression tests since strong localization effects (misorientation or strain or both) are obviously not desired for such tests.

Group 4 effect of friction in the case of a nearly stable orientation (all pillars with same initial thickness and same nearly stable initial orientation, different friction coefficients):   The last example is about a nearly stable single crystal. The initial orientation before deformation deviates by only 0.1° from the exact $[0\,0\,1]$ compression axis (figure 5.22). Although this deviation appears as a small orientation difference the example in the second part of this section shows the importance of small deviation from ideal conditions. Here, one particular important effect is that it is sufficient to break the symmetry of the 8 slip systems with equal Schmid factors, which characterizes the preceding tests with a perfect $[0\,0\,1]$ compression axis. For the present case one slip system has a larger Schmid factor than all others at the onset of loading.

The resulting orientation spread during deformation is again, like for the other examples, relatively large (figure 5.22b). However, compared to the results shown above, the present simulations show a different reorientation tendency. As documented in the inverse pole figure for the case with zero friction (left column in figure 5.22b) the orientation distribution evolves towards a pronounced $[1\,0\,1]$ alignment. This orientation is indeed the most stable orientation for compression of face-centered cubic single crystals under pure friction-free compressive loading. However, like in the other cases discussed before, some of the orientation spread observed in this inverse pole figure cannot be attributed to classical Schmid-type orientation evolution owing to the strong inclination of the overall sample.

The other two simulations with non-zero friction coefficient (middle and right column in figures 5.22a and b reveal a more homogeneous orientation change towards both the $[1\,1\,1]$ and the $[1\,0\,1]$ axis. The sample with a (small) friction coefficient of 0.05 shows a slightly more pronounced tendency of rotations towards $[1\,0\,1]$ (figure 5.22b).

Concerning the geometrical stability the present results reveal that a diameter-to-length ratio below 0.4 leads to a pronounced shape instability in all cases studied, irrespective of the initial crystallographic orientation of the compressed specimen. Like for the other orientations discussed above non-zero friction conditions generally exert a stabilizing effect on the course of the compression test even when a substantial evolution of orientation scatter takes place.

The stability becomes evident also from the flow curves, figure 5.22c. For the unstable case with zero friction the Considère analysis reveals the onset of instability at an engineering strain of 0.18, which is the smallest for all cases studied. The other two stress–strain curves obtained for non-zero friction conditions remain stable during compression.
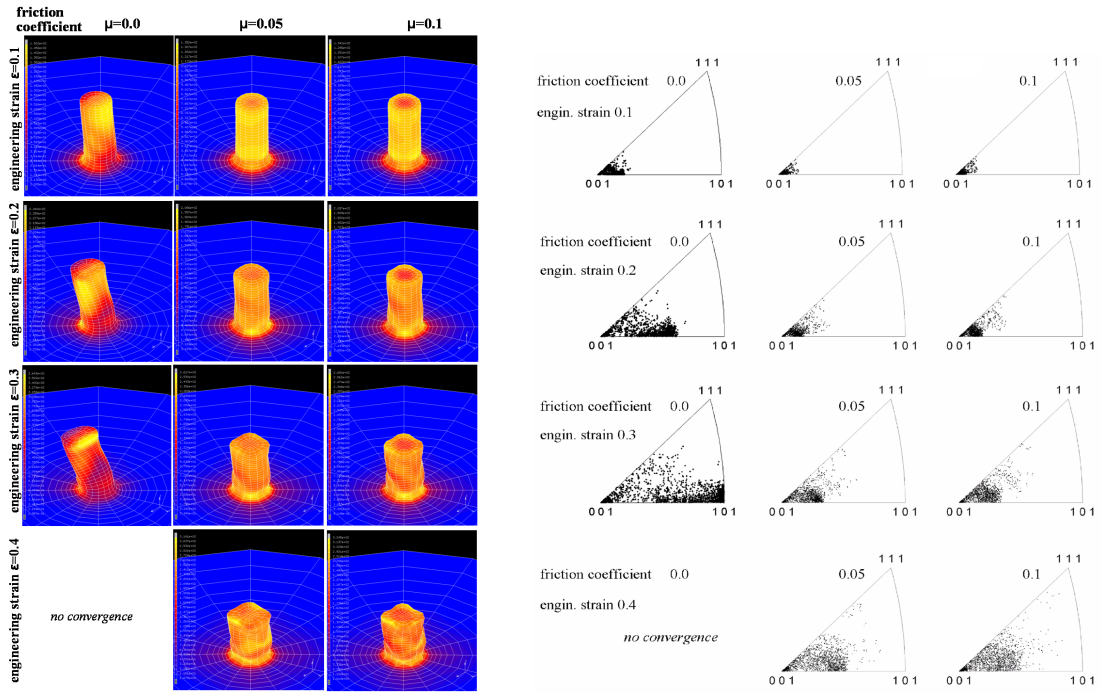
(a) Presentation of the pillar shapes. Color code: equivalent von Mises stress from blue (low) to yellow (large). Individually chosen color spread for each image to reveal patterning phenomena.

(b) Orientation scatter in inverse pole figures.
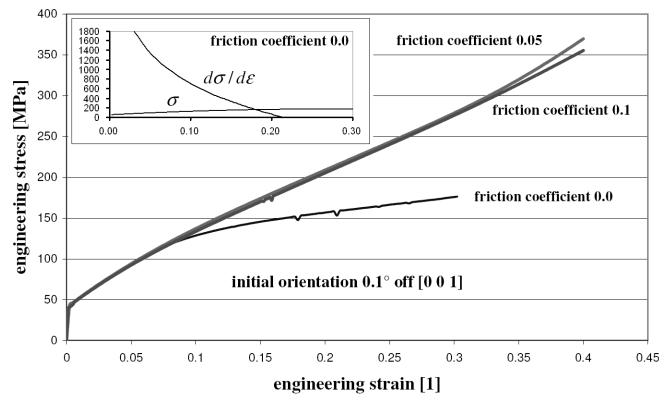
(c) Engineering stress vs. engineering strain curves for the three cases with different friction coefficients ($\sigma =$ stress, $d\sigma/d\epsilon =$ hardening).

Figure 5.22: Crystallographic orientation distribution and shapes of pillars with identical initial diameter-to-length ratio of 0.4, which were deformed assuming different Coulomb friction coefficients (0.0 (left column), 0.05 (middle column), 0.1 (right column)). Starting single crystal orientation: near [0 0 1] compression axis (0.1° initial deviation)

5.3.3.2 Conclusions

Crystal plasticity finite element simulations of cylindrical Cu single crystal compression tests have been performed. The main parameters were the initial crystallographic orientation, sample geometry (diameter-to-length ratio), and friction. The main results and conclusions are

- Geometrical stability: A diameter-to-length ratio below 0.4 (slim samples) leads to a pronounced shape instability for the stable and unstable orientations inspected. This observation does not match classical isotropic plastic buckling theory but it rather resembles an unidirectional bulk shear process of the entire specimen with two main localization zones, one close to the bottom of the pillar and one in the contact zone to the tool. This effect is attributed to the discreteness of the plastic slip in the present crystal plasticity finite element simulation approach. Samples with larger values for the diameter-to-length ratio revealed higher orientation and shape stability during compression.

- Non-zero friction conditions reduce shape instability irrespective of the initial crystallographic orientation of the compressed specimen.

- The initial anisotropy in the form of a different initial crystal orientation has—together with the magnitude of the friction coefficient—an influence on the deformation-induced orientation evolution, its spread, and the overall sample shape during compression.

- Pronounced deformation-induced orientation changes including the evolution of substantial orientation gradients (orientation scatter) within the originally homogeneous single crystals take place already at engineering compressive strains of about 0.2.

- The evolution of orientation scatter during compression within the originally homogeneous single crystals is weaker when the friction coefficient is higher.

- The documented orientation changes during compression are in part due to sample inclination rather than to crystallographic reorientation only.

5.3.4 Prediction of Active Slip Systems in Micro-Pillar Compression

The combination of white beam Laue diffraction and micro-compression was developed to study the evolving microstructure in micro-pillars during their deformation. The group of Van Swygenhoven at PSI (Switzerland) performed compression experiments combined with Laue diffraction on a number of Ni and Au pillars, see figure 5.23 (Maaß et al., 2009). Despite many differences between the individual pillars one common feature was found in the *in situ* Laue diffraction patterns. When deforming the pillar plastically the positions of the Laue peaks start moving. From the direction of movement one can calculate which slip systems are active. The group of Van Swygenhoven realized that at some point the peaks started moving into a different direction, figure 5.24. Moreover the slip system responsible for the initial peak movement did not correspond with the slip system with the highest Schmid factor for simple compression, only after the change in direction the high Schmid factor system was identified as the most active one. Therefore, the group decided to use the change in peak movement direction as the onset of plasticity and introduced the term "Laue yield" for it. However, this point does not coincide with any special feature of the stress–strain curves shown in figure 5.23.

The question what caused the activity of the non-expected slip system at the beginning of the compression experiment remained unclear. Therefore, the simulation framework introduced in the previous section was applied to the deformation of Au $[1\,2\,3]$ and Ni $[1\,2\,3]$ pillars. For this crystal orientation under simple compression the $(\bar{1}\,1\,1)[1\,0\,1]$ slip system has the highest Schmid factor of 0.47. Accordingly simulations using an ideal setup always predicted the activity of that slip system irrespective of the friction coefficient used. As shown previously solely the geometric stability was increased by a higher friction coefficient, figure 5.25. Only when deviations from the ideal setup were allowed the experimental findings could be reproduced. Figure 5.26 shows that when a tool inclination of 2° was assumed the $(1\,1\,1)[1\,0\,\bar{1}]$ and $(1\,1\,1)[0\,1\,\bar{1}]$ slip systems are more active at the beginning of the deformation despite their lower Schmid factors of 0.18 and 0.35, respectively. However, after some initial settlement of the whole setup the expected slip system takes over and becomes the most active one. The intersection of the slip activity curves marks the point where in the experiment the peaks of the Laue pattern change the direction of movement. Hence the simulations suggest that some initial misalignment between the compression tool and the pillar surface is responsible for the phenomena found in the experiment. This kind of misalignment is quite possible due to the small scale of the whole setup.

This example nicely illustrates the ability of CPFEM simulations to help in interpreting complex experiments. Even though it cannot provide the final prove for the underlying physical process it can be very helpful to distinguish the likely options from the less likely ones.
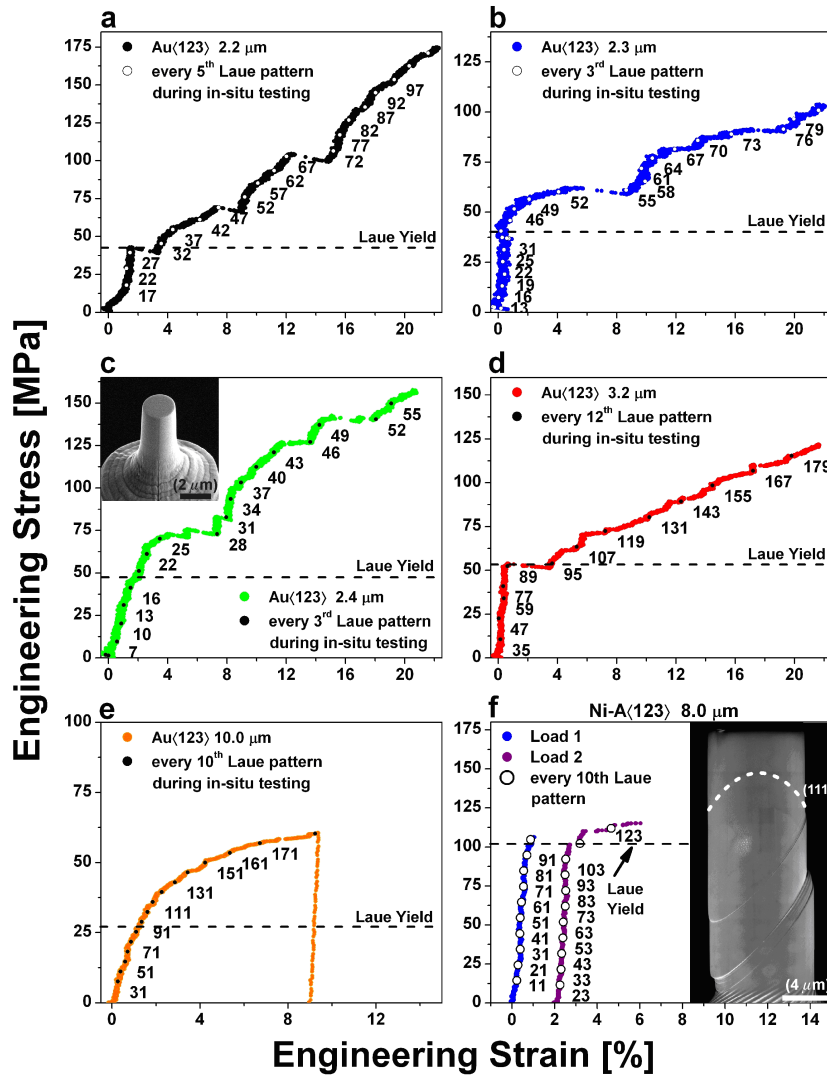
Figure 5.23: (a-d) stress–strain curves of four tested ⟨1 2 3⟩-micropillars, (e) flow curve of a 10.0 µm ⟨3 4 6⟩-pillar from another study (Maaß et al., 2007), and (f) the load–unload performed on the 8.0 µm Ni-A⟨1 2 3⟩-sample. An inset in (c) displays the undeformed pillar, and the deformed Ni-A is depicted as an inset in (f).(Figure taken from Maaß et al. (2009))
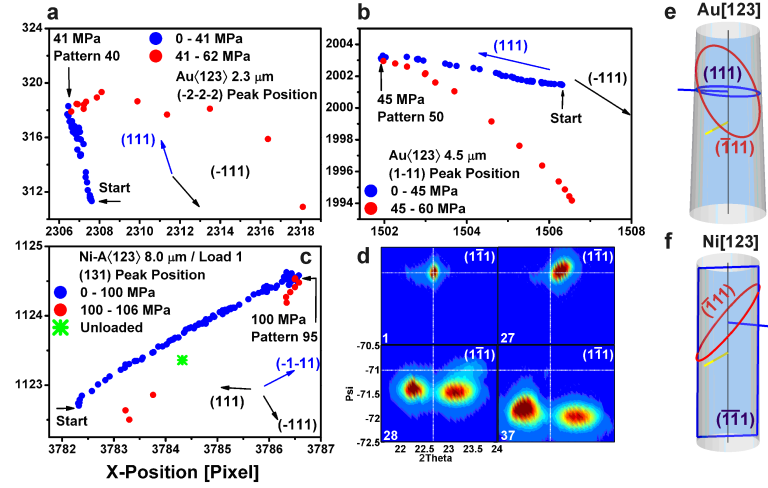
Figure 5.24: (a,b) Peak movement of the $(\overline{2}\,\overline{2}\,\overline{2})$ and $(1\,\overline{1}\,1)$-peak of the 2.3 and 4.5 µm Au pillar respectively, showing the change in Laue spot path; (c) the $(1\,\overline{3}\,1)$ Ni-A reflection traced during load 1 shown in figure 5.23d, also evidencing a change in peak movement; (d) shows the movement of the $(1\,\overline{1}\,1)$-reflection of the 2.2 µm Au$\langle1\,2\,3\rangle$-pillar in angular measures, with the initial peak (1), the peak before the change in path (27) followed by a change in peak path and peak splitting (28) at 1.5 % strain and at 4.3 % strain (37), the initial peak position with a dotted cross; (e,f) in blue the initially activated low Schmid factor plane with the corresponding rotation axis, and in red the predicted slip plane, the yellow line indicates the incoming beam axis. (Laue pattern numbering analogous to the stress–strain curves shown in figure 5.23)
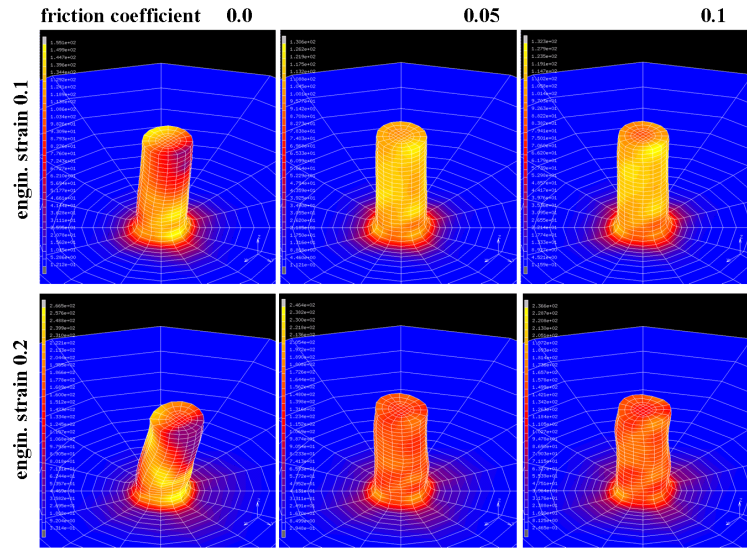
Figure 5.25: Pillar shapes found for different values of the friction coefficient.
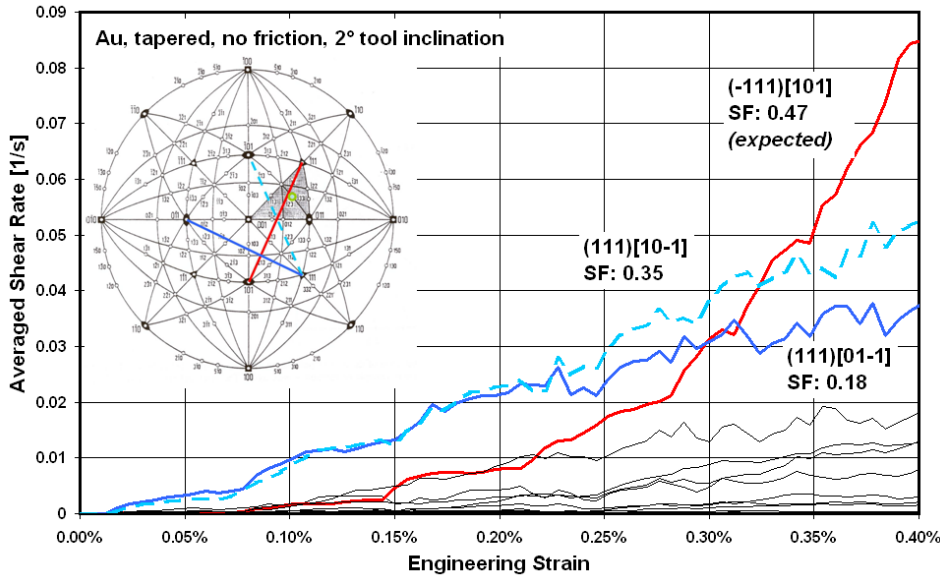
Figure 5.26: Average shear rates on all 12 slip systems for the compression of the Au micro-pillar of the same geometry and taper as investigated in the experiments. The boundary conditions were compression at zero friction and a tool inclination of 2° off the ideal punch direction (SF: Schmid factor).

5.4 On the Origin of Deformation Induced Rotation Patterns Below Nanoindents

5.4.1 Introduction

The observation of deformation-induced crystallographic lattice rotations caused by nanoindentation has recently attracted attention (Larson et al., 2002; Yang et al., 2004; McLaughlin et al., 2005; Lloyd et al., 2005; Zaafarani et al., 2006; Bouvier and Needleman, 2006; Kiener et al., 2006; Kysar et al., 2007; Brown, 2007). These orientation patterns were observed experimentally (Yang et al., 2004; McLaughlin et al., 2005; Lloyd et al., 2005; Zaafarani et al., 2006; Kysar et al., 2007) and also in corresponding simulations (Zaafarani et al., 2006; Bouvier and Needleman, 2006). Concerning the experimental work it is important that the same rotation patterns were identified by using three different types of techniques performed by different groups, namely, synchrotron wide-angle Bragg diffraction (Larson et al., 2002), electron back scatter diffraction (EBSD) in 2-D (Kysar et al., 2007) and in 3-D (Zaafarani et al., 2006), and transmission electron microscopy (TEM) (McLaughlin et al., 2005; Lloyd et al., 2005). Simulations using the viscoplastic crystal plasticity model presented in section 2.3 (Zaafarani et al., 2006) could already capture some important features of the experimentally observed orientation patterns. However, irrespective of some success along this line one must also state that a detailed simulation does not necessarily replace crisp understand-

ing of the main mechanism that is responsible for the fact that such patterns exist at all. In other words, although good agreement was obtained in the study between experiment and theory on this phenomenon (Zaafarani et al., 2006), it remained unclear why these deformation-induced patterns consist of multiple narrow zones of alternating crystalline rotations and counter-rotations of equal magnitude in close sequence. In this section we, therefore, try to elucidate the general crystallographic principle behind these patterns. For this purpose we take the following approach: First, the rotation patterns are investigated by a high resolution 3-D EBSD technique (EBSD tomography) for a nanoindent performed by a conical indenter with spherical tip in a copper single crystal. Next, we conduct advanced crystal plasticity finite element simulations using the dislocation density based constitutive model introduced in section 4.1 (Ma and Roters, 2004; Ma et al., 2006a). Finally, the results are discussed in terms of a geometrical model that simplifies the boundary conditions imposed during indentation in terms of a compressive state normal to the local tangent of the indent rim. This simplified assumption allows one to identify the dominant slip systems and the crystallographic principle behind the resulting re-orientations. The finite element simulations also predict the pile-up patterning around the indents, which can be related to the dislocation density evolution.

5.4.2   Modeling and Simulation

5.4.2.1   Parameter Fitting

The dislocation density based model presented in section 4.1 was used for the simulations, however, as the deformation takes place at room temperature the thermal annihilation term, equation (4.12), was neglected.

The evolution equations involve a number of material parameters (c_1 to c_6), which have to be fitted using experimental data. For the determination of the proper values of the material parameters a compression test was performed on a copper single crystal. The shape of the compression sample was a cylinder with dimensions $3\,\mathrm{mm} \times 4.5\,\mathrm{mm}$. The compression speed was $0.1\,\mathrm{mm\,s^{-1}}$ resulting in an average overall strain rate of $4.3 \times 10^{-4}\,\mathrm{s^{-1}}$. As the compression axis was in the [1 1 1] crystal direction no rotation was expected (the [1 1 1] orientation is stable under compression). Due to the high symmetry of this orientation the deformation is achieved by the activation of at least 6 slip systems. A shear stress–shear strain curve for a single slip system was extracted from the experiments by using the appropriate Schmid factor and by comparing it to a corresponding curve that was calculated analytically from the evolution equations. Figure 5.27 illustrates a very good agreement between model and experiment. Table 5.3 comprises the fitted parameters and the main constants.

However, as the scale of the two experiments (compression vs. nanoindentation) differs in size, the fitted values may also be different for the two scales. This applies in the current case for the value of the initial dislocation density. Although the original single crystal fit procedure provided a value of $5 \times 10^{10}\,\mathrm{m^{-2}}$ a higher value of $1 \times 10^{12}\,\mathrm{m^{-2}}$
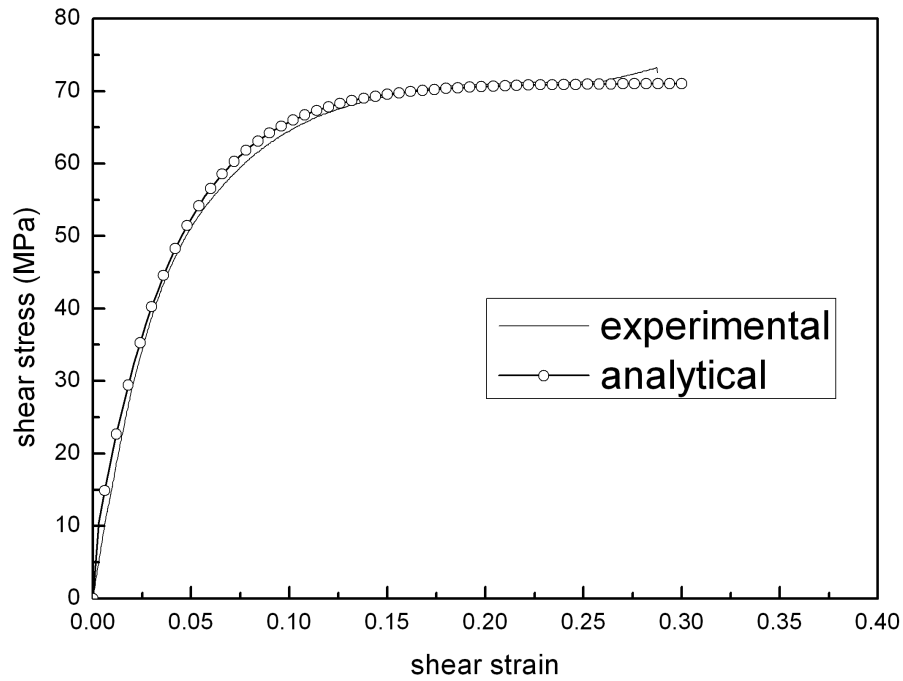
Figure 5.27: Fitted shear stress–shear strain curve

Table 5.3: Summary of crystal constants and parameters used in the model

Material constant	Unit	Value	Parameter	Unit	Value
shear modulus, G	GPa	75.4	for passing stress, c_1	-	0.1
Burgers vector, b	m	2.56×10^{-10}	for jump width, c_2	-	1.95
attacking frequency, ν_0	s^{-1}	1×10^{10}	for obstacle width, c_3	-	0.3
act. energy of slip, Q_{cut}	J	6.33×10^{-19}	for lock formation, c_4	-	0.037
Poisson ratio , ν	-	0.33	for dipole formation, c_5	-	0.04
			for athermal annihilation, c_6	-	50
			initial disloc. density, ρ_0	m^{-2}	5×10^{10}
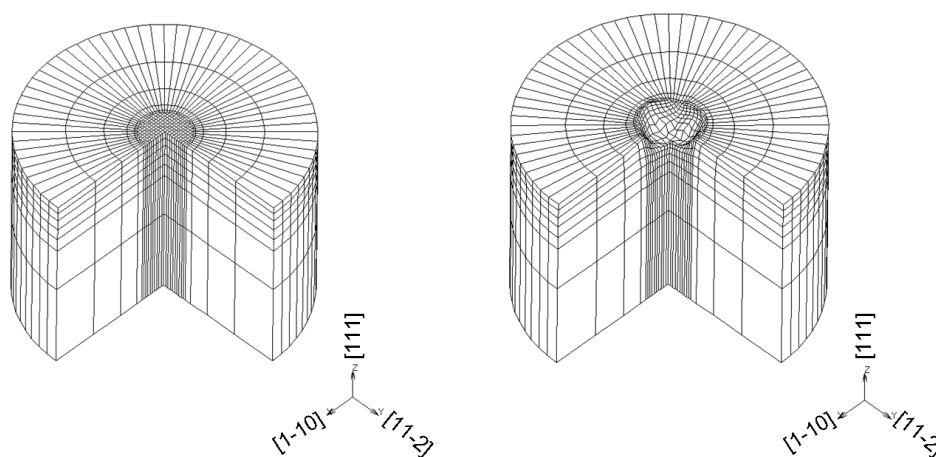
Figure 5.28: The mesh used in the finite element simulation (one quarter of the mesh
is not shown); left: undeformed mesh, right: mesh after deformation.

was chosen in the actual simulations since the simulated force–depth curves revealed in
this case a better match when compared with the ones observed in the nanoindentation
experiments. Even though this seems like a large discrepancy it can be understood by
local deviations from the average dislocation density and also the rapid increase of the
dislocation density at the very beginning of plastic deformation.

At first sight the dislocation-based model uses a similar number of fit parameters as
phenomenological models. However, it must be emphasized that a major advantage of
the dislocation-based model is that all parameters have a physical meaning and that
they can be further coupled to metallurgical mechanisms and multiscale models. All
parameters that were used lie within the ranges expected according to Ma and Roters
(2004).

5.4.2.2   The Finite Element Model

The mesh consisted of 4312 elements and 5224 nodes, figure 5.28 left. The elements
were of 3-D-hexahedral type with 8 integration points. Near the center of the indented
area a finer mesh was used due to the high deformation gradients expected in this
zone, figure 5.28 right. The lower face of the cylinder was fixed. Otherwise, each node
possessed three translational and three rotational degrees of freedom.

The tip with a radius of 1.5 µm was modeled as a rigid body. The simulation was
performed with displacement control up to an indentation depth of 1 µm in the negative
$[1\,1\,1]$ crystallographic direction. The initial orientation of the single crystal sample was
chosen by selecting appropriate Euler angles ($\varphi_1 = 0°, \phi = 54.74°, \varphi_2 = 45°$, Bunge's
notation) such that the x, y, z coordinate system represents the $[1\,\overline{1}\,0]$, $[1\,1\,\overline{2}]$, and $[1\,1\,1]$
crystal directions, respectively, figure 5.28.
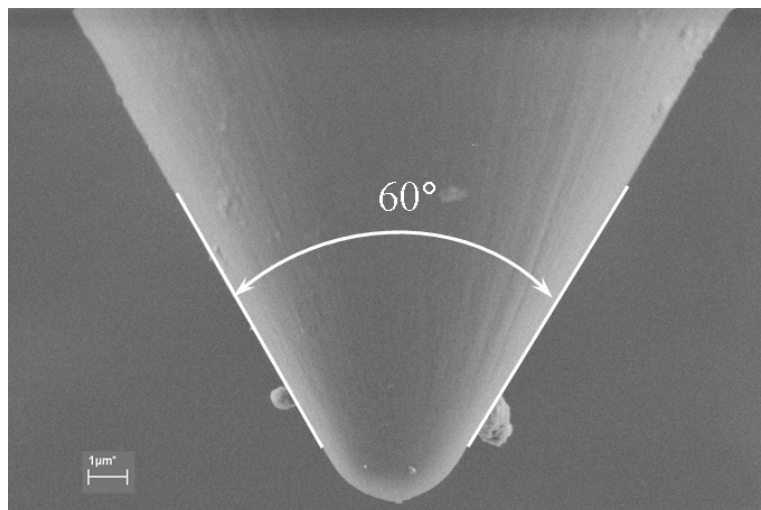
Figure 5.29: SEM image of the diamond indenter tip used in the experiments.

5.4.3 Experimental Procedure

Nanoindents were conducted using different forces on a Cu single crystal with a Hysitron nanoindenter system (TriboIndenter). The largest indent amounted to 1 µm depth. The force direction was in the negative [1 1 1] direction of the crystal. The tip had a conical shape with spherical tip in order to avoid any symmetry in the experiment other than that of the crystal. A SEM image of the indenter tip used is shown in figure 5.29. The EBSD experiments were conducted by using a joint high-resolution field emission SEM-EBSD setup together with a focused ion beam (FIB) system in the form of a cross-beam 3-D crystal orientation microscope (3-D EBSD). Details of this experimental approach are given in Zaafarani et al. (2006) and Konrad et al. (2006). The gallium$^+$ beam was directed normal to the (1 1 1) plane producing successive parallel milled areas as illustrated in figure 5.31. After each milling step an EBSD map was taken, figure 5.31. By the alternating milling and EBSD steps a tomographic 3-D EBSD image of the spatial crystal misorientation distribution underneath the nanoindent was reconstructed. Further details on the indentation procedure are given in Zaafarani et al. (2006) and Wang et al. (2004).

5.4.4 Comparison Between Experiment and Simulation

5.4.4.1 Rotation Patterns in Crystal Misorientation Presentation

The set of successive sections shown in figure 5.32 compares the misorientation of the crystal in the measured (1 1 $\bar{2}$) serial sections, figures 5.32a1–a4 with the simulations, figures 5.32b1–b4. All sections shown are near the indent center. The large accumulated strains in this region allow a more detailed study of the misorientation. The color code
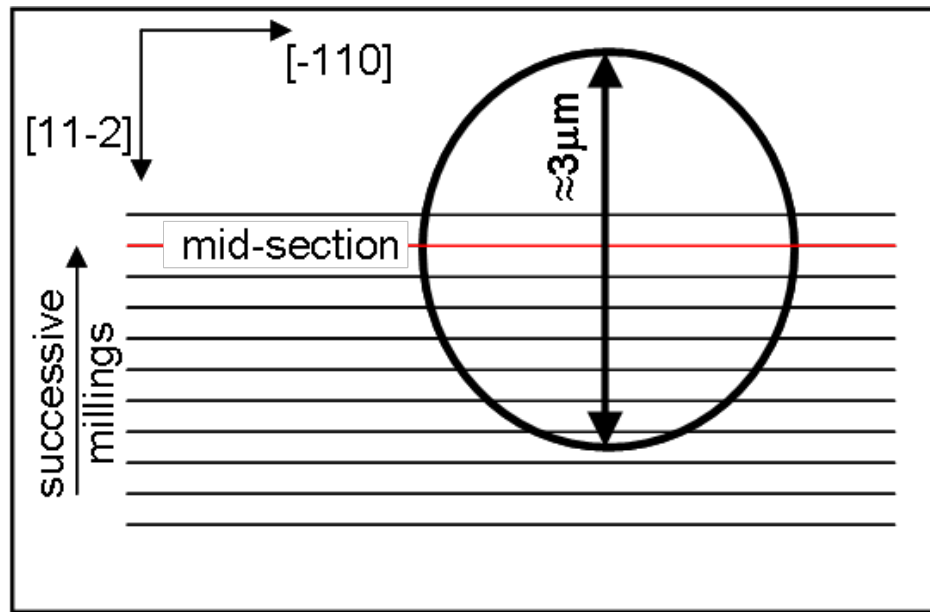
Figure 5.30: Top view presenting the cutting planes relative to the indent position.
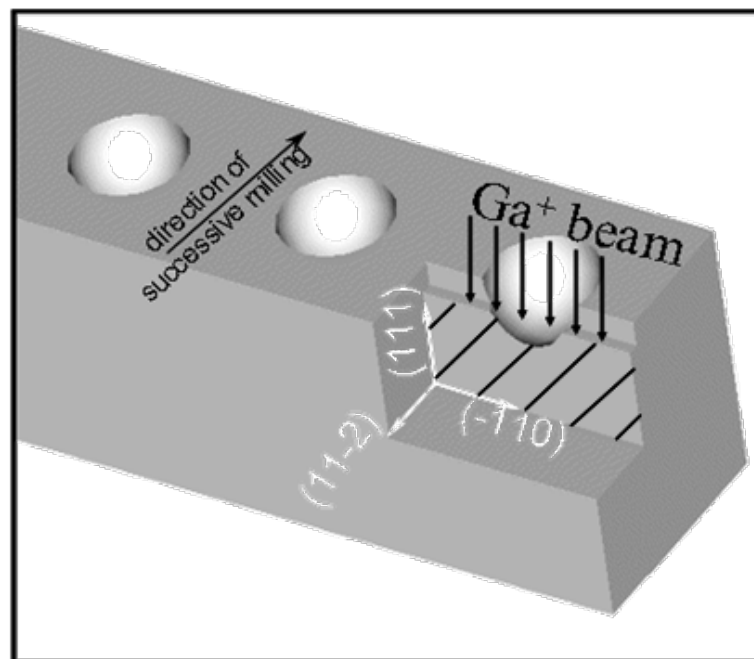
Figure 5.31: Schematic drawing of the successive section milling and EBSD measurement.
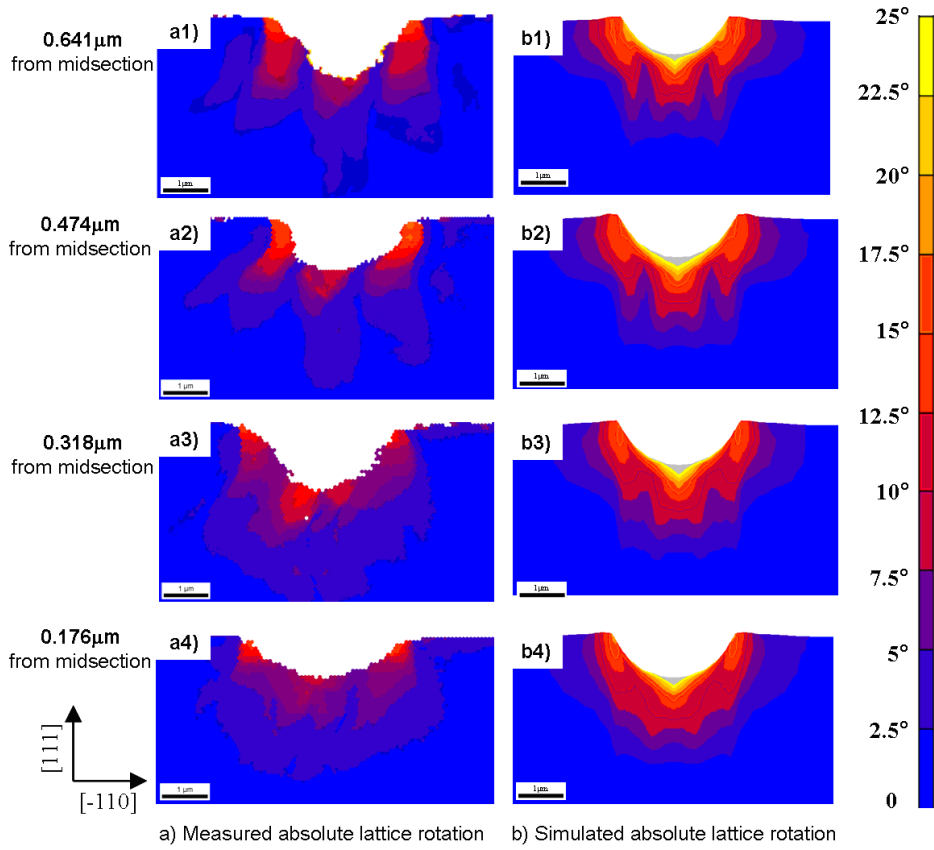
Figure 5.32: Misorientation maps (absolute lattice rotation) underneath the indentation at different cross sections, comparison between experimental and simulation results. (The seemingly shallower indent near the center is due to edge effects and milling-induced curvature.)

indicates the magnitude of the misorientation relative to the initial undeformed crystal orientation.

The measurements reveal a pronounced deformation-induced crystal rotation pattern underneath the indent. The alternating rotation and re-orientation zones are arranged directly underneath the indent. The measurements show that at the sides of the nanoindent only very small crystallographic rotations took place. The pattern underneath the indent near the center section can be characterized by six rotation zones, which are separated by narrow rotation-free areas, figure 5.32a4. The maximum values of the misorientation angles can be observed at the surface directly at the contact layer.

5.4.4.2 Rotation Patterns in Axis-angle Presentation

The orientation maps are also represented in the form of rotation angles about the $[1\,1\,\overline{2}]$ crystal direction in the sample reference system (one should note that in Zaafarani et al.
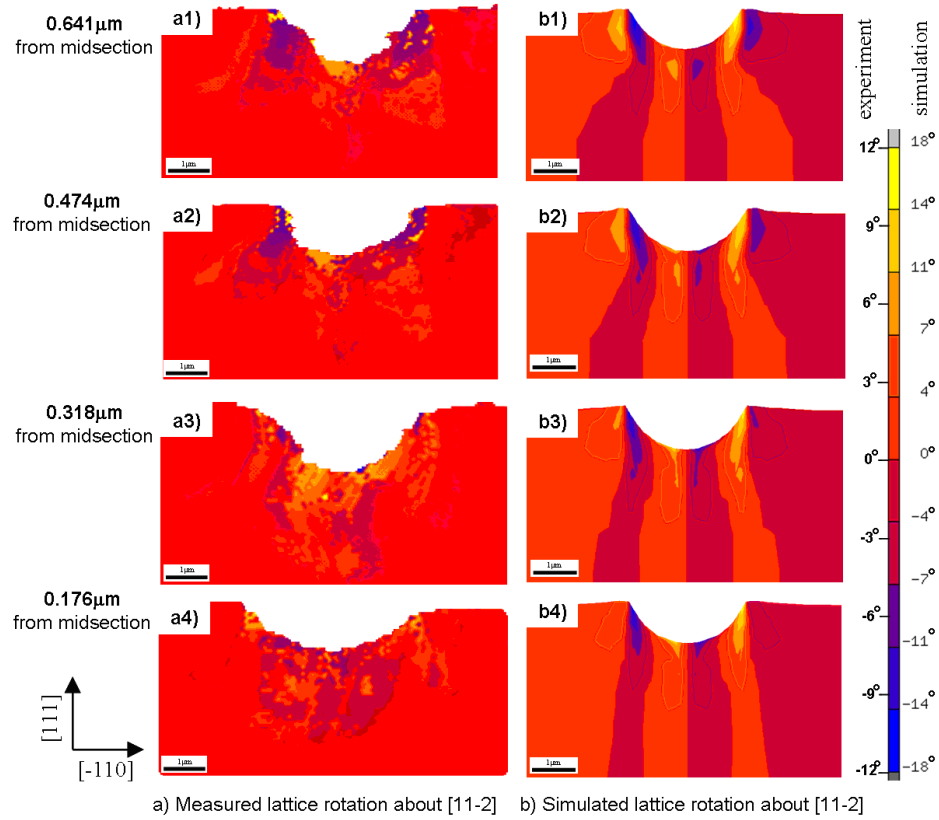
Figure 5.33: Comparison between crystal rotation about the direction $[1\,1\,\bar{2}]$ in the sample reference system underneath the indent at different cross sections between experimental and simulation results (positive values mean counter clockwise rotation). Note that in Zaafarani et al. (2006) the axis rotation is given in the crystal coordinate system.
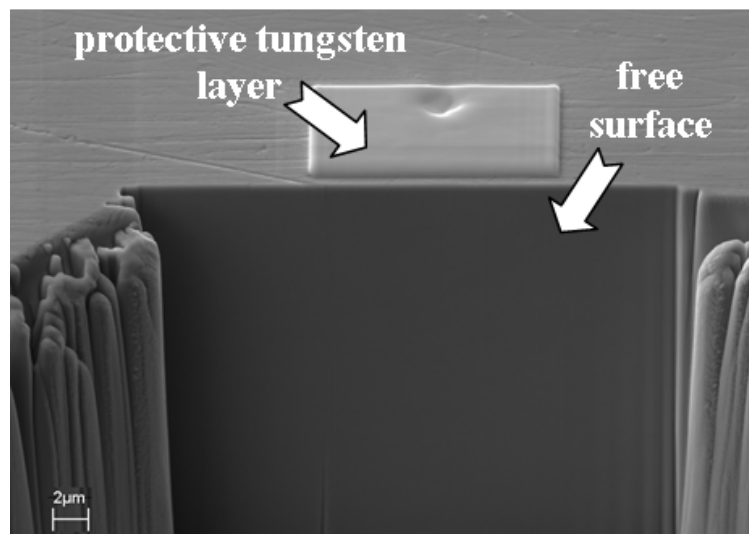
Figure 5.34: SEM image of the serial sectioning process.

(2006) the axis rotation is given in the crystal coordinate system). The maps are plotted on the $(1\,1\,\bar{2})$ planes in figures 5.33a1–a4 at different spacing to the center of the indent. The maps reveal pronounced lattice rotations about the $[1\,1\,\bar{2}]$ axis below the indent and lower values at the rims of the indent. The measurements also show frequent and quite abrupt changes in the sign of the rotation direction along and near the surface when presented in the form of $[1\,1\,\bar{2}]$ axis rotations. The rotations decrease further away from the contact zone. The comparison to the dislocation-based crystal plasticity finite element model shows that it succeeded in capturing fine details of the crystallography of the rotation patterning, figures 5.33b1–b4. Concerning the absolute values of the rotation angles about the $[1\,1\,\bar{2}]$ axis a maximum rotation angle of 14° was observed in the experiment. The corresponding maximum in the dislocation-based crystal plasticity model is about 23°. This deviation could be due to edge effects at the contact zone and milling-induced curvature caused by the ion beam so that no complete EBSD mapping could be achieved up to the actual contact interface. In this region though, maximum rotation values are likely to occur. Also, the lateral resolution of the measurement, which was conducted using an 80 nm step size, was probably not fine enough to capture all effects at the actual contact surface.

5.4.4.3   Effect of the Free Surface

One drawback of the focused ion beam technique for serial sectioning is that the method is destructive. This means that any error in the milling procedure requires full repetition of the entire experiment. Another problem of the method lies in the fact that the approach steadily produces new free surfaces for EBSD characterization, figure 5.34. This might probably have a small effect on the measured orientations compared to a (hypothetical) state of a bulk crystal without free surfaces.
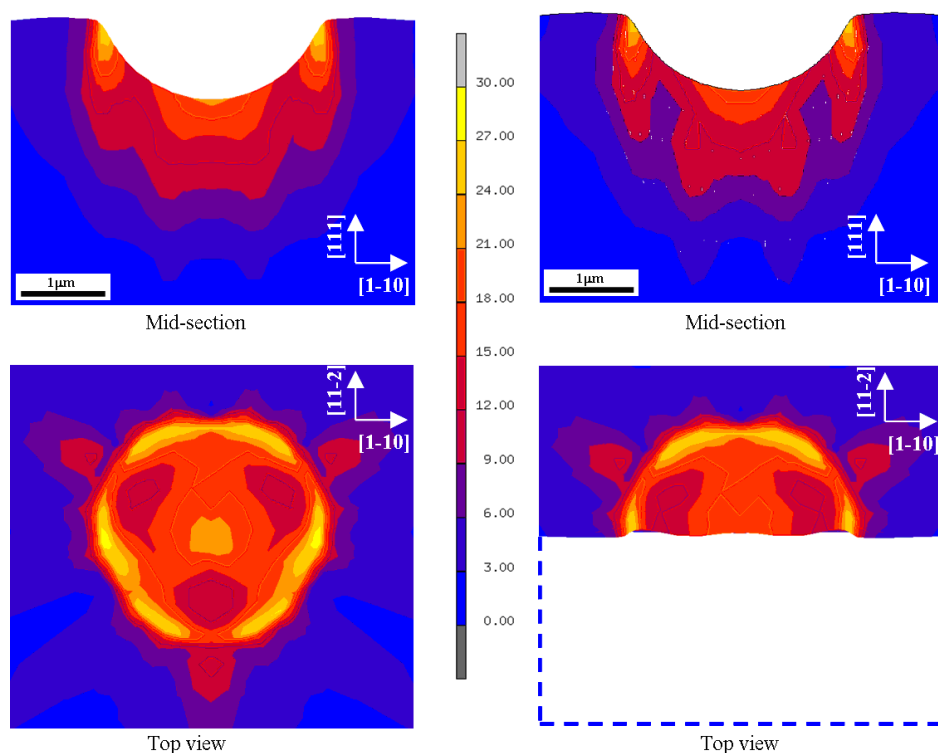
Figure 5.35: Effect of free surface milling on the total crystal rotation at the center cross section. left) non-relaxed right) relaxed.

With the help of the FE simulation the error caused by the free surface can be estimated. For this purpose the boundary conditions were changed to mimic a free surface (relaxed model). This approach simulates the effect of cutting the surface free. The misorientation patterns predicted in the two model variants are compared in figure 5.35. The comparison shows that although the misorientation pattern remains almost unchanged some deviations occur in the absolute values. The difference varies between 5 % and 8 % from the initial model (which is here referred to as the non-relaxed model variant).

5.4.5   Discussion

The phenomenon addressed in this section is a gradual formation of systematic orientation patterns in the deformed zone underneath an indent caused by conical nanoindentation with spherical tip. The patterns are particularly characterized by systematic arrangements of rotation and counter-rotation fields as presented in figures 5.32 and 5.33. These rotation- and counter-rotation patterns were confirmed both by the measurements and by the simulations.

The first approach to better understand the rotation patterns is to conduct a detailed analysis of some selected nodes in the finite element analysis. On the surface of the
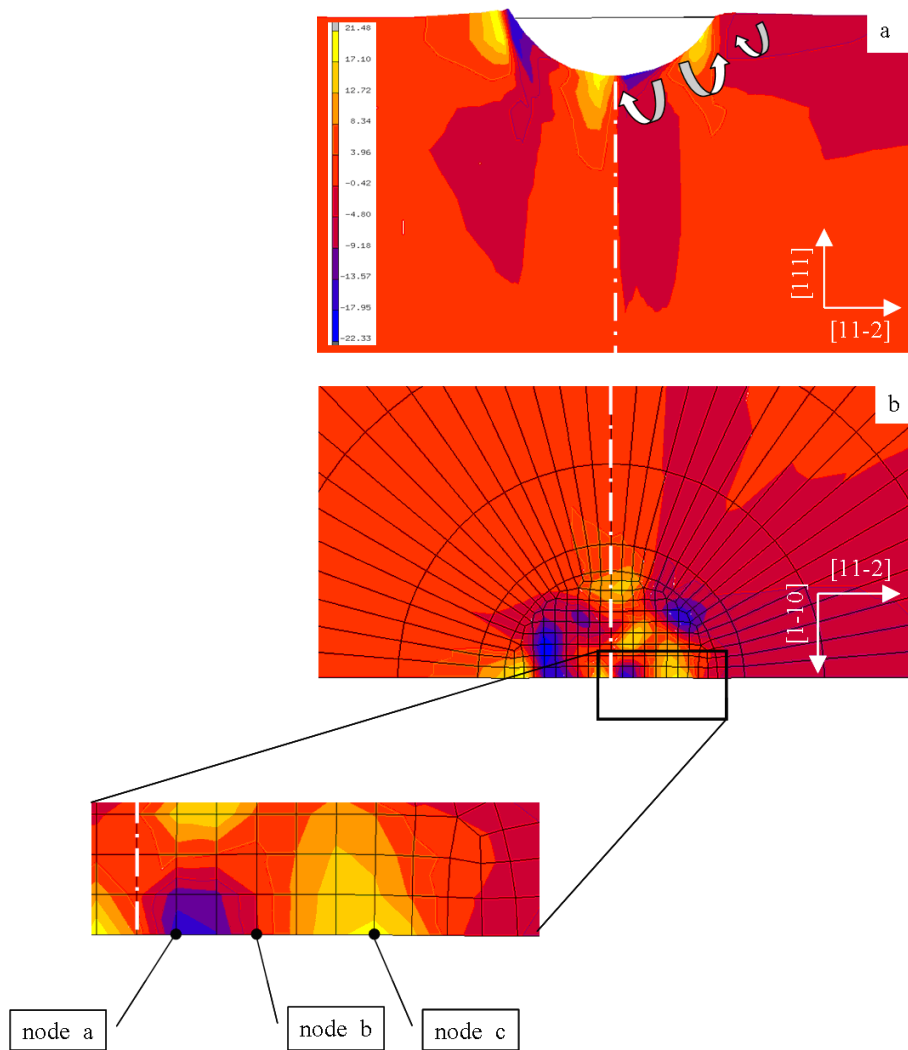
Figure 5.36: Three nodes with different rotations on the $(1\,\overline{1}\,0)$ plane are chosen for investigation (a) $[1\,\overline{1}\,0]$ rotations on a front view at the middle cross section (b) Same rotations on the surface of the crystal.

sample along the $[1\,1\,\overline{2}]$ crystallographic direction the rotations about the $[1\,\overline{1}\,0]$ axis indicate the mentioned phenomenon as shown in figure 5.36a. Three regions are inspected by selecting corresponding nodes, figure 5.36. Node a is chosen very close to the center, where the crystal reveals a negative rotation. While node c represents the neighboring positive rotation area, node b stands for the crossover region between the two counter rotated areas. This means that at node b almost no crystal rotation is expected to take place.

Figure 5.37 shows the evolution of the rotation about the $[1\,\overline{1}\,0]$ direction (x axis) and the corresponding slip system activity during the indentation. It can be seen that close to the center (node a) the crystal undergoes a small positive rotation at the beginning of the indentation, which soon reverses its sense. Moving outwards from the center

(nodes b and c), the positive rotation increases until it dominates the whole indentation process. A likely interpretation of this observation is that the crystal rotation behavior is influenced by two different mechanisms. The first one is caused by the spatial rotations due to the geometry of the indenter. This means that certain rigid-body rotations are imposed by the antisymmetric portion of the external displacement gradient tensor that is generated by the indentation process. The local crystallographic slip is responsible for the second kind of rotation.

In a second approach to better understand the reason for the rotation patterns we consider as a simple approximation the compression force exerted by the indenter as the only loading source. This force acts almost perpendicular to the local contact surface tangent between tool and crystal (schematic image in figure 5.38). The components of the contact force at the selected nodes are extracted from the simulation results. Knowing the orientation of the crystal at each node allows the determination of the crystallographic direction of the loading axis during the whole indentation process.

This is shown in the schematic image on the right hand side of figure 5.38 where a simplification is described that is used to track the changes in the single crystal kinematics during indentation in terms of a Sachs loading case under simple compression perpendicular to the local contact interface.

In the projection shown in figure 5.38 the corresponding evolution of the compression axis is plotted for the various nodes. For all nodes the compression axis lies on the $[0\,0\,\bar{1}]$ - $[\bar{1}\,\bar{1}\,\bar{1}]$ boundary. This is expected due to the symmetry of the problem resulting in a rotation about the $[1\,\bar{1}\,0]$ axis. The movement of the compression axis along the $[0\,0\,\bar{1}]$ - $[\bar{1}\,\bar{1}\,\bar{1}]$ boundary results in simultaneous slip on pairs of two slip systems as can be seen in figure 5.37. It can also be observed that at the beginning of the indentation process the axis rotates towards the $[\bar{1}\,\bar{1}\,\bar{1}]$ direction for all selected nodes ($1 \rightarrow 2$ in figure 5.38), before it reverses its motion towards the $[0\,0\,\bar{1}]$ pole, ($2 \rightarrow 3$ in figure 5.38). This confirms the results of figure 5.37.

The question that arises is: Why does the compression axis reverse its sense of rotation? The answer to that question can be given by monitoring the slip systems involved in the process. At the beginning of the indentation three pairs of slip systems are activated, as indicated in figure 5.37. Slip system pair (1) consists of $[1\,0\,\bar{1}](\bar{1}\,\bar{1}\,\bar{1})$ and $[0\,1\,\bar{1}](\bar{1}\,\bar{1}\,\bar{1})$, pair (2) of $[\bar{1}\,0\,\bar{1}](1\,\bar{1}\,\bar{1})$ and $[0\,\bar{1}\,\bar{1}](\bar{1}\,1\,\bar{1})$ and pair (3) of $[\bar{1}\,1\,0](1\,\bar{1}\,\bar{1})$ and $[\bar{1}\,1\,0](\bar{1}\,1\,\bar{1})$. It is well known (Hosford, 1993) that for a single crystal under compression the rotation of the compression axis towards the slip plane normal of the active slip system is the primary rotation. Therefore, and also from figures 5.38 and 5.39, one can see that the slip system pair (1) causes the compression axis to rotate towards the $[\bar{1}\,\bar{1}\,\bar{1}]$ pole following the re-orientation route ($1 \rightarrow 2$) leading to an initial positive crystal rotation. However, this rotation reduces its Schmid factor and hence the shear activity is lowered, as can be seen in figure 5.37 (node a).

On the other hand the two further slip system pairs (2) and (3) remain fully active with progressing indentation. Each pair tends to rotate the compression axis according
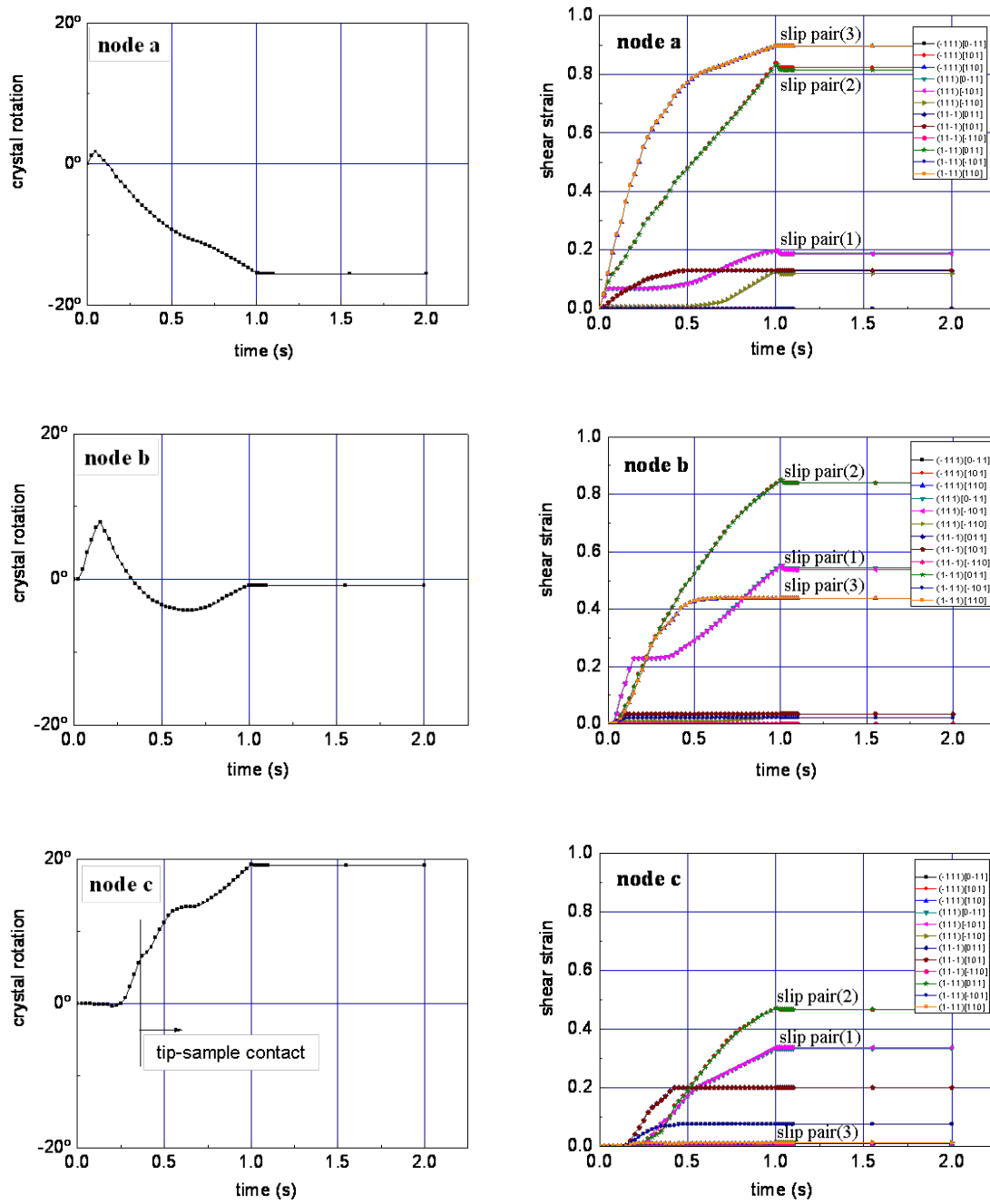
Figure 5.37: The evolution of the total crystal rotation about $[1\,\overline{1}\,0]$ and corresponding slip system activity during indentation.
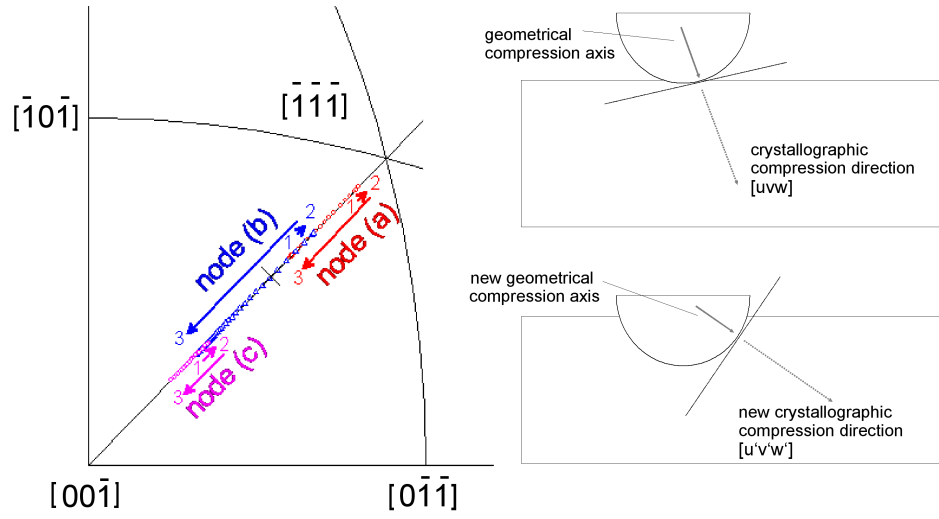
Figure 5.38: Inverse pole figure revealing the rotation of the compression axis during indentation at the selected node positions a, b and c. The black cross represents the $[1\,1\,\bar{2}]$ direction. The schematic image on the right hand side shows a simplification that describes the changes in the single crystal kinematics during indentation in terms of a Sachs loading case under simple compression tangential to the local contact interface.

to route $(2 \rightarrow 3)$, figure 5.38, towards the $[0\,0\,\bar{1}]$ pole, which lies on the great circle going through the two slip plane normals of the pairs, $(\bar{1}\,1\,\bar{1})$ and $(1\,\bar{1}\,\bar{1})$. Position (2) (see figure 5.38) for node a is in figure 5.37 located where the two rotation mechanisms equilibrate and the crystal reverses its sense of rotation. Route $(2 \rightarrow 3)$ describes a compression axis rotation in the positive direction around $[1\,\bar{1}\,0]$, *i.e.* a negative crystal rotation occurs.

The same slip mechanism occurs for node b. The difference with respect to node a is caused by the tip geometry. By moving outward along the tip the direction of the compression axis moves away from the $(\bar{1}\,\bar{1}\,\bar{1})$ pole (figure 5.38). This results in a decreased slip activity of slip system pair (3) on the one hand and on the other hand extends the activity of the slip system pair (1). This explains the higher value of the initial positive lattice rotation illustrated in figure 5.37 for node b compared with node a. At the end of the indentation the two opposite rotations compensate each other resulting in an almost zero total rotation of the crystal. It is expected that by indenting further, the rotation-free zone will move further outward away from the center of the indent.

For node c the slip state is more complicated as the contact with the indenter tip occurs only after more than $35\,\%$ of the indentation process. This means that other loading components influence the initial rotations of the crystal leading to a more complicated slip system activity as shown in figure 5.37. Nevertheless, one can observe that the initial tendency of a positive crystal rotation still prevails. Although the same change of the compression axis rotation occurs, due to the high crystal rotations before the contact
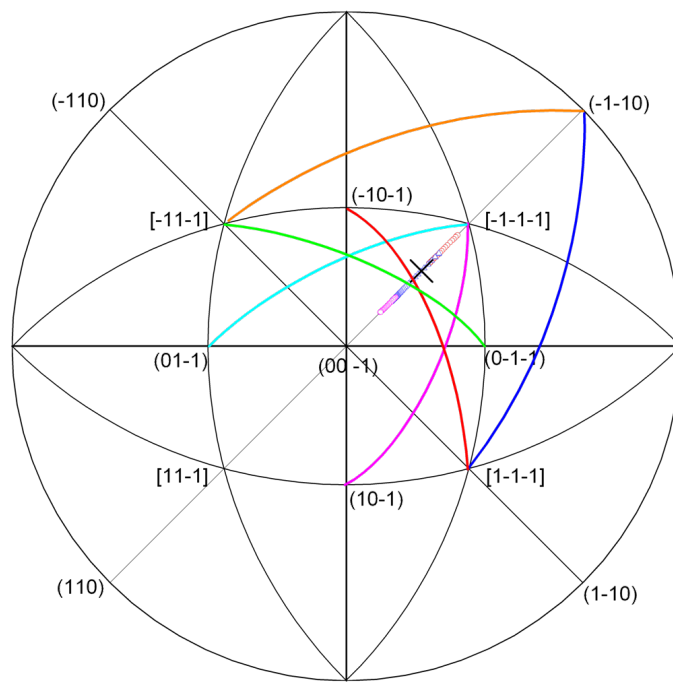
Figure 5.39: The active slip systems in the indentation process with a conical indenter. The black cross represents the $[1\,1\,\overline{2}]$ direction. The curved lines connect the slip normal and slip direction of a specific slip system. See also magnification in figure 5.38.

with the tip is established, this is sufficient only to decelerate the rotation of the crystal but not to reverse it.

5.4.6 Conclusion

The main results and conclusions are:

- A physically-based constitutive crystal plasticity finite element analysis reveals better agreement with the nanoindentation experiments than a phenomenological viscoplastic material model.

- The complex rotation pattern induced during conical indentation, which is characterized by several rotation zones, is well predicted when using a physics-based constitutive crystal plasticity finite element model. While the crystal rotates in a certain direction in the zone near the indenter axis, the neighboring zone shows opposite rotation.

- The change of the crystal rotation directions can be explained by the different active slip systems due to the geometry of the indenter causing a gradual change in the loading axis during indentation.

- Although the model succeeded to predict the pile-up out-of-plane pattern and the rotation pattern under the indent, it slightly overestimates the crystal rotations.

- For the small deformation scales discussed here there might be an effect of the free surfaces created by the focused ion beam technique. Further experimental study in that direction needs to be done in order to estimate the deviation in the measurements with respect to the material condition without milling.

Part II

Crystal Plasticity at Large Microstructural Scales

Chapter 6

Special Aspects of Large Scale Plasticity Simulations

Large scale refers to all kinds of simulations with more than one crystal assigned to one integration point (*cf.* chapter 3). While in principle this can be only two grains the number is usually much higher. On the component scale millions of grains are contained in the volume connected to one integration point. In case of multiphase materials the situation is even more complex as in general it is not possible to assign only grains of one phase to an integration point. On the other hand most of the details important for small scale simulations are less important when the task is to compute the homogenized constitutive response of a cluster of grains.

Even on a component scale crystalline materials in general show an anisotropic mechanical behavior. The reason is that the orientation distribution of the grains is usually not random, what would result in a quasi isotropic behavior. The orientation distribution function (ODF also named (crystallographic) texture) can be experimentally measured and approximated by single orientations. However, the number of orientations needed for a good approximation is usually much larger than the number of orientations that can be computationally handled at a single integration point. Therefore the task in large scale simulations is twofold. First, one needs an algorithm to approximate crystallographic textures by single orientations and distribute them in a finite element mesh. Secondly, the constitutive response of all grains assigned to one integration point must be homogenized into one global response. These two tasks are discussed in the following sections.

Finally, some materials show additional deformation mechanisms besides dislocation slip. The most important ones are twinning and displacive phase transformations. Therefore, one section discusses how one of them, namely twinning, can be incorporated into a large scale crystal plasticity framework.

Chapter 7

Advanced Models for Large Scale Simulations

7.1 Macro Texture Discretization

Preferred crystallographic orientation of crystallites, *i.e.* texture in polycrystalline metals, ceramics or polymers affects in particular the anisotropy of many physical properties, *e.g.* elastic and plastic mechanical response, electrical conductivity, piezoelectricity, or magnetic susceptibility (Wenk and Van Houtte, 2004). The orientation, g, of a crystallite can be specified by a set of three Euler angles $g = \{\varphi_1, \phi, \varphi_2\}$ within Euler space $\{[0; 2\pi], [0; \pi], [0; 2\pi]\}$ using the notation of Bunge (1982). If either crystal or sample symmetry is present, *e.g.* rolled sheet material of cubic lattice structure, the fundamental zone, Z, of Euler space required to uniquely characterize the texture is accordingly smaller. Crystallographic texture is quantified by the orientation distribution function (ODF), which defines the probability $f(g)$ that a volume fraction, $\mathrm{d}V/V$, of the polycrystalline aggregate is taken up by crystallites of an orientation between g and $g + \mathrm{d}g$:

$$\upsilon \equiv \frac{\mathrm{d}V}{V} = f(g)\,\mathrm{d}g \; . \tag{7.1}$$

For the system of rotational axes connected to the above chosen definition of g, the infinitesimal volume, $\mathrm{d}g$, of orientation space follows as:

$$\mathrm{d}g = \frac{1}{8\pi^2}\,\mathrm{d}\varphi_1\,\mathrm{d}\varphi_2\,\mathrm{d}\cos\phi \; , \tag{7.2}$$

where the normalization factor $1/8\pi^2$ arises due to the requirement that $\oint \mathrm{d}V/V \equiv 1$. [1]

Experimentally, an ODF is accessible either directly from electron backscatter diffraction (EBSD) data on a large number of (surface) grains or by calculation from X-ray or

---

[1] Note that $f(g) \equiv 1$ for a purely random orientation distribution.
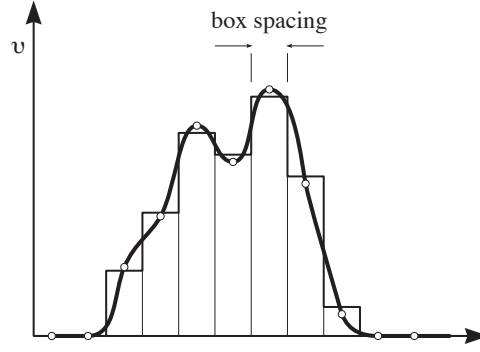
Figure 7.1: Simplified one-dimensional orientation distribution function. Circles indicate exact ODF values on the orientation grid; stepped function corresponds to average values for each box according to equation (7.3).

neutron diffraction-based pole figures. The numerical approximation of an ODF can be done in two different fashions. One possibility invokes continuous functions, *e.g.* based on a series expansion in generalized spherical harmonics (Bunge, 1982) or superposition of bell-shaped (ideal) component functions, and records the comparatively small set of parameters necessary to uniquely define this continuous function. Such representation allows to calculate the value of the ODF at any given orientation. The second possibility subdivides the Euler space into boxes of equal angular extension—typically $5 \times 5 \times 5$ cubic degrees—and records discrete values, f_i, at the central orientations defined by this grid. Ideally,

$$f_i = \oint_{\text{box}_i} f(g)\, dg \left/ \oint_{\text{box}_i} dg \right. , \tag{7.3}$$

i.e. the values correspond to the ODF average within the ith box. If the f_i correspond to exact values of the ODF at the central orientations, equation (7.3) is still valid to a good approximation as long as second derivatives in $f(g)$ remain small for the chosen grid spacing. Figure 7.1 illustrates the differences between these two cases in a simplified manner.

Both ODF representations are usually not well suited in the quantitative modeling of texture effects on above mentioned physical properties. Frequently, a finite ensemble of grain orientations—still representing the ODF as accurately as possible—is required. The prediction of anisotropic plastic deformation with correlated texture evolution, see *e.g.* Sarma and Dawson (1996b); Bachu and Kalidindi (1998); Bate and An (2004); Raabe et al. (2005), may serve as prominent example for this case. So far, only very few methods to sample such a representative set from a given ODF have been published. The proposed schemes can be divided into two methodologically different groups.

In the first group, the number of required orientations is prescribed and their individual, variable weights get selected. This can be achieved by constructing a nearly equi-distant grid in Euler space as suggested by Kocks et al. (1991) and Helming et al. (1998). The weight of orientations on this grid is fitted by comparing recalculated to measured pole

figures. Any weights below a threshold may be dropped to reduce the number of orientations considered. Another option, called the "Limited Orientation Distance" method, was introduced for discrete ODFs by Tóth and Van Houtte (1992). They suggested a procedure that iteratively starts at that "seed" orientation that exhibits the maximum ODF intensity. All intensity of neighboring orientations having a disorientation to the seed below a threshold value, *i.e.* having limited orientation distance, is concentrated into the seed's weight and then subtracted from the ODF. Recently, a sophisticated method also employing a threshold in disorientation was suggested by Melchior and Delannay (2006). Starting from a large ensemble of orientations chosen in a probabilistic manner from a given discrete ODF (see next paragraph for details), these orientations are grouped together to form grains, which then get assigned the mean of their constituent orientations. The grouping respects that the maximum disorientation among constituent orientations in a single grain remains below a given threshold (of a few degrees).

For the second group, each sample out of a prescribed number, N^*, has equal weight and the orientations required for a statistical representation of the ODF are chosen. The straightforward probabilistic sampling would accept a randomly selected orientation g_i with probability

$$p(g_i) = \frac{f(g_i)\,\sin\phi_i}{\max\left(f(g)\,\sin\phi\right)_{g\in Z}}\ .\tag{7.4}$$

Tóth and Van Houtte (1992) (see also Melchior and Delannay (2006)) elegantly increased the computational efficiency of such sampling by introducing a cumulative probability density of orientations. Its inversion is then used as a mapping-function between N^* uniformly distributed numbers in the range $[0;1]$ and orientations. Since an integration path connecting boxes in Euler space is essential to their "STAT" method, it can only operate on discrete representations of an ODF. The expected value for the resulting volume fraction, $v_i^* \equiv \mathrm{d}V_i^*/V$, of orientation g_i in both of these probabilistic sampling methods is $v_i^* \propto f(g_i)\sin\phi_i$ since $p(g_i) \propto f(g_i)\sin\phi_i$, *i.e.* they produce unbiased discretizations of the original ODFs (Tóth and Van Houtte, 1992, also see equation (7.9)).

In this section two discretization schemes are introduced. The *Texture Component Method* is based on an ODF approximation using continuous functions (the texture components), which are finally sampled into individual orientations for the FE simulation. The *Hybrid IA Scheme* is based on a direct sampling of the discretized ODF data.

7.1.1   The Texture Component Method

The basic idea of the texture component method is the approximation of X-ray textures in the form of the orientation distribution function (ODF) by a discrete set of simple distribution functions (texture components) defined in orientation space. It was developed by Lücke et al. (1981, 1986) and later on facilitated and implemented into an easy

to use computer program[2] by Helming (1996) (also see Helming et al., 1994).

7.1.1.1   Approximation of X-Ray Textures Using Texture Components

The mathematical reproduction of the orientation distribution function $f(g)$ by texture component functions can be expressed by the superposition

$$f(g) = F + \sum_{c=1}^{C} I^c f^c(g) = \sum_{c=0}^{C} I^c f^c(g) \quad \text{where} \quad I^0 = F, \ f^0(g) = 1 \ , \qquad (7.5)$$

g is the crystallographic orientation and F is the volume portion of all randomly oriented crystals (random texture component). F may be understood as the intensity of the only global component used in the approximation, equivalent to $f^c(g) = 1$ for each orientation point in Euler space, $g \in G$. The intensity I^c describes the volume fraction of all crystallites belonging to the component c. $f^c(g)$ describes the orientation density of the component.

Helming (1996) uses two types of model functions for $f^c(g)$, namely, fiber components and spherical components. The fiber components are characterized by the fiber axis $\mathbf{f}^c$ and the scatter width a^c, while the spherical components are characterized by a preferred orientation g^c and a scatter width b^c. In both cases a modified Gauss distribution

$$f^c(g) = \frac{\exp(S^c \cos \omega^c)}{I_0(S^c) - I_1(S^c)} \qquad (7.6)$$

is used for $f^c(g)$, where I_0 and I_1 are generalized Bessel functions and S^c is defined as

$$S^c = \frac{\ln 2}{1 - \cos \left(\frac{a^c}{2} \right)} \ ; \qquad (7.7)$$

for the spherical components a^c has to be substituted by b^c. ω^c is the orientation distance ($\omega^c = g - \mathbf{f}^c$ or $\omega^c = g - g^c$, respectively). In case of the fiber components equation (7.6) is only used for rotation axes that are perpendicular to $\mathbf{f}^c$. If the rotation axis is parallel to $\mathbf{f}^c$ an equal distribution is used. For the spherical components equation (7.6) is always used, independent of the rotation axis.

7.1.1.2   Representation of Texture Components in a Crystal Plasticity FEM

A big advantage of the texture component method is the fact that a very comprehensive data set is obtained for the description of statistical textures. In most cases only very few (3 or less) components are needed to obtain a texture approximation, which sufficiently reproduces the materials mechanical anisotropy. Obviously it is not the aim here to get a

---

[2]The software "Multex 1.0" can be downloaded from http://www.texture.de.

(a) The preferred orientation g^c in terms of its respective Euler triple $(\varphi_1, \phi, \varphi_2)$ is assigned to each integration point. In this state the sample is a perfect single crystal.

(b) he mapped single orientations are systematically rotated to reproduce exactly the original texture function, which was prescribed in the form of a texture component.
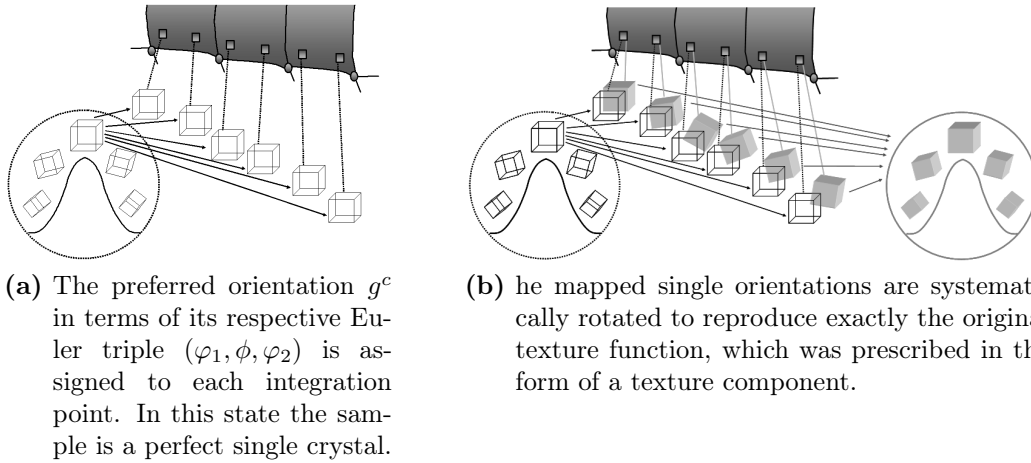
Figure 7.2: Schematic drawing showing the mapping of a spherical texture component onto a FE mesh.

perfect simulation of the deformation texture. Nevertheless, the component information has to be passed into a crystal plasticity FE calculation. The following paragraphs describe the procedure how these texture components are mapped to a finite element mesh. It is important at this point that this procedure should be independent of the number of integration points in the mesh, which is the reason why discrete data sets can not be used in this context.

Spherical Components   As mentioned above the spherical components are fully described by three measures: the preferred orientation g^c, the scatter width b^c and the intensity or volume fraction I^c. The preferred orientation is described in terms of Euler angles in Bunge notation $(\varphi_1, \phi, \varphi_2)$, which means that for every spherical texture component five numbers have to be passed into the FE calculation.

Then, in a first step g^c is assigned to all integration points (figure 7.2a). In a second step the orientation of every integration point is modified statistically in such fashion that the entity of all integration points reproduces the distribution function f^c (figure 7.2b). In other words, the orientation scatter b^c described initially by a texture component function f^c is in the finite element mesh represented by a systematically re-oriented set of orientations, each assigned to one integration point, which reproduces the original spherical scatter prescribed by that component. This means that the scatter, which was originally only given in orientation space, is now represented by a distribution in real space and in orientation space, *i.e.* the initial spherical distribution is transformed into a spherical *and* spatial distribution.

Fiber Components   The fiber components are also fully described by three measures: the fiber axis $\mathbf{f}^c$, the scatter width a^c and the intensity or volume fraction I^c. As the fiber
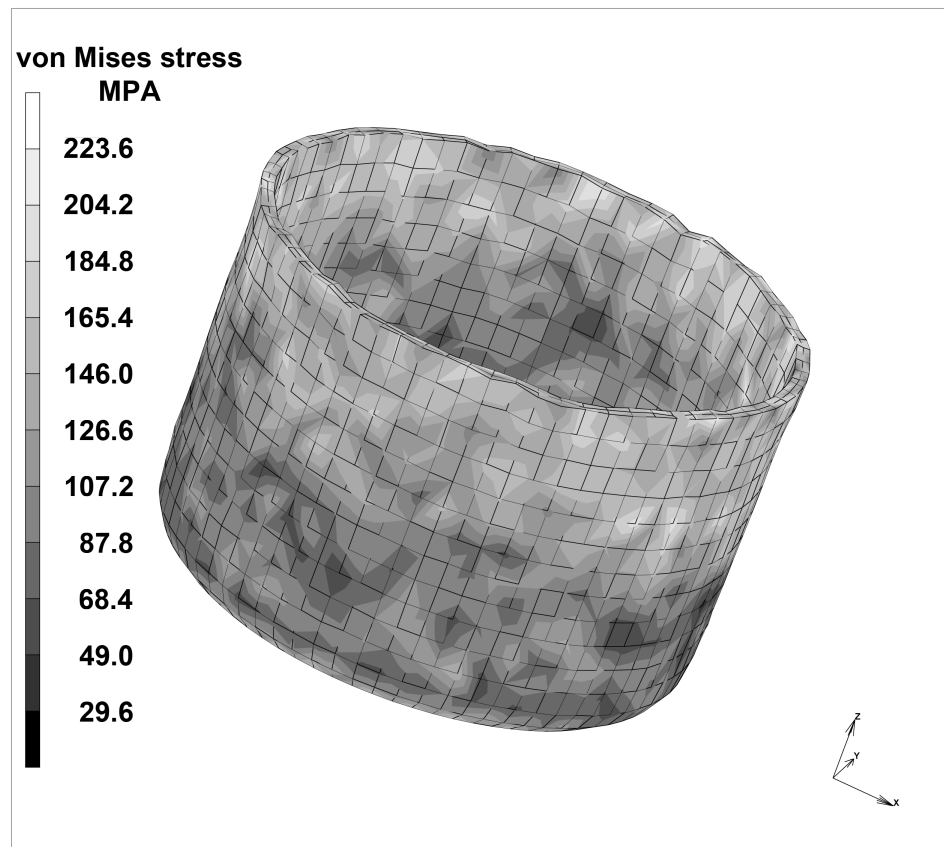
Figure 7.3: Cup drawn from a circular sheet with initially random texture.

axis is specified once in the sample coordinate system and once in the crystal coordinate system using spherical coordinates, in the case of fiber components six numbers have to be passed into the FEM calculation. Then, in a first step the crystal has to be rotated in such a way that the direction of $\mathbf{f}^c$ specified in the crystal coordinate system coincides with that given in the sample coordinate system. After that, a rotation about the fiber axis is performed using an arbitrary rotation angle. Finally, a statistical rotation about an axis perpendicular to $\mathbf{f}^c$ is performed in such a way that, again, the distribution function f^c (figure 7.2b) is reproduced by the entirety of all integration points.

7.1.1.3 The Random Texture Component

The random texture component, F in equation (7.5), is mapped to the FE mesh by assigning one or more randomly picked orientation(s) to each integration point. Here it is important to ensure that the number of integration points is high enough so that the material really behaves isotropic. Figure 7.3 illustrates this for a cup drawn from a circular sheet. Ideally the rim of the cup should be absolutely flat, but as the method uses discrete orientations there will always be some scatter. The influence of the number of randomly assigned orientations on this scatter is shown in figure 7.4. It can be seen
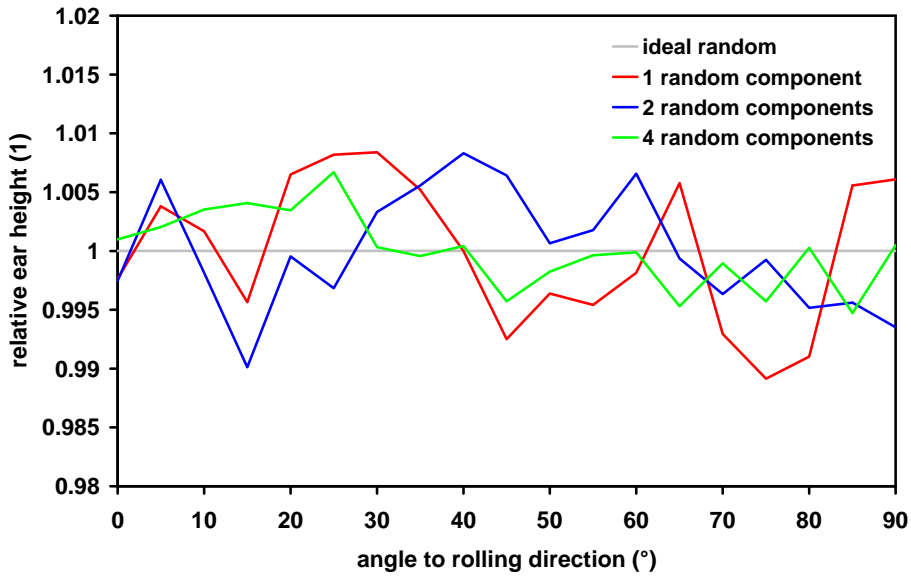
Figure 7.4: Influence of the number of random components on the earing profile.

that a clear improvement over the use of one random component is achieved only if four random components are used. As this markedly increases the computing time in most cases the use of one random component is favorable.

After decomposing and representing the initial texture components as a lateral and spherical single orientation distribution in the mesh, the texture component concept is no longer required in the further procedure. This is due to the fact that during the subsequent crystal plasticity finite element simulation each individual orientation originally pertaining to one of the texture components can undergo an *individual* orientation change as in the conventional crystal plasticity methods. This means that the texture component method loses its significance during the simulation. In order to avoid confusion one should, therefore, underline that the texture component method is used to *feed* textures into finite element simulations on a strict physical and quantitative basis. The components as such, however, are in their original form as compact functions not tracked during the simulation. It must also be noted that the orientation points that were originally obtained from the components do not represent individual grains but portions of an orientation distribution function.

The described re-orientation procedures are formulated as a weighted sampling Monte Carlo integration scheme in Euler space. It is important in this context that the use of a homogenization scheme (section 7.2) locally allows one to map more than one crystallographic orientation on each integration point and to assign to each of them an individual volume fraction I^c. This means that the procedure of mapping and rotating single orientations according to the initial texture component scatter width is individually conducted for all prescribed components extracted from initial experimental or theoretical data.

7.1.2   The Hybrid IA Scheme

The hybrid IA scheme (Eisenlohr and Roters, 2008) simplifies and scrutinizes an idea originally mentioned in the work of Leffers and Juul Jensen (1986) (see also Xie and Nakamachi (2002)). It approximates the ratio among all volume fractions following from the discrete ODF representation by integer numbers. It is fully deterministic for large N^* and partly probabilistic for small N^* as will be explained in section 7.1.2.3. The reconstruction quality of the integral approximation and of probabilistic sampling will be quantitatively compared in section 7.1.2.2. In the limit of small numbers of sampled orientations, *i.e.* order 10^2, both methods give identically crude results. However, starting at the computationally interesting range of around 10^3–10^4 sampled orientations the proposed method matches a given texture significantly closer than probabilistic sampling does.

We want to draw a set of N^* samples from a discrete ODF representation with the aim that the texture resulting from distributing those sampled orientations over N^* grains of equal volume, V/N^*, reproduces the original polycrystalline texture as closely as possible. In general, the number, N^*, of orientations in the texture reconstruction is a prescribed quantity and depends on the required (or desired) degree of discretization for the texture-sensitive simulation under consideration.

Euler space is discretized into unit boxes of dimension $\Delta\varphi_1 \times \Delta\phi \times \Delta\varphi_2$ centered on a regular[3] grid. For a given crystal and/or sample symmetry the fundamental zone, Z, of Euler space intersects only with N out of the total $4\pi^3/(\Delta\varphi_1\Delta\phi\,\Delta\varphi_2)$ boxes. Let the discrete ODF,

$$f_i = \oint_{Z\cap\mathrm{box}_i} f(g)\,\mathrm{d}g \left/ \oint_{\mathrm{box}_i} \mathrm{d}g \right. \tag{7.8}$$

with $i = 1, 2, \ldots, N$, be defined at the center of each box. Note the scaling of f_i with the degree of overlap between a box and the fundamental zone.

The volume fraction $v_i \equiv \mathrm{d}V_i/V$ of crystallites with orientations falling into the ith box (of the fundamental zone) follows from equations (7.1), (7.2) and (7.8) as

$$v_i = \frac{f_i}{\oint_Z \mathrm{d}g} \frac{\Delta\varphi_1\,\Delta\varphi_2\,2\sin(\Delta\phi/2)\,\sin\phi_i}{8\pi^2} \tag{7.9}$$

with ϕ_i being the box center's ϕ value. As for the continuous ODF, the f_i fulfill the normalization requirement such that

$$\sum_{i=1}^{N} v_i \equiv 1 \; . \tag{7.10}$$

---

[3]Grid regularity is no requirement but chosen for easier illustration.

Now, based on its volume fraction, v_i, each orientation, g_i, of the N ones present in the fundamental zone of the discrete ODF is selected for a number of times

$$n_i^* = \text{round}\,(C\,v_i)\ .\tag{7.11}$$

To yield an overall set of N^* samples the constant C has to be iteratively adjusted to fulfill

$$\sum_{i=1}^{N} n_i^* \overset{!}{=} N^*\ .\tag{7.12}$$

This iterative procedure is easily solved by, for instance, a binary search algorithm. However, depending on the input ODF there are cases where no exact solution for a given N^* is found due to limited numerical precision in C.

Since all N^* grains in the reconstruction are set to occupy an equal volume, the volume fraction of a reconstructed orientation is identical to its number fraction

$$v_i^* = n_i^*/N^*\ .\tag{7.13}$$

Figure 7.5 presents three examples for the reconstruction scheme specified by equations (7.11) and (7.12). From comparison between the different choices for the scaling constant C in cases a), b), and c) in figure 7.5 it becomes obvious that C (necessarily) increases with an increase in N^* and that the value of C fully determines the resulting frequency distribution of orientations in the reconstructed ODF. Naturally, the agreement between original and reconstructed ODF continuously improves with an increase in N^* (and thus in C), since a fraction of two large integers generally can represent ratios among arbitrary v_i more accurately than a fraction of two smaller integers.

7.1.2.1 Analysis

The benchmark probabilistic sampling was implemented according to equation (7.4) as well as by using the more efficient "STAT" method of Tóth and Van Houtte (1992).

Three textures are used exemplarily in this study to assess the quality of the integer approximation (IA) method outlined in section 7.1.2: two real textures and an artificial random texture with $f(g) = 1 \pm 10^{-4}$. The real textures were measured by EBSD in a rolled duplex steel on a population of about 10^5 ferritic (α-Fe) and austenitic (γ-Fe) grains, respectively. Both sets of grain orientations were transformed with OIM[TM] Analysis[4] using discrete binning with a Gaussian spread of 5 degrees to yield discrete ODFs of $5 \times 5 \times 5$ cubic degrees box size. The cubic lattice structure of both phases together with the monoclinic symmetry present on the sample's longitudinal section allows to reduce the required part of Euler space to the region $\{[0;\pi],[0;\pi],[0;\pi/2]\}$.

---

[4]Version 4.6 by EDAX, Inc., Mahwah, New Jersey, USA.
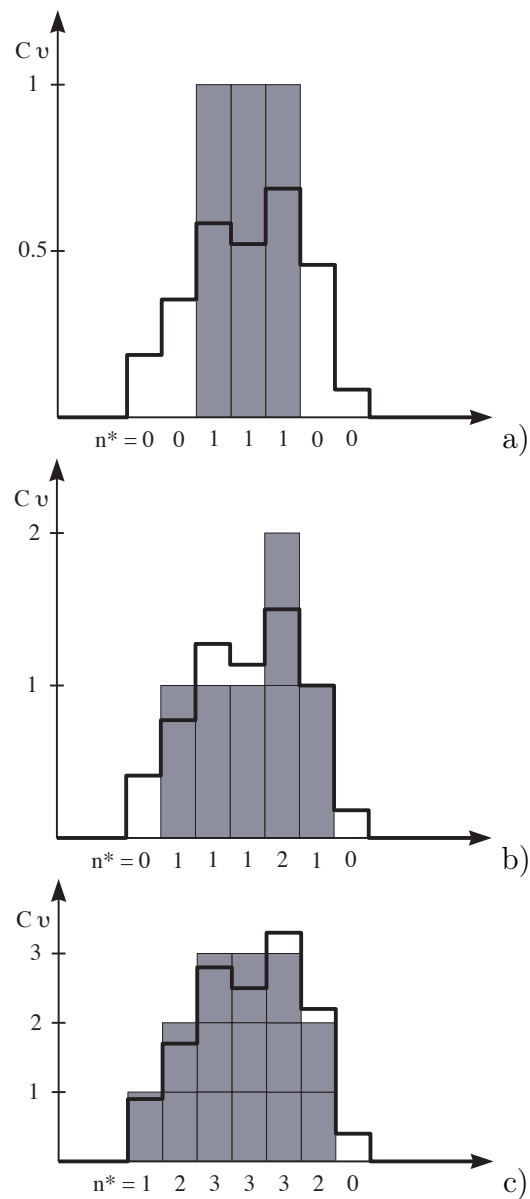
Figure 7.5: Exemplary reconstructions of the simplified ODF from figure 7.1 ($N = 7$). Solid stepped function corresponds to average ODF (see figure 7.1) scaled by a constant C. Shaded vertical bars indicate $n^* = \text{round}(C\,v)$, *i.e.* after rounding to the closest integer. The chosen scaling factors are possible solutions for requested a) $N^* = 3$, b) $N^* = 6$, and c) $N^* = 14$.
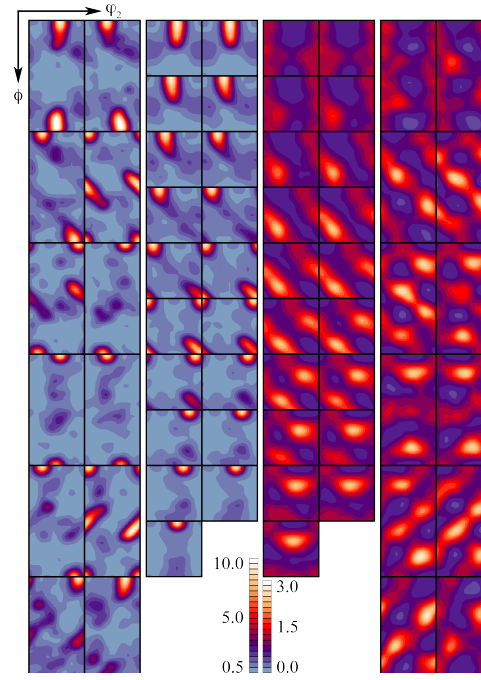
Figure 7.6: Per phase (α/γ-Fe) textures of rolled duplex steel that are used in this study. From left to right: α-monoclinic, α-orthotropic, γ-orthotropic, and γ-monoclinic. Range of ϕ, φ_2 and step size in φ_1 is $[0;\pi], [0;\pi/2]$ and 15 degrees in case of monoclinic and $[0;\pi/2], [0;\pi/2]$ and 5 degrees for the case of (enforced) orthotropic sample symmetry, respectively. $\varphi_1 = 0$ in upper left corner. Note the different maximum intensities in the ODFs of α and γ.
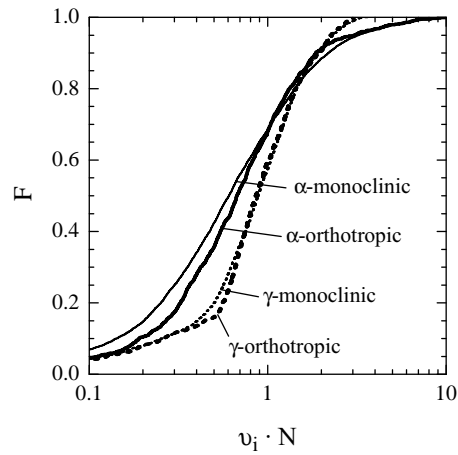
Figure 7.7: Cummulative frequency F of normalized volume fractions v_i for the four ODFs depicted in figure 7.6.

To check for the influence of N, the measured crystal orientation data were additionally processed in OIM$^{\text{TM}}$ Analysis assuming orthotropic sample symmetry. This assumption is not altering the experimental textures to a great extent, as can be seen by visual comparison of the respective ODFs shown in figure 7.6 and in a more quantitative fashion from the distributions of v_i depicted in figure 7.7, which exhibit only small variations between the respective monoclinic and orthotropic cases. The orthotropic symmetry assumption further reduces the representative part of Euler space by a factor of four to $\{[0; \pi/2], [0; \pi/2], [0; \pi/2]\}$. The three-fold symmetry of cubic crystals is leveraged to finally restrict both above parts to their region III[5] by scaling all $f(g_i)$ with the fraction of overlap between region III and the volume of the ith box (see equation (7.8)). Thus, both of the two monoclinic and two orthotropic textures are characterized by $36 \times 36 \times 18 = 23328$ and $18 \times 18 \times 18 = 5832$ discrete f_i, respectively, of which only $N = 6048$ and 1512 values are non-zero, i.e. overlap with region III. These four ODFs are referred to as α-monoclinic, γ-monoclinic, α-orthotropic, and γ-orthotropic in the following (see figure 7.6). In the case of the artificial random texture three combinations of angular resolution and Euler (sub)space were set up: 5 degrees on $\{[0; 2\pi], [0; \pi], [0; 2\pi]\}$ and $\{[0; \pi/2], [0; \pi/2], [0; \pi/2]\}$, and 3 degrees on $\{[0; \pi/2], [0; \pi/2], [0; \pi/2]\}$, which results in $N = 72 \times 36 \times 72 = 186624$, $18 \times 18 \times 18 = 5832$, and $30 \times 30 \times 30 = 27000$ discrete f_i. In these cases, three-fold cubic symmetry is not used to further shrink the considered fundamental zone as was done for the experimental textures.

In order to quantify the similarity between the original ODF and its reconstructed versions, two means are used in this study. The first is the root mean squared deviation (RMSD), which in the case of discrete ODFs given on N grid points in Euler space can be defined as:

$$\text{RMSD} = \sqrt{\sum_{i=1}^{N} \left(v_i - v_i^*\right)^2} \tag{7.14}$$

with v_i and v_i^* $(= n_i^*/N^*)$ being the volume fractions corresponding to orientation g_i in the original and reconstructed ODF, respectively. Secondly, we use the slope, a, and the correlation factor, f_C, of a linear regression performed on the set of points (v_i, v_i^*), which was introduced by Tarasiuk and Wierzbanowski (1996):

$$a = \frac{N \sum_{i=1}^{N} v_i v_i^* - \sum_{i=1}^{N} v_i \sum_{i=1}^{N} v_i^*}{N \sum_{i=1}^{N} v_i v_i - \sum_{i=1}^{N} v_i \sum_{i=1}^{N} v_i} \tag{7.15}$$

$$f_C = \frac{\sum_{i=1}^{N} v_i v_i^* / N - \langle v_i \rangle \langle v_i^* \rangle}{\sqrt{\langle v_i^2 \rangle - \langle v_i \rangle^2} \sqrt{\langle v_i^{*2} \rangle - \langle v_i^* \rangle^2}} \tag{7.16}$$

where $\langle x \rangle = \sum_{i=1}^{N} x_i / N$ denotes the arithmetic mean of x.

---

[5]This fundamental region of Euler space for cubic crystal symmetry is defined by $|\cos \phi| \leq \min \left(\left| (1 + \cos^2 \varphi_2)^{-0.5} \cos \varphi_2 \right|, \left| (1 + \sin^2 \varphi_2)^{-0.5} \sin \varphi_2 \right| \right)$.
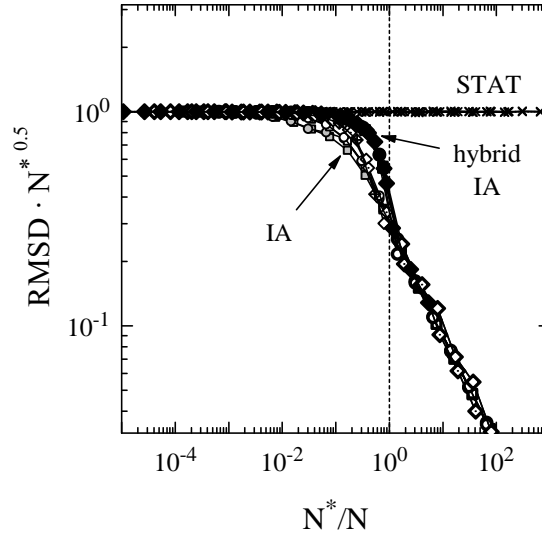
Figure 7.8: Normalized RMSD (see equation (7.14)) as function of normalized number
of sampled orientations for all seven (four experimental plus three random) investigated ODFs. Crosses, open symbols, and filled symbols indicate results of STAT,
IA, and hybrid IA reconstruction method, respectively. Note the strong overlap
of the seven results for each individual method corresponding to respective master
curves.

7.1.2.2   Results

This section compares the IA method to probabilistic sampling with respect to the reconstruction quality achieved on strong, intermediate and random textures. As expected,
both ways of probabilistic sampling, *i.e.* based on equation (7.4) as well as the STAT
method, yielded identical results. Therefore, only those of the more efficient STAT
method are used as benchmark for comparisons.

Root mean squared deviation   Figure 7.8 presents in summary the RMSD between
the original and reconstructed versions of the experimental and random textures. Despite the large differences among all input ODFs, each result of the STAT as well as of
the IA method falls, to a very good approximation, onto two individual master curves
(all crosses and open symbols in figure 7.8) when normalizing the number of sampled
orientations, N^*, by the number, N, of non zero-valued boxes, *i.e.* boxes within the
fundamental zone, in each of the discrete input ODFs. (Details regarding the "hybrid
IA" method additionally shown in figures 7.8–7.11 will be given in section 7.1.2.3.) Respecting the normalization of the ordinate by $\sqrt{N^*}$, it is seen that for fully probabilistic
sampling the RMSD is inversely proportional to $\sqrt{N^*}$, which is in accordance with a
Poisson process. In contrast, the IA method exhibits similar characteristic only in the
limit of small (normalized) $N^*/N < 10^{-2}$. For larger sampling numbers $N^*/N > 1$ the

RMSD falls in proportion to N^*, which is remarkably more rapid than in the case of the STAT method.

Correlation   The second measure of quality to compare original to reconstructed ODFs evaluates the correlation between the volume fractions v_i^* and v_i through a linear regression. This correlation would be perfect if $v_i^* = v_i$ for all $i = 1, 2, \ldots, N$, *i.e.* agreement for all boxes within the fundamental zone of the discrete ODF. To illustrate the correlation resulting from both discretization methods we first plot v_i^* against v_i for three different N^*/N in figure 7.9 (taking the α-orthotropic texture as example). The correlation resulting from the IA method is presented in the top row and that from the STAT method in the bottom row of figure 7.9.

The IA method always produces a step-function $v_i^*(v_i)$ due to the scaling and integer rounding operation involved in equation (7.11). With respect to the slope, a, of the linear regression this leads to a systematic over-weighting $v_i^* > v_i$, or $a > 1$, the larger v_i (see steep solid line in top row of figure 7.9). As seen from the sequence in figure 7.9 (top, left to right), this over-weighting diminishes with increasing N^*/N and the regression slope asymptotically settles at $a = 1$. In contrast, the slope in the case of the STAT method is close to one for all three cases visualized. (Note that the total number of data points shown in each of the nine frames of figure 7.9 far exceeds the visual impression, hence apparent and calculated linear regression may differ.)

The scatter of points around the linear regression line decreases with increasing N^*/N for both methods. However, regarding the correlation factor, f_C, the IA method is advantageous compared to the STAT method for all N^*/N illustrated in figure 7.9 since a step-function shows only limited scatter. The result of the IA method at $N^*/N = 2$ can be regarded as a perfect match in terms of both measures, a and f_C, while the cloud of points resulting from the STAT method still exhibits significant scatter around the ideal correlation.

The dependence of a and f_C on N^*/N is illustrated in figures 7.10 and 7.11 over a large range of normalized sample numbers and for all seven investigated textures. Each data point represents the average from 10 individual reconstructions.

It can be seen from figure 7.10 (bottom) that, irrespective of N^*/N, the correlation resulting from the STAT method is—*on average*—ideal for all textures investigated. This is a consequence of the fact that the STAT method is an unbiased estimator of the original ODF (Tóth and Van Houtte, 1992). However, the standard deviation (indicated by error bars in figure 7.10) increases markedly with decreasing $N^*/N < 0.1$.

In the case of the IA method, the plot in figure 7.10 (top) underlines the result already anticipated from figure 7.9: at small sample numbers the systematic over-weighting of large v_i manifests itself by a large value $a > 1$. The maximum value that a attains for small sample numbers increases in the order of textures of random, γ, and α, *i.e.* correlates with the fraction of large v_i present in the respective ODFs (see figure 7.7).
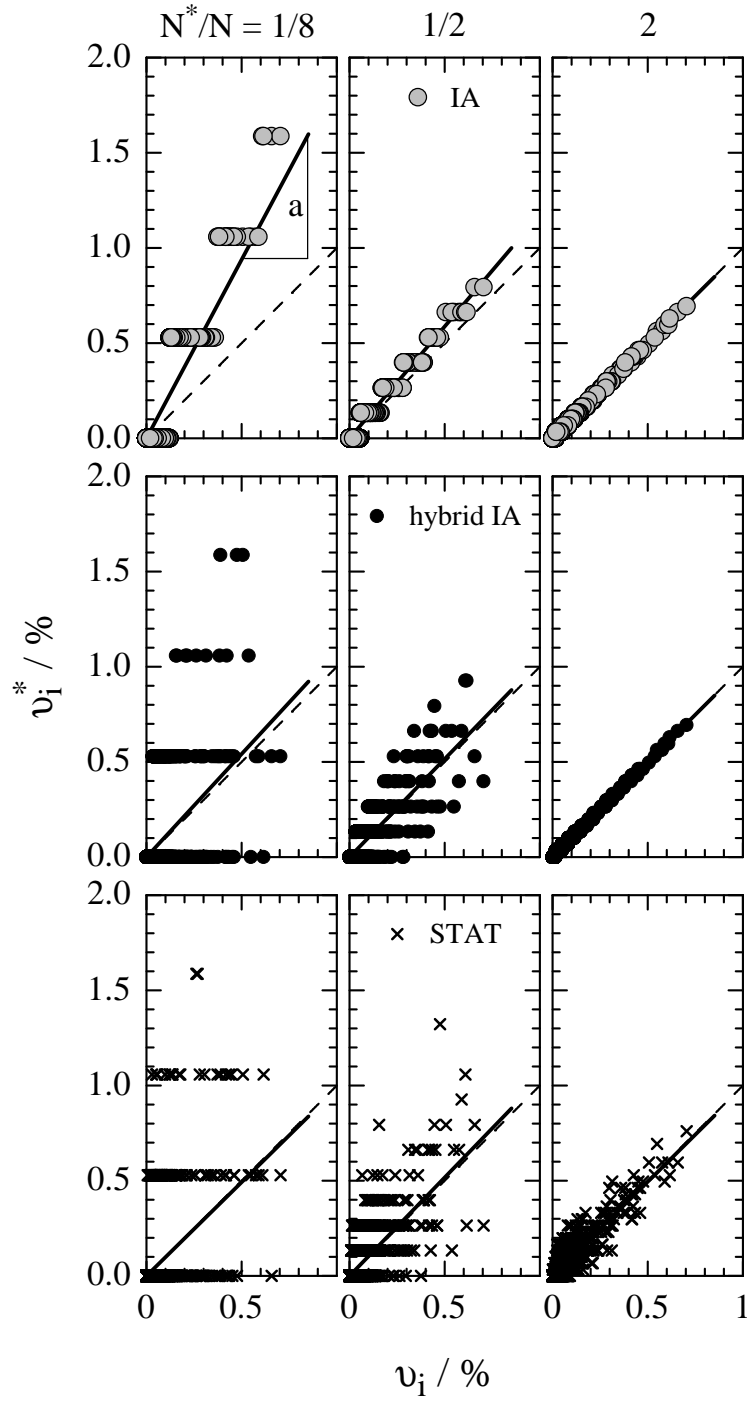
Figure 7.9: Correlation between reconstructed v_i^* and v_i from α-orthotropic ODF for three values of N^* ($N = 1512$). Methods used in top, central and bottom row are IA, hybrid IA and STAT, respectively. Thick lines of slope a follow from linear regression (see equation (7.15)). Dashed lines indicate ideal correlation $v_i^* = v_i$ ($a = 1$).
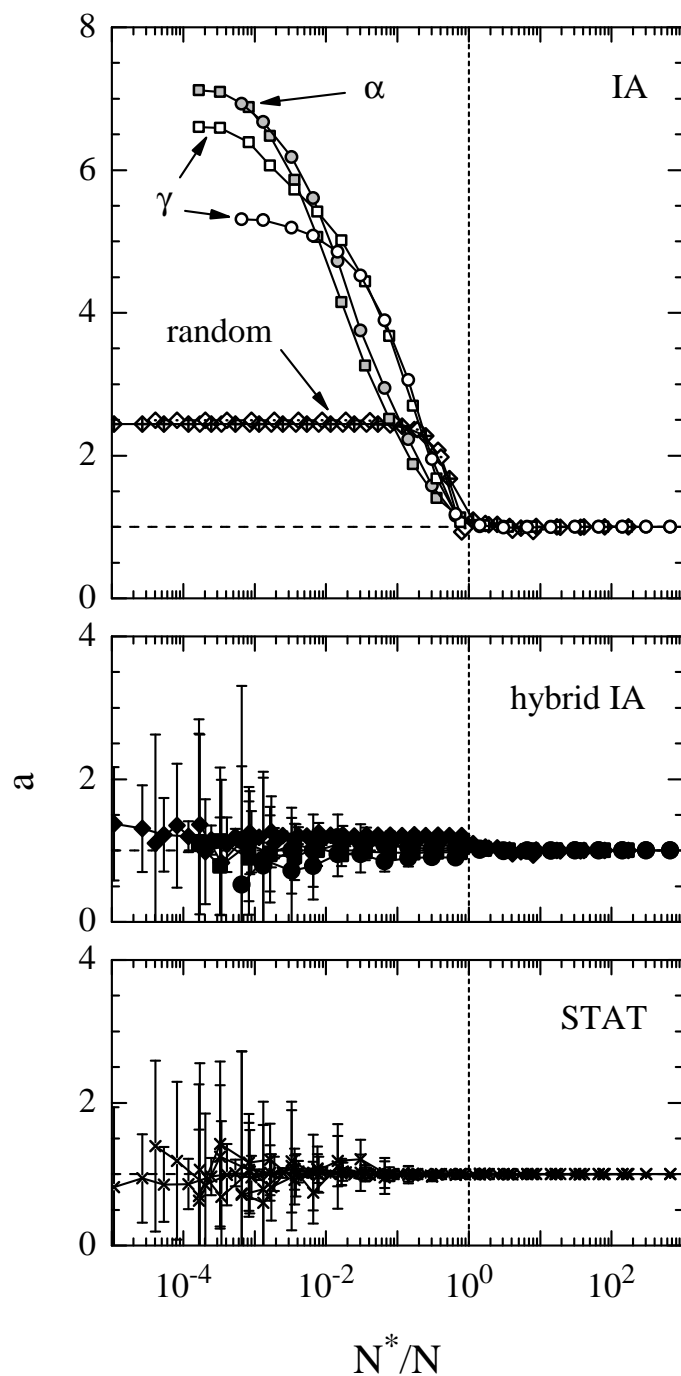
Figure 7.10: Slope a resulting from linear regression (see equation (7.15)) as function of normalized sample number. The orthotropic and monoclinic sample symmetry for the measured textures (α and γ) are indicated by circles and squares, respectively.
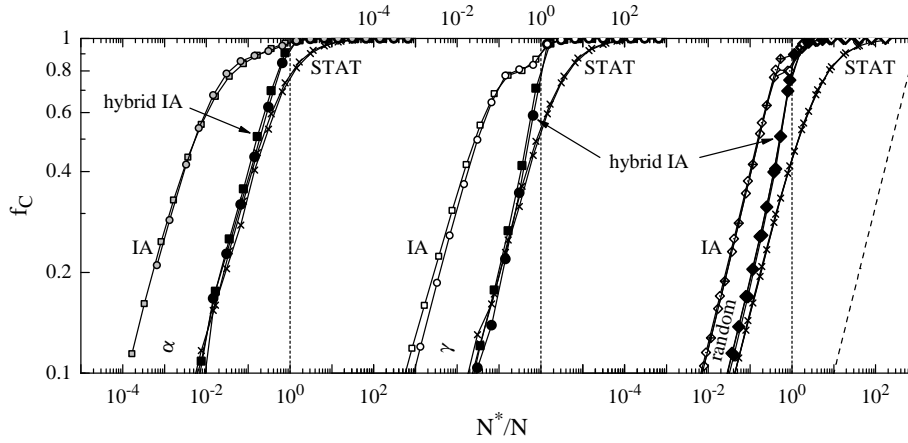
Figure 7.11: Correlation factor f_C resulting from linear regression (see equation (7.16)) as function of normalized sample number. Results on both α (left), both γ (center), and the three random (right) textures are shifted horizontally against each other by a constant factor, *i.e.* the vertical dotted line always corresponds to $N^*/N = 1$. The orthotropic and monoclinic sample symmetry for the measured textures (α and γ) are indicated by circles and squares, respectively.

With increasing N^*/N the correlation slope decreases in a rather similar fashion for all textures and the correlation between v_i^* and v_i finally turns ideal for $N^*/N > 1$.

The correlation factor, *i.e.* the degree of linearity between v_i^* and v_i, is plotted in figure 7.11 for the measured textures (left and center) and the random textures (right). Again, the normalization, N^*/N, of the sample number condenses similar ODFs onto individual master curves. With increasing normalized sample number, the correlation factor increases from values close to zero to its maximum value of one. In all cases, this increase of f_C initially follows in proportion to $\sqrt{N^*}$ (compare with dashed line in figure 7.11).

Despite the normalization, for a fixed N^*/N the resulting f_C differ slightly among the α, γ, and random textures and are always larger for those ODFs with a larger fraction of large v_i, *i.e.* better for sharper textures. The sharpness of texture also determines the factor in N^*/N by which the results from the IA method surpass those of the STAT method. In the present case, this factor ranges from about 10 for the random texture to 100 for the rather sharp α texture, see right and left of figure 7.11, respectively.

7.1.2.3 Discussion

We demonstrated in the previous section that the fully deterministic discretization of ODFs by means of the IA method shows advantages over probabilistic sampling but also has shortcomings, the most significant being the systematic over-weighting of large v_i for small sample numbers, which results in a pronounced sharpening of the reconstructed
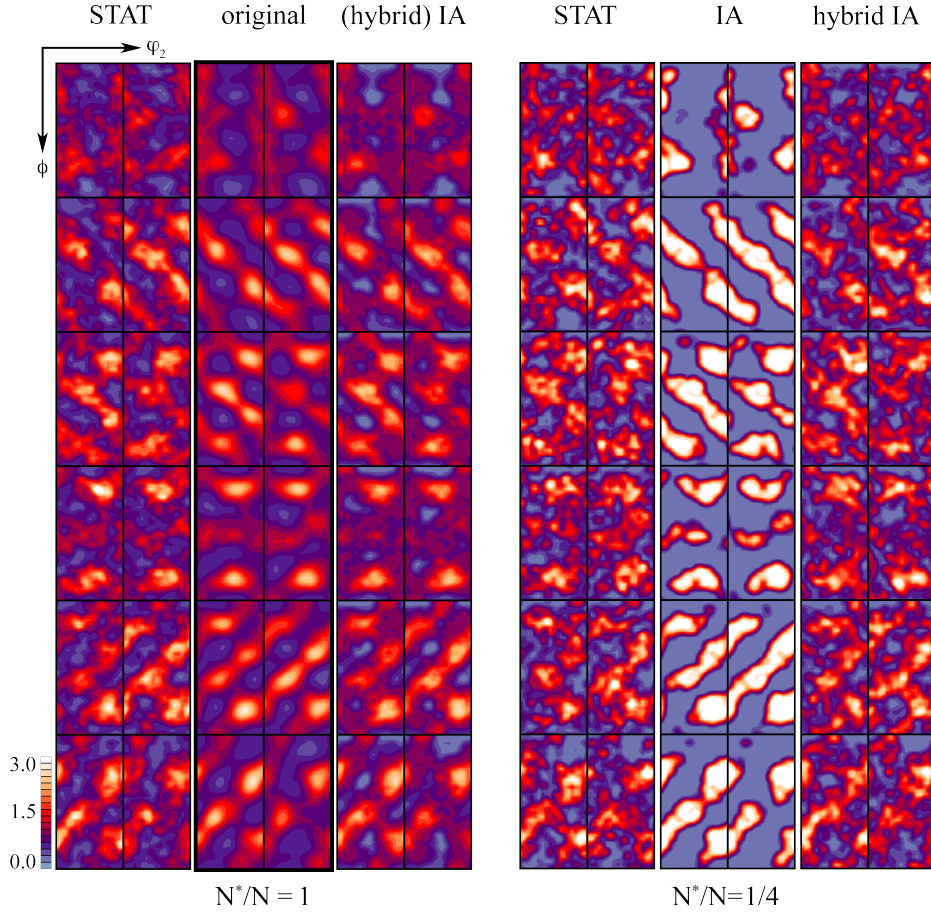
Figure 7.12: ODF of γ-monoclinic texture (framed at left center, $N = 6048$, see also figure 7.6 right) compared to its reconstructed versions from the STAT, IA, and hybrid IA method at $N^*/N = 1$ and $1/4$ (left and right).

texture. A discrimination line regarding the reconstruction quality can be drawn at normalized sample numbers $N^*/N \approx 1$. If $N^*/N > 1$ the reconstructed ODF resulting from the IA method is always superior to the respective result of probabilistic sampling. In the case $N^*/N < 1$ this statement is only true when considering the RMSD or f_C as measure for the reconstruction quality. However, the crucial quality measure is given by the correlation slope, a, since systematic deviations between original and reconstructed ODF are to be avoided. Yet, due to the integer rounding involved, the correlation between v_i^* and v_i resulting from the IA method exhibits exactly such systematic deviation for $N^*/N < 1$. As a consequence, the texture corresponding to the orientations sampled following the IA method turns progressively sharper than the original texture with decreasing sample number. This feature is illustrated in figure 7.12 where original and reconstructed ODFs of the γ-monoclinic texture are compared (left center and right center in figure 7.12).

To overcome this inherent problem of the IA method, we propose a combination of deter-

ministic and probabilistic sampling—termed "hybrid IA" in the following—by modifying the IA method as follows: if the requested number, N^*, of sampled orientations is less than the number of boxes in the fundamental zone of the original ODF, *i.e.* if $N^*/N < 1$, we nevertheless generate a population of N discrete orientations according to the original IA method (following equations (7.11) and (7.12)) but then select a random subset containing only the requested $N^* < N$ orientations from the population of N orientations.

As the reconstruction quality resulting from the IA method for $N^*/N \approx 1$ is virtually perfect (see figures 7.8, 7.10, and 7.11), we consider the population of N discrete orientations as (almost) identical to the original ODF. Thus the reintroduced probabilistic sampling from this population is (almost) an unbiased estimator of the original ODF (as shown by Tóth and Van Houtte (1992)), hence, the correlation between v_i^* and v_i following from the hybrid IA method will be ideal *on average.* Figure 7.10 indeed shows that $a \approx 1$ for $N^*/N < 1$ when applying the hybrid IA method to any of the investigated textures.

Since the variance in possible outcomes of drawing a subset containing N^* out of N orientations goes to zero with $N^* \to N$, the hybrid IA method should result in a smooth transition between the characteristics of the STAT method for $N^* \ll N$ and those of the (deterministic) IA method for $N^* \approx N$, eventually being identical to the latter for $N^* \geq N$. This notion is readily confirmed in figure 7.8 where the transient between RMSD $\propto 1/\sqrt{N^*}$ and RMSD $\propto 1/N^*$ turns slightly sharper for the hybrid IA method. Also, in figure 7.11 the smooth saturation of f_C is virtually absent but $f_C = 1$ is rapidly achieved by the hybrid IA method. Looking at these findings from a reverse angle, it becomes clear that some quality improvements (*i.e.* higher f_C and lower RMSD) in deterministic over probabilistic sampling are readily lost if more samples are generated than actually aimed for, *i.e.* $\sum_{i=1}^{N} n_i^* > N^*$, since that would require to chose a (random) subset from them. Figures 7.8 and 7.11 suggest that the (hybrid) IA method becomes equal to the STAT method if only less than 10% of the deterministically generated orientations enter into the ODF reconstruction. Therefore, adjustment of the scaling factor C in equation (7.11) should be done to a high accuracy to avoid significant deviations from the intended number, N^*, of orientations.

7.1.2.4   Conclusion

This section compared the quality of reconstructing a given texture by a set of discrete orientations. The two methods tested were probabilistic sampling employing the efficient STAT method proposed by Tóth and Van Houtte (1992) as well as the deterministic integer approximation (IA) method originally mentioned by Leffers and Juul Jensen (1986). In terms of the root mean squared deviation (RMSD, see equation (7.14)) the IA method yields equal or better reconstructions of the ODF than the STAT method. When employing the correlation factor introduced by Tarasiuk and Wierzbanowski (1996) as quality measure the IA method even performs far better compared to the STAT method.

However, the IA method has an inherent shortcoming since at small sample numbers it systematically over-weights those orientations that already have a high probability in the original texture on the expense of those of low probability. This leads to a significant sharpening of the reconstructed ODF compared to the original one. As this problem is absent in probabilistic sampling owing to its reconstructions being unbiased estimators of the original texture (Tóth and Van Houtte, 1992), a combination of both methods is proposed ("hybrid IA") by altering the IA method: at small sample numbers, a certain degree of probabilistic sampling is reintroduced by selecting a subset of discrete orientations from a fixed population that is itself determined by invoking the IA method. This new hybrid IA method blends the advantages of both former methods. Its reconstruction quality of all strong, intermediate, and random textures investigated in this section is equal to deterministic sampling, *i.e.* far better than probabilistic sampling, for $N^* \geq N$. At small N^*/N the method does not exhibit the detrimental texture sharpening inherent to the IA method, thus settles at the quality of probabilistic sampling for $N^* < N/10$.

7.2   Homogenization Schemes

Simulation of forming operations for polycrystalline metals poses significant challenges. At the component scale, the solution to the corresponding boundary value problem of continuous displacement and stress equilibrium is commonly sought by employing the finite element method (FEM). The kinematical description of the material in question routinely relies on the continuum mechanical framework of either finite or infinitesimal strain. In either case, to solve the above boundary value problem, knowledge of the constitutive response at the material point level is essential. This, however, is difficult since the macroscopic volume represented by individual material points of a polycrystal comprises a large number of crystallites when dealing with typical relations between component and grain size. The interaction among such extensive ensembles is very complex due to the heterogeneous and anisotropic elastic and plastic deformation of each grain. Since virtually all forming operations lead to preferred crystal orientations, *i.e.* crystallographic texture, macroscopic isotropy in the mechanical behavior is rather an exception than the rule. While modeling the crystal plasticity of individual grains has seen decent progress, estimates of ensemble behavior are still to be improved. The most simple averaging schemes are based on the assumptions of Voigt (1889) and Reuss (1929), which are, respectively, equal strain and equal stress among all grains (*i.e.* microscopic and macroscopic boundary conditions are identical).[6] However, the drastic simplifications of both usually do not match experimentally observed behavior. More advanced formulations may be distinguished into the two families of (semi-) analytical and numerical (full-field) methods. Examples for the former include models based on interacting grains in a (small) cluster, *e.g.* LAMEL (Van Houtte et al., 1999, 2002; Delannay et al., 2002) and ALAMEL (Van Houtte et al., 2005) by Van Houtte and coworkers and the GIA

---

[6]Despite the fact that both assumptions had been developed for purely elastic materials, they are transferable to elasto-plastic behavior when total strain and stress are considered, respectively.

model elaborated by Crumbach et al. (2004, 2006a, b). Furthermore, matrix–inclusion-based models, *e.g.* the viscoplastic self-consistent (VPSC) formalism of Molinari et al. (1987) (see also Lebensohn and Tomé (1993)), fall into this category. Direct numerical homogenization methods are computationally the most expensive ones and aim to solve the local displacement fluctuation field within a sufficiently large grain ensemble, *i.e.* a representative volume element, subjected to the homogeneous boundary conditions of the respective material point. The majority of recent contributions discretized this boundary value problem by means of numerical solution techniques such as the finite element method, see *e.g.* Smit et al. (1998); Miehe et al. (1999, 2002); Feyel and Chaboche (2000); Kouznetsova et al. (2001, 2002), or alternatively using a Fourier series approach on a regular grid (Moulinec and Suquet, 1998; Lebensohn, 2001).

7.2.1   The Isostrain and Isostress Scheme

The isostrain assumption states that all crystals of the body deform exactly as the entire body. It is often also referred to as full constraints (FC) Taylor assumption as Taylor (1938) first applied it for the prediction of the deformation behavior of polycrystals. In a large strain framework it can formally be written as equality of the deformation gradient of each grain with the average deformation gradient of the body $\mathcal{B}$

$$\boldsymbol{F}^g = \bar{\boldsymbol{F}} \quad \forall \ g \in \mathcal{B} \tag{7.17}$$

or in rate form

$$\dot{\boldsymbol{F}}^g = \dot{\bar{\boldsymbol{F}}} \quad \forall \ g \in \mathcal{B} \tag{7.18}$$

at any time. Depending on its orientation a different stress $\boldsymbol{S}$ will be required in each grain g to obtain the prescribed deformation. The isostrain scheme, therefore, violates stress equilibrium. The average stress is calculated as the average of the stresses of all grains:

$$\bar{\boldsymbol{S}} = \sum_{g=1}^{N} \nu^g \boldsymbol{S}^g \tag{7.19}$$

with ν^g the volume fraction of grain g. Due to the severe constraints the isostrain assumption imposes on the grains, this stress marks an upper bound for any homogenization scheme.

The isostress assumption marks the lower bound for the constitutive response of a polycrystal. Here the same stress is imposed on all grains and each grain deforms accordingly. Again due to its orientation each grain might deform differently, *i.e.* the isostress assumption violates strain compatibility. In case of the isostress assumption care has to be taken as to which stress is prescribed. While the strain is frame independent, prescribing the first Piola-Kirchhoff stress $\boldsymbol{P}$, the second Piola-Kirchhoff stress $\boldsymbol{S}$, or the Cauchy stress $\boldsymbol{\sigma}$ will each lead to a slightly different deformation of the grains. Sachs (1928) used yet another equal stress criterion, namely equal resolved shear stress on the slip
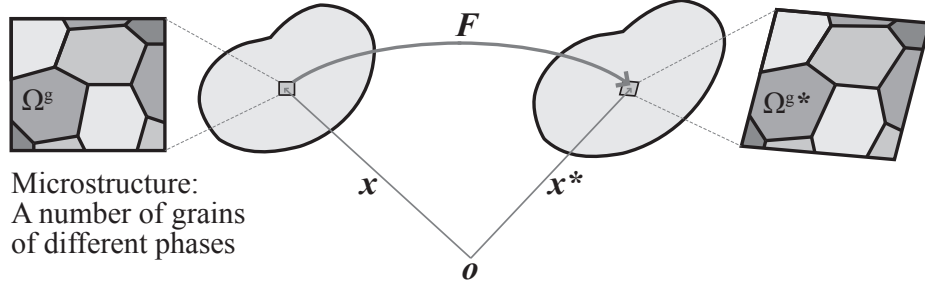
Figure 7.13: Deformation of a composite microstructure that contains several grains of potentially different phases.

system with the highest Schmid factor. In this case none of the afore mentioned stresses fulfills stress equilibrium nor is strain compatibility given.

In connection with CPFEM the isostrain scheme can be easily implemented, as the FE simulation prescribes the deformation gradient for each integration point and expects a stress response. An isostress scheme is, however, more complicated to implement.

7.2.2　Weighted-Taylor Homogenization Scheme with Iso-work-rate Condition

We consider a multiphase microstructure containing a number of grains with different properties (see figure 7.13). This microstructure is subjected to an effective deformation described by the deformation gradient $\bar{\boldsymbol{F}}$.

Suppose that, in a rate-form, the deformation gradient in each grain (sub-region) is given by

$$\dot{\boldsymbol{F}}^g = \lambda^g \dot{\bar{\boldsymbol{F}}} \tag{7.20}$$

for $g = 1, \ldots, N$ where λ^g is a scalar parameter describing the weight (or magnitude) of the rate of the deformation gradient in sub-region Ω^g, relative to the overall value. Equation (7.20) enhances the isostrain homogenization scheme discussed above by adding more flexibility in distributing the deformation in each sub-region. From this point of view, the FC Taylor scheme is the special case where $\lambda^g = 1$ for all $g = 1, \ldots, N$.

Using a simple rule of mixture, the rate of the overall deformation gradient can be written as the volume average of the rate of the deformation gradient of each grain

$$\dot{\bar{\boldsymbol{F}}} = \sum_{g=1}^{N} \nu^g \dot{\boldsymbol{F}}^g \ , \tag{7.21}$$

where $\nu^g = 1/V_0^g$ is the volume fraction of sub-region Ω^g in the undeformed state. Substituting equation (7.20) into (7.21), yields a restriction for the scalar parameters:

$$\sum_{g=1}^{N} \nu^g \lambda^g = 1 \ . \tag{7.22}$$

Let the work-rate in sub-region Ω^g be defined as the product of the first Piola-Kirchhoff stress in the undeformed configuration, which is conjugated to the rate of the deformation gradient, and the rate of the deformation gradient. In this case, the values of the weight parameters λ^g are determined such that the rate of (mechanical) work carried by each sub-region is uniform (iso-work-rate criteria), which can be formulated as

$$\boldsymbol{P}^g \dot{\boldsymbol{F}}^g = \boldsymbol{P}^N \dot{\boldsymbol{F}}^N \tag{7.23}$$

for $g = 1, \ldots, N - 1$.

The first Piola-Kirchhoff stress is a function of the deformation gradient $\boldsymbol{F}^g$, which is described by the material constitutive model. Consequently, the first Piola-Kirchhoff stress is, in general, a function of the weight parameters,

$$\boldsymbol{P}^g = \boldsymbol{P}^g(\boldsymbol{\lambda}) \tag{7.24}$$

with $\boldsymbol{\lambda} = \{\lambda^g, \ g = 1, \ldots, N\}$.

Using equations (7.20) and (7.24), the iso-work-rate condition shown in equation (7.23) can be written as

$$\left[\lambda^g \boldsymbol{P}^g(\boldsymbol{\lambda}) - \lambda^N \boldsymbol{P}^N(\boldsymbol{\lambda})\right] \cdot \bar{\dot{\boldsymbol{F}}} = 0 \tag{7.25}$$

for $g = 1, \ldots, N - 1$. The weight parameters λ^g can be obtained by solving the non-linear equations described by the iso-work-rate condition (equation (7.25)) and the criterion given in equation (7.22).

To solve this non-linear problem a Newton-Raphson scheme is employed. Obviously, the implementation of the iso-work-rate weighted-Taylor scheme is computationally more complicated than the FC Taylor scheme, particularly since it requires to solve the non-linear equations (7.22) and (7.25).

Furthermore, the effective first Piola-Kirchhoff stress can be obtained as the volume average of the corresponding stress in each sub-region:

$$\bar{\boldsymbol{P}} = \sum_{g=1}^{N} \nu^g \boldsymbol{P}^g \ . \tag{7.26}$$

In Tjahjanto et al. (2007) the iso-work-rate weighted-Taylor scheme has been tested on predicting the deformation behavior of a multiphase TRIP-assisted steel. In order to simulate the transformation of face-centered cubic austenite into body-centered tetragonal martensite, the martensitic phase transformation model developed by Turteltaub

and Suiker (2006) was applied. It was shown that the predictions using this scheme were superior to predictions made using the FC Taylor scheme. In addition the scheme is easy to implement into a CPFEM framework and the computational demands are only slightly higher than for the FC Taylor scheme. Nevertheless, the iso-work-rate weighted-Taylor scheme was outrun by the Relaxed Grain Cluster scheme presented in the next section.

7.2.3   The Relaxed Grain Cluster Scheme

The concept of the Relaxed Grain Cluster (RGC) scheme is based on the GIA model (Crumbach et al., 2004, 2006a, b), which itself extends the LAMEL model (Van Houtte et al., 1999, 2002; Delannay et al., 2002). The generalization of the original GIA concept comprises mainly two aspects:

- Deformation kinematics are formulated within a finite deformation framework as compared to the framework of (symmetric) infinitesimal strain employed (and violated by non-symmetric relaxations) in GIA. Extension from the infinitesimal strain formulation to the finite deformation framework adequately captures the large strains as well as rigid-body rotations that grains may experience in, for instance, forming operations. Furthermore, mismatch due to elastic deformations and rigid-body rotations are accounted for in this formalism.

- The local constitutive model at the grain level is separated from the macro-scale homogenization formulation. This allows the RGC scheme to be implemented in conjunction with various micro-scale constitutive models, whereas the original GIA formulation is limited to single-crystal viscoplastic constitutive laws, i.e., excluding all elastic effects.

The RGC scheme simplifies the situation at a macro-scale material point by approximating it with a cluster containing $N = p \times q \times r$ hexahedral (and homogeneously deforming) grains as shown in figure 7.14a. The interfaces α of each grain g are characterized by their outward pointing normals $\boldsymbol{n}_\alpha^g$ and follow the convention illustrated in figure 7.14b with respect to the cluster frame.

In order for each individual grain to be able to deviate from the average cluster deformation gradient, $\bar{\boldsymbol{F}}$, so-called *relaxation vectors* $\boldsymbol{a}_\alpha^g$ are attached to all interfaces of all grains (see figure 7.14b). They quantify the displacement of the corresponding interface α relative to the overall deformation $\bar{\boldsymbol{F}}$, such that the individual deformation gradient, $\boldsymbol{F}^g$, experienced by a particular grain follows as

$$\boldsymbol{F}^g = \bar{\boldsymbol{F}} + \frac{1}{V^g} \sum_{\alpha=1}^{3} \left(A_\alpha^g \boldsymbol{a}_\alpha^g \otimes \boldsymbol{n}_\alpha^g + A_{-\alpha}^g \boldsymbol{a}_{-\alpha}^g \otimes \boldsymbol{n}_{-\alpha}^g \right) , \qquad (7.27)$$

(a) Cluster of $p \times q \times r$ hexahedral grains at macro-scale material point.

(b) Hexahedral grain g of dimensions d_1, d_2, d_3. Interfaces are characterized by outward normals $\boldsymbol{n}_\alpha^g$, which are aligned with the cluster axes. Each interface α carries an attached relaxation vector $\boldsymbol{a}_\alpha^g$.
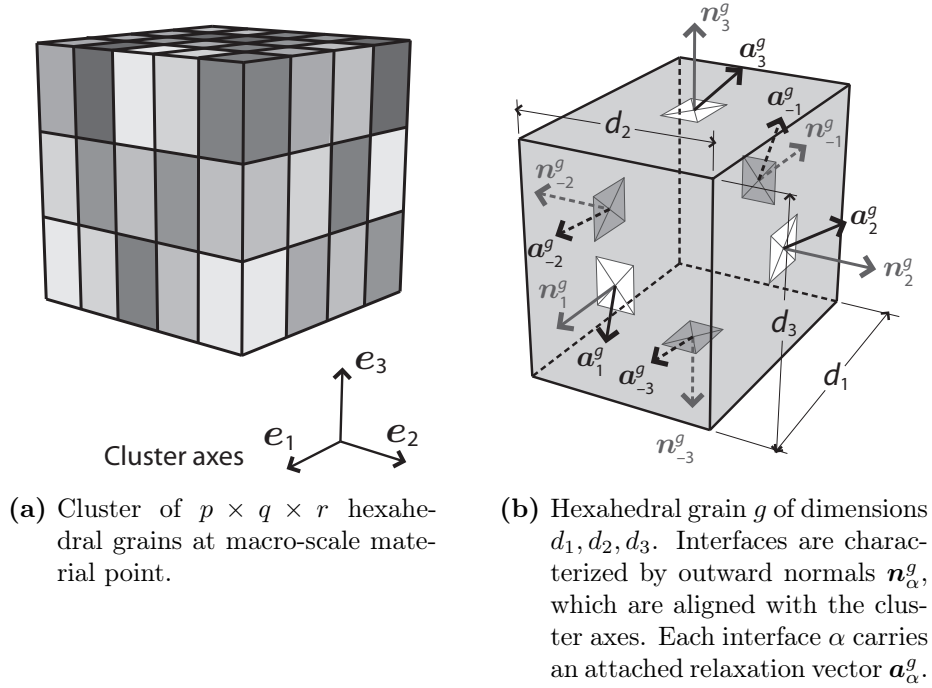
Figure 7.14: Material point representation in the Relaxed Grain Cluster scheme.

with V^g the volume of grain g and A_α^g the area of the respective interface in the undeformed configuration, *i.e.* all six interface displacements contribute to the deviation of the local deformation gradient from the macro-scale one. At the same time this formulation guarantees that

$$\bar{\boldsymbol{F}} = \frac{1}{\bar{V}} \sum_{g=1}^N V^g \boldsymbol{F}^g \, , \quad \text{where} \quad \sum_{g=1}^N V^g = \bar{V} \, , \tag{7.28}$$

with $\bar{V}$ the total volume of the cluster in the undeformed configuration and N the number of grains in the cluster, is always fulfilled.

The relaxation vectors are subject to two constraints. First, for any two grains g_1 and g_2 the relaxation vectors assigned by either of them to their shared interface α, are set to be identical,

$$\boldsymbol{a}_\alpha^{g_1} = \boldsymbol{a}_{-\alpha}^{g_2} \, , \tag{7.29}$$

as shown in figure 7.15a for an exemplary grain pair with an interface normal along $\boldsymbol{e}_1$. The contribution of such an individual relaxation vector to the grain deformation gradient (given by equation (7.27)) is illustrated in figure 7.15b for the same grain pair. Second, since the overall relaxation behavior is not altered by a constant offset in all those relaxation vectors that belong to a row of interfaces that is aligned with one of the crystal axes, we can (most conveniently) assure periodic boundary conditions by setting

(a) Exemplary pair of grains g_1 and g_2, which are neighbors along e_1 and share a common interface. Since the same interface is targeted, the two respective relaxation vectors are set equal $a_1^{g_1} = a_1^{g_2}$ for both grains.

(b) Combined relaxation of grains g_1 and g_2 due to the relaxation vector shown in (a).

(c) Periodic boundary conditions require equal relaxation vectors at opposite exterior interfaces. A vanishing relaxation vector for exterior interfaces is most convenient and does not alter the overall relaxation due to displacements of all same-oriented interior interfaces in between them.

Figure 7.15: Relaxation vectors on interior and exterior interfaces of the grain cluster.

(a) Grain pair exhibiting non-matching relaxation vectors ($\boldsymbol{a}_2^{g_2} \neq \boldsymbol{a}_2^{g_1}$) on neighboring interfaces having a common orientation ($\boldsymbol{n}_2$).

(b) Discontinuity in the gradients of displacement and deformation across the shared interface of the grain pair resulting from the non-matching relaxation shown in (a).
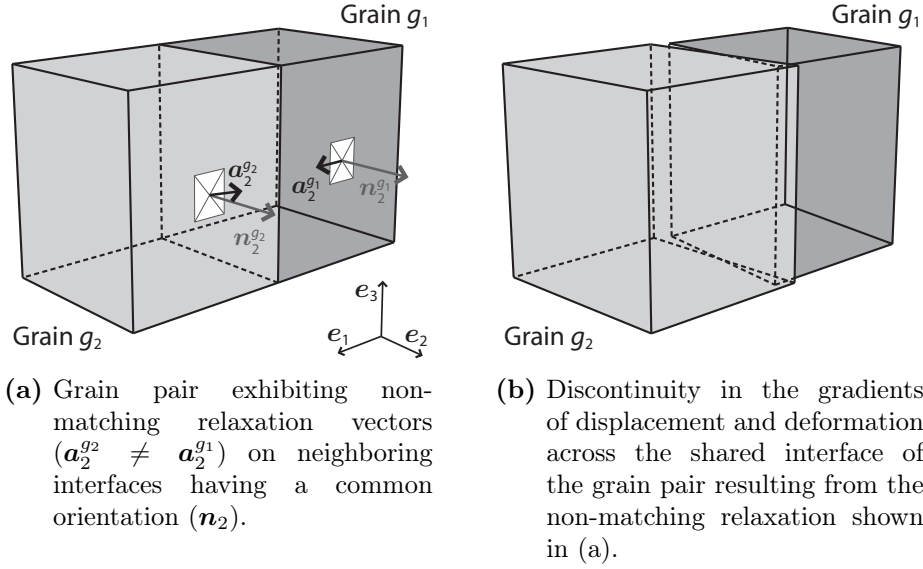
Figure 7.16: Source of mismatch within the grain cluster. Non-equal relaxation vectors on neighboring and same-oriented interfaces results in overlaps and gaps across perpendicular interfaces sharing a trace with the former two.

the relaxation vectors on all exterior interfaces to zero as shown in figure 7.15c. With above conditions in place, the deformation state of the cluster is determined once all independent[7] relaxation vectors are known.

From figure 7.15b we observe that the relaxation resulting from a relative displacement of an interface maintains the tight connection between the two neighboring grains. A different picture emerges when we consider the effect of two neighboring interfaces of same orientation on which the respective relaxation vectors *differ*. This is shown in figure 7.16 and results in a discontinuity in the gradients of displacement as well as deformation across the interface shared by both grains. In order to quantify the magnitude of such overlaps and gaps, a measure, which is similar to the surface dislocation tensor of Bilby (1955), is used

$$\boldsymbol{M}_\alpha^g = -\frac{1}{2}\big(\boldsymbol{n}_\alpha^g \times \Delta\boldsymbol{F}_\alpha^{g\mathrm{T}}\big)^{\mathrm{T}} \quad \text{or}$$

$$\text{in index notation} \quad [M_\alpha^g]_{ij} = -\frac{1}{2}\,[n_\alpha^g]_k\,[\Delta F_\alpha^g]_{il}\,\epsilon_{jkl}\,, \quad (7.30)$$

in which $\Delta\boldsymbol{F}_\alpha^g$ denotes the jump in deformation gradient between grain g and the neighboring grain sharing interface α.

Based on the mismatch measure, a (penalty) energy density, $\mathcal{R}_\alpha^g$, associated with interface α of grain g is introduced. An expression for the penalty energy is rationalized by

---

[7]A cluster of size $p \times q \times r$ has in total $(p-1)qr + p(q-1)r + pq(r-1)$ interior interfaces at which independent grain deformation relaxation can occur.

considering the density of dislocations that could accommodate such deformation mis-match. According to Nye (1953) and Bilby (1955) the presence of a dislocation network can be *uniquely* translated into a tensorial representation of deformation mismatch in the case of three-dimensional and two-dimensional dislocation networks, respectively. However, the inverse is not true. If the mismatch is known then only a minimum content of geometrically necessary dislocation (GND) density can be derived using various optimization procedures (see, *e.g.* Arsenlis and Parks (1999)). In general, the larger the mismatch the more dislocations are required to accommodate it. This would imply a linear relation between mismatch and penalty energy, the latter could be identified with the line energy of the dislocations in the accommodating network. However, since the accommodation by dislocations is unlikely to be perfect, there will additionally be redundant (statistically stored, SSD) dislocations present. Assuming that the number of these SSDs grows increasingly more rapid with mismatch than the GND content suggests an *over-proportional* growth of penalty energy with increasing mismatch. In order to phenomenologically capture such an over-proportionality, a hyperbolic sine function is employed as the relation between magnitude,

$$\|\boldsymbol{M}_\alpha^g\| = (\boldsymbol{M}_\alpha^g \cdot \boldsymbol{M}_\alpha^g)^{\frac{1}{2}} \ , \tag{7.31}$$

of mismatch and the penalty energy density (per unit area)

$$\mathcal{R}_\alpha^g = \frac{G^g b^g}{2} \frac{\xi}{c} \sinh \left(c \|\boldsymbol{M}_\alpha^g\| \right) \ , \tag{7.32}$$

where G^g denotes the equivalent shear modulus and b^g the magnitude of the Burgers vector of grain g.

Two dimensionless parameters are introduced in equation (7.32), namely ξ, a scalar describing the effective weight of the penalty function, and c, a parameter that sets the over-proportionality of the penalty function with respect to the magnitude of the mismatch. The "penalty-free" model is obtained for $\xi = 0$, whereas $\xi \to \infty$ gives a very strong penalty function, which results in a "fully compatible" local deformation mode. The penalty energy function (7.32) shows a linear behavior if $c \to 0$.

The magnitude of penalty energy at interface α of grain g is given by $\mathcal{R}_\alpha^g \tilde{A}_\alpha^g$, where $\tilde{A}_\alpha^g$ is the corresponding area of the interface in the *deformed configuration*. The overall penalty energy density (per unit reference volume) $\bar{\mathcal{R}}$ is computed as

$$\bar{\mathcal{R}} = \frac{1}{\bar{V}} \sum_{g=1}^{N} V^g \mathcal{R}^g \ , \tag{7.33}$$

where the penalty energy density (per unit reference volume) of each individual grain is obtained as

$$\mathcal{R}^g = \frac{1}{V^g} \sum_{\alpha=1}^{3} \left(\tilde{A}_\alpha^g \mathcal{R}_\alpha^g + \tilde{A}_{-\alpha}^g \mathcal{R}_{-\alpha}^g \right) \ . \tag{7.34}$$

It is assumed that the deformed area $\tilde{A}_\alpha^g$ is connected to the corresponding undeformed area A_α^g as $\tilde{A}_\alpha^g = \vartheta_\alpha A_\alpha^g$, where

$$\vartheta_\alpha = (\det \bar{F}) \left\{ \bar{C}^{-1} n_\alpha^g \cdot n_\alpha^g \right\}^{\frac{1}{2}} \tag{7.35}$$

with $\bar{C} = \bar{F}^T \bar{F}$ being the Cauchy–Green stretch tensor. Note that $n_\alpha^g = e_\alpha$ and, thus, $\{\bar{C}^{-1} n_\alpha^g \cdot n_\alpha^g\}$ gives the $\alpha\alpha$-th component of $\bar{C}^{-1}$ with respect to the cluster basis $\{e_1, e_2, e_3\}$. Hence, the penalty energy density $\mathcal{R}^g$ in (7.34) can be expressed as

$$\mathcal{R}^g = \frac{1}{V^g} \sum_{\alpha=1}^{3} \left(\vartheta_\alpha A_\alpha^g \mathcal{R}_\alpha^g + \vartheta_{-\alpha} A_{-\alpha}^g \mathcal{R}_{-\alpha}^g \right) . \tag{7.36}$$

Expression (7.35) suggests that the value ϑ_α evolves with deformation. But the evolution of ϑ_α depends on the overall deformation gradient $\bar{F}$ only.

A second contribution to the cluster energy results from the work dissipated in its deformation. Let P^g be the first Piola–Kirchhoff stress tensor of grain g, which is a function of the local deformation gradient F^g through the local constitutive model, $P^g = \tilde{P}^g(F^g)$. The resulting effective first Piola–Kirchhoff stress tensor, denoted as $\bar{P}$, is then again computed as the volumetric average of the local stresses P^g as

$$\bar{P} = \frac{1}{\bar{V}} \sum_{g=1}^{N} V^g P^g . \tag{7.37}$$

The constitutive energy (or work) density of grain g per unit volume in the reference configuration at time t, denoted by $\mathcal{W}^g$, is given by

$$\mathcal{W}^g = \int_0^t P^g(\tau) \cdot \dot{F}^g(\tau) \mathrm{d}\tau , \tag{7.38}$$

where $\dot{F}^g$ is the rate of change of the deformation gradient of grain g. It is assumed that the total work density of the cluster, $\bar{\mathcal{W}}$, can be obtained as the volumetric average of the work density of all grains as

$$\bar{\mathcal{W}} = \frac{1}{\bar{V}} \sum_{g=1}^{N} V^g \mathcal{W}^g . \tag{7.39}$$

The RGC scheme now postulates that the relaxation behavior of the overall cluster— determined by the set of all relaxation vectors $a = \{a_\alpha^g\}$—is such that for a given $\bar{F}$ the total energy $\bar{\mathcal{W}} + \bar{\mathcal{R}}$ is minimum, i.e.

$$\hat{a} = \mathrm{Min} \left\{ \bar{\mathcal{W}}(a) + \bar{\mathcal{R}}(a) \right\} . \tag{7.40}$$

It has to be noted that $\bar{\mathcal{W}}$ is, in general, a non-convex function of the F^g, which might lead to (i) multiple local minima, prompting algorithmic difficulties in finding the global

minimum, and (ii) non-unique global minima. The convexity of the overall energy density can, however, be enforced by the introduction of the penalty term $\bar{\mathcal{R}}$. Thus, relying on a convex overall energy density, the solution of the energy minimization problem in equation (7.40) corresponds to the stationary point

$$\frac{\partial \left(\bar{\mathcal{W}} + \bar{\mathcal{R}}\right)}{\partial \boldsymbol{a}}\Bigg|_{\hat{\boldsymbol{a}}} = \boldsymbol{0} \ . \tag{7.41}$$

Equation (7.41) has to hold individually for each relaxation vector attached to an (interior) interface out of the set $\hat{\boldsymbol{a}}$. Selecting an arbitrary interface, which is shared between grains g_1 and g_2 and has a normal $\boldsymbol{n}_\alpha^{g_1}$ and $\boldsymbol{n}_{-\alpha}^{g_2}$ when referred to from the two grains respectively, we find that equation (7.41) is equivalent to an equation of force equilibrium (or balance of traction) at the shared interface:

$$\frac{\partial \left(\bar{\mathcal{W}} + \bar{\mathcal{R}}\right)}{\partial \boldsymbol{F}^{g_1}} \frac{\partial \boldsymbol{F}^{g_1}}{\partial \boldsymbol{a}_\alpha^{g_1}} + \frac{\partial \left(\bar{\mathcal{W}} + \bar{\mathcal{R}}\right)}{\partial \boldsymbol{F}^{g_2}} \frac{\partial \boldsymbol{F}^{g_2}}{\partial \boldsymbol{a}_{-\alpha}^{g_2}} =$$
$$\frac{A_\alpha^{g_1}}{V^{g_1}} \left(\boldsymbol{P}^{g_1} + \boldsymbol{R}^{g_1}\right) \boldsymbol{n}_\alpha^{g_1} + \frac{A_{-\alpha}^{g_2}}{V^{g_2}} \left(\boldsymbol{P}^{g_2} + \boldsymbol{R}^{g_2}\right) \boldsymbol{n}_{-\alpha}^{g_2} = \boldsymbol{0} \ . \tag{7.42}$$

In equation (7.42) the terms $\boldsymbol{R}^g$ are shorthand for the derivative of the overall penalty energy density $\bar{\mathcal{R}}$ with respect to the grain deformation gradient $\boldsymbol{F}^g$. It is a stress-like penalty associated with the mismatch at all interfaces of grain g and can be obtained as

$$\boldsymbol{R}^g := \frac{\partial \bar{\mathcal{R}}}{\partial \boldsymbol{F}^g} = \sum_{\beta=1}^{3} \left\{ \frac{\vartheta_\beta \lambda_\beta^g}{2} \left(\frac{\boldsymbol{M}_\beta^{g\mathrm{T}}}{\|\boldsymbol{M}_\beta^g\|} \times \boldsymbol{n}_\beta^g\right)^T \xi \cosh\left(c\|\boldsymbol{M}_\beta^g\|\right) \right.$$
$$\left. + \frac{\vartheta_{-\beta} \lambda_{-\beta}^g}{2} \left(\frac{\boldsymbol{M}_{-\beta}^g{}^{\mathrm{T}}}{\|\boldsymbol{M}_{-\beta}^g\|} \times \boldsymbol{n}_{-\beta}^g\right)^T \xi \cosh\left(c\|\boldsymbol{M}_{-\beta}^g\|\right) \right\} , \tag{7.43}$$

or in components

$$[R^g]_{ij} = \sum_{\beta=1}^{3} \left\{ \frac{\vartheta_\beta \lambda_\beta^g}{2} \frac{1}{\|\boldsymbol{M}_\beta^g\|} \left[M_\beta^g\right]_{ik} \left\{n_\beta^g\right\}_l \epsilon_{klj} \xi \cosh\left(c\|\boldsymbol{M}_\beta^g\|\right) \right.$$
$$\left. + \frac{\vartheta_{-\beta} \lambda_{-\beta}^g}{2} \frac{1}{\|\boldsymbol{M}_{-\beta}^g\|} \left[M_{-\beta}^g\right]_{ik} \left\{n_{-\beta}^g\right\}_l \epsilon_{klj} \xi \cosh\left(c\|\boldsymbol{M}_{-\beta}^g\|\right) \right\} . \tag{7.44}$$

where λ_β^g represents the average modulus of the penalty stress $\boldsymbol{R}^g$ at interface β, summarizing the contributions from the two grains situated on either side of the interface, i.e. grain g itself and grain g_β, which is the neighbor of g across the interface β,

$$\lambda_\beta^g = \frac{1}{2} \left(\frac{G^g b^g}{d_\beta^g} + \frac{G^{g_\beta} b^{g_\beta}}{d_\beta^{g_\beta}}\right) \ . \tag{7.45}$$

In the case of hexahedral grains, $d_\beta^g = V^g/A_\beta^g$ represents the dimension of grain g in the direction parallel to $\boldsymbol{e}_\beta$. This indicates that the penalty stress tensor $\boldsymbol{R}^g$ is inversely proportional to the grain size.

It is important to realize that, in contrast to the first Piola–Kirchhoff stress $\boldsymbol{P}^g$, the penalty stress $\boldsymbol{R}^g$ depends not only on the deformation gradient of grain g, but also on the deformation gradients of the neighboring grains, since the mismatch tensors $\boldsymbol{M}_\beta^g$ comprise the jump in deformation gradient between grain g and its neighbors.

The sum of the volumes of the individual grains in the current (or deformed) configuration, computed by $\sum_{g=1}^N V^g \det \boldsymbol{F}^g$, is consistent with the current volume of the cluster, given by $\bar{V} \det \bar{\boldsymbol{F}}$, only if all grain deformation gradients $\boldsymbol{F}^g$ are fully compatible. Due to relaxations, the misfit at grain interfaces may cause violation of the above volumetric consistency condition. In order to prevent this, an additional constraint is imposed to the set of relaxation vectors $\boldsymbol{a}$ during the search for the total energy minimizer, namely, a volume consistency condition, such that the overall volume of the cluster must be consistent with the sum of the volumes of the individual grains,

$$\sum_{g=1}^N V^g \det(\boldsymbol{F}^g(\boldsymbol{a})) \overset{!}{=} \bar{V} \det \bar{\boldsymbol{F}} \, . \tag{7.46}$$

In summary, the minimization of the total cluster energy $\bar{\mathcal{W}} + \bar{\mathcal{R}}$, which is equivalent to establishing the balance of traction (see equation (7.42)) at each interior interface, yields all relaxation vectors. From those the partitioning of the overall deformation $\bar{\boldsymbol{F}}$ into individual grain deformations $\boldsymbol{F}^g$ is determined by equation (7.27). The local stress responses $\boldsymbol{P}^g$, given by the corresponding (but independent) constitutive laws $\tilde{\boldsymbol{P}}^g(\boldsymbol{F}^g)$, are averaged according to equation (7.37) and compose the overall stress of the cluster $\bar{\boldsymbol{P}}(\bar{\boldsymbol{F}})$.

7.2.3.1   Comparison to Other Averaging Methods

In the present analysis, a polycrystalline dual-phase microstructure is represented by one cubic cluster that consists of eight cubical grains of equal volume. Grains 1 and 8 are assigned the properties of a hard phase, whereas the remaining six grains are of a soft phase. In the undeformed state, this configuration makes a dual-phase microstructure with the composition of 25 vol% hard phase and 75 vol% soft phase, since the initial grain volume fraction $V_0^g = 0.125$, for all grains $g = 1, \ldots, 8$. The material properties and crystallographic orientations assigned to the individual grains of the cluster are given in tables 7.1 and 7.2. The spatial arrangement of grains is shown in figure 7.18. For comparison, the finite element method is used to simulate the behavior of the grain cluster. Two different levels of mesh resolution have been used, namely (i) coarse mesh, where each individual grain is represented by a single linear hexahedral element, and (ii) fine mesh, where each grain is discretized into $8^3 = 512$ linear hexahedral elements. In the finite element simulations, periodicity conditions are imposed on the external nodes.

Table 7.1: Material parameters of the single crystal elasto-plasticity model (section 2.3) and the corresponding assigned value(s).

Model parameters	Grains $g = 1$ and 8	Grains $g = 2$ to 7
Elastic moduli (in Voigt's notation)	$\mathbb{C}_{11} = 213.6\,\text{GPa}$	$\mathbb{C}_{11} = 149.5\,\text{GPa}$
	$\mathbb{C}_{12} = 120.8\,\text{GPa}$	$\mathbb{C}_{12} = 72.5\,\text{GPa}$
	$\mathbb{C}_{44} = 56.6\,\text{GPa}$	$\mathbb{C}_{44} = 45.3\,\text{GPa}$
Kinetic model for plastic slip	$\dot{\gamma}_0 = 0.001\ \text{s}^{-1}$	
	$m = 0.02$	
Slip resistance and hardening	$\tau_0 = 224\,\text{MPa}$	$\tau_0 = 56\,\text{MPa}$
	$\tau_\text{s} = 448\,\text{MPa}$	$\tau_\text{s} = 224\,\text{MPa}$
	$h_0 = 400\,\text{MPa}$	$h_0 = 600\,\text{MPa}$
	$a = 3.0$	$a = 4.0$
	$q_{\alpha,\beta} = 1.4$ (non-coplanar)	

Table 7.2: Crystallographic orientation of the constituent grains of the cluster, in Bunge Euler angles.

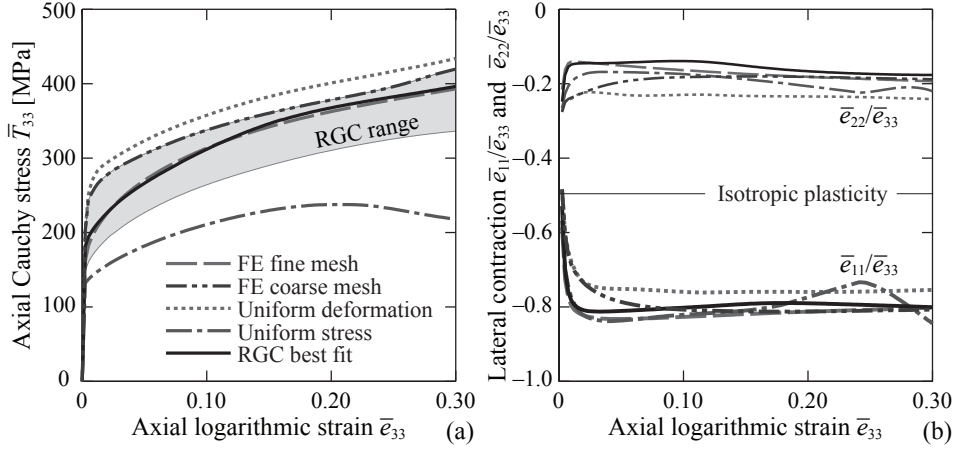| Grain	Euler angles (°)			Grain	Euler angles (°)		
	φ_1	ϕ	φ_2		φ_1	ϕ	φ_2
1	0.00	18.43	8.98	2	38.57	0.00	0.00
3	12.68	45.00	0.00	4	25.71	45.00	35.26
5	19.29	26.57	0.00	6	32.14	26.57	24.09
7	6.43	45.00	19.47	8	45.00	33.69	15.50

Figure 7.17: Comparison of the cluster response in terms of (a) the axial flow stress and (b) the relative contraction in the lateral directions during uniaxial tensile deformation as predicted by various homogenization schemes.

The prediction of the RGC scheme in terms of the axial stress–strain response and the relative lateral contractions are compared to the results obtained using other averaging schemes in figure 7.17a and b, respectively. The result of a finite element (FE) simulation with fine mesh is used as benchmark.

In figure 7.17a, the upper limit in axial stress–strain response is given by the uniform deformation assumption, $\boldsymbol{F}^g = \bar{\boldsymbol{F}}$, for all grains $g = 1, \ldots, 8$. In contrast, the lower limit is obtained for the calculation with a uniform stress distribution, $\boldsymbol{P}^g = \bar{\boldsymbol{P}}$. The gray-shaded area represents the range of axial stress–strain response that can be obtained by the RGC scheme. As discussed in the previous sections, the upper limit of this area results from a very high penalty weight ξ (*i.e.* fully compatible case). It can be seen that, for this particular arrangement of grains, the upper limit obtained using the RGC scheme is yet lower than the prediction resulting from the Taylor assumption. In fact, the RGC upper bound coincides with the result of a FE simulation with coarse mesh (one element per grain, linear shape function). On the other hand, the lower bound for the RGC prediction is given by the penalty-free case, which results from very low values of ξ. This range (*i.e.* the gray-shaded area) is considerably narrowed down in comparison to the range between the minimum and maximum response set by the uniform stress and uniform deformation models, respectively. The stress–strain response of the FE simulation with fine mesh (512 elements per grain) falls within the RGC range and the best fit to this result is obtained by the RGC scheme with $\xi = 5.2$ and $c = 13$.

Regarding the relative lateral contractions, all homogenization schemes fall rather close to the benchmark set by the fine mesh FE simulation for this particular arrangement of grains. The exception being the Taylor scheme that significantly underestimates the
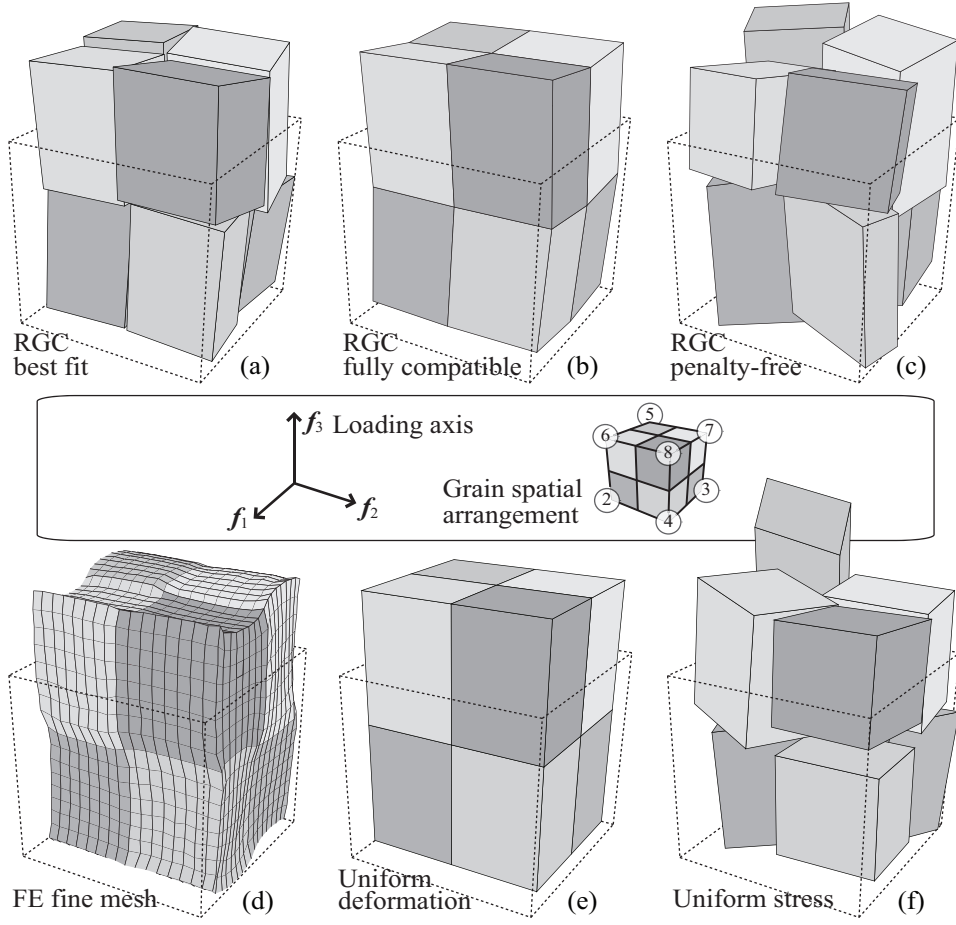
Figure 7.18:   Deformation of individual grains after an applied axial strain $\bar{e}_{33} = 0.30$ calculated using (a–c) RGC scheme, (d) finite element simulation, (e) uniform deformation and (f) uniform stress assumptions.

anisotropy effect and falls closest to the line characterizing isotropy (figure 7.17b). Out of all schemes investigated, especially in comparison with the coarse mesh FE simulation, the RGC scheme with the best fitted penalty parameters matches most closely the benchmark when the full range of strain up to $\bar{e}_{33} = 0.30$ is taken into account.

In order to give a better insight, figures 7.18a–f visualize the deformation of individual grains in the cluster resulting from different homogenization schemes at an axial strain of 0.30. These visualizations are constructed by plotting the deformed shape of the initially cubical grains, which is characterized by the grain deformation gradient $\boldsymbol{F}^g$. Figures 7.18a–c show the grain deformation when using the RGC scheme with, respectively, the best fitted parameters, fully compatible case, and penalty-free case. The visualization of the deformation of individual grains obtained from the FE simulation (with fine mesh), uniform deformation, and uniform stress assumptions are respectively

Table 7.3: Comparison between computational cost, in terms of CPU-time, used by various averaging schemes during uniaxial tensile simulations.

Averaging scheme	CPU-time (s)
Uniform deformation	16
Uniform stress	1509
FE simulations	123 (coarse mesh); 229890 (fine mesh)
Relaxed Grain Cluster	69 (fully compatible); 81 (best fit); 346 (penalty-free)

depicted in figures 7.18d–f.

The deformation of each grain predicted by the best fit RGC scheme shows a remarkably good correlation to the result of the FE simulation with fine mesh (compare figure 7.18a to figure 7.18d). This comparison shows that the RGC scheme is not only able to capture the overall response, but also to adequately mimic the local deformation of the individual grains resulting from the FE simulation. For the fully compatible RGC case shown in figure 7.18b, a small amount of relaxation causes a subtle but important deviation of the local grain deformations from the result of the Taylor model where all grains deform uniformly (see figure 7.18e). These relaxations, though very limited, correspond to a noticeable improvement in the prediction of the stress–strain response in comparison to that computed with the uniform deformation (figure 7.17a).

The penalty-free case shown in figure 7.18c deviates rather strongly from the two other RGC cases (figures 7.18a and b) in terms of the total amount of mismatch and in particular the deformation mode observed for individual grains. This indicates that variations of the penalty parameters ξ and c do not only scale the length of the relaxation vectors but also alter their direction and, thus, change the deformation mode of the grains.

7.2.3.2 Concluding Remarks

The RGC homogenization scheme has been used to calculate the mechanical response of a polycrystalline dual-phase grain cluster. The results show that the range of the cluster response predicted by the RGC scheme is narrower than the minimum–maximum range set by the uniform stress and uniform deformation assumptions, respectively. By adjusting the parameters ξ and c of the RGC scheme, which are related to the penalty term accounting for incompatibility at the interfaces due to relaxations, it is possible to closely match the benchmark stress–strain response of a high-resolution FE simulation of this cluster. In addition, the RGC scheme is able to approximate the effective lateral strain contractions, as well as the local deformation of individual grains as predicted by FE simulation. This result shows that the present model for the penalty energy is

adequate to mimic the effect of the condition of nodal displacement continuity imposed in the FE simulation.

Table 7.3 compares the CPU-times used for simulating uniaxial tension with various schemes. The computational time used by the RGC scheme strongly depends on the amount of relaxations. The penalty-free RGC model that allows a larger amount of relaxation requires about five times the computational effort of the fully compatible case, where the amount of relaxation is very limited. The best fit RGC scheme runs about five times slower than the Taylor scheme, which is due to the Newton–Raphson procedure to obtain a convergent solution of the force equilibrium condition (equation (7.42)). Nonetheless, the simulations using the RGC scheme are, on average, about three orders of magnitude faster than the benchmark FE method. This shows that the present RGC scheme is able to refine the accuracy of the overall prediction within reasonable bounds of additional computational cost.

Furthermore, the RGC scheme has been used for simulating the texture evolution during cold rolling (reported in Eisenlohr et al. (2009)). Particularly in comparison to different variants of the GIA model, the texture evolution predicted by the RGC scheme comes significantly closer to experimental reference data. Note that the formalism of the RGC scheme used in Eisenlohr et al. (2009) slightly differs from the one outlined here. Nevertheless, it can be concluded that the extension to the finite deformation framework, thus accounting for large strains and rigid-body rotations of grains (which are to be expected in forming operations), is critical to this result.

7.3   Twinning as Additional Deformation Mechanism

In this section we discuss how crystal plasticity models can be extended in the case of additional deformation processes being active besides dislocation slip. In the case of mechanical twinning the active twin systems can be interpreted as additional unidirectional slip systems. The extension of $\boldsymbol{L}_\mathrm{p}$ is then straightforward. However, two main difficulties arise: first, how does the presence of the twins alter the hardening behavior and second, how does the twinned volume fraction evolve. Kalidindi discusses these questions in Kalidindi (1998) for the case when the phenomenological constitutive model presented in section 2.3 is used. In the following we will introduce the extension of a dislocation density based constitutive model. As basis a local version of the non-local model presented in section 4.2 is used. In this context local means that we will not treat any dislocation fluxes. Therefore, there will be no polar dislocation ensembles and internal stresses arising from them. Moreover, only unsigned edge dislocations are discussed in the model.
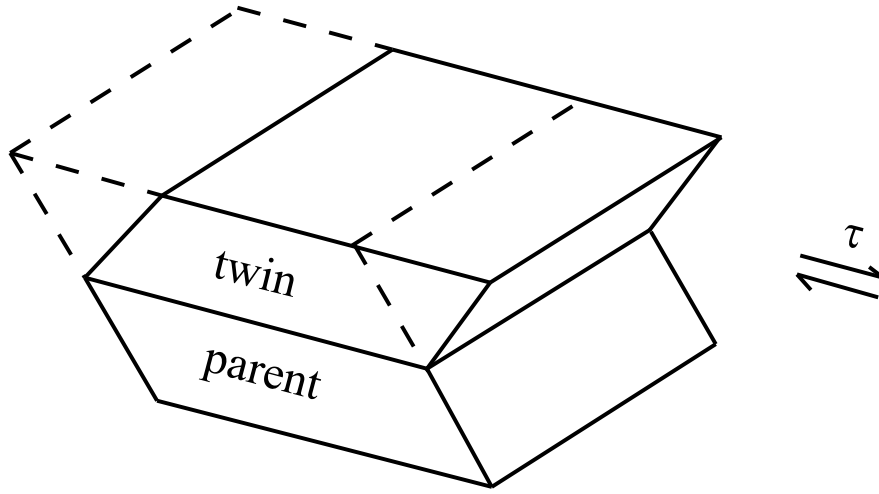
Figure 7.19: Under an applied stress, one half of the initial volume (dashed lines) shears to form a twin (solid lines) (after Hirth and Lothe (1982)).

7.3.1 Microstructural state variables

7.3.1.1 Dislocation Densities

The dislocation structure at the material point is characterized by edge dislocation densities, $\rho^\alpha_{\text{edge}}$, where $\alpha = 1, \ldots, N_{\text{slip}}$ indicates the slip system.

As in section 4.2 the dislocations in dipole configuration are counted separately, $\rho^\alpha_{\text{dipole}}$. Again it holds that dipoles are stable against dissociation by the resolved shear stress τ^α if the mutual elastic interaction between the two constituents is strong enough, *i.e.* if the distance between the glide planes of the two dislocations does not exceed

$$\hat{d}^\alpha_{\text{edge}} = \frac{1}{8\pi} \frac{G\,b}{|\tau^\alpha|} \frac{1}{1-\nu} \; , \tag{7.47}$$

where G is the shear modulus, b the length of the Burgers vector, and ν the Poisson ratio. On the other hand, there exists a minimum glide plane separation, $\check{d}^\alpha_{\text{edge}}$, below which the dipole spontaneously disintegrates.

7.3.1.2 Twinned Volume Fractions

A mechanical twin formally corresponds to a sheared volume for which the lattice orientation is transformed into its mirror image across a so-called *twin* or *composition* or *habitus plane* (central dividing plane in figure 7.19 between parent and twin). A vector of the initial lattice is moved into its new position in the twin through a transformation/rotation matrix $\boldsymbol{Q}$. The same expression for $\boldsymbol{Q}$ was derived for face-centered cubic
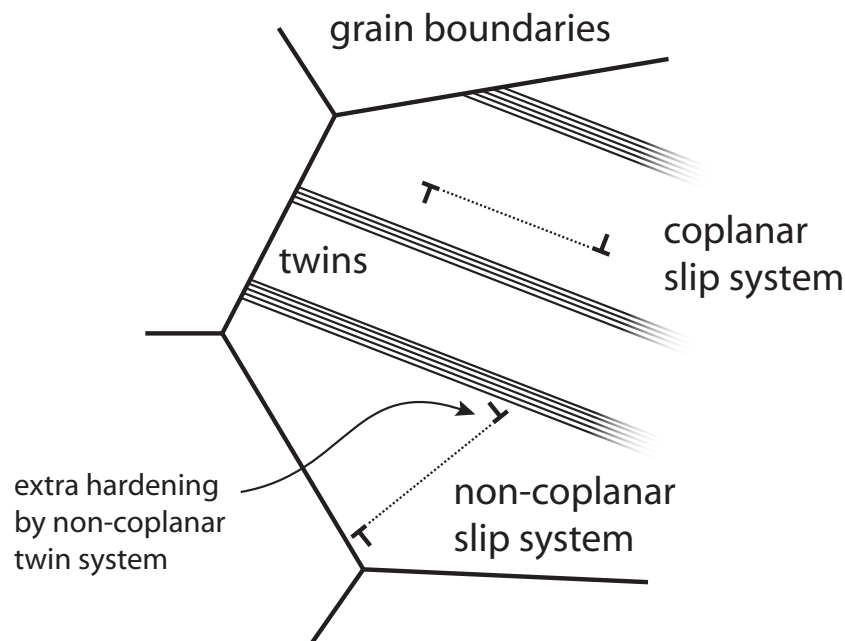
Figure 7.20: Illustration of the selective hardening role of twin boundaries during dislocation motion for fcc structures.

(fcc) and body-centered cubic (bcc) twins (Van Houtte, 1978; Hirth and Lothe, 1982), exploiting the equivalence of rotating half of the crystal by an angle π either around the twin direction or around the twin normal

$$\boldsymbol{Q} = 2\,\boldsymbol{n} \otimes \boldsymbol{n} - \delta_{ij} \,, \tag{7.48}$$

where $\boldsymbol{n}$ is the twin plane unit normal and δ_{ij} Kronecker's symbol.

Similar to the description of the dislocation structure, the twin microstructure is characterized by twin volume fractions, f^{β}, where $\beta = 1, \ldots, N_{\text{twin}}$ indicates the twin system. Here twinning is treated as unidirectional shear on the habitus plane, *i.e.* formally similar to bidirectional dislocation slip. In this framework, fcc twins are of type $\{1\,1\,1\}$ $\langle 1\,1\,2 \rangle$, bcc twins of type $\{1\,1\,2\}$ $\langle 1\,1\,1 \rangle$, and hexagonal twins of type $\{1\,0\,\bar{1}\,2\}$ $\langle 1\,0\,\bar{1}\,1 \rangle$.

7.3.2 Microstructure Evolution

7.3.2.1 Dislocation Multiplication / Athermal Storage

Dislocation multiplication is formally treated in the same way as in section 4.2.2.1, namely as being proportional to the inverse mean free path of the dislocations

$$\mathrm{d}\rho = \frac{|\mathrm{d}\gamma^\alpha|}{b^\alpha \, \lambda^\alpha} \, . \tag{7.49}$$

However, due to the presence of twins in the microstructure the evaluation of λ^α has to account for the twins as additional obstacles to dislocation motion. The mean distance between two twin lamellae on twin system β can be calculated as (Fullman, 1953; Allain et al., 2002)

$$d^\beta_{\mathrm{twin}} = \frac{s^\beta \, (1 - f)}{f^\beta} \, . \tag{7.50}$$

Here f is the total volume of twins, $f = \sum_{\beta=1}^{N_{\mathrm{twin}}} f^\beta$ and s^β the mean thickness of a twin, the latter assumed to be constant in the model. In addition the grain size, d_{grain}, is taken into account as upper limit to the mean free path of the dislocations, so that finally the mean free path can be calculated according to

$$\frac{1}{\lambda^\alpha} = \frac{1}{d_{\mathrm{grain}}} + \frac{\sqrt{\rho^\alpha_{\mathrm{f}}}}{c} + \sum_{\beta=1}^{N_{\mathrm{twin}}} \xi_{\alpha\beta} \frac{1}{d^\beta_{\mathrm{twin}}} \, . \tag{7.51}$$

Here c is a constant of the order 10 to 100 and $\xi_{\alpha\beta}$ is a slip–twin interaction parameter. As can be seen in figure 7.20 not all twins act as obstacles for dislocations on slip system α. Therefore, $\xi_{\alpha\beta}$ evaluates to 0 if planes α and β are coplanar or β is a cross slip plane for α. In all other cases $\xi_{\alpha\beta} = 1$.

7.3.2.2 Dislocations in Dipole Configuration

The evolution of dislocations in dipole configuration is treated analogously to sections 4.2.2.2 and 4.2.2.3.

Formation by glide The transfer rate from single dislocations to dipoles due to gliding can be expressed as:

$$\mathrm{d}\rho^\alpha_{\mathrm{dipole}} = \frac{2 \, \hat{d}^\alpha_{\mathrm{edge}}}{b^\alpha} \rho^\alpha_{\mathrm{edge}} \, |\mathrm{d}\gamma^\alpha| \, , \tag{7.52}$$

where $\hat{d}^\alpha_{\mathrm{edge}}$ is given by equation (7.47).

Athermal annihilation   Out of all dipoles newly formed by glide (equation (7.52)) those that happen to have a glide plane separation below $\check{d}^\alpha_{\text{edge}}$ annihilate instantaneously:

$$\mathrm{d}\rho^\alpha_{\text{edge}} = -\frac{2\,\check{d}^\alpha_{\text{edge}}}{b^\alpha}\rho^\alpha_{\text{edge}}\,|\mathrm{d}\gamma^\alpha|\ . \tag{7.53}$$

In addition to these close encounters among single dislocations, a second athermal annihilation opportunity is due to moving single dislocations knocking out a compatible constituent from an already existing dipole:

$$\mathrm{d}\rho^\alpha_{\text{edge}} = -\frac{2\,\check{d}^\alpha_{\text{edge}}}{b^\alpha}\,\rho^\alpha_{\text{dipole}}\,|\mathrm{d}\gamma^\alpha|\ . \tag{7.54}$$

This process does not alter the overall density of single dislocations since the remaining dipole constituent substitutes for the annihilated single dislocation.

Thermally activated annihilation   The mutual elastic interaction between dipole constituents provides the driving force for their out-of-glide-plane motion. The resulting annihilation rate then reads

$$\dot{\rho}^\alpha_{\text{dipole}} = \rho^\alpha_{\text{dipole}}\frac{2\,v^\alpha_{\text{climb}}}{\left(\hat{d}^\alpha_{\text{edge}} - \check{d}^\alpha_{\text{edge}}\right)/2}\ , \tag{7.55}$$

since all dipoles would be annihilated if half the average dipole separation is overcome by climb with the velocity

$$v^\alpha_{\text{climb}} = \frac{D_0\,\Omega}{b\,k_{\text{B}}T}\exp\left(-\frac{Q_{\text{SD}}}{k_{\text{B}}T}\right)\frac{G\,b}{2\pi(1-\nu)}\frac{2}{\hat{d}^\alpha_{\text{edge}} + \check{d}^\alpha_{\text{edge}}}\ . \tag{7.56}$$

7.3.2.3   Evolution of Twin Volume Fraction

The evolution of the twin volume fraction is the most crucial part of any constitutive model including twinning. This is due to the fact that there is no general agreement on a model for twin nucleation. In this work we adopt the nucleation model of Mahajan and Chin (1973). These authors assume that twin nuclei in fcc materials are formed by the reaction of two coplanar slip dislocations, *e.g.* $\frac{1}{2}\langle 0\,1\,\bar{1}\rangle + \frac{1}{2}\langle 1\,0\,\bar{1}\rangle = 3\times\frac{1}{6}\langle 1\,1\,\bar{2}\rangle$. This reaction leads to a dislocation arrangement as shown in figure 7.21. The critical event for the growth of the nucleus is the correlated bow-out of the three partial dislocations D1–D3 with original length L_0 between the pinning points. The energy change during this process determines, whether or not the twin will grow. This energy change is composed out of three contributions:

1. The plastic work done by the dislocation motion can be calculated as

$$Q_{\text{work}} = -\,3\,b_{\text{S}}\,\tau\,A(r,L_0)\,. \tag{7.57}$$

   Here b_s is the burgers vector of the moving partials, τ is the applied stress and $A(r,L_0)$ is the area swept by the dislocation.
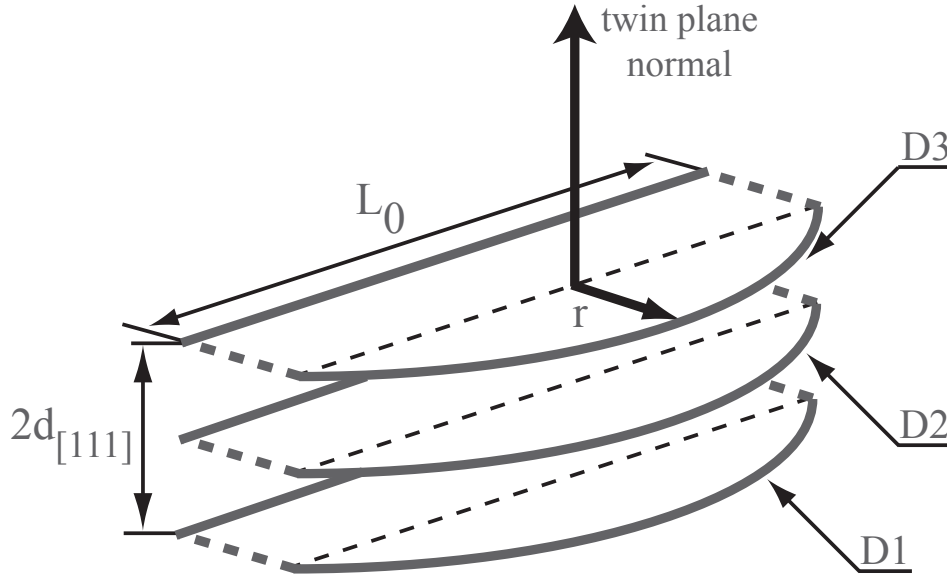
Figure 7.21: Schematic representation of a twin nucleus according to Mahajan and Chin (1973). The correlated bowing out of the three twinning partial dislocations D1, D2, and D3 is the critical event for the growth of the twin.

2. At the same time two twin interfaces are created at the top and the bottom of the twin. Making use of the fact that the stacking fault energy γ_{sf} is approximately twice the twin boundary energy, the energy associated with these interfaces is

$$Q_{sf} = \gamma_{sf} \, A(r, L_0) \, . \tag{7.58}$$

3. Finally, the energy of the three extending dislocation lines has to be provided. In the far field they can be approximated by a super dislocation with Burgers vector $3 \cdot b_S$. Therefore, the associated energy reads

$$Q_{line} = \frac{9}{2} G b_S^2 \, B(r, L_0) \tag{7.59}$$

with $B(r, L_0)$ the additional length due to the the bow-out.

The area function $A(r, L_0)$ and the line length $B(r, L_0)$ are given by

$$A(r, L_0) = \frac{L_0 \, r}{4} - \frac{L_0^3}{16 \, r} + \left(\frac{r^2}{4} + \frac{L_0^4}{64 \, r^2} + \frac{L_0^2}{8} \right) \arcsin \left(\frac{4 \, L_0 \, r}{L_0^2 + 4 \, r^2} \right) \tag{7.60}$$

and

$$B(r, L_0) = \left(r + \frac{L_0^2}{4 \, r} \right) \arcsin \left(\frac{4 \, L_0 \, r}{L_0^2 + 4 \, r^2} \right) - L_0 \tag{7.61}$$

for $r \le L_0/2$ and

$$A(r, L_0) = \frac{L_0 \, r}{4} - \frac{L_0^3}{16 \, r} + \left(\frac{r^2}{4} + \frac{L_0^4}{64 \, r^2} + \frac{L_0^2}{8} \right) \left(\pi - \arcsin \left(\frac{4 \, L_0 \, r}{L_0^2 + 4 \, r^2} \right) \right) \tag{7.62}$$
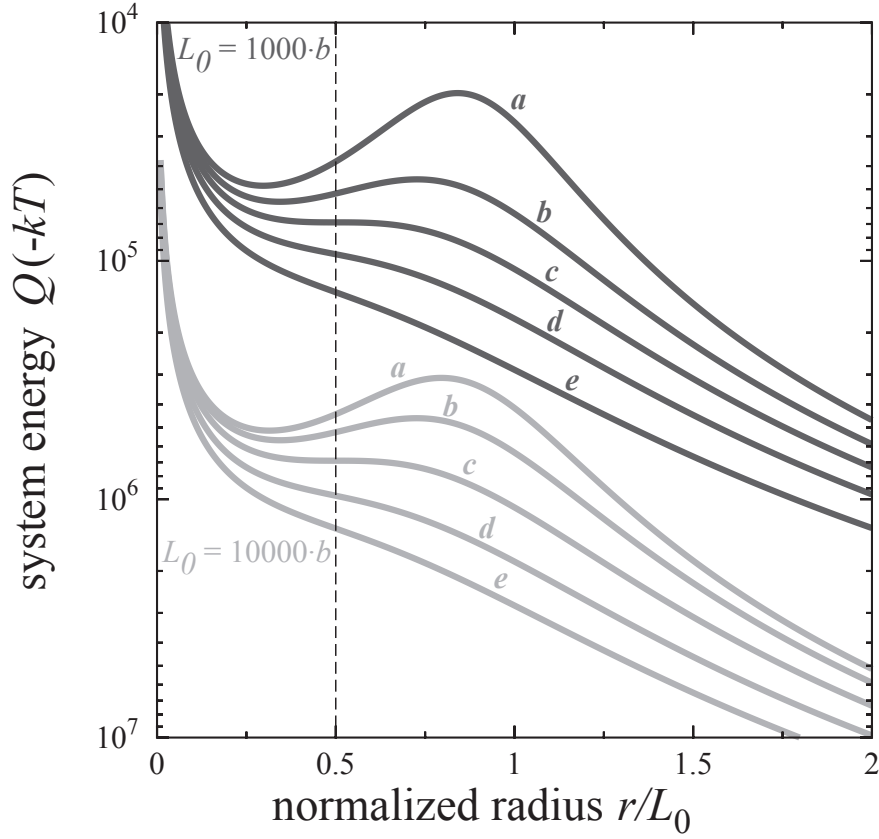
Figure 7.22: Energy associated with the correlated bow-out of the three partial dislocations. Dark gray curves are calculated for $L_0 = 1000b$, light gray curves are obtained for $L_0 = 10000b$, for different applied shear stress levels (see table 7.4).

and

$$B(r, L_0) = \left(r + \frac{L_0^2}{4\,r} \right) \left(\pi - \arcsin \left(\frac{4\,L_0\,r}{L_0^2 + 4\,r^2} \right) \right) - L_0 \qquad (7.63)$$

for $r > L_0/2$, respectively.

Figure 7.22 shows the total energy of the correlated bow-out of the three partial dislocations for different line lengths L_0 and different applied stress levels (table 7.4) as function of the bow-out radius r. It is noteworthy that in any case energy is gained during the bow-out process. However, for low applied stresses (curves a and b), there is a local energy minimum. For high applied stresses (curves d and e) the energy is constantly decreasing and for a particular stress level (curve c) a saddle point is found at $r = L_0/2$. Looking at the energy levels in figure 7.22 any increase in the bow-out energy would be too large to be overcome by thermal activation. We, therefore, define that stress resulting in the curve with the saddle point as critical stress for twin formation. This

Table 7.4: Stress levels applied in figure 7.22

Curve	$L_0 = 1000b$ τ (MPa)	$L_0 = 10000b$ τ (MPa)
a	125	53.3
b	130	53.6
c	136	54.2
d	145	55.2
e	160	56.5

stress can be calculated as

$$\tau_\text{c}^\beta = \frac{\gamma_\text{sf}}{3\,b^\beta} + \frac{3G\,b^\beta}{L_0} \,, \tag{7.64}$$

where we now again use β as index for the twin system, *i.e.* b^β is identical to b_S in equations (7.57) and (7.59).

Using this critical stress the twin nucleation rate can be calculated as

$$\dot{N}^\beta = \dot{N}_0 \, \exp\left[-\left(\frac{\tau_\text{c}^\beta}{\tau^\beta}\right)^r\right] \,, \tag{7.65}$$

where $\dot{N}_0$ and r are fitting constants.

As there is a permanent gain in energy during the bow-out process we assume that the twin grows instantaneously until it encounters some obstacle. Such obstacle could either be a grain boundary or another non-coplanar twin. The volume of the new twin can then be calculated as

$$V^\beta = \frac{\pi}{6}\, s^\beta \, \lambda^{\beta 2} \,, \tag{7.66}$$

here λ^β is the effective distance between obstacles to twin growth and can be calculated as

$$\frac{1}{\lambda^\beta} = \frac{1}{d_\text{grain}} + \sum_{\beta'=1}^{N_\text{twin}} \xi_{\beta\beta'} \, \frac{1}{d_\text{twin}^{\beta'}} \,, \tag{7.67}$$

where the twin-twin interaction parameter $\xi_{\beta\beta'}$ is 0 for coplanar twin systems $\beta\beta'$ and 1 for non-coplanar systems.

7.3.3   Dislocation Kinetics

As in section 4.2.3 it is assumed that the dislocation glide velocity is determined by forest dislocation cutting, however, using a slightly modified version of equation (4.45)

$$v^\alpha = v_0 \, \exp\left[-\frac{Q_0}{k_\text{B}T}\left(1 - \left(\frac{|\tau^\alpha|}{\hat{\tau}^\alpha}\right)^p\right)^q\right] \text{sgn}\,(\tau^\alpha) \tag{7.68}$$

where p and q are numerical parameters to adjust the obstacle profile (Kocks et al., 1975, page 141). The current model was especially developed to model the behavior of so-called TWIP steels. Therefore, the mechanical threshold stress, $\hat{\tau}^{\alpha}$, was extended by a term accounting for the additional friction stress due to the carbon content of the steel:

$$\hat{\tau}^{\alpha} = k_{\text{friction}} G \sqrt{c} + G\, b \left(\sum_{\alpha'=1}^{N_{\text{slip}}} \xi_{\alpha\alpha'} \left(\rho_{\text{edge}}^{\alpha'} + \rho_{\text{dipole}}^{\alpha'} \right) \right)^{0.5} . \tag{7.69}$$

k_{friction} is a fitting parameter and c the carbon content in at %.

The rate of crystallographic shear follows from Orowan's equation:

$$\dot{\gamma}^{\alpha} = \rho^{\alpha}\, b\, v^{\alpha} . \tag{7.70}$$

7.3.4   Shear Rate due to Twinning

As stated before, the process of twinning can be interpreted as shearing the respective volume with the habitus plane as shear plane. The resulting shear for each twin system β can thus be calculated as

$$\dot{\gamma}^{\beta} = \gamma_{\text{twin}}^{\beta} \dot{f}^{\beta} = \gamma_{\text{twin}}^{\beta} \left(1 - f\right) V^{\beta} \dot{N}^{\beta} \tag{7.71}$$

here $\gamma_{\text{twin}}^{\beta}$ is the characteristic twin shear.[8]

7.3.5   A Modified CPFE Framework Including Deformation Twinning

The CPFE framework discussed in this section follows the outline introduced in chapter 2.2. However, adding mechanical twinning as a possible plastic shear mode requires introduction of some additional model ingredients. The activation of a twin system β implies that a fraction $\mathrm{d}f^{\beta}$ of the single crystalline parent volume (matrix) reorients by $\boldsymbol{Q}^{\beta}$. Figure 7.23 illustrates the decomposition of the global deformation gradient $\boldsymbol{F}$ when a twin system operates. Considering the formal similarity between slip and mechanical twinning, the velocity gradient $\boldsymbol{L}_{\text{p}}$ is extended by the contribution due to twinning to read

$$\boldsymbol{L}_{\text{p}} = \left(1 - \sum_{\beta=1}^{N_{\text{twin}}} f^{\beta} \right) \sum_{\alpha=1}^{N_{\text{slip}}} \dot{\gamma}^{\alpha}\, \boldsymbol{m}^{\alpha} \otimes \boldsymbol{n}^{\alpha} + \sum_{\beta=1}^{N_{\text{twin}}} \dot{\gamma}^{\beta}\, \boldsymbol{m}_{\text{twin}}^{\beta} \otimes \boldsymbol{n}_{\text{twin}}^{\beta} , \tag{7.72}$$

where N_{slip} is the number of slip systems and N_{twin} the number of twin systems. It should be noted that the present description does not explicitly account for the morphology and topology of the deformation twins. Instead a twinned region is specified by its volume

---

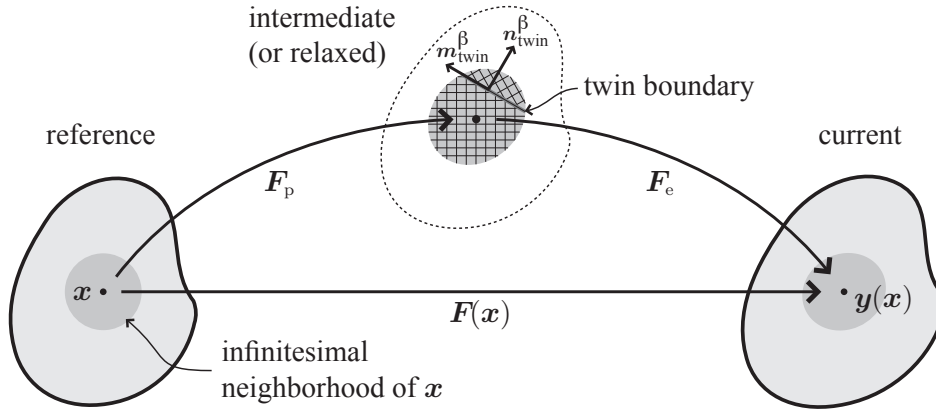[8] $\sqrt{2}/2$ for fcc and bcc crystal structures.

Figure 7.23: Schematic representation of the three configurations and the corresponding decomposition of the deformation gradient $\boldsymbol{F}$ into elastic and plastic contributions, modified by Kalidindi (1998, 2001) to account for mechanical twinning.

fraction only. The Cauchy stress $\bar{\boldsymbol{\sigma}}$ of the composite (matrix plus twins) is related to the volume average of the stress over all constituents

$$\bar{\boldsymbol{\sigma}} = \frac{\boldsymbol{F}_{\mathrm{e}}}{J^{\mathrm{e}}} \left[\left(1 - \sum_{\beta=1}^{N_{\mathrm{twin}}} f^{\beta} \right) \mathbb{C} + \sum_{\beta=1}^{N_{\mathrm{twin}}} f^{\beta} \mathbb{C}^{\beta} \right] \boldsymbol{E}_{\mathrm{e}} \, \boldsymbol{F}_{\mathrm{e}}^{\mathrm{T}} \,, \tag{7.73}$$

where $\mathbb{C}_{ijkl}^{\beta} = Q_{im}^{\beta} Q_{jn}^{\beta} Q_{ko}^{\beta} Q_{lp}^{\beta} \mathbb{C}_{mnop}$ is the elasticity tensor of the matrix rotated into the respective twin orientation and $\boldsymbol{E}_{\mathrm{e}}$ Green's Lagrangian strain derived from the non-plastic deformation gradient $\boldsymbol{F}_{\mathrm{e}}$. It is worth noting that a small homogenization error may occur when following this procedure, which is due to the generation of an orientation dispersion in the twinned fraction. This deviation occurs whenever the plastic spin of a twin variant is not equal to the plastic spin of the matrix. In the current approach this does indeed happen as no plastic velocity gradient is given in the twinned regions.

The present expression for $\boldsymbol{L}_{\mathrm{p}}$ does not consider subsequent dislocation slip within twins. This approximation is often suitable for extremely thin fcc and bcc twins. However, experimental evidence for dislocation activity in mechanical twins has been reported when twins are larger, *e.g.* in high-manganese TWIP steels Meng et al. (2007) (due to large strains) and in hexagonal metals (Mg, Zr due to small twin shear). It may, therefore, be useful to allow for dislocation slip in twinned regions. In that case, Kalidindi (2001) proposed to modify the plastic velocity gradient as follows

$$\boldsymbol{L}_{\mathrm{p}} = \left(1 - \sum_{\beta=1}^{N_{\mathrm{twin}}} f^{\beta} \right) \sum_{\alpha=1}^{N_{\mathrm{slip}}} \dot{\gamma}^{\alpha} \, \boldsymbol{m}^{\alpha} \otimes \boldsymbol{n}^{\alpha} + \sum_{\beta=1}^{N_{\mathrm{twin}}} \gamma_{\mathrm{twin}} \dot{f}^{\beta} \, \boldsymbol{m}_{\mathrm{twin}}^{\beta} \otimes \boldsymbol{n}_{\mathrm{twin}}^{\beta} +$$

$$\sum_{\beta=1}^{N_{\mathrm{twin}}} \sum_{\alpha=1}^{N_{\mathrm{slip}}} f^{\beta} \dot{\gamma}^{\beta,\alpha} Q^{\beta} \boldsymbol{m}^{\alpha} \otimes \boldsymbol{n}^{\alpha} Q^{\beta \mathrm{T}} \,. \tag{7.74}$$

Furthermore, the twinning of primary twins (secondary twinning) might be considered as well. At first view, the modification of $\boldsymbol{L}_\mathrm{p}$ appears rather straightforward. However, difficulties arise from the increase in the number of shear rates and/or twin volume fractions that have to be tracked in this approach, rendering such model highly impractical.

Chapter 8

Large Scale Application Examples

Four different examples of the application of CPFEM at large scales, *i.e.* at the component scale, are presented. This kind of simulation relies on a precise representation of the crystallographic texture and an appropriate homogenization scheme at the material point level.

Deep drawing is a standard material test for the characterization of the planar material anisotropy. Here both aspects, texture discretization and material point homogenization, can be nicely studied as earing profiles and drawing forces resulting from the simulations can be easily compared with experimentally obtained ones.

Lankford values are another important measure for the anisotropy of sheet material. However, the experimental evaluation is rather demanding. Therefore simulations can be used to replace the experiment, this is also one application of the so-called virtual laboratory discussed later.

Stress–strain curves are still the most important measure for the characterization of the mechanical properties of a material. In tabulated form they can *e.g.* serve for characterizing the hardening behavior in FE simulations.

The virtual laboratory, *i.e.* simulations using Representative Volume Elements (RVE), can be used to determine almost any mechanical property.

8.1   Simulation of Deep Drawing

In this section, four application examples of the CPFEM to deep drawing are presented. The first example is a 3104 aluminum alloy, where deep drawing of hot and cold band is studied. The second example shows how through-thickness texture gradients can be taken into account on the example of a ferritic 17 %Cr (X6Cr17, AISI 430) stainless steel. The third example demonstrates how CPFEM simulations can be used for optimizing the earing behavior during cup drawing. Finally, the fourth example shows the determination of drawing forces in case of a dual phase steel.

Table 8.1: Texture components used for fitting the texture of AA3104 hot band (Helming et al., 1994; Helming, 1996; Raabe and Roters, 2004). Orthotropic sample symmetry has been taken into account.

Euler angles (°)			scatter (°)	intensity
φ_1	ϕ	φ_2	b^c	I^c
197.9	6.5	245.0	15.2	0.29
random			-	0.71
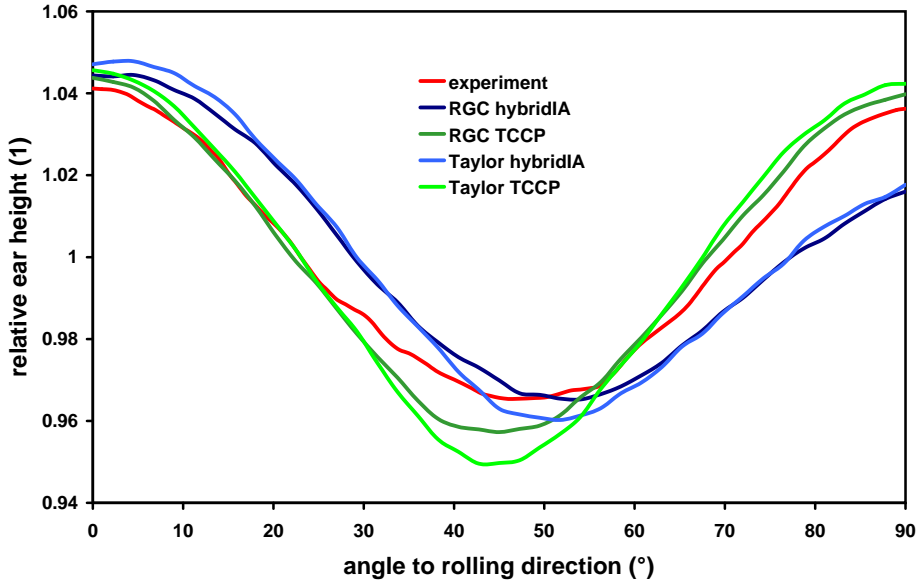
Figure 8.1: Experimental and simulated earing profiles for AA3104 hot band.

8.1.1   Earing Behavior of AA3104 Hot and Cold Band

The simulations in this section compare different texture discretization and material point homogenization schemes as introduced in the preceding chapters. Four simulations are carried out for both AA3104 hot and cold band. Two simulations use the hybridIA scheme introduced in section 7.1.2 to sample orientations directly from the ODF data while the two others use a texture component representation (section 7.1.1) of the texture for the generation of the single orientations. The texture components used are specified in tables 8.1 and 8.2. It should be noted that the assignment of the individual orientations to the integration points is done in a different way than in earlier publications (Roters, 2003, 2004). In those simulations components were used per integration point, *i.e.* for the hot band each integration point was assigned four orientations from the one gauss component (obeying the orthotropic sample symmetry) plus one for the random component. In contrast, in the simulations shown here, each integration

Table 8.2: Texture components used for fitting the texture of AA3104 cold band (Helming et al., 1994; Helming, 1996; Raabe and Roters, 2004). Orthotropic sample symmetry has been taken into account.

Euler angles (°)			scatter (°)	intensity
φ_1	ϕ	φ_2	b^c	I^c
141.1	37.5	10.6	16.8	0.38
108.9	29.3	34.2	14.5	0.30
random			-	0.32
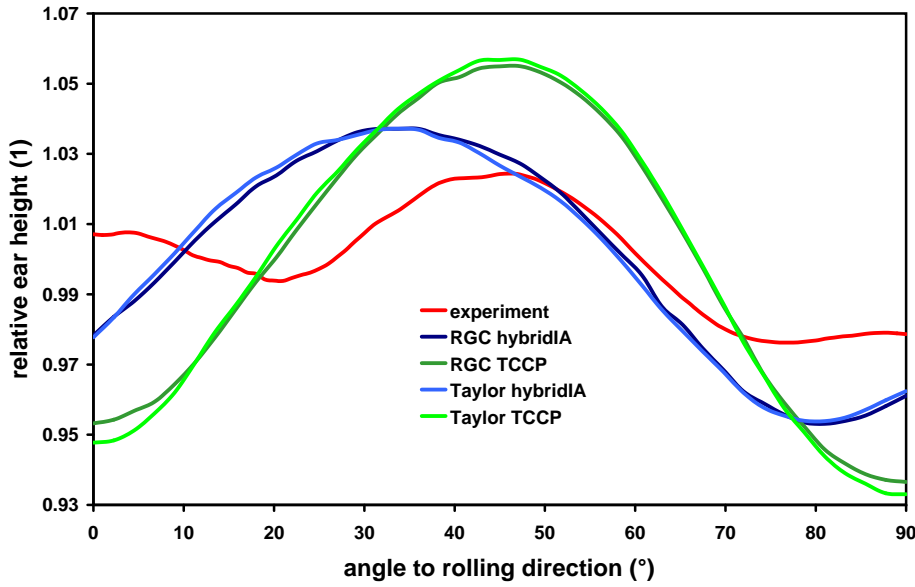
Figure 8.2: Experimental and simulated earing profiles for AA3104 cold band.

point was randomly assigned eight orientations from a set of 201600 orientations (eight times the number of integration points used in the model), which was either created using the hybridIA scheme or sampled from the texture components. In both cases sample symmetry was taken into account. Material point homogenization was achieved once using the Taylor assumption (equal deformation gradient for each grain at one integration point) and once using the RGC scheme introduced in section 7.2.3.

The resulting earing profiles are shown in figures 8.1 and 8.2 together with the experimentally measured earing profiles in terms of the relative ear height (normalized by the average height). It can be clearly seen that in both cases the result depends much more on the texture discretization than on the homogenization scheme used. One explanation for this is the fact that the texture evolution is not very pronounced during deep drawing, therefore, one does not expect large differences in the predictions for the two schemes. For the hot band both discretization schemes perform about equally good.

Figure 8.3: Mapping of the through-thickness texture gradient in the FE-mesh of the blank.

While the use of texture components result in a too low minimum, the hybridIA scheme underestimates the height of the 90° ear. For both schemes the position of the minimum is slightly shifted, however, in opposite directions. In case of the cold band both schemes perform less good, however, with a clear advantage for the hybridIA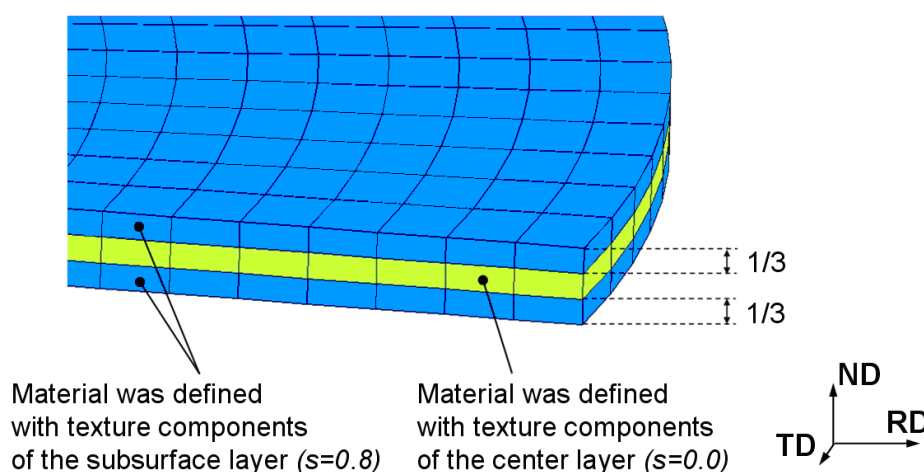 scheme. In this case a general drawback of the texture component method is clearly observable, namely the tendency to overestimate the overall anisotropy. This is less obvious for the hot band due to the large random fraction in that texture.

8.1.2 Effect of Texture Gradients on Earing Behavior of X6Cr17

The deep drawing simulation in this section includes the through-thickness texture gradient of the starting hot band of a ferritic 17 %Cr (X6Cr17, AISI 430) stainless steel (Raabe and Lücke, 1993; Fedosseev and Raabe, 1994). In the simulation this is achieved by using three elements to mesh the blank thickness. For taking the texture gradient into account different texture components are assigned to the center element layer than to the outer ones (figure 8.3). For simulations without through-thickness gradient the same set of components is assigned to all three element layers. Table 8.3 shows the two sets of texture components for the center layer ($s = 0$) and the subsurface layer ($s = 0.8$). The simulation considers $\{1\,1\,0\}\langle1\,1\,1\rangle$, $\{1\,1\,2\}\langle1\,1\,1\rangle$, and $\{1\,2\,3\}\langle1\,1\,1\rangle$ slip systems (Raabe, 1995). Besides the experiment, the results are compared to another FE simulation based on a Hill48 yield surface (Hill, 1948) calibrated using experimental r-values ($r_0 = 1.387, r_{45} = 0.817, r_{90} = 0.92$).

Figure 8.4 shows the predicted and the measured earing profiles. The ear profile predicted by the simulation with the texture components of only the center layer ($s = 0.0$)

Table 8.3: Texture components used for fitting the texture of ferritic 17 %Cr (X6Cr17, AISI 430) stainless steel (also see section 7.1.1).

position	Euler angles (°)			scatter (°)	intensity
	φ_1	ϕ	φ_2	b^c	I^c
center, $s = 0$					
	257.6	119.9	122.9	16.8	0.1684
	238.9	83.1	81.6	20.1	0.1436
	47.4	133.1	52.9	19.1	0.1176
	137.0	62.0	32.6	15.3	0.0996
	209.7	72.7	68.7	11.4	0.0420
	125.5	57.2	44.0	16.5	0.0100
	random			-	0.4188
subsurface, $s = 0.8$					
	262.3	96.9	20.6	20.9	0.2452
	251.0	59.0	42.1	21.7	0.2224
	121.7	84.6	6.2	16.0	0.1136
	218.1	113.9	28.0	13.5	0.0820
	155.1	45.5	42.3	13.0	0.0736
	231.0	55.6	51.4	7.2	0.0104
	random			-	0.2528
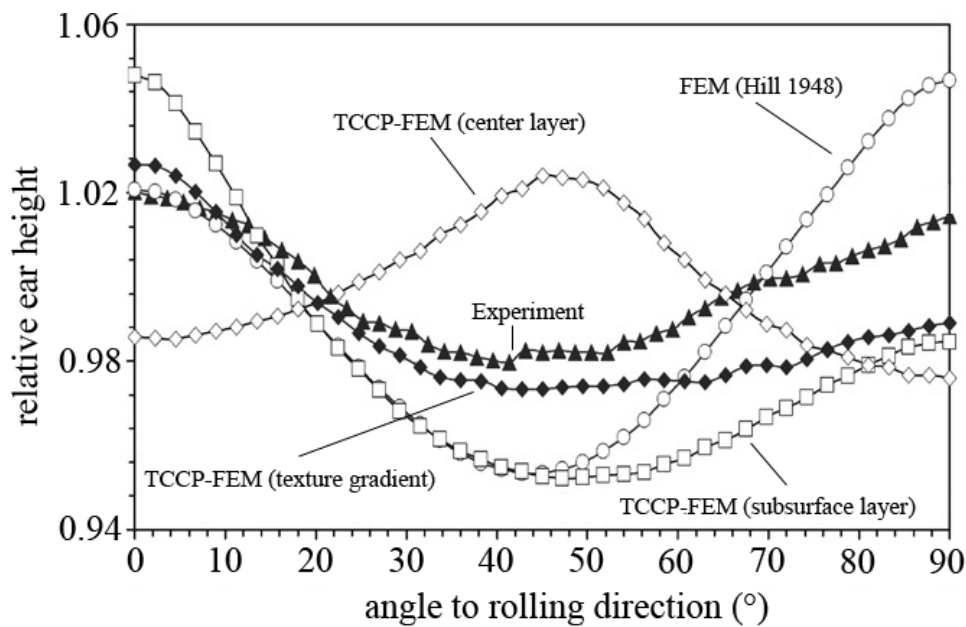
Figure 8.4: Experimental and simulated earing profiles for ferritic 17 %Cr (X6Cr17, AISI 430) stainless steel.

reveals a shape with a broad *maximum* around 45°. On the other hand, the profile simulated with the texture of only the sub-surface layer ($s = 0.8$) is characterized by a broad *minimum* in the same region (45°). The reason for this difference is that the texture components fitted from each respective layer of the material reproduced different initial textures and, consequently, different anisotropy. The course of the ear profile calculated by using only the texture components of the sub-surface layer, $s = 0.8$, can be presumably explained by the influence of the relatively weak intensity of the $\{1\,1\,1\}\langle1\,1\,2\rangle$ component of the starting texture in this layer. The high orientation density of the $\{1\,1\,1\}\langle1\,1\,2\rangle$ texture component in the initial texture of the center layer ($s = 0.0$) is responsible for the ear shape with the strong peak at 45° observed for the simulation that was performed by using the texture components of this layer. The results also show that the texture component CPFE simulation that used the gradient texture (1/3 of the through-thickness volume occupied by the center layer texture ($s = 0.0$) and 2/3 of the volume occupied by the sub-surface layer texture ($s = 0.8$) where 1/3 accounts for the bottom and 1/3 for the top surface region, respectively) fits the experimental data better than that obtained from the Hill48 yield surface prediction.

8.1.3　Optimization of Earing Behavior

In the early industrial practice, texture was regarded as a property of polycrystals that was simply inherited from the preceding processing steps without conducting particular anisotropy optimization. This means that textures were known as an inevitable side-effect of materials processing, which was hard to avoid and often accepted as it was. In contrast, modern industrial process design gradually aims at optimizing microstructures and properties during production, *i.e.* its goal consists in considering metallurgical mechanisms such as crystal plasticity, recrystallization, grain growth, and phase transformation for the design of well-tailored crystallographic textures with respect to certain desired anisotropy properties of the final product.

The most recent phase in the advancement of quantitative texture and anisotropy engineering consists in the introduction of inverse texture simulation methods. Such approaches are designed for the physically based tailoring of optimum textures for final products under consideration of prescribed processing and materials conditions on an inverse basis. This means that variational texture optimization can nowadays be conducted in a way to match some desired final anisotropy and can help to identify beneficial corresponding processing parameters. This amounts to a tenet change in the sense that the process should no longer determine the textures but the desired textures should determine the process.

As shown in the previous section, elastic-plastic anisotropy during deep drawing may entail earing. One important consequence of that is—besides the irregular shape of the drawn specimen—an inhomogeneous distribution of the mechanical properties and of the wall thickness due to volume conservation and the kinematically necessary strain rate variation. The trivial solution for the control and minimization of earing would
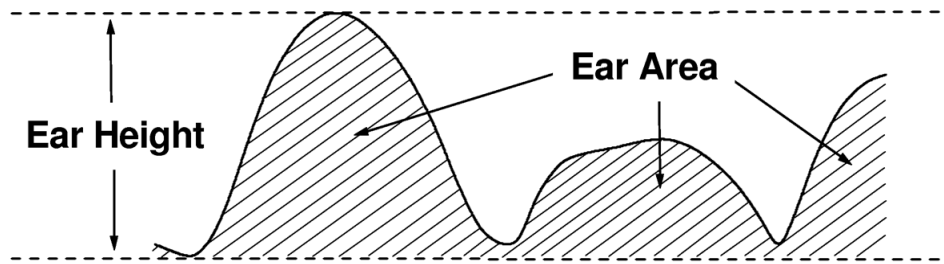
Figure 8.5: Earing is quantified in terms of the ear height and the ear area. The ear height describes the difference between the highest point on the rim and the lowest point on the profile of the drawn cup. The ear area integrates the entire surface between these two extremal values.

be the presence of a random crystallographic texture prior to loading. However, such a supposed obvious approach is prevented due to two reasons. First, random starting textures do generally not remain random when the material is plastically deformed. This applies in particular to sheet forming operations. Second, complete spherical and spatial randomization of textures is very difficult. Most metallurgical and mechanical processes promote rather than reduce orientation distributions. This applies in particular to most face-centered cubic (fcc) metals, in particular to those without bulk phase transformation during forming such as aluminum.

Therefore, a more practical approach for reducing shape anisotropy lies in combining the texture components constituting the initial sheet in such a way that the resulting ear profile—accounting also for texture changes during forming—can be minimized owing to the mutual compensation of the shape anisotropy contributions introduced by the individual texture components during forming.

As example, a combination of S ($\varphi_1 = 50°, \phi = 35°, \varphi_2 = 70°$) and Cube ($\varphi_1 = 0°, \phi = 0°, \varphi_2 = 0°$) texture components for aluminum, which are typical rolling and annealing components of this material and produce opposite earing, are chosen. Ear profiles were computed for different combinations of the two components. The aim of this simulation series is the prediction of the optimum texture composition for minimum earing. Earing is quantified in terms of the ear height and ear area (figure 8.5). The ear height describes the difference between the highest and the lowest point on the profile of the drawn cup. The ear area integrates the entire surface between these two extremal values.

Figure 8.6 shows the influence of a mixture of the S and the Cube texture components on the shape after cup drawing. The simulation results present the ear profiles for different ratios of the volume fractions of the two texture components. Figure 8.6a shows that an optimum profile is obtained for a combination of 62.75 vol % of the S component and 37.25 vol % of the Cube component in case that the orientational scatter width amounts to 0° prior to elastic-plastic loading (combination of two originally perfect single crystals). Figure 8.6b reveals that this result applies for both, the ear height and the ear area. Figure 8.6b also substantiates that the dependence of earing in terms of height
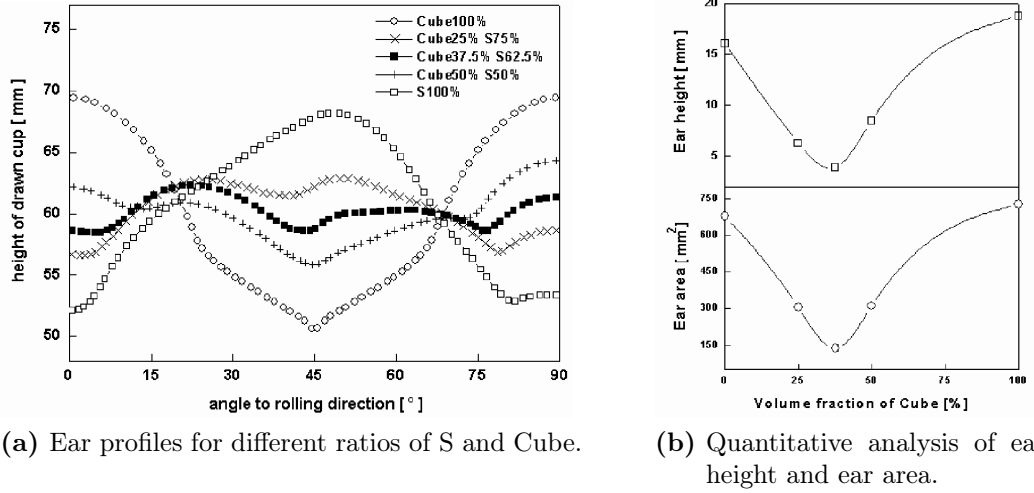
(a) Ear profiles for different ratios of S and Cube.

(b) Quantitative analysis of ear height and ear area.

Figure 8.6: Minimization of ear formation by mixing the S and Cube texture components. The simulation results show that the ear behavior can be minimized by mixing S and Cube texture components at an optimum ratio of about 62.75 vol % / 37.25 vol % (S/Cube).

and area on the texture composition reveals a steep change in the vicinity of the earing minimum, *i.e.* small modifications in the ratio of the volumes of the two texture components entail a strong change in earing. This means that even minor texture changes can lead to a remarkable optimization or degradation of the ear profile. It is important to note in this context that the ideal components with 0° orientation scatter width, which characterize the starting texture, develop during the simulation into an array of similar orientations each of which may undergo individual reorientations according to the local boundary conditions. It is the special advantage of the (texture component) crystal plasticity finite element method to take these individual local reorientation- and strain-paths properly into account.

It is of some interest in this context to observe that the optimum volume ratio between the S orientation and the Cube orientation amounts to about 1.67:1 (62.75 vol % : 37.25 vol %) rather than to 1:1. The initial assumption that an optimum ratio between the two texture components might amount to 1:1 was suggested by figure 8.6a, which shows that the ear profiles created by the S or the Cube component alone are opposite indicating the possibility of mutual compensation. The fact that 1.67:1 and not 1:1 is the optimum ratio underlines that the interaction of different texture components is highly non-linear. It is also important to learn from this ratio that the volume fraction of the S component must obviously be much larger than that of the Cube component in order to compensate the anisotropy. This means that the Cube orientation has a much larger effect on the overall anisotropy during deep drawing than the S orientation.

8.1.4   Cup Drawing of Dual Phase Steel

The key problem in simulating dual phase steels on a component scale is that the two phases can, from a practical point of view, not be spatially resolved in the FE model[1], *i.e.* the homogenization scheme has to correctly predict the behavior of the phase mixture based on the single phase properties. The classical isostrain (Taylor) homogenization scheme (section 7.2.1) is not capable of doing this as the assumption of equal deformation in both phases always leads to a too stiff response of the dual phase material. However, the newly developed Relaxed Grain Cluster (RGC) scheme (section 7.2.3) is able to handle multi-phase materials. Therefore, in this section we first present the fitting procedure for the material model and then perform a cup drawing simulation.

8.1.4.1   Fitting Procedure for Material Model Parameters

The parameter fitting is done in a two step procedure. First the constitutive parameters are adopted for the two phases (figure 8.7). To do this an analytical shear stress–shear curve is calculated using the phenomenological viscoplastic model presented in section 2.3, which is then transformed into the macroscopic stress–strain curve with the help of the Taylor factor. As the materials show an almost random texture a Taylor factor of 2.73 is used, which is applicable for body-centered cubic materials with random texture under tensile deformation (Rosenberg and Piehler, 1971). The resulting parameters are listed in table 8.4 and the corresponding curves are shown in figure 8.7. Then, in a second step, the RGC parameters are adopted to correctly describe the stress–strain curve of the dual phase steel with a martensite fraction of 14 %. Figure 8.8 shows that the dual phase stress–strain curve lies in the range covered by the RGC homogenization scheme and that a suitable parameter set can be found (table 8.5). The figure also shows that the stress-strain curve obtained using the Taylor homogenization scheme overestimates the material stiffness significantly.

8.1.4.2   Cup Drawing Simulation

The focus of the cup drawing simulation is put on the drawing force as due to the almost random texture no significant earing is present. Only a quarter of the sheet is modeled in the simulation due to symmetry. The mesh is shown in figure 8.9. There are only two elements used over the sheet thickness, which is too little for a correct bending stiffness prediction, however, was chosen to save computation time. All in all, 2850 hexahedral elements with linear shape function and full integration are used. The tools are modeled as rigid surfaces and a friction coefficient of 0.04 is used. The full FE model is shown in figure 8.10. Simulations are performed using a random starting texture. Each integration point was assigned eight grains. As homogenization scheme the Taylor

---

[1]Theoretically this is always possible by infinitesimal mesh refinement but it is computationally way too expensive for practical application.
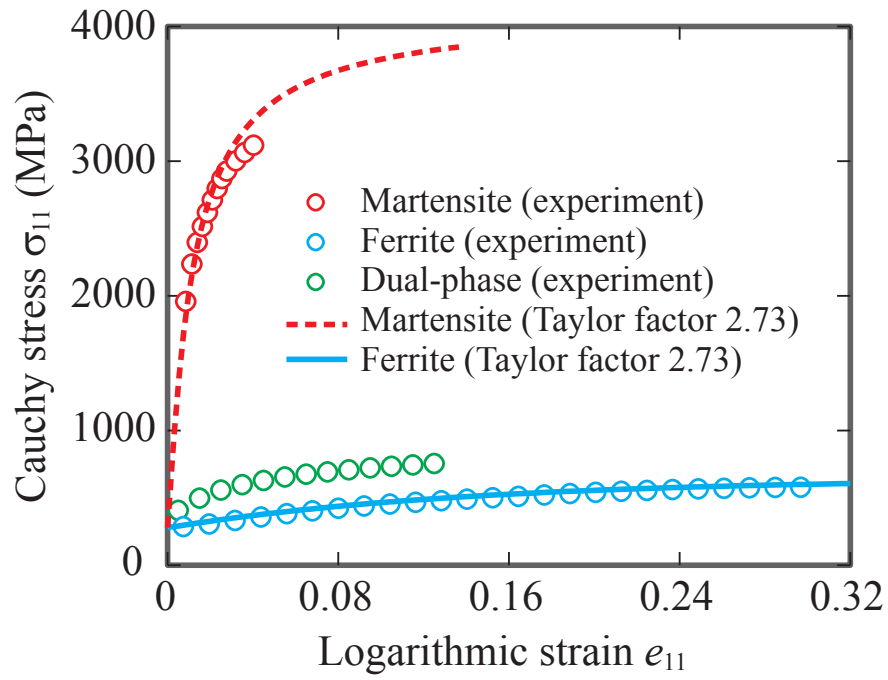
Figure 8.7: Comparison of single phase stress–strain curves. Material parameters for both phases are given in table 8.4
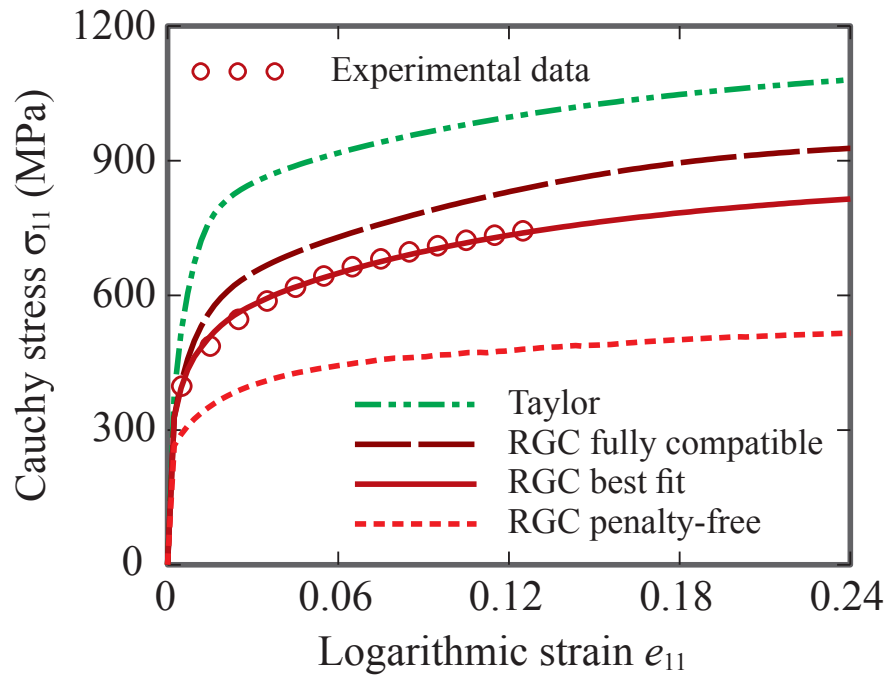

Figure 8.8: Resulting stress–strain curves for the dual phase steel with a martensite fraction of 14 % using different homogenization assumptions.

Table 8.4: Hardening parameters derived from calibration of the single phase materials.

Parameter	Ferrite	Martensite
τ_0 (MPa)	100	702
τ_s (MPa)	235	1510
h_0 (MPa)	610	56300
a	1	2
q	1	1

Table 8.5: RGC parameters used for the dual phase steel stress–strain curves.

Parameter	fully compatible	penalty-free	best fit
c	1000	0.1	2
ξ	1000	0.1	13
$d_1(\mu\text{m})$	4	4	4
$d_2(\mu\text{m})$	4	4	4
$d_3(\mu\text{m})$	2	2	2

scheme was used as well as the RGC scheme in the fully compatible and the penalty-free mode. For the RGC scheme $2 \times 2 \times 2$ clusters with a random cluster orientation were used. The material parameters for martensite were in both cases randomly assigned to 14 % of the grains while the other grains used the ferrite parameters.

Figure 8.11 shows the results for the cup height. Both the Taylor scheme and the fully compatible version of the RGC predict the cup height about correct, while the penalty free RGC clearly overestimates the cup height due to the too soft material response. As expected, no pronounced earing is visible both in the experiment as well as in the simulations. Based on this result only, the Taylor scheme seems superior as the computation times using the RGC are up to one order of magnitude higher than for the Taylor scheme (see section 7.2.3). However, the situation changes when looking at the punch force shown in figure 8.12. As stated above the use of only two elements over the sheet thickness actually results in a too stiff bending behavior of the sheet. Using more elements would therefore somewhat reduce the punch force in all simulation cases. Even taking this into account the Taylor scheme clearly overestimates the experimentally measured punch force, which, however, lies within the range covered by the RGC scheme. Consequently, as for the stress–strain curve an optimum RGC parameter set could be found for correctly predicting the punch force, which is an important process parameter in sheet metal forming.
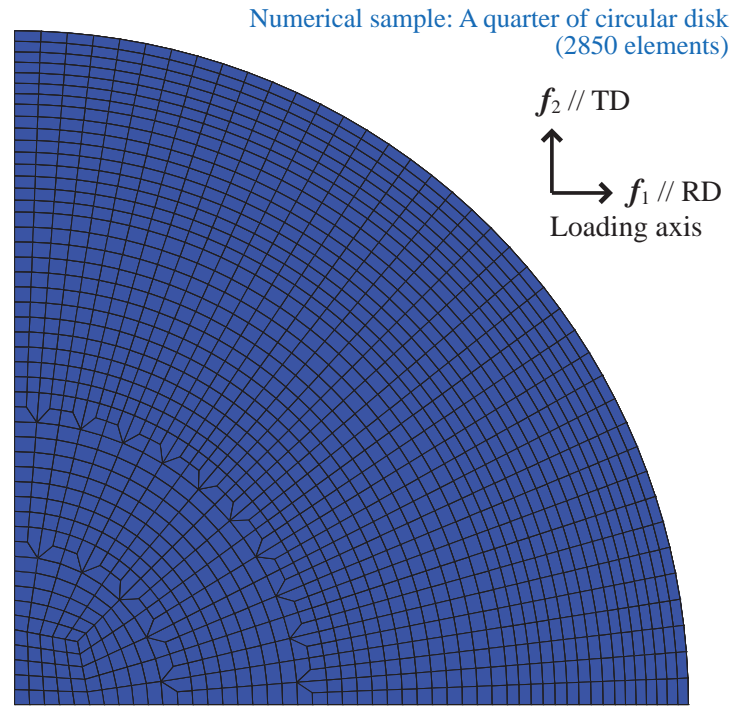
Figure 8.9: FE mesh used for modeling the sheet. There are two elements over the sheet thickness resulting in a total number of 2850 hexahedral elements.
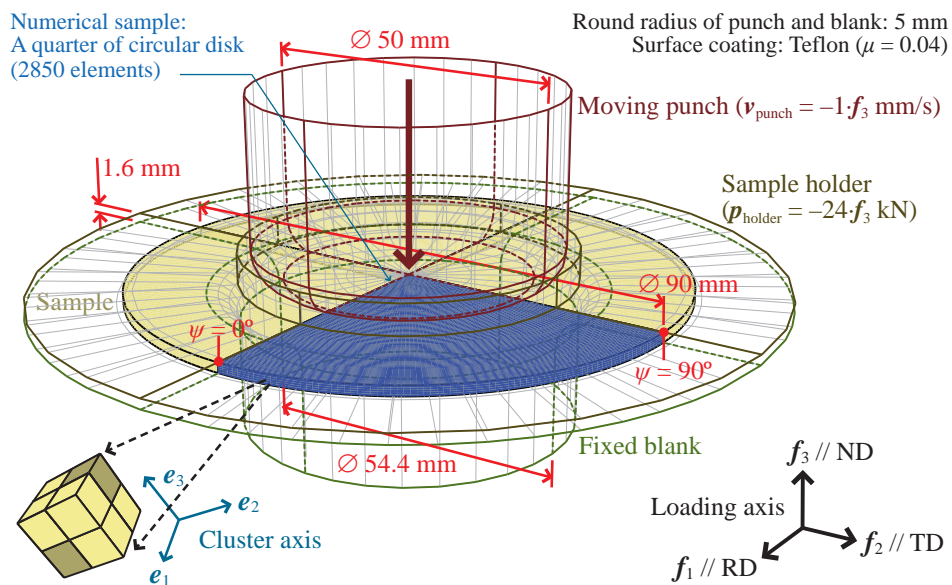
Figure 8.10: Model setup for the cup drawing simulations.
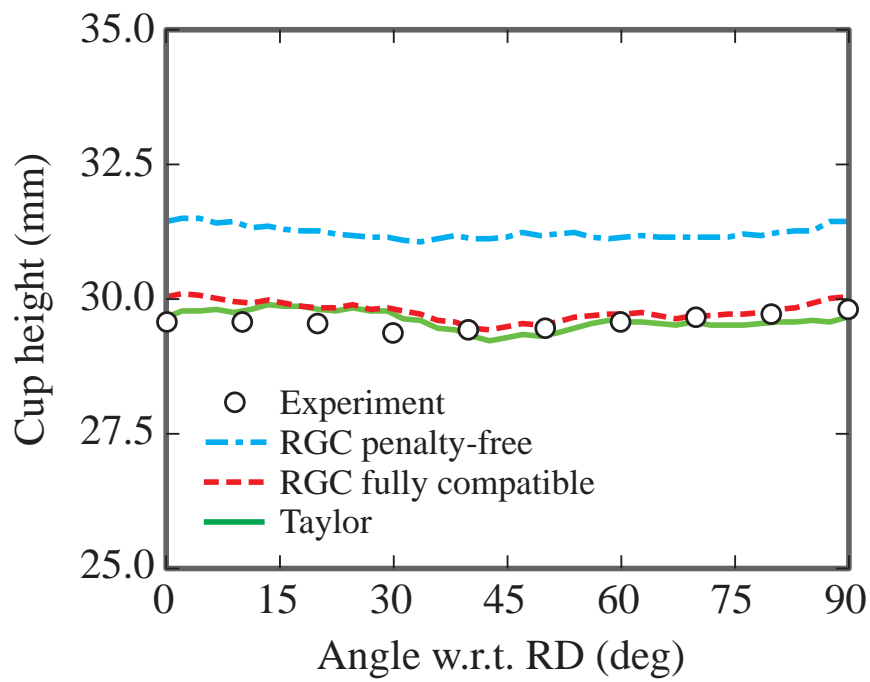
Figure 8.11: Experimental and simulated cup height.
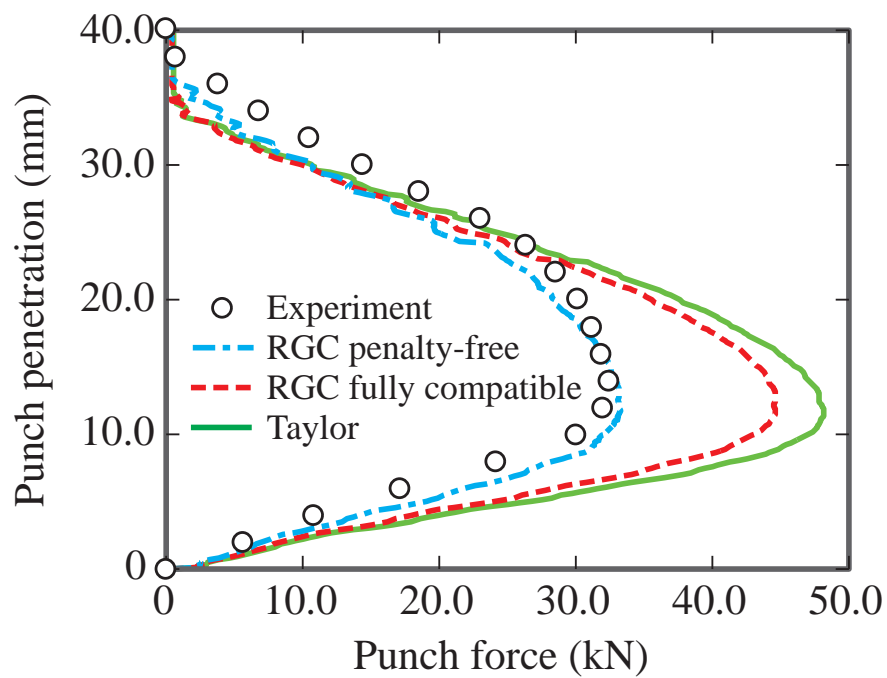
Figure 8.12: Experimental and simulated punch force.
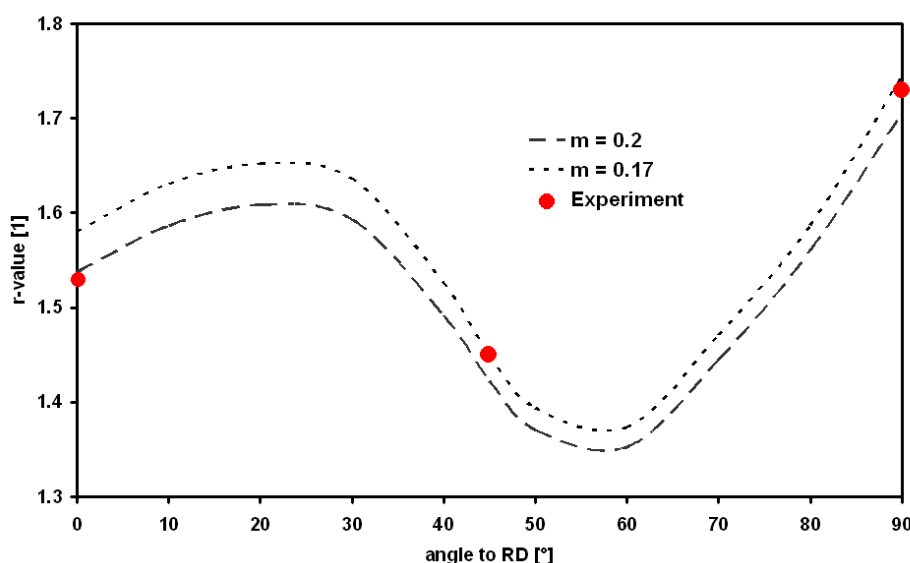
Figure 8.13: Comparison of simulated (lines) and experimental (symbols) values of the r-value for a DC04 deep drawing steel at 20 % strain. The two curves show results for different values of the strain rate sensitivity m (see equation (2.6)).

8.2 Lankford (R-) Value Simulation

The Lankford value (also referred to as r-value), *i.e.* the ratio of strains ϵ_{22} and ϵ_{33} for a tensile test in 1 direction, is an important measure for the in-plane anisotropy of sheet materials. It is also required for the calibration of anisotropic yield models, *e.g.* the frequently used Hill 48 model (Hill, 1948). Experimentally, the r-value is usually measured for three directions only, namely for 0°, 45° and 90° with respect to the rolling direction. Starting with an experimentally measured texture, the CPFEM approach can be used to predict r-values for any angle by simply rotating the initial texture by the respective angle. As the material orientation is specified by Euler angles the angle between rolling direction and tensile direction can be easily adopted by modifying angle φ_1. Moreover such predictions do not only provide the r-value(s) for a given strain (in engineering applications the r-value is measured at 20 % strain) but also yield information on the development of the r-value as a function of strain.

In the simulation the r-value is then determined as the ratio of ϵ_{22} and ϵ_{33} for the center node of the mesh. Figure 8.13 shows a comparison of simulated and experimental values of the r-value for a low-carbon automotive deep drawing steel (DC04). While there are only three experimental points available, the r-value was simulated in steps of 5°. It should be mentioned that the specified strain rate sensitivities are those of the individual slip systems and need not necessarily coincide with the macroscopic strain rate sensitivity value of the sheet.
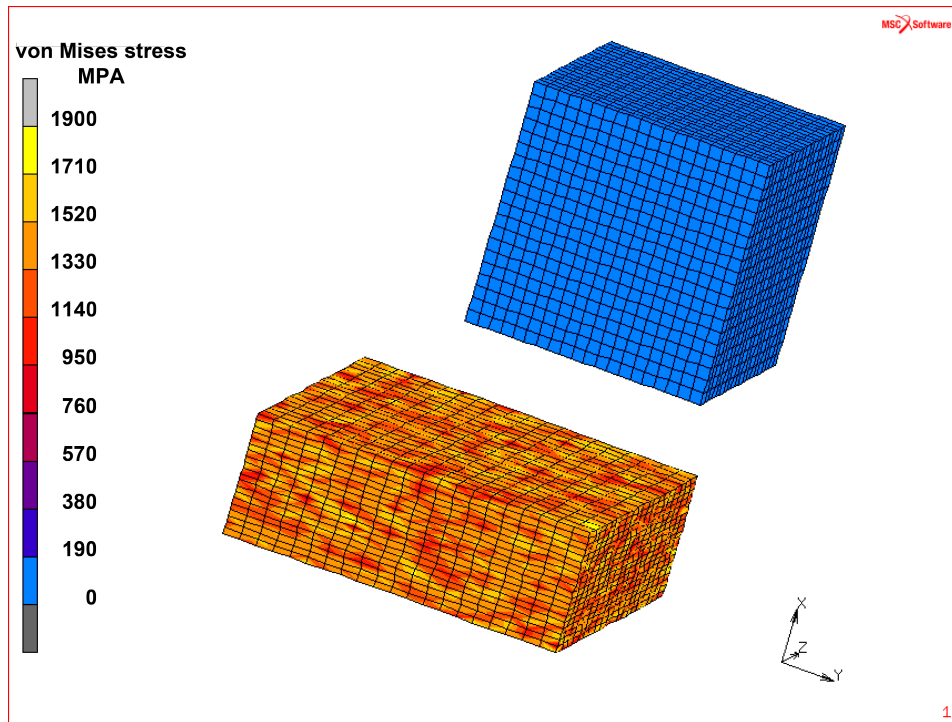
Figure 8.14: Finite element mesh used for the simulation of the compression test; initial mesh and mesh after 50 % height reduction in compression (about 70 % true strain). Periodic boundary conditions apply and the loading is in the negative x direction.

8.3 Simulating Stress–Strain Curves of an Fe-23%Mn TWIP Steel

In a first test the twinning model introduced in section 7.3 was used to simulate the stress–strain curve of an Fe-23%Mn TWIP steel. The FE model before and after deformation is shown in figure 8.14. The initial mesh is a $20 \times 20 \times 20$ cube of eight noded brick elements with linear shape function and full integration. Periodic boundary conditions are imposed and the x direction is the compression axis. As the material does not show significant anisotropy a random starting texture is used.

First, a high temperature curve measured at 673 K was used to fit the constitutive parameters for the dislocation density part of the model excluding twinning. This procedure is based on the finding that at such high temperature no twinning takes place (Allain et al., 2004). Then, in a second step, only the parameters of the twinning model were used to fit a room temperature (296 K) stress–strain curve. The parameters found are listed in table 8.6.

As can be seen from figure 8.15 a good fit could be achieved for the 673 K curve. The

Table 8.6: Constitutive parameters derived from calibration of the Fe-23%Mn TWIP steel stress-strain curves (see section 7.3 for notation).

Parameter	296 K	673 K
C_{11}	$175\,\mathrm{GPa}$	$175\,\mathrm{GPa}$
C_{12}	$115\,\mathrm{GPa}$	$115\,\mathrm{GPa}$
C_{44}	$135\,\mathrm{GPa}$	$135\,\mathrm{GPa}$
d_{grain}	$10\,\mathrm{\mu m}$	$10\,\mathrm{\mu m}$
k_{friction}	2.9×10^{-4}	2.9×10^{-4}
N_{slip}	12	12
b	$2.56 \times 10^{-10}\,\mathrm{m}$	$2.56 \times 10^{-10}\,\mathrm{m}$
$\rho_{\mathrm{edge},0}$	$1 \times 10^{12}\,\mathrm{m}^{-2}$	$1 \times 10^{12}\,\mathrm{m}^{-2}$
$\rho_{\mathrm{dipol},0}$	$1\,\mathrm{m}^{-2}$	$1\,\mathrm{m}^{-2}$
Q_0	$4.8 \times 10^{-19}\,\mathrm{J}$	$4.8 \times 10^{-19}\,\mathrm{J}$
v_0	$1 \times 10^{4}\,\mathrm{m\,s}^{-1}$	$1 \times 10^{4}\,\mathrm{m\,s}^{-1}$
c	30	30
D_0	$4 \times 10^{-5}\,\mathrm{m}^2\,\mathrm{s}^{-1}$	$4 \times 10^{-5}\,\mathrm{m}^2\,\mathrm{s}^{-1}$
Q_{SD}	$3.3 \times 10^{-19}\,\mathrm{J}$	$3.3 \times 10^{-19}\,\mathrm{J}$
p	1.15	1.15
q	1	1
Ω	$1 \times b^3$	$1 \times b^3$
$\check{d}_{\mathrm{edge}}$	$2.5 \times b$	$2.5 \times b$
$\xi_{\alpha\alpha'}$	0.122 (self, coplanar, Lomer)	0.122
	0.007 (Hirth)	0.007
	0.137 (glissile)	0.137
	0.625 (collinear)	0.625
N_{twin}	12	0
b_{twin}	$1.47 \times 10^{-10}\,\mathrm{m}$	-
s	$5 \times 10^{-8}\,\mathrm{m}$	-
L_0	$750 \times b$	-
$\dot{N}_0$	$6 \times 10^{17}\,\mathrm{s}^{-1}$	-
r	3	-
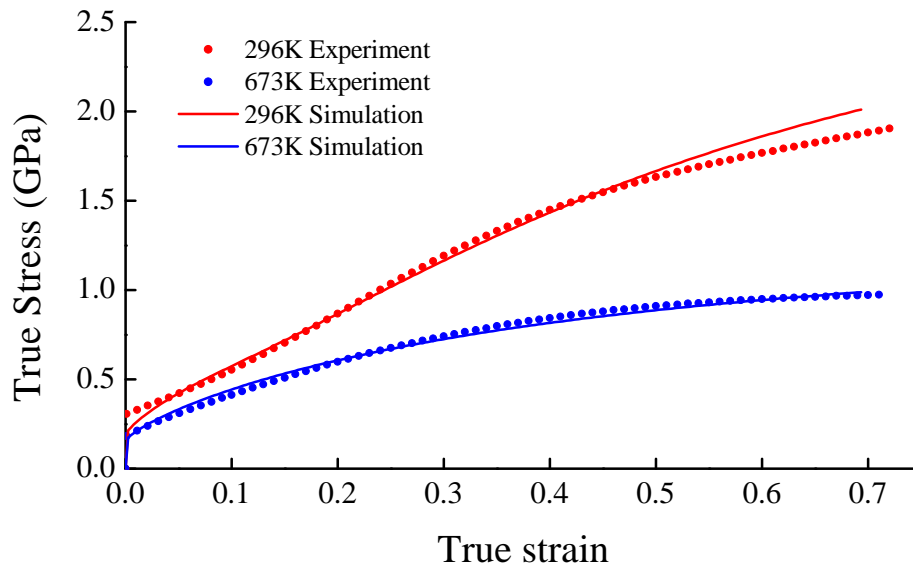
Figure 8.15: Comparison of simulated (lines) and experimental (symbols) stress-strain curves of an Fe-23%Mn TWIP steel.
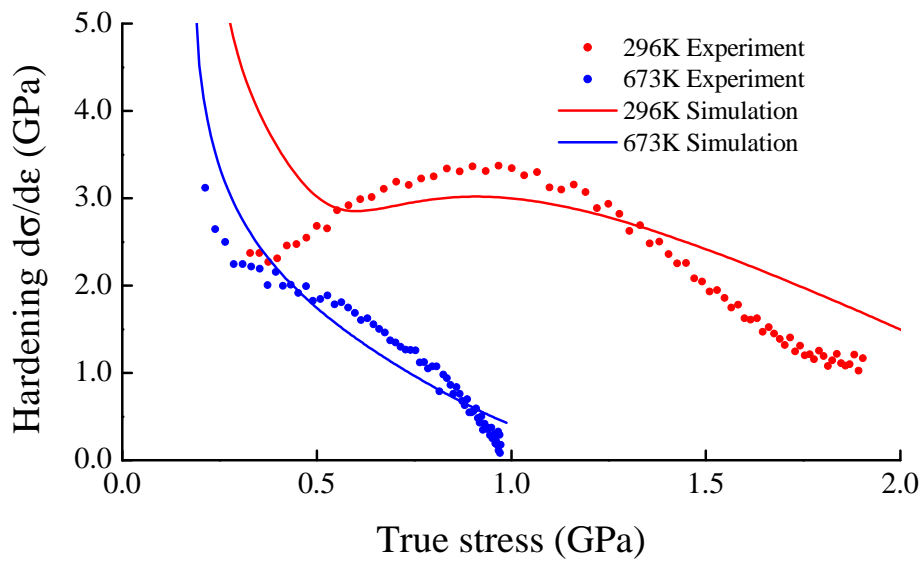
Figure 8.16: Comparison of simulated (lines) and experimental (symbols) hardening curves of an Fe-23%Mn TWIP steel.
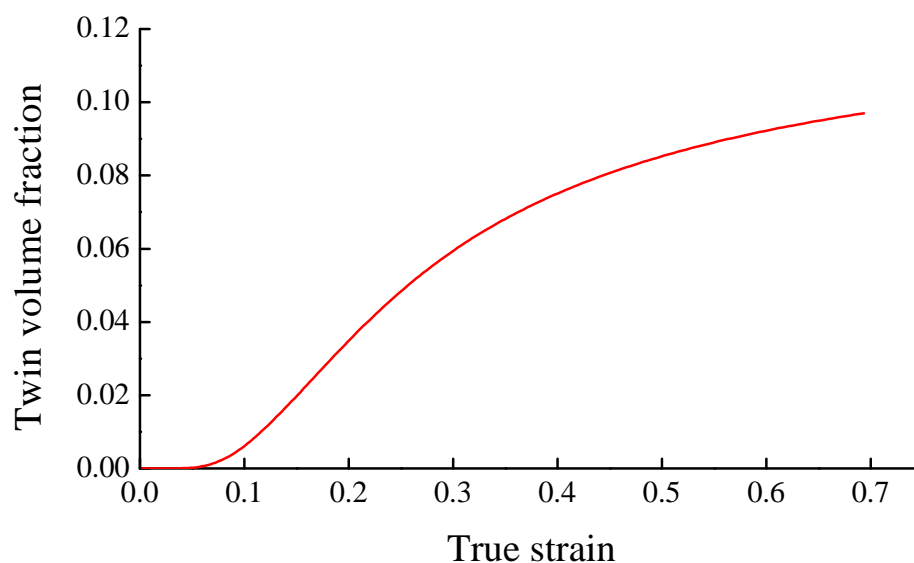
Figure 8.17: Development of twin volume fraction during the 296 K compression test.

hardening curve in figure 8.16, which is the derivative of the stress–strain curve, shows a similarly good correspondence. However, the initial hardening is somewhat too high, which is compensated by a too low hardening afterwards, *i.e.* the second derivative is not correctly predicted.

The fit for the 296 K curve in figure 8.15 is slightly worse, however, one has to keep in mind that only the remaining parameters of the twinning part of the model were used in the fitting procedure. The initial yield point is too low but the stress level of the experimental curve is reached at about 4dash5 % strain. This is also the strain range were twinning sets in (figure 8.17). It can be concluded that the hardening at 296 K is clearly dominated by the twinning process. As can be seen in figure 8.16 the hardening rate increases again after twinning sets in. After a maximum at a stress of about 1 GPa the hardening rate decreases again. However, the decrease is too slow in the simulation, so that the predicted stress is too high, *i.e.* stress saturation is not achieved in the simulation. This behavior is most likely caused by the fact that also the twin volume fraction does not show saturation within the simulated range of strain. Further investigations are thus necessary to improve the modeling of the development of the twin volume fraction. Unfortunately, there are no reliable experimental data for the evolution of the twin volume fraction available as twins in these materials are extremely thin. This situation might improve with emerging new measurement techniques such as electron channeling contrast imaging under controlled diffraction conditions (cECCI, Gutierrez-Urrutia et al., 2009).

8.4 The Virtual Laboratory – Representative Volume Element Simulations for Engineering Applications

8.4.1 Introduction

Predicting springback of complex industrial parts after stamping and (particularly) trimming still lacks accuracy. The direct use of constitutive models involving crystallographic slip for industrial forming simulations at the component scale is currently not realistic, owing to the high computational costs. Nevertheless, these complex models, which incorporate microstructure information like slip systems and orientation distribution, when applied to a so called Representative Volume Element (RVE) can be used as virtual laboratory to calibrate empirical constitutive models.

In this section such a calibration of an empirical constitutive model (yield locus) used at the component scale on the basis of virtual deformation tests of a representative volume element is demonstrated. The constitutive response of the RVE is modeled with crystal plasticity FEM and calibrated against a standard tensile test. Due to the large flexibility in boundary conditions applied to the RVE, it becomes then possible to mimic more complex strain paths, like biaxial tensile, compressive or shear tests, in order to extract the required parameters of the analytical material description. This procedure is frequently termed *virtual material testing* and, provided the virtual specimen is sufficiently reliable, allows for testing along strain paths that would be very expensive or even impossible to perform in reality. The application of the crystal plasticity FEM for the virtual testing is demonstrated for two ferritic steel grades (DC04 and H320LA). The Vegter et al. (2003) yield locus is used as the analytical material model allowing for the simulation of a typical industrial part in PAM-STAMP 2G.

8.4.2 The Virtual Specimen (RVE)

The virtual specimen employed in the present work consists of $10 \times 10 \times 10$ differently oriented grains, each discretized by one finite element. This grain aggregate is considered representative of the microstructure and associated texture, hence serves as a representative volume element. The initial texture was discretized using the texture component method (section 7.1.1). The phenomenological model described in section 2.3 served as constitutive law in which the hardening behavior of the 48 slip systems is assumed identical.

The virtual specimen is calibrated by determining the slip system hardening parameters on the basis of uniaxial tensile test data along the rolling direction (0° see figures 8.18a and 8.19a). This leads to the hardening parameters given in table 8.7. The quality of the model prediction is evaluated by comparing the remaining experimental data (stress–strain response and r-value of tensile tests in different directions and tension–compression tests) to corresponding simulations.

Table 8.7: Hardening parameters derived from calibration of the virtual specimen.

Parameter	DC04	H320LA
h_0	1293	5569
τ_s	48	101
a	7	3.5

Generally, the predicted stress–strain responses for tensile loading under 45° and 90° agree well with the corresponding experiments (see figures 8.18 and 8.19), with the exception of a slight underestimation (deviating less than 10 %) in the case of DC04 under 45° (figure 8.18b). However, the prediction for r-values is far from perfect. In particular, for the cold rolling steel DC04 the simulated r-values for 0° and 90° are strongly underestimated (figure 8.18a and c) in the case of the steel H320LA the discrepancies are less severe as can be seen in figure 8.19.

A further validation of the calibration was done against a more complicated test involving load reversal, *i.e.* tension–compression. Figure 8.20 compares experiment and simulation of unidirectional tension and reverse-loading into compression after about 0.08 strain. The predicted equivalent stress agrees quite well and the observed Bauschinger effect (lower flow stress after change of loading direction) is nicely reproduced. Compared to simulation, the measured curve after load reversal exhibits less strain hardening (even softening) after compressive strains of about 0.05. This softening is caused by buckling of the specimen in compression. An important point to notice is that the virtual specimen on the basis of the phenomenological constitutive model exhibits a Bauschinger effect, even without explicitly incorporating kinematic hardening into the constitutive law.

8.4.2.1 Influence of Finite Element Type

The approximation of displacement field gradients depends on the polynomial degree of the finite element shape function (as well as the integration scheme used). Therefore, simulations with four different element types (linear and quadratic shape functions, reduced and full integration scheme) were compared. The resulting stress–strain response, evolution of r-value, and exemplary displacement fields are shown in figure 8.21.

In view of the accuracy with respect to experimental results, the deviation between the four different element types regarding the stress–strain response as well as the r-value evolution is minor. It can be noted that elements with full integration scheme lead to a slightly higher tensile strength than those with reduced integration. The RVE discretized by finite elements using reduced integration and linear shape functions (Abaqus notation "C3D8R", 8 nodes) exhibits the largest fluctuation in displacements. While quadratic elements (and full integration) can reproduce inhomogeneous deformation more accurately, the significant reduction in computation time with only small differences in the
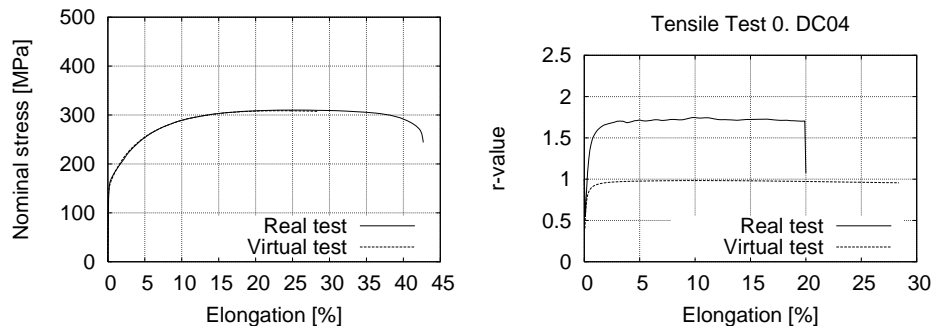
(a) Calibration data on nominal stress (left) for uniaxial tension along 0°. R-value (right) resulting from the calibration.
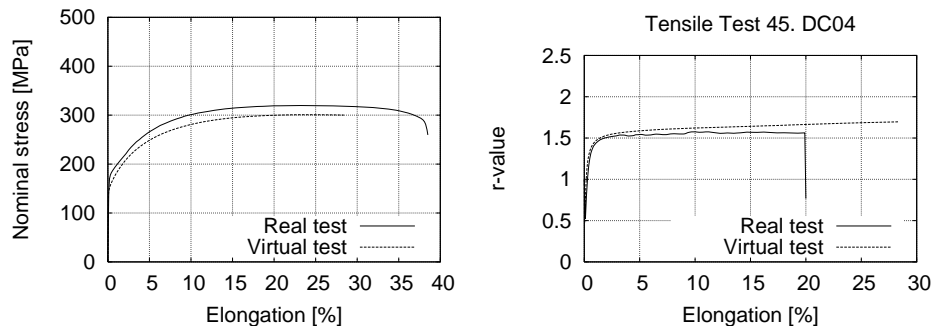
(b) Prediction of nominal stress and r-value for uniaxial tension along 45°.
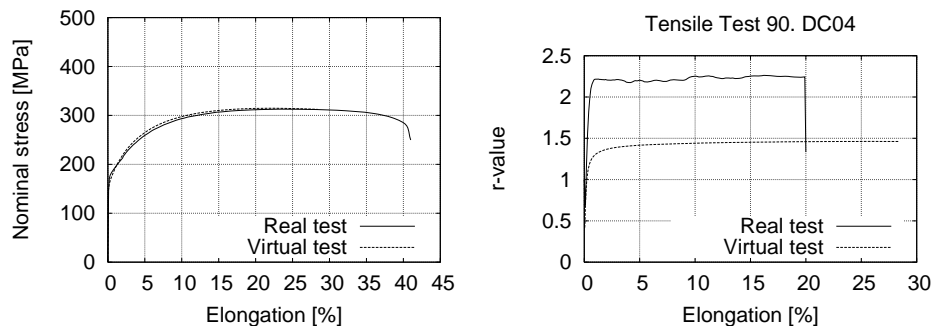
(c) Prediction of nominal stress and r-value for uniaxial tension along 90°.

Figure 8.18: Calibration basis and resulting predictions of uniaxial stress–strain response and strain evolution of the r-value for DC04 steel.
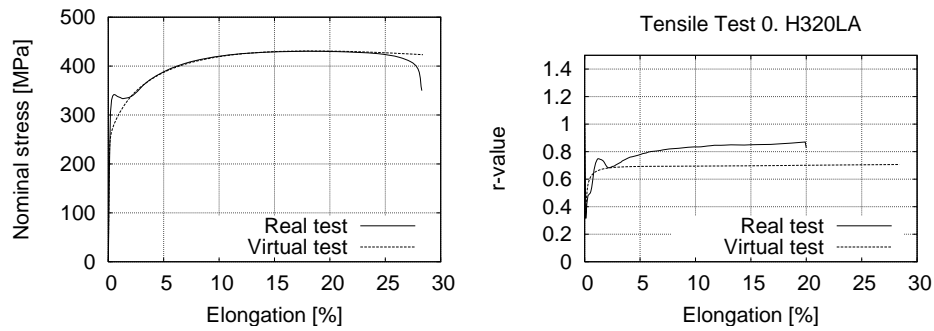
(a) Calibration data on nominal stress (left) for uniaxial tension along 0°. R-value (right) resulting from the calibration.
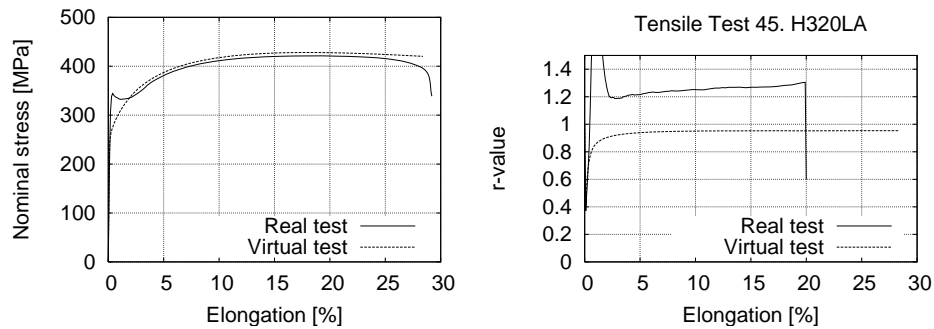
(b) Prediction of nominal stress and r-value for uniaxial tension along 45°.
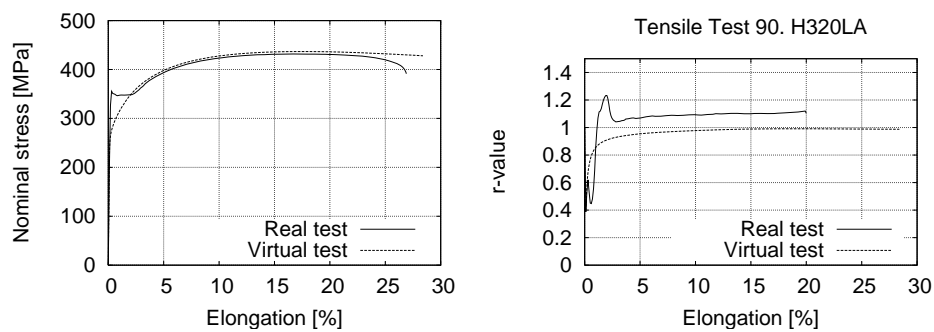
(c) Prediction of nominal stress and r-value for uniaxial tension along 90°.

Figure 8.19: Calibration basis and resulting predictions of uniaxial stress–strain response and strain evolution of the r-value for H320LA steel.
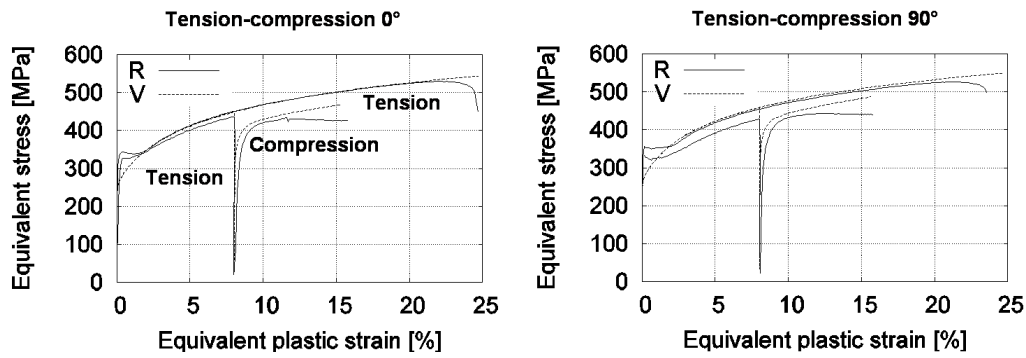
Figure 8.20: The reversal of the loading direction from tension to compression results in a lower equivalent stress compared to the level observed under continued tensile loading (Bauschinger effect). This effect is found in real tension–compression tests (R) and is well reproduced by the virtual specimen (V).
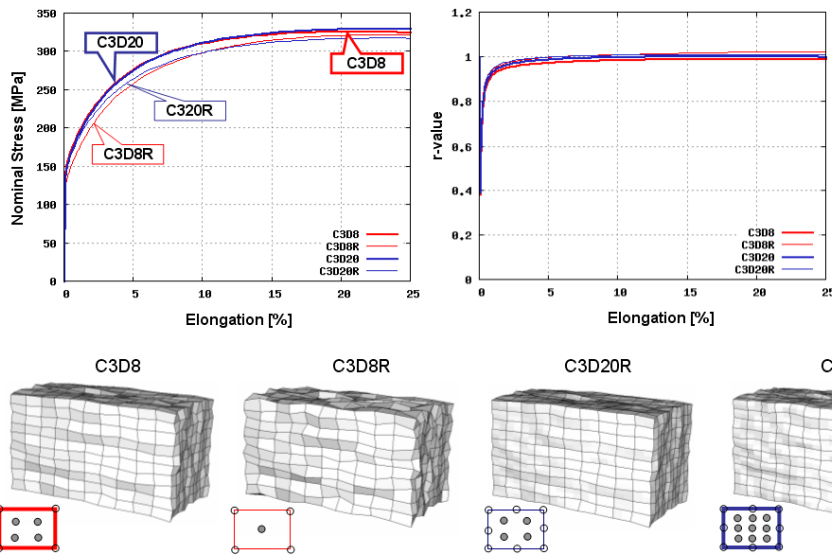
Figure 8.21: Stress–strain response and r-values for different element types.

calculated tensile strength justifies the use of "C3D8R" elements in all subsequently presented simulations.

8.4.3   Stamping and trimming simulation

The material model as proposed by Vegter et al. (2003) and implemented in PAM-STAMP 2G (ESI Group, 2004) is, essentially, a very flexible description of the yield locus based on interpolation of experimental data by means of a cubic Bezier-spline (figure 8.22). The interpolation requires at least the following deformation tests:

- A stack compression test with measurement of ovalization.
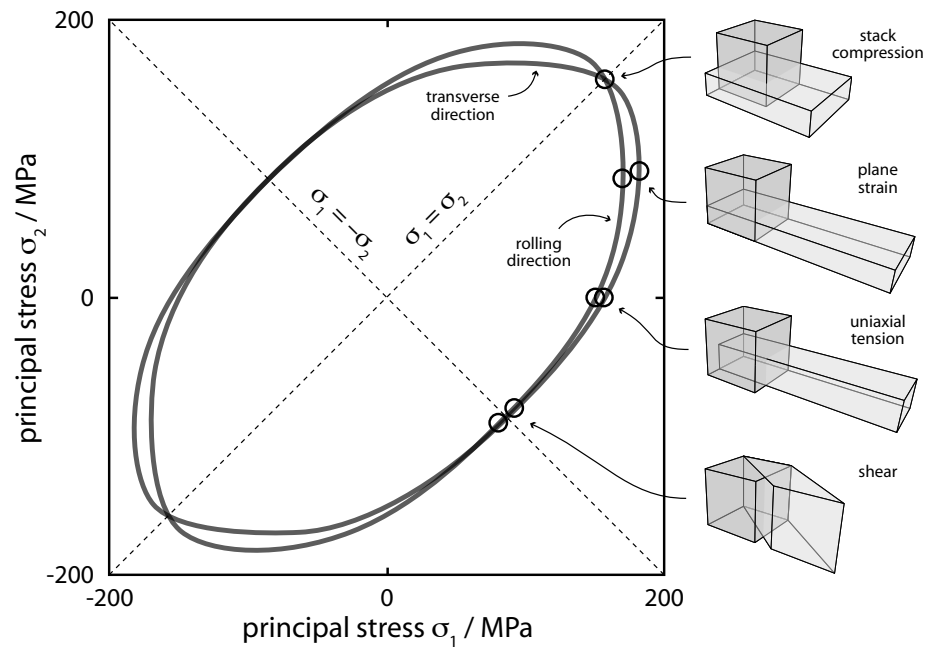
Figure 8.22: The Vegter et al. (2003) yield locus derived from virtual test data. Corresponding individual deformation tests are schematically depicted at right.

- Three uniaxial tensile tests (0°, 45°, 90°) with lateral strain measurement.

- Three tensile tests with constrained lateral strain (plane strain, 0°, 45°, 90°). Contrary to real tests, the lateral stress can be identified in virtual tests.

- Three shear tests, providing yield locus data in the lower right quadrant for different principal stress directions with respect to the rolling direction.

The required parameters (see table 8.8) are determined from all virtual deformation experiments at 1 % accumulated shear deformation on the slip systems, which corresponds to approximately 0.4 % plastic strain.

With above yield locus parameterization, stamping, trimming, and springback of a car boot made of H320LA are simulated (figure 8.23). For comparison, two additional simulations were carried out. One using a simple yield locus (Hill48; Hill, 1948) fitted to tensile data from experiments and another in which the Vegter parameterization relied on experimentally determined r-values instead of those resulting from the virtual deformation tests.

The differences between optically scanned and simulated geometries are illustrated in figure 8.24. The maximum deviation of the simulation using purely virtual test data (center row) is larger than that of the simple yield locus. If the r-values of the virtually fitted Vegter model are replaced by measured ones, the discrepancy is reduced. However, the remaining disagreement is only marginally less than that resulting from the Hill48 yield locus.

Table 8.8: Parameters for the Vegter yield locus (PAM-STAMP 2G (ESI Group, 2004)) obtained from virtual deformation tests on H320LA.

	angle to rolling direction (°)		
Parameter	0	45	90
σ-uniaxial	1	1.01	1.029
r-uniaxial	0.624	0.798	0.950
σ-plane strain	1.1	1.14	1.16
α-plane strain	0.5	0.5	0.5
σ-pure shear	0.5615	0.5743	0.603
r-biaxial	0.75	-	-
σ-biaxial	1.004	-	-

Figure 8.23: Stamping part of car boot. Photographs and visualized measured data. After stamping and after trimming.

yield criteria	test data	r0	r45	r90	max. difference [mm]	7.0 5.6 4.2 2.8 1.4 0.0 mm
Hill 48	real correspond to DIN	0.815	1.245	1.087	5.7	
Vegter	virtual, 0.4% plastic strain	0.624	0.798	0.950	6.9	
Vegter	virtual and real (r-values)	0.815	1.245	1.087	5.6	

Figure 8.24: Shape deviation between measured and simulated geometry for different material models and different types of test data for parameter fitting.

8.4.4 Conclusions

Springback simulation and compensation generate an increasing demand for precise material models. Microstructural approaches like texture-based crystal plasticity require, however, still too many resources in terms of memory and computational power for a direct simulation of industrial sheet metal forming. Therefore, more sophisticated empirical models are likely to emerge. The resulting increased flexibility (and accuracy) of those models entails a higher experimental effort for parameter identification. In this context, virtual specimens with microstructure-based constitutive laws may be used to move the effort from real-world mechanical testing to computer simulation.

In the present section a virtual specimen was used to demonstrate the process from model calibration over virtual deformation tests to simulation of a real part. The particular setting of the constitutive model and RVE setup still lacks the important capability to predict the r-values correctly. On the other hand, the satisfactory prediction of the Bauschinger effect encourages further work. Shortcomings of the presented virtual specimen could be addressed by

- improving the texture sampling for better reproduction of the measured pole figures by discrete grain orientations,[2]

- accounting for anisotropy of the grain shape, *i.e.* use more than one element per grain,

- improving the calibration procedure, which should include the latent hardening matrix.

Even with the given restrictions, it was shown that material parameters obtained from texture data and tensile tests using the virtual test program can compete in simulation quality with the full parameter set obtained experimentally.

---

[2]Can today be achieved by the hybridIA scheme (section 7.1.2), which was not available at the time of the study.

Part III

A General Multiscale Crystal Plasticity Implementation

Chapter 9

Structure of the General Multiscale CPFEM Framework

As far as the FE method is concerned, CPFE approaches can be regarded as a class of constitutive material models. Therefore, they can be implemented directly into an FE code when available in source form. In the case of commercial FE codes, CPFE constitutive laws are implemented in the form of a user subroutine, *e.g.* HYPELA2 in MSC.Marc (MSC, 2010) or UMAT/VUMAT in Abaqus (Dassault Systèmes, 2010). This is also the way the MPIE implementation is realized.

Depending on whether the FE code is implicit or explicit, the purpose of a material model is one- or twofold: 1. Calculate the stress $\boldsymbol{\sigma}$ required to reach the final deformation gradient (implicit and explicit); 2. Calculate the Jacoby matrix $\boldsymbol{J} = \partial\boldsymbol{\sigma}/\partial\boldsymbol{E}$ (implicit only, $\boldsymbol{E}$ is the symmetric strain tensor). In addition, the state variables of the constitutive model need to be updated, which can be regarded as a subtask of task 1.

Integration schemes for calculating the stress will be presented in chapter 10. As these are computationally rather demanding most implementations reported in literature strongly intermix the integration scheme with the constitutive model in order to optimize the numerical performance. The MPIE implementation takes the contrary approach as it tries to be as general as possible. Therefore, it is implemented in a modularized way that strictly separates the numerics from the constitutive model(s).

From the viewpoint of FEM the material model provides a way to determine the stress necessary to achieve a prescribed deformation. However, taking into account the previous parts of this work, there is no unique way to solve this problem but there is a variety of both homogenization schemes and constitutive models to answer this question. In order to offer full flexibility in choosing both, a homogenization scheme and a constitutive model, the MPIE material subroutine is implemented in a strictly modularized way (see table 9.1). To achieve this, the subroutine is split into several files, each of which serves a specific task.

First of all there are the interface routines towards the general purpose FEM programs, *i.e.* Marc and Abaqus, `mpie_cpfem_marc.f90`, `mpie_cpfem_abaqus_std.f`, and `mpie_cpfem_abaqus_exp.f`.[1] These contain the FEM package specific interface routine, *i.e.* hypela2 in case of MSC.Marc and UMAT or VUMAT in case of Abaqus. The main task of these routines is to call the generic CPFEM routine of the MPIE code. This routine is part of the source file `CPFEM.f90` and determines whether new results need to be calculated or whether predetermined values are to be returned. In case calculations need to be done, it calls the routine that calculates the material point behavior, which is part of `homogenization.f90`. This file branches into the different homogenization schemes included in the files `homogenization_isostrain.f90` and `homogenization_RGC.f90`. The homogenization scheme identifies the deformation gradients of the individual grains and refers to `crystallite.f90` for the stress evaluation on a single grain basis. `crystallite.f90` contains the code of the integration scheme presented in section 10.2. It is worthwhile to mention that this integration scheme is independent of the underlying constitutive model. It solely relies on information on $\boldsymbol{L}_\mathrm{p}$, its tangent, and the state evolution, no matter how these are determined. This information is provided by the constitutive models located in the file `constitutive.f90`, which in turn branches into the individual constitutive models contained in files `constitutive_*.f90`. Here * is a placeholder for either `phenopowerlaw`, `dislotwin`, `nonlocal` or `j2`, which contain the specific constitutive models as described in chapters 2 and 4 plus a standard J2 law.

Additional source files are: `lattice.f90`, which contains all the information about the lattice geometry for face-centered cubic, body-centered cubic, and hexagonal crystals, `material.f90`, which parses the file `material.config` (see chapter 11) and assigns material properties to the integration points, and `mesh.f90`, which contains the routines that parse the FEM input files and extract all mesh properties important for the subroutine.

Finally, there are several auxiliary routines, which, depending on their purpose, are contained in the files: `debug.f90`: output of debug information, `FEsolving.f90`: evaluation of FEM solver parameters, `IO.f90`: generic I/O operations, `math.f90`: mathematical functions and subroutines, `numerics.f90`: handling of numerical parameters,[2] and `prec.f90`: precision of integer and floating point variables.

Due to the modularized structure providing additional homogenization schemes or constitutive models is just a matter of providing additional files `homogenization_*.f90` and `constitutive_*.f90`, respectively and extending the master files `homogenization.f90` and `constitutive.f90`. The integration into FE solvers other than Marc and Abaqus would need an additional interface file `mpie_cpfem_fesolver.f90` and adapting parts of `mesh.f90` for evaluating the respective input file format.

---

[1]All code is written in Fortran 90 free format style, however, Abaqus does not allow the `.f90` file extension for user subroutine files.

[2]`numerics.f90` uses standard values for the numerical parameters, the optional file `numerics.config` can be used to change these values, if desired, without recompiling the subroutine.

Table 9.1: Source files of the MPIE CPFEM implementation.

purpose	file name[1]
FEM interface routines	`mpie_cpfem_marc.f90`
	`mpie_cpfem_abaqus_std.f`
	`mpie_cpfem_abaqus_exp.f`
generic CPFEM routine	`CPFEM.f90`
homogenization schemes	`homogenization.f90`
	`homogenization_isostrain.f90`
	`homogenization_RGC.f90`
integration scheme	`crystallite.f90`
constitutive models	`constitutive.f90`
	`constitutive_phenopowerlaw.f90`
	`constitutive_dislotwin.f90`
	`constitutive_nonlocal.f90`
	`constitutive_j2.f90`
lattice properties	`lattice.f90`
material configuration	`material.f90`
mesh properties	`mesh.f90`
auxiliary routines	`debug.f90`
	`FEsolving.f90`
	`IO.f90`
	`math.f90`
	`numerics.f90`
	`prec.f90`

Chapter 10

The Integration Scheme

The stress calculation is usually implemented using a predictor–corrector scheme. Figure 10.1 visualizes the setup of the clockwise loop of calculations to be performed. In principle, one could start predicting any of the quantities involved, follow the circle, and compare the resulting quantity with the predicted one. Subsequently the prediction would be updated using for instance a Newton–Raphson scheme. Various implementations were suggested using either the elastic deformation gradient $\boldsymbol{F}_{\mathrm{e}}$ (Sarma and Zacharia, 1999), the plastic deformation gardient $\boldsymbol{F}_{\mathrm{p}}$ (Maniatty et al., 1992), the second Piola–Kirchhoff stress $\boldsymbol{S}$ (Kalidindi et al., 1992), or the shear rates $\dot{\gamma}^{\alpha}$ (Peirce et al., 1983) as a starting point. While they certainly all should lead to the same results, there are two numerical aspects to consider: First, the inversion of the Jacoby matrix occurring in the Newton–Raphson algorithm; second, the character of the equations to evaluate.

Regarding the first point, one has to realize that the dimension of the Jacoby matrix for the Newton–Raphson scheme is equal to the number of independent variables of the quantity that is used as predictor. These are nine variables for $\boldsymbol{F}_{\mathrm{e}}$, eight for $\boldsymbol{F}_{\mathrm{p}}$ (due to volume conservation) and six for $\boldsymbol{S}$ (due to the symmetry of the stress tensor). However, if the $\dot{\gamma}^{\alpha}$ are chosen, there are at least 12 variables (slip systems in fcc crystals), up to 48 (slip systems in bcc crystals), or even more in the case of additional twinning. Inverting such large matrices (*e.g.* 48×48) is numerically quite demanding, which is the reason why such implementations require some effort in reducing the number of (active) slip systems (Cuitiño and Ortiz, 1992).

The second point concerns the numerical convergence behavior of the overall system. When starting an iteration from any other quantity than $\dot{\gamma}^{\alpha}$, the procedure involves calculating the slip rates from the stress. This is usually done using a power or exponential law. The slope of these functions is rapidly increasing, *i.e.* small variations in stress lead to increasingly larger deviations in the strain rate. Therefore, for large deformations, where convergence becomes a main issue, the iteration behavior of the stress loop becomes worse. However, when starting from $\dot{\gamma}^{\alpha}$, the inverse tendency applies, *i.e.* stress
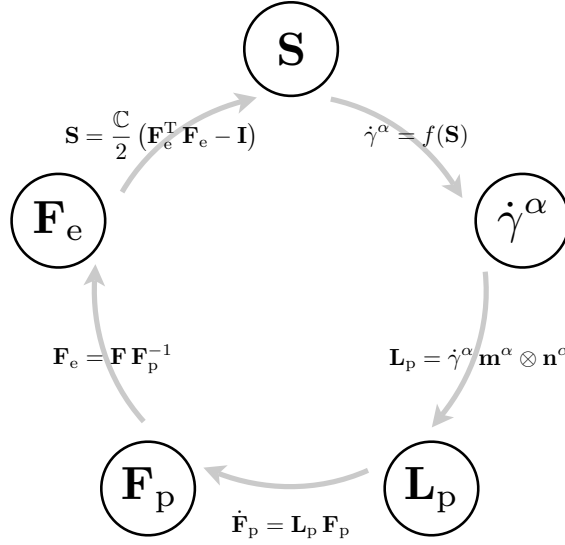
Figure 10.1: Clockwise loop of calculations during stress determination(S second Piola–Kirchhoff stress, $\dot{\gamma}^\alpha$ shear rate, L_p plastic velocity gradient, m^α slip direction, n^α slip plane normal, F_p plastic deformation gradient, F_e elastic deformation gradient, $\mathbb{C}$ elasticity tensor, I identity matrix).

variations with varying shear rates get smaller and smaller. This is why the second approach promises a better numerical stability at large strains, however, at the cost of dealing with a large Jacoby matrix.

Calculating the Jacoby matrix ($J = \partial\sigma/\partial E$) for implicit FE codes in the case of a crystal plasticity constitutive model has to be done numerically by perturbing E, as there is in general no closed analytical form for this expression. This numerical evaluation includes at least six stress evaluations, which makes it computationally expensive.

10.1 Explicit Versus Implicit Integration Methods

When discussing explicit versus implicit integration schemes one has to distinguish between two aspects. Firstly, the FE solver can follow an explicit or implicit approach, and secondly, the material model can be iterated using explicit or implicit integration schemes. Concerning the first point, Harewood and McHugh (2007) recently compared the efficiency of both methods when applying crystal plasticity models to forming problems. As could be expected, the outcome of this comparison is to some extent problem-dependent. As a rule, the explicit scheme generally seemed favorable when contact is involved.

Regarding the material model itself, *i.e.* the material subroutine in the case of commercial FE solvers, anything from explicit to fully implicit integration methods is possible.

The task of the material model is twofold. First, the stress necessary to achieve the prescribed deformation has to be determined; second, the material state has to be updated. In most codes first the stress is determined implicitly for a fixed state of the material and in a subsequent step the material state is updated. In the case of a fully implicit implementation the stress then has to be determined again until convergence is achieved, while in a semi-implicit code the calculation is stopped after the state was updated. An advantage of the fully implicit scheme is that it truly converges to the correct solution (if it converges at all), whereas the explicit solution converges generally but not necessarily to the correct solution. Since explicit schemes typically use very small time steps, semi-implicit integration schemes should generally work satisfactorily with respect to precision, while they are at the same time faster than a fully implicit scheme.

10.2   The Integration Scheme

We utilize the multiplicative decomposition of the total deformation gradient

$$\boldsymbol{F} = \boldsymbol{F}_\mathrm{e}\boldsymbol{F}_\mathrm{p} \quad \Longleftrightarrow \quad \boldsymbol{F}_\mathrm{e} = \boldsymbol{F}\,\boldsymbol{F}_\mathrm{p}^{-1} \tag{10.1}$$

into a purely plastic deformation gradient, $\boldsymbol{F}_\mathrm{p}$, and an "elastic" deformation gradient, $\boldsymbol{F}_\mathrm{e}$, which also accounts for rigid-body rotation. Using the definition of the Green–Lagrange strain tensor we arrive at the elastic strain measure

$$\boldsymbol{E}_\mathrm{e} = \frac{1}{2}\left(\boldsymbol{F}_\mathrm{e}^\mathrm{T}\boldsymbol{F}_\mathrm{e} - \boldsymbol{I}\right). \tag{10.2}$$

The work-conjugate stress measure (second Piola–Kirchhoff stress) is

$$\boldsymbol{S} = \mathbb{C}:\boldsymbol{E}_\mathrm{e} = \frac{1}{2}\,\mathbb{C}:\left(\boldsymbol{F}_\mathrm{p}^{-\mathrm{T}}\boldsymbol{F}^\mathrm{T}\boldsymbol{F}\,\boldsymbol{F}_\mathrm{p}^{-1} - \boldsymbol{I}\right). \tag{10.3}$$

The plastic velocity gradient is given by

$$\boldsymbol{L}_\mathrm{p} = \dot{\boldsymbol{F}}_\mathrm{p}\boldsymbol{F}_\mathrm{p}^{-1} \quad \Longleftrightarrow \quad \dot{\boldsymbol{F}}_\mathrm{p} = \boldsymbol{L}_\mathrm{p}\boldsymbol{F}_\mathrm{p}. \tag{10.4}$$

In a fully-implicit formulation, the rate of change of the plastic deformation gradient is written as

$$\dot{\boldsymbol{F}}_\mathrm{p} = \frac{\boldsymbol{F}_\mathrm{p}(\tau) - \boldsymbol{F}_\mathrm{p}(t)}{\Delta t} = \boldsymbol{L}_\mathrm{p}(\tau)\boldsymbol{F}_\mathrm{p}(\tau), \tag{10.5}$$

where $\tau = t + \Delta t$. Rearranging equation (10.5) gives

$$\boldsymbol{F}_\mathrm{p}(\tau)^{-1} = \boldsymbol{F}_\mathrm{p}(t)^{-1}\left[\boldsymbol{I} - \Delta t\,\boldsymbol{L}_\mathrm{p}(\tau)\right] \tag{10.6a}$$

$$\boldsymbol{F}_\mathrm{p}^{-\mathrm{T}}(\tau) = \left[\boldsymbol{I} - \Delta t\,\boldsymbol{L}_\mathrm{p}^\mathrm{T}(\tau)\right]\boldsymbol{F}_\mathrm{p}(t)^{-\mathrm{T}}. \tag{10.6b}$$

Combination of equations (10.3) and (10.6) allows to express the second Piola–Kirchhoff stress at the end of the time step, *i.e.* at time τ, in terms of known quantities at either times t or τ plus the unknown plastic velocity gradient at time τ:

$$S(\tau) = \frac{1}{2}\,\mathbb{C} : \left\{ \underbrace{\left[I - \Delta t\,L_{\mathrm{p}}{}^{\mathrm{T}}(\tau)\right]}_{B^{\mathrm{T}}}\underbrace{F_{\mathrm{p}}(t)^{-\mathrm{T}}F^{\mathrm{T}}(\tau)F(\tau)\,F_{\mathrm{p}}(t)^{-1}}_{A}\underbrace{\left[I - \Delta t\,L_{\mathrm{p}}(\tau)\right]}_{B} - I \right\} \ .$$
(10.7)

Hence, with an estimate, $\underset{\sim}{L}_{\mathrm{p}}$, of the plastic velocity gradient at time τ an estimated stress, $\underset{\sim}{S}$, can be derived. This stress together with an estimated microstructure $x(\tau)$ at the end of the time step would produce a plastic velocity gradient

$$L_{\mathrm{p}}(\tau) = L_{\mathrm{p}}\left(\underset{\sim}{S}(\tau), x(\tau)\right) \ ,$$
(10.8)

which is given by the underlying constitutive model. Equally, the microstructural evolution—given as the time-derivative of constitutive state variables—is a function of these quantities at time τ:

$$\dot{x}(\tau) = \dot{x}\left(\underset{\sim}{S}(\tau), x(\tau)\right) \ .$$
(10.9)

The set of coupled, non-linear algebraic equations (10.7)–(10.9) is solved using a two-step iterative scheme, where the first level of iterations solves for $L_{\mathrm{p}}(\tau)$ with $x(\tau)$ fixed at its best available estimate and the second level updates the material state $x(\tau)$ based on the converged second Piola–Kirchhoff stress, S, from the first level.

10.2.1 Stress Level Iterations

We define the residual, R_n, after n iterations of the stress loop to be the difference between the guessed velocity gradient $\underset{\sim}{L}_{\mathrm{p}}$ and L_{p} resulting from the constitutive model (equation (10.8)):

$$R_n = \underset{\sim}{L}_{\mathrm{p},n} - L_{\mathrm{p}}\left(\underset{\sim}{S}\left(\underset{\sim}{L}_{\mathrm{p},n}\right)\right) \ .$$
(10.10)

A Newton–Raphson scheme is employed according to

$$\underset{\sim}{L}_{\mathrm{p},n+1} = \underset{\sim}{L}_{\mathrm{p},n} - \left[\left. \frac{\partial R_n}{\partial \underset{\sim}{L}_{\mathrm{p}}} \right|_{\underset{\sim}{L}_{\mathrm{p},n}} \right]^{-1} : R_n$$
(10.11)

in order to correct the guess of $\underset{\sim}{L}_{\mathrm{p}}$ from increment n. The Jacobian required for the correction is derived in the following way:

$$\begin{aligned}
\frac{\partial R_{ij}}{\partial \underset{\sim}{L}_{\mathrm{p}kl}} &= \frac{\partial \underset{\sim}{L}_{\mathrm{p}ij}}{\partial \underset{\sim}{L}_{\mathrm{p}kl}} - \frac{\partial L_{\mathrm{p}ij}}{\partial \underset{\sim}{S}_{mn}}\frac{\partial \underset{\sim}{S}_{mn}}{\partial \underset{\sim}{L}_{\mathrm{p}kl}} \\
&= \delta_{ik}\delta_{jl} - \frac{\partial L_{\mathrm{p}ij}}{\partial \underset{\sim}{S}_{mn}}\frac{\partial \underset{\sim}{S}_{mn}}{\partial \underset{\sim}{L}_{\mathrm{p}kl}} \ .
\end{aligned}$$
(10.12)

The partial derivative $\partial \boldsymbol{L}_{\mathrm{p}}/\partial \underset{\approx}{\boldsymbol{S}}$ is known from the constitutive law. From equation (10.7) one can derive the partial derivative of the second Piola–Kirchhoff stress with respect to the (guessed) plastic velocity gradient, which is needed to solve equation (10.12):

$$
\begin{aligned}
\frac{\partial \underset{\approx}{\boldsymbol{S}}}{\partial \underset{\sim}{\boldsymbol{L}}_{\mathrm{p}}} \quad = \quad \underset{\approx}{\boldsymbol{S}}_{,\underset{\sim}{\boldsymbol{L}}_{\mathrm{p}}} = \quad & \frac{1}{2}\left[\mathbb{C}:\left(\boldsymbol{B}^{\mathrm{T}}\boldsymbol{A}\boldsymbol{B}-\boldsymbol{I}\right)\right]_{,\underset{\sim}{\boldsymbol{L}}_{\mathrm{p}}} \\
= \quad & \frac{1}{2}\left[\mathbb{C}:\left(\boldsymbol{B}^{\mathrm{T}}\boldsymbol{A}\boldsymbol{B}-I\right)_{,\underset{\sim}{\boldsymbol{L}}_{\mathrm{p}}}+\left(\boldsymbol{B}^{\mathrm{T}}\boldsymbol{A}\boldsymbol{B}-\boldsymbol{I}\right):\mathbb{C}_{,\underset{\sim}{\boldsymbol{L}}_{\mathrm{p}}}\right] \\
= \quad & \frac{1}{2}\,\mathbb{C}:\left(\boldsymbol{B}^{\mathrm{T}}_{,\underset{\sim}{\boldsymbol{L}}_{\mathrm{p}}}\boldsymbol{A}\boldsymbol{B}+\boldsymbol{B}^{\mathrm{T}}\boldsymbol{A}\boldsymbol{B}_{,\underset{\sim}{\boldsymbol{L}}_{\mathrm{p}}}\right) \\
= \quad & -\frac{\Delta t}{2}\,\mathbb{C}:\left(\underset{\sim}{\boldsymbol{L}}_{\mathrm{p}}^{\mathrm{T}}{}_{,\underset{\sim}{\boldsymbol{L}}_{\mathrm{p}}}\boldsymbol{A}\boldsymbol{B}+\boldsymbol{B}^{\mathrm{T}}\boldsymbol{A}\underset{\sim}{\boldsymbol{L}}_{\mathrm{p},\underset{\sim}{\boldsymbol{L}}_{\mathrm{p}}}\right)\ . \quad (10.13)
\end{aligned}
$$

Rewriting this using index notation results in:

$$
\begin{aligned}
\frac{\partial \underset{\approx}{S}_{ij}}{\partial \underset{\sim}{L}_{\mathrm{p}kl}} \quad = \quad & -\frac{\Delta t}{2}\,C_{ijmn}\left(\frac{\partial \underset{\sim}{L}_{\mathrm{p}mq}^{\mathrm{T}}}{\partial \underset{\sim}{L}_{\mathrm{p}kl}}A_{qp}B_{pn}+B_{mp}^{\mathrm{T}}A_{pq}\frac{\partial \underset{\sim}{L}_{\mathrm{p}qn}}{\partial \underset{\sim}{L}_{\mathrm{p}kl}}\right) \\
= \quad & -\frac{\Delta t}{2}\,C_{ijmn}\left[\delta_{qk}\,\delta_{ml}\,(AB)_{qn}+(B^{\mathrm{T}}A)_{mq}\,\delta_{qk}\,\delta_{nl}\right] \\
= \quad & -\frac{\Delta t}{2}\left[C_{ijln}\,(AB)_{kn}+C_{ijml}\,(B^{\mathrm{T}}A)_{mk}\right]\ . \quad (10.14)
\end{aligned}
$$

The stress loop is considered converged if all components of $\boldsymbol{R}_n$ fall within a relative tolerance with respect to the corresponding components in $\underset{\sim}{\boldsymbol{L}}_{\mathrm{p}}$.

10.2.2 Material State Iterations

For the material state loop the residual, $\boldsymbol{r}_n$, is defined in terms of the difference between a guessed amount of structure evolution and the respective evolution following from the constitutive model (equation (10.9):

$$
\boldsymbol{r}_n = \left[\underset{\sim}{\boldsymbol{x}}_n - \boldsymbol{x}(t)\right] - \Delta t\,\dot{\boldsymbol{x}}(\underset{\approx}{\boldsymbol{S}}_n,\underset{\sim}{\boldsymbol{x}}_n)\,. \quad (10.15)
$$

The material state is considered converged if all components of $\boldsymbol{r}_n$ fall within a relative tolerance with respect to the corresponding components in $\boldsymbol{x}$.

In case a non-local material model as introduced in chapter 4 is used both integration loops rely on non-local data. Therefore, they can only be solved for all integration points at once, when a fully implicit integration is aimed for. As the information from neighboring integration points is not available within user subroutines of commercial FEM packages the next section describes how these informations can be obtained.

10.2.3   Solution Scheme for Non-Local Models

The solution of non-local constitutive models such as introduced in sections 4.1 and 4.2 requires some information from the neighboring integration points. In commercial FE solvers this information is usually not available. To overcome this problem the following scheme was developed in Ma et al. (2006a):

- The iterations of the FE solver are separated into odd and even iterations.

- Even iterations (starting from 0) are used to collect the necessary informations for all integration points. Without performing any further calculation an arbitrary constant stress tensor is fed back into the FE algorithm. By doing so the global convergence cannot be obtained in any even-valued iteration step. Moreover, a diagonal matrix with very large values is assigned to the Jacoby matrix, $\boldsymbol{J}$, namely

$$J_{ijkl} = \begin{cases} 0 & \text{for} \quad i \neq k, \ j \neq l \\ \text{const} & \text{for} \quad i = k, \ j = l \end{cases}$$

  where const is set to a very high value, *e.g.* 10^{50}.

- Odd iterations are used to perform the stress calculation. Due to the form of $\boldsymbol{J}$ returned in the even iteration the displacements $\boldsymbol{u}$ are not changed by the FE solver as $\Delta \boldsymbol{u} \propto \boldsymbol{J}^{-1}$, *i.e.* all informations required for solving the non-local constitutive equations are readily available from the previous even iteration.

Even though the number of iterations required by the FE solver is doubled by this procedure the additional computation time is negligible as the even iterations require almost no time and inverting the special Jacoby matrix returned in these iterations is very easy due to its diagonal form. Moreover, all calculations can now be performed during a single call of the material subroutine, which gives additional optimization possibilities (see section 10.3).

10.2.4   Homogenization Iterations

In case that the Relaxed Grain Cluster scheme (section 7.2.3) is used for material point homogenization an additional iteration loop is required on the material point level to determine the deformation gradients for the individual grains and fulfill equation (7.40).

10.3   Parallelization Strategies

Most of the material models and homogenization schemes presented in this work are computationally demanding, *i.e.* simulations using these models run significantly longer

Table 10.1: Effect of domain decomposition on a direct CPFEM simulation of an 8 grain aggregate. The mesh contains $8 \times 8 \times 8$ hexahedral elements with periodic boundary conditions. The sample is deformed by 25% unidirectional tension (200 increments) or simple shear (400 increments). Results are from single runs on a 16 core Operon workstation running at $2.4\,\mathrm{GHz}$. CPU time is specified for a single domain.

| | Uniaxial tension | | | | | |
Job	unsymmetric	symmetric	ddm2	ddm4	ddm8	ddm16
CPU time (s)	3470	3640	1300	510	300	190
Wall time (s)	3480	3650	1470	570	320	210
	Simple shear					
Job	unsymmetric	symmetric	ddm2	ddm4	ddm8	ddm16
CPU time (s)	6710	5900	2470	930	560	360
Wall time (s)	6730	5910	2570	1100	600	400

than FEM simulations using standard material models as provided with the general FEM packages. Therefore, parallelization is an important way of reducing the runtime of the simulations[1].

Many FEM packages today offer different possibilities of parallelization. First there is domain decomposition. In this case the FE model is split into several parts. Each of these submodels is then solved in an individual simulation run, all of which run in parallel. As the different domains share some nodes on their boundaries some interprocess communication is required to insure continuity across the boundaries of the domains. While this communication certainly poses some overhead on the simulation the reduction of computation time is still significant as the solution procedure of FE models scales nonlinearly with the model size, *i.e.* splitting a model in half can reduce the computation time by more than a factor of two, see table 10.1 and figure 10.2. The main drawback of domain decomposition is that it can not be used in the case a non-local constitutive model is used as there is no way to obtain information from another domain, *i.e.* the scheme described in section 10.2.3 does not work. Another drawback, at least in the case of commercial FE solvers, is the fact that for running several jobs in parallel the respective licenses are required. Furthermore, domain decomposition might have some detrimental effect on the overall convergence behavior, *e.g.* most of the computations in section 8.1.1 were run using seven domains but two of them (cold band with Taylor homogenization) had to be run in a single domain. The second way to make use of parallelization offered by commercial FE software is the use of parallel solvers. In this

---

[1]This statement refers to wall time, overall CPU time is usually not reduced.
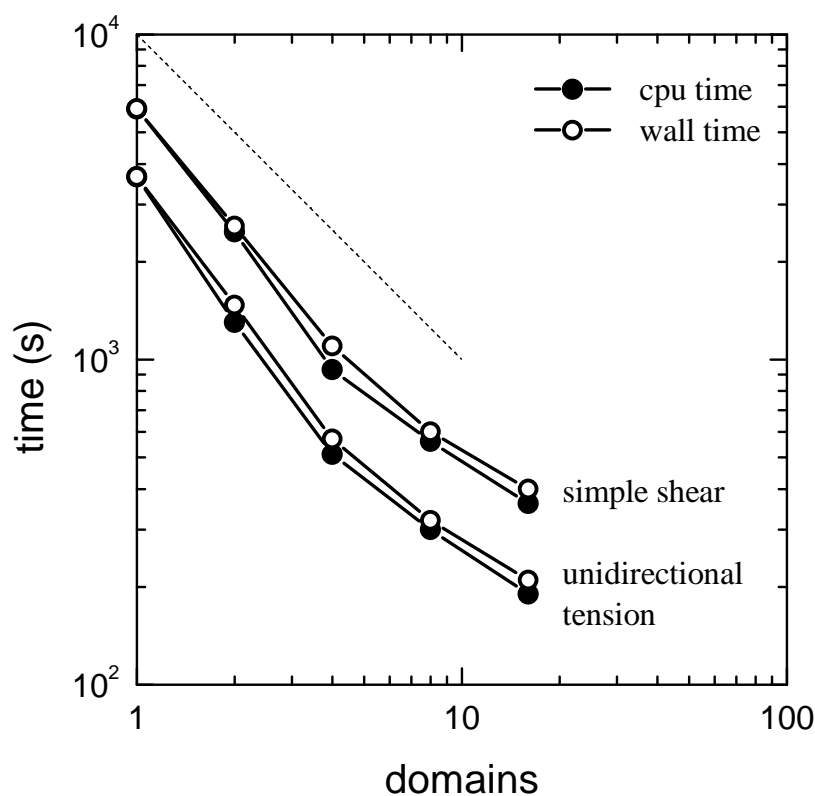
Figure 10.2: Effect of domain decomposition on a direct CPFEM simulation of an 8 grain aggregate. The mesh contains 8x8x8 hexahedral elements with periodic boundary conditions. The sample is deformed by 25 % unidirectional tension (200 increments) or simple shear (400 increments). Results are from single runs on a 16 core Operon workstation running at 2.4 GHz.

case only the solution part of the FE code runs in parallel. As this is in general realized by multi-threading usually only a single license is required. The disadvantage is that multi-threading works on single machines only, while domain decomposition is usually realized using the message passing interface (MPI) and therefore the jobs can be run on several machines in a network. With the trend towards multi-core CPUs this difference, however, becomes less and less important as single workstations can easily have 32 and more cores. As like in all cases of parallelization the incremental efficiency decreases with the number of CPUs (more precisely cores), the use of more than eight CPUs is often not efficient (see *e.g.* table 10.1, however, the efficiency certainly depends on the model used).

When domain decomposition is not usable, either due to a lack of licenses or because

a non-local material model as described in chapter 4 is used, there still remains the possibility to use parallelization in the material subroutine. The algorithm used to obtain the non-local information introduced in section 10.2.3 can also be used for parallelization. As stated in section 10.2.3 once the non-local information is collected all calculations can be performed in the first call of the subroutine in the following iteration. In fact, when using a non-local material model and fully implicit integration they have to be performed in that call. In praxis this means that one or several loops are run over all integration points of the model using the material subroutine. These loops can be easily parallelized using *e.g. OpenMP*[2]. As the collecting iteration costs almost no time the same procedure can be used for the parallelization of any material model and not only non-local ones. It has to be mentioned though that the scheme described in section 10.2.3 can only be used when all elements use the user material subroutine, as the stiffness information returned by regular material models can not be modified as required by the scheme. This is the reason why the MPIE CPFEM implementation also provides a simple J2 material model.

---

[2]Information on OpenMP can be found at http://openmp.org.

Chapter 11

Material Representation

The MPIE CPFEM implementation uses a very flexible material representation that allows the description of single crystals as well as multi-phase materials. To achieve this all material information is stored in a configuration file named `material.config`, which is read during the initialization of the material subroutine.

The file is divided into several sections. Each section starts with a label of the form `<keyword>`, where valid keywords are: `homogenization`, `microstructure`, `crystallite` `phase` and `texture`. The sections can hold multiple entries, each of which starts with a label of the form `[entryname]`, where entryname is an arbitrary string.

In the FE model a material is assigned to an element by specifying a homogenization scheme and a microstructure. For this purpose the entries in the sections are consecutively numbered so that they can be addressed by their position within the section. This way it is possible to use different materials, even using different constitutive models, within one FE model. Even though the material assignment in the FE model is by element, the properties are finally assigned by integration point, *i.e.* even though they always belong to the same material the properties of the integration points of a single element might differ in certain aspects, *e.g.* crystal orientation. If this behavior is not wanted the flag `/elementhomogenous/` can be used in the section `microstructure` to force identical behavior of all integration points of a single element.

The format of the material file entries is specified in the following.

11.1 `<homogenization>`

The homogenization schemes are discussed in section 7.2. Currently the Taylor scheme and the Relaxed Grain Cluster scheme are available in the subroutine. The keyword `type` specifies which scheme should be used, *i.e.* `isostrain` for Taylor or `RGC` for RGC. In addition, the number of grains has to be specified by the keyword `Ngrains`. While for

the Taylor scheme any number of grains can be specified, for the RGC scheme it depends
on the specified cluster size. In addition the grain dimensions and the parameters c and
ξ have to be specified for the RGC. Finally, the RGC scheme can produce some optional
output specified by the keyword (output).

Example section:

```
#------------------#
<homogenization>
#------------------#

[SX]
type isostrain
Ngrains 1

[RGC]
type RGC
ngrains 8
clustersize 2 2 2                    # product of these numbers must be equal to ngrains(!)
clusterorientation 0.0 0.0 0.0       # orientation of cluster in terms of 313 Euler-angles in degree
                                     # (random if not present)
grainsize 4.0e-6 4.0e-6 2.0e-6       # in m
overproportionality 2.0e+0           # typical range between 0.001 to 1000
scalingparameter 1.0e+1              # typical range between 0.001 to 1000
(output) constitutivework
(output) magnitudemismatch
(output) penaltyenergy
(output) volumediscrepancy
(output) averagerelaxrate
(output) maximumrelaxrate

[Taylor4]
type isostrain
Ngrains 4
```

11.2   `<microstructure>`

Each microstructure is build up by several constituents (keyword (constituent)). The
constituents are characterized by three entries: phase, texture, and fraction. Phase
and texture each refer to the number of an entry of the respective section and fraction
specifies the volume fraction of the constituent. The fractions have to add up to 1 for
each microstructure. The keyword crystallite is used to specify the output on the
single crystal level by choosing the respective entry in section <crystallite>. Finally,
as stated above, the flag /elementhomogeneous/ enforces identical properties for all
integration points of an element.

Example section:

```
#------------------#
<microstructure>
#------------------#

[aluminum_CubeSX]
/elementhomogeneous/      # put this flag to set ips identical in one element
```

```
                              # (somewhat like reduced integration)
crystallite 2
(constituent) phase 1 texture 2 fraction 1.0

[random_copper]
crystallite 1
(constituent) phase 2 texture 1 fraction 1.0

[DPsteel]
crystallite 1
(constituent) phase 3 texture 3 fraction 0.8
(constituent) phase 4 texture 4 fraction 0.2
```

11.3   <crystallite>

The section <crystallite> is exclusively used to trigger output on the single crystal
level. Each quantity is specified by the keyword (output). Possible values of this key-
word are: phase, volume, orientation (quaternion), eulerangles (Bunge notation),
grainrotation, f, fe, fp, ee, p, and s.

Example section:

```
#------------------#
<crystallite>
#------------------#

[all]
(output) phase
(output) volume
(output) orientation    # specified as quaternion
(output) eulerangles    # Bunge notation
(output) grainrotation  # deviation from initial orientation as axis (1-3) and angle in degree (4)
(output) f              # deformation gradient tensor; synonyms: "defgrad"
(output) fe             # elastic deformation gradient tensor
(output) fp             # plastic deformation gradient tensor
(output) ee             # elastic strain as Green-Lagrange tensor
(output) p              # first Piola-Kirchhoff stress tensor; synonyms: "firstpiola", "1stpiola"
(output) s              # second Piola-Kirchhoff stress tensor; synonyms: "tstar", "secondpiola", "2ndpiola"

[Eulerangles only]
(output) eulerangles
```

11.4   <phase>

The phase section can contain any number of phases. The most important entry for each
phase is the key constitution. Its value defines which constitutive model is to be used
for this phase. Valid entries are: j2, phenopowerlaw (see section 2.3), nonlocal (see
section 4.2) and dislotwin (see section 7.3). In the following lines the model parameters
required need to be set by keyword value pairs, these are, however, model dependent.
The optional keyword (output) can be used with any constitutive model to specify
additional output quantities. Its values are again model dependent.

Example section:

```
#------------------#
<phase>
#------------------#

[Aluminum_J2isotropic]

constitution          j2

(output)              flowstress
(output)              strainrate

c11                   110.9e9
c12                   58.34e9
taylorfactor          3
tau0                  31e6
gdot0                 0.001
n                     20
h0                    75e6
tausat                63e6
a                     2.25
relevantResistance    1


[Aluminum_phenopowerlaw]
# slip only
constitution          phenopowerlaw

(output)              resistance_slip
(output)              shearrate_slip
(output)              resolvedstress_slip
(output)              totalshear
(output)              resistance_twin
(output)              shearrate_twin
(output)              resolvedstress_twin
(output)              totalvolfrac

lattice_structure     fcc
Nslip                 12  0  0  0        # per family
Ntwin                  0  0  0  0        # per family

c11                   106.75e9
c12                   60.41e9
c44                   28.34e9

gdot0_slip            0.001
n_slip                20
tau0_slip             31e6               # per family
tausat_slip           63e6               # per family
a_slip                2.25
gdot0_twin            0.001
n_twin                20
tau0_twin             31e6               # per family
s_pr                  0                  # push-up factor for slip saturation due to twinning
twin_b                0
twin_c                0
twin_d                0
twin_e                0
h0_slipslip           75e6
h0_sliptwin           0
h0_twinslip           0
h0_twintwin           0
interaction_slipslip  1 1 1.4 1.4 1.4 1.4
interaction_sliptwin  1 1 1 1 1 1 1 1 1 1 1 1 1 1 1 1 1 1 1 1
```

```
interaction_twinslip    1 1 1 1 1 1 1 1 1 1 1 1 1 1 1 1
interaction_twintwin    1 1 1 1 1 1 1 1 1 1 1 1 1 1 1 1 1 1 1 1 1
relevantResistance      1

[Aluminum_nonlocal]

constitution            nonlocal
/nonlocal/

(output)                rho
(output)                rho_edge
(output)                rho_screw
(output)                rho_sgl
(output)                rho_sgl_edge
(output)                rho_sgl_edge_pos
(output)                rho_sgl_edge_neg
(output)                rho_sgl_screw
(output)                rho_sgl_screw_pos
(output)                rho_sgl_screw_neg
(output)                rho_sgl_mobile
(output)                rho_sgl_edge_mobile
(output)                rho_sgl_edge_pos_mobile
(output)                rho_sgl_edge_neg_mobile
(output)                rho_sgl_screw_mobile
(output)                rho_sgl_screw_pos_mobile
(output)                rho_sgl_screw_neg_mobile
(output)                rho_sgl_immobile
(output)                rho_sgl_edge_immobile
(output)                rho_sgl_edge_pos_immobile
(output)                rho_sgl_edge_neg_immobile
(output)                rho_sgl_screw_immobile
(output)                rho_sgl_screw_pos_immobile
(output)                rho_sgl_screw_neg_immobile
(output)                rho_dip
(output)                rho_dip_edge
(output)                rho_dip_screw
(output)                excess_rho
(output)                excess_rho_edge
(output)                excess_rho_screw
(output)                rho_forest
(output)                delta
(output)                delta_sgl
(output)                delta_dip
(output)                shearrate
(output)                resolvedstress
(output)                resolvedstress_internal
(output)                resolvedstress_external
(output)                resistance
(output)                rho_dot
(output)                rho_dot_sgl
(output)                rho_dot_dip
(output)                rho_dot_gen
(output)                rho_dot_gen_edge
(output)                rho_dot_gen_screw
(output)                rho_dot_sgl2dip
(output)                rho_dot_dip2sgl
(output)                rho_dot_ann_ath
(output)                rho_dot_ann_the
(output)                rho_dot_flux
(output)                rho_dot_flux_edge
(output)                rho_dot_flux_screw
(output)                dislocationvelocity
(output)                fluxDensity_edge_pos_x
(output)                fluxDensity_edge_pos_y
(output)                fluxDensity_edge_pos_z
(output)                fluxDensity_edge_neg_x
```

```
(output)              fluxDensity_edge_neg_y
(output)              fluxDensity_edge_neg_z
(output)              fluxDensity_screw_pos_x
(output)              fluxDensity_screw_pos_y
(output)              fluxDensity_screw_pos_z
(output)              fluxDensity_screw_neg_x
(output)              fluxDensity_screw_neg_y
(output)              fluxDensity_screw_neg_z
(output)              d_upper_edge
(output)              d_upper_screw
(output)              d_upper_dot_edge
(output)              d_upper_dot_screw

lattice_structure     fcc
Nslip                 12  0  0  0              # number of slip systems per family

c11                   106.75e9
c12                   60.41e9
c44                   28.34e9

burgers               2.86e-10  0  0  0        # Burgers vector in m
rhoSglEdgePos0        1e11  0  0  0            # Initial positive edge single dislocation density in m/m**3
rhoSglEdgeNeg0        1e11  0  0  0            # Initial negative edge single dislocation density in m/m**3
rhoSglScrewPos0       1e11  0  0  0            # Initial positive screw single dislocation density in m/m**3
rhoSglScrewNeg0       1e11  0  0  0            # Initial negative screw single dislocation density in m/m**3
rhoDipEdge0           1e8  0  0  0             # Initial edge dipole dislocation density in m/m**3
rhoDipScrew0          1e8  0  0  0             # Initial screw dipole dislocation density in m/m**3
v0                    1e-4  0  0  0            # prefactor for dislocation velocity
Q0                    3e-19                    # activation energy for dislocation glide
dDipMinEdge           1e-9  0  0  0            # minimum distance for stable edge dipoles in m
dDipMinScrew          1e-9  0  0  0            # minimum distance for stable screw dipoles in m
lambda0               100  0  0  0             # prefactor for mean free path
atomicVolume          1.7e-29
D0                    1e-4                     # prefactor for self-diffusion coefficient
Qsd                   2.3e-19                  # activation enthalpy for seld-diffusion
relevantRho           1e3                      # dislocation density considered relevant
interaction_SlipSlip  0.122  0.122  0.625  0.07  0.137  0.122  # Dislocation interaction coefficient


[TWIP steel FeMnC]

constitution          dislotwin

#(output)             edge_density
#(output)             dipole_density
#(output)             shear_rate_slip
#(output)             mfp_slip
#(output)             resolved_stress_slip
#(output)             threshold_stress_slip
#(output)             twin_fraction
#(output)             shear_rate_twin
#(output)             mfp_twin
#(output)             resolved_stress_twin
#(output)             threshold_stress_twin

### Material parameters ###
lattice_structure fcc
C11                   175.0e9        # From Music et al. Applied Physics Letters 91, 191904 (2007)
C12                   115.0e9
C44                   135.0e9
grainsize             2.0e-5         # Average grain size [m]
SolidSolutionStrength 1.5e8          # Strength due to elements in solid solution

### Dislocation glide parameters ###
Nslip                 12 0 0 0
slipburgers           2.56e-10 0 0 0 # Burgers vector of slip system [m]
```

```
rhoedge0            1.0e12 0 0 0   # Initial dislocation density [m/m**3]
rhoedgedip0         1.0 0 0 0      # Initial dislocation density [m/m**3]
Qedge               3.7e-19 0 0 0  # Activation energy for dislocation glide [J]
v0                  1.0e-4 0 0 0   # Initial glide velocity [m/s]
CLambdaSlip         10.0 0 0 0     # Adj. parameter controlling dislocation mean free path
D0                  4.0e-5         # Vacancy diffusion prefactor [m**2/s]
Qsd                 4.5e-19        # Activation energy for climb [J]
pexponent           1.0            # p-exponent in glide velocity
qexponent           1.0            # q-exponent in glide velocity
Catomicvolume       1.0            # Adj. parameter controlling the atomic volume [in b]
Cedgedipmindistance 1.0            # Adj. parameter controlling the minimum dipole distance [in b]
relevantRho         1.0e-200
interactionSlipSlip 0.122 0.122 0.625 0.07 0.137 0.122 # Interaction coefficients (Kubin et al. 2008)

### Twinning parameters ###
Ntwin               12
twinburgers         1.47e-10       # Burgers vector of twin system [m]
twinsize            5.0e-8         # Twin stack mean thickness [m]
L0                  442.0          # Length of twin nuclei in Burgers vectors
maxtwinfraction     1.0            # Maximum admissible twin volume fraction
Ndot0               0.0            # Number of potential sources per volume per time [1/m**3.s]
rexponent           10.0           # r-exponent in twin formation probability
Cmfptwin            1.0            # Adj. parameter controlling twin mean free path
Cthresholdtwin      1.0            # Adj. parameter controlling twin threshold stress
interactionSlipTwin 0.0 1.0        # Dislocation-Twin interaction coefficients
interactionTwinTwin 0.0 1.0        # Twin-Twin interaction coefficients
```

11.5 `<texture>`

Material textures can be described according to the two methods introduced in section 7.1, *i.e.* the texture component method or the hybridIA scheme. The texture component entry knows the two component types introduced in section 7.1.1, namely fiber and spherical components, indicated by the keywords (`fiber`) and (`gauss`), respectively. If the volume fractions of all components specified do not add up to 1, random orientations are assigned to the remaining volume fraction. In particular, this means that the seemingly empty entry [`random`] in the example below creates a random texture. For the hybridIA scheme the file containing the ODF intensities has to be specified.

Example section:

```
#------------------#
<texture>
#------------------#

[random]

[CubeSX]
(gauss) phi1 0.0 Phi 0.0 phi2 0.0 scatter 0.0 fraction 1.0

[example_fiber]
#   fiber axis in spherical coordinates: alpha crystal system, beta sample system
(fiber)   alpha1 0.0 alpha2 10.0 beta1 20.0 beta2 30.0 scatter 10.0 fraction 1.0

[experimental_ODF]
(hybridIA) experimental_texture.odf
```

Chapter 12

Conclusions and Outlook

The CPFE method is a powerful and comprehensive theoretical approach for the inclusion of micro-mechanical models and concepts in a unified theory of crystal plasticity including proper boundary condition treatment capable of treating a wide range of mechanical problems in materials science and engineering. The formulation of the constitutive laws within the CPFE approach allows the user to map such different deformation mechanisms as dislocation slip, twinning, grain boundary shear and, in part, also their interactions, rendering the method a multi-mechanism and multi-physics approach.

Its greatest potential lies, therefore, in the mesoscopic (inter-grain scale, grain cluster scale) and microscopic regime (grain scale, intra-grain scale) as demonstrated in part I of this thesis. It was further shown that the CPFE method, when formulated in conjunction with an appropriate homogenization scheme, is also suited to predict macroscopic mechanical behavior in metal forming, tool design, and process engineering (part II of this thesis). The particular strength of the finite element method lies in studying the influence of boundary conditions on mechanical or microstructural predictions. This advantage renders the CPFE method an ideal companion for the synergistic analysis of complex mechanical tests where a detailed sensitivity check is of relevance for a proper interpretation of the experimental observations.

Another more practical advantage of the method is that it can be used in conjunction with commercial or academic finite element solvers in the form of user-defined material subroutines. The MPIE implementation described in part III of this thesis is available as freeware for non-commercial use upon request[1].

In summary, the CPFEM is an extremely versatile method, however, up to now this versatility is not fully exploited by the CPFEM implementations. The MPIE implementation with its strictly modular concept for the first time combines all aspects described above in one code. The implementation of additional constitutive models just requires the development of one additional module that contains in total nine subroutines and

---

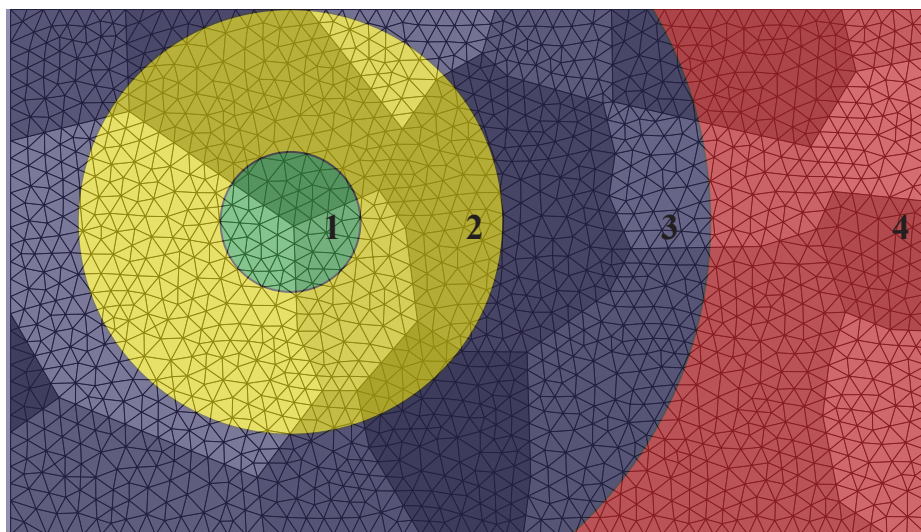[1]The author can be contacted at f.roters@mpie.de.

Figure 12.1: Schematic drawing of a hierarchical FE model of an oligocrystal. Only the center region of interest uses the complex dislocation density based non-local model (1), while the outer regions use increasingly simpler models: local dislocation density based (2), phenomenological (3), and J2 (4). These regions provide reasonable boundary conditions to the innermost region of interest, while at the same time minimizing the computational effort.

functions. It can therefore be expected that in the future a number of additional constitutive models will be added to the code. Actually, at the time being a model for Titanium is under development. It is a dislocation density based model including twinning and adopted to the hexagonal crystal structure.

According to chapter 9 the crystal plasticity user subroutines just provide a material point model and in case of CPFEM the FEM is used to solve the elasto-plastic boundary value problem. However, also other solvers could be used for this purpose. Lebensohn facilitated a method based on direct Fast Fourier Transformation (FFT, Lebensohn, 2001; Lebensohn et al., 2008) originally introduced by Moulinec and Suquet (1998). Though being less general than the FEM, *e.g.* being restricted to periodic structures, this method is computationally extremely fast and offers a lot of potential for future application. To exploit this potential in combination with multiple constitutive models a new interface module is currently developed to combine the MPIE crystal plasticity implementation with these FFT based solvers.

Finally, the combination of different homogenization schemes and constitutive models in one code offers for the first time the possibility to combine them within one FE model. This is especially of interest for building so called *hierarchical* models. One of the main deficiencies of complex non-local constitutive models like the one presented in section 4.2 is the long computing time. Therefore, they can only be applied to

rather small models including just a few crystals. This has the drawback that idealized boundary conditions have to be applied. Figure 12.1 shows how this shortcoming can be overcome by combining several constitutive models in one FE model. Only the innermost region uses the complex dislocation density based non-local model and is embedded into several regions using increasingly simpler constitutive models. While saving a lot of computing effort these regions are still sufficient to provide realistic boundary conditions to the center region of interest.

Bibliography

Afrin and Ngan 2006 N. Afrin and A. H. W. Ngan. Creep of micron-sized Ni_3Al columns. *Scripta Mater.*, 54:7–12, 2006.

Cited on page 72.

Allain et al. 2002 S. Allain, J.-P. Chateau, and O. Bouaziz. Constitutive model of the TWIP effect in a polycrystalline high manganese content austenitic steel. *Steel Res.*, 73:299–302, 2002.

Cited on page 151.

Allain et al. 2004 S. Allain, J.-P. Chateau, and O. Bouaziz. A physical model of the twinning-induced plasticity effect in a high manganese austenitic steel. *Mat. Sci. Eng. A*, 387–389:143–147, 2004.

Cited on page 173.

Anand and Su 2005 L. Anand and C. Su. A theory for amorphous viscoplastic materials undergoing finite deformations, with application to metallic glasses. *J. Mech. Phys. Solids*, 53:1362–1396, 2005.

Cited on page 6.

Anand and Su 2007 L. Anand and C. Su. A constitutive theory for metallic glasses at high homologous temperatures. *Acta Mater.*, 55:3755–3747, 2007.

Cited on page 6.

Arsenlis and Parks 1999 A. Arsenlis and D. M. Parks. Crystallographic aspects of geometrically-necessary and statistically-stored dislocation density. *Acta Mater.*, 47:1597–1611, 1999.

Cited on pages 6, 16, 23, 24, and 140.

Arsenlis and Parks 2002 A. Arsenlis and D. M. Parks. Modeling the evolution of crystallographic dislocation density in crystal plasticity. *J. Mech. Phys. Solids*, 50:1979–2009, 2002.

Cited on pages 6, 16, 23, 24, 25, 28, 38, and 60.

Arsenlis et al. 2004 A. Arsenlis, D. M. Parks, R. Becker, and V. V. Bulatov. On the evolution of crystallographic dislocation density in non-homogeneously deforming crystals. *J. Mech. Phys. Solids*, 52:1213–1246, 2004.

Cited on pages 3, 6, 16, 23, 24, and 25.

Asaro and Rice 1977 R. J. Asaro and J. R. Rice. Strain localization in ductile single crystals. *J. Mech. Phys. Solids*, 25:309–338, 1977.

Cited on page 6.

Ashby 1970 M. F. Ashby. The deformation of plastically non-homogeneous materials. *Phil. Mag.*, 21:399–424, 1970.

Cited on page 8.

Bachu and Kalidindi 1998 V. Bachu and S. R. Kalidindi. On the accuracy of the predictions of texture evolution by the finite element technique for fcc polycrystals. *Mat. Sci. Eng. A*, 257:108–117, 1998.

Cited on pages 16 and 114.

Bate and An 2004 P. S. Bate and Y. G. An. Plastic anisotropy in AA5005 Al-1Mg: predictions using crystal plasticity finite element analysis. *Scripta Mater.*, 51:973–977, 2004.
Cited on page 114.

Beaudoin et al. 1996 A. J. Beaudoin, H. Mecking, and U. F. Kocks. Development of localized orientation gradients in fcc polycrystals. *Philos. Mag. A*, 73:1503–1517, 1996.
Cited on page 16.

Becker 1991 R. Becker. Analysis of texture evolution in channel die compression — I. Effects of grain interaction. *Acta Metall. Mater.*, 39:1211–1230, 1991.
Cited on pages 16 and 19.

Becker 1998 R. Becker. Effects of strain localization on surface roughening during sheet forming. *Acta Mater.*, 46:1385–1401, 1998.
Cited on page 10.

Becker et al. 1991 R. Becker, J. F. Butler, H. Hu, and L. A. Lalli. Analysis of an Aluminum Single Crystal with Unstable Initial Orientation (001) [111] in Channel Die Compression. *Metall. Trans. A*, 22:45–58, 1991.
Cited on page 16.

Bilby 1955 B. A. Bilby. Types of dislocation source. In *Report of the Conference on Defects in Crystalline Solids (Bristol, 1954)*, pages 124–133. The Physical Society, London, UK, 1955.
Cited on pages 139 and 140.

Bishop and Hill 1951a J. F. W. Bishop and R. Hill. A Theory of the Plastic Distortion of a Polycrystalline Aggregate under combined stresses. *Phil. Mag.*, 42:414–427, 1951a.
Cited on page 3.

Bishop and Hill 1951b J. F. W. Bishop and R. Hill. A Theoretical Derivation of the Plastic Properties of a Polycrystalline Face Centered Metal. *Phil. Mag.*, 42:1298–1307, 1951b.
Cited on page 3.

Bouvier and Needleman 2006 S. Bouvier and A. Needleman. Effect of the number and orientation of active slip systems on plane strain single crystal indentation. *Modelling Simul. Mater. Sci. Eng.*, 14:1105–1125, 2006.
Cited on page 93.

Brown 2007 L. M. Brown. Slip Circle Constructions for Inhomogeneous Rotational Flow. *Mat. Sci. Forum*, 550:105–117, 2007.
Cited on page 93.

Bunge 1982 H. J. Bunge. *Texture Analysis in Materials Science.* Butterworths, London, 1982.
Cited on pages 113 and 114.

Cheong and Busso 2004 K.-S. Cheong and E. P. Busso. Discrete dislocation density modelling of single phase FCC polycrystal aggregates. *Acta Mater.*, 52:5665–5675, 2004.
Cited on page 6.

Clark et al. 1992 W. A. T. Clark, R. H. Wagoner, Z. Y. Shen, T. C. Lee, I. M. Robertson, and H. K. Birnbaum. On the criteria for slip transmission across interfaces in polycrystals. *Scripta Metall. Mater.*, 26:203–206, 1992.
Cited on page 24.

Courant 1943 R. Courant. Variational methods for the solution of problems of equilibrium and vibrations. *Bull. Amer. Math. Soc.*, 49:1–23, 1943.
Cited on page 15.

Crumbach et al. 2004 M. Crumbach, M. Goerdeler, G. Gottstein, L. Neumann, H. Aretz, and R. Kopp. Through-process texture modelling of aluminium alloys. *Modelling Simul. Mater. Sci. Eng.*, 12:S1–S18, 2004.
Cited on pages 133 and 136.

Crumbach et al. 2006a M. Crumbach, M. Goerdeler, and G. Gottstein. Modelling of recrystallisation textures in aluminium alloys: I. Model set-up and integration. *Acta Mater.*, 54:3275–3289, 2006a.

Cited on pages 133 and 136.

Crumbach et al. 2006b M. Crumbach, M. Goerdeler, and G. Gottstein. Modelling of recrystallisation textures in aluminium alloys: II. Model performance and experimental validation. *Acta Mater.*, 54:3291–3306, 2006b.

Cited on pages 133 and 136.

Cuitiño and Ortiz 1992 A. M. Cuitiño and M. Ortiz. Computational modelling of single crystals. *Modelling Simul. Mater. Sci. Eng.*, 1:225–263, 1992.

Cited on page 191.

Curtin and Miller 2003 W. A. Curtin and R. E. Miller. Atomistic/continuum coupling in computational materials science. *Modelling Simul. Mater. Sci. Eng.*, 11:R33–R68, 2003.

Cited on page 3.

Dassault Systèmes 2010 *Abaqus User Subroutines Reference Manual Version 6.10*. Dassault Systèmes, 2010.

Cited on page 187.

Delannay et al. 2002 L. Delannay, S. R. Kalidindi, and P. Van Houtte. Quantitative prediction of textures in aluminium cold rolled to moderate strains. *Mat. Sci. Eng. A*, 336: 233–244, 2002.

Cited on pages 132 and 136.

Demir et al. 2009 E. Demir, D. Raabe, N. Zaafarani, and S. Zaefferer. Experimental investigation of geometrically necessary dislocations beneath small indents of different depths using EBSD tomography. *Acta Mater.*, 57:559–569, 2009.

Cited on page 8.

Demir et al. 2010 E. Demir, D. Raabe, and F. Roters. The mechanical size effect as a mean-field breakdown phenomenon: Example of microscale single crystal beam bending. *Acta Mater.*, 58:1876–1886, 2010.

Cited on page 8.

Dimiduk et al. 2005 D. M. Dimiduk, M. D. Uchic, and T. A. Parthasarathy. Size affected single slip behavior of pure Ni microcrystals. *Acta Mater.*, 53:4065–4077, 2005.

Cited on page 72.

Eisenlohr and Roters 2008 P. Eisenlohr and F. Roters. Selecting a set of discrete orientations for accurate texture reconstruction. *Comp. Mater. Sci.*, 42:670–678, 2008.

Cited on pages 16 and 120.

Eisenlohr et al. 2009 P. Eisenlohr, D. D. Tjahjanto, T. Hochrainer, F. Roters, and D. Raabe. Comparison of texture evolution in fcc metals predicted by various grain cluster homogenization schemes. *Int. J. Mat. Res.*, 100:500–509, 2009.

Cited on page 148.

ESI Group 2004 *PAM-STAMP 2G, Version 2004.1 Standard. Stamping solutions manual*. ESI Group, Paris, 2004.

Cited on pages 181 and 183.

Evers et al. 2002 L. P. Evers, D. M. Parks, W. A. M. Brekelmans, and M. G. D. Geers. Crystal plasticity model with enhanced hardening by geometrically necessary dislocation accumulation. *J. Mech. Phys. Solids*, 50:2403–2424, 2002.

Cited on pages 6, 23, and 24.

Evers et al. 2004a L. P. Evers, W. A. M. Brekelmans, and M. G. D. Geers. Non-local crystal plasticity model with intrinsic SSD and GND effects. *J. Mech. Phys. Solids*, 52:2379–2401, 2004a.

Cited on pages 6, 23, and 24.

Evers et al. 2004b L. P. Evers, W. A. M. Brekelmans, and M. G. D. Geers. Scale dependent crystal plasticity framework with dislocation density and grain boundary effects. *Int. J. Solids Struct.*, 41:5209–5230, 2004b.

Cited on pages 6, 23, 24, and 25.

Fedosseev and Raabe 1994 A. Fedosseev and D. Raabe. Application of the method of superposition of harmonic currents for the simulation of inhomogeneous deformation during hot rolling of FeCr. *Scripta Metall.*, 30:1–6, 1994.

Cited on page 162.

Feyel and Chaboche 2000 F. Feyel and J. L. Chaboche. FE^2 multiscale approach for modelling the elastoviscoplastic behaviour of long fibre SiC/Ti composite materials. *Comput. Methods Appl. Mech. Eng.*, 183:309–330, 2000.

Cited on page 133.

Fleck and Hutchinson 1997 N. A. Fleck and J. W. Hutchinson. *Advances in Applied Mechanics*, volume 33, chapter Strain gradient plasticity, pages 1825–1857. Academic Press, New York, 1997.

Cited on page 16.

Fleck et al. 1994 N. A. Fleck, G. M. Muller, M. F. Ashby, and J. W. Hutchinson. Strain gradient plasticity: Theory and experiment. *Acta Metall. Mater.*, 42:475–487, 1994.

Cited on page 16.

Fullman 1953 R. L. Fullman. Measurement of particle sizes in opaque bodies. *Trans. Met. Soc. AIME*, 197:447–452, 1953.

Cited on page 151.

Gao and Huang 2003 H. Gao and Y. Huang. Geometrically necessary dislocation and size-dependent plasticity. *Scripta Mater.*, 48(2):113–118, 2003.

Cited on page 16.

Gao et al. 1999 H. Gao, Y. Huang, W. D. Nix, and J. W. Hutchinson. Mechanism-based strain gradient palsticity — I. Theory. *J. Mech. Phys. Solids*, 47:1239–1263, 1999.

Cited on page 16.

Greer et al. 2005 J. R. Greer, W. C. Oliver, and W. D. Nix. Size dependence of mechanical properties of gold at the micronscale in the absence of strain gradients. *Acta Mater.*, 53: 1821–1830, 2005.

Cited on page 72.

Gutierrez-Urrutia et al. 2009 I. Gutierrez-Urrutia, S. Zaefferer, and D. Raabe. Electron channeling contrast imaging of twins and dislocations in twinning-induced plasticity steels under controlled diffraction conditions in a scanning electron microscope. *Scripta Mater.*, 61:737–740, 2009.

Cited on page 176.

Harewood and McHugh 2007 F. J. Harewood and P. E. McHugh. Comparison of the implicit and explicit finite element methods using crystal plasticity. *Comp. Mater. Sci.*, 39: 481–494, 2007.

Cited on page 192.

Harren and Asaro 1989 S. V. Harren and R. J. Asaro. Nonuniform deformations in polycrystals and aspects of the validity of the Taylor model. *J. Mech. Phys. Solids*, 37:191–232, 1989.

Cited on page 15.

Harren et al. 1988 S. V. Harren, H. Dève, and R. J. Asaro. Shear band formation in plane strain compression. *Acta Metall.*, 36:2435–2480, 1988.

Cited on page 15.

Helming 1996 K. Helming. *Texturapproximation durch Modellkomponenten.* Cuvillier Verlag Göttingen, 1996.

Cited on pages 116, 160, and 161.

Helming et al. 1994 K. Helming, R. A. Schwarzer, B. Rauschenbach, S. Geier, B. Leiss, H. Wenk, K. Ullemeier, and J. Heinitz. Texture estimates by means of components. *Z. Metallkd.*, 85:545–553, 1994.

Cited on pages 116, 160, and 161.

Helming et al. 1998 K. Helming, R. Tamm, and B. Fels. An automated component method. *Mat. Sci. Forum*, 273–275:119–124, 1998.

Cited on page 114.

Hill 1948 R. Hill. A theory of the yielding and plastic flow of anisotropic metals. *Proc. R. Soc. Lond. A*, 193:281–297, 1948.

Cited on pages 162, 172, and 182.

Hirth and Lothe 1982 J. P. Hirth and J. Lothe. *Theory of Dislocations.* Krieger Publishing Company–John Wiley & Sons, Ltd., 2nd edition, 1982.

Cited on pages 46, 49, 149, and 150.

Hosford 1993 W. F. Hosford. *The mechanics of crystals and textured polycrystals.* Oxford University Press, 1993.

Cited on page 104.

Hutchinson 1976 J. W. Hutchinson. Bounds and self-consistent estimates for creep of polycrystalline materials. *Proc. R. Soc. Lond. A*, 348:101–127, 1976.

Cited on page 18.

Kalidindi 1998 S. R. Kalidindi. Incorporation of deformation twinning in crystal plasticity models. *J. Mech. Phys. Solids*, 46:267–290, 1998.

Cited on pages 6, 16, 148, and 157.

Kalidindi 2001 S. R. Kalidindi. Modeling anisotropic strain hardening and deformation textures in low stacking fault energy fcc metals. *Int. J. Plasticity*, 17:837–860, 2001.

Cited on pages 16 and 157.

Kalidindi et al. 1992 S. R. Kalidindi, C. A. Bronkhorst, and L. Anand. Crystallographic texture evolution in bulk deformation processing of fcc metals. *J. Mech. Phys. Solids*, 40: 537–569, 1992.

Cited on page 191.

Kiener et al. 2006 D. Kiener, R. Pippan, C. Motz, and H. Kreuzer. Microstructural evolution of the deformed volume beneath microindents in tungsten and copper. *Acta Mater.*, 54: 2801–2811, 2006.

Cited on page 93.

Kocks 1966 U. F. Kocks. A statistical theory of flow stress and work-hardening. *Phil. Mag.*, 13:541, 1966.

Cited on page 19.

Kocks 1976 U. F. Kocks. Laws of work-hardening and low temperature creep. *J. Eng. Mater. Tech.*, 98:76–83, 1976.

Cited on pages 19 and 38.

Kocks et al. 1975 U. F. Kocks, A. S. Argon, and M. F. Ashby. In B. Chalmers and J. W. Christian, editors, *Thermodynamics and kinetics of slip*, volume 19 of *Progress in Materials Science.* Pergamon Press, 1975.

Cited on page 156.

Kocks et al. 1991 U. F. Kocks, J. S. Kallend, and A. C. Biondo. Accurate representation of gerenal textures by a set of weighted grains. *Texture Microstruct.*, 14–18:199–204, 1991.

Cited on page 114.

Konrad et al. 2006 J. Konrad, S. Zaefferer, and D. Raabe. Investigation of orientation gradients around a hard Laves particle in a warm rolled Fe3Al-based alloy by a 3D EBSD-FIB technique. *Acta Mater.*, 54:1369–1380, 2006.

Cited on page 97.

Kouznetsova et al. 2001 V. Kouznetsova, W. A. M. Brekelmans, and F. P. T. Baaijens. An approach to micro-macro modeling of heterogeneous materials. *Computational Mechanics*, 27:37–48, 2001.

Cited on page 133.

Kouznetsova et al. 2002 V. Kouznetsova, M. G. D. Geers, and W. A. M. Brekelmans. Multi-scale constitutive modelling of heterogeneous materials with a gradient-enhanced computational homogenization scheme. *Int. J. Numer. Meth. Eng.*, 54:1235–1260, 2002.

Cited on page 133.

Kraska et al. 2009 M. Kraska, M. Doig, D. Tikhomirov, D. Raabe, and F. Roters. Virtual material testing for stamping simulations based on polycrystal plasticity. *Comp. Mater. Sci.*, 46:383–392, 2009.

Cited on page 10.

Kröner 1958 E. Kröner. *Kontinuumstheorie der Versetzungen und Eigenspannungen.* Springer, Berlin, 1958.

Cited on page 8.

Kröner 1961 E. Kröner. On the plastic deformation of polycrystals. *Acta Metall.*, 9:155–161, 1961.

Cited on page 3.

Kröner 1981 E. Kröner. *Physics of defects*, chapter Continuum theory of defects, page 217. North-Holland Publishing Company, Amsterdam, Netherlands, 1981.

Cited on page 8.

Kubin et al. 2008 L. Kubin, B. Devincre, and T. Hoc. Modeling dislocation storage rates and mean free paths in face-centered cubic crystals. *Acta Mater.*, 56:6040–6049, 2008.

Cited on page 41.

Kuo 2004 J.-C. Kuo. *Mikrostrukturmechanik von Bikristallen mit Kippkorngrenzen.* PhD thesis, RWTH Aachen, 2004.

Cited on page 58.

Kuo et al. 2003 J.-C. Kuo, S. Zaefferer, Z. Zhao, M. Winning, and D. Raabe. Deformation Behaviour of Aluminium-Bicrystals. *Adv. Eng. Mater.*, 5:563–566, 2003.

Cited on pages 8 and 23.

Kysar et al. 2007 J. W. Kysar, Y. X. Gan, T. L. Morse, X. Chen, and M. E. Jones. High strain gradient plasticity associated with wedge indentation into face-centered cubic single crystals: Geometrically necessary dislocation densities. *J. Mech. Phys. Solids*, 55:1554–1573, 2007.

Cited on page 93.

Lan et al. 2005 Y. J. Lan, N. M. Xiao, D. Z. Li, and Y. Y. Li. Mesoscale simulation of deformed austenite decomposition into ferrite by coupling a cellular automaton method with a crystal plasticity finite element model. *Acta Mater.*, 53:991–1003, 2005.

Cited on page 6.

Larson et al. 2002 B. C. Larson, W. Yang, G. E. Ice, J. G. Swadener, J. D. Budai, and J. Z. Tischler. Three-dimensional X-ray structural microscopy with submicrometre resolution. *Nature*, 415:887–890, 2002.

Cited on pages 8 and 93.

Lücke et al. 1981 K. Lücke, J. Pospiech, K. H. Virnich, and J. Jura. On the problem of the reproduction of the true orientation distribution from pole figures. *Acta Metall.*, 29:167–185, 1981.

Cited on page 115.

Lücke et al. 1986 K. Lücke, J. Pospiech, J. Jura, and J. Hirsch. On the presentation of orientation distribution functions by model functions. *Z. Metallkd.*, 77:312–321, 1986.

Cited on page 115.

Lebensohn 2001 R. A. Lebensohn. N-site modeling of a 3D viscoplastic polycrystal using Fast Fourier Transform. *Acta Mater.*, 49:2723–2737, 2001.

Cited on pages 133 and 210.

Lebensohn and Tomé 1993 R. A. Lebensohn and C. N. Tomé. A self-consistent anisotropic approach for the simulation of plastic deformation and texture development of polycrystals: Application to zirconium alloys. *Acta Metall. Mater.*, 41:2611–2624, 1993.

Cited on page 133.

Lebensohn et al. 2008 R. A. Lebensohn, R. Brenner, O. Castelnau, and A. D. Rollett. Orientation image-based micromechanical modelling of subgrain texture evolution in polycrystalline copper. *Acta Mater.*, 56:3914–3926, 2008.

Cited on page 210.

Lee 1969 E. H. Lee. Elastic-plastic deformation at finite strains. *J. Appl. Mech. ASME*, 36:1–6, 1969.

Cited on page 17.

Leffers and Juul Jensen 1986 T. Leffers and D. Juul Jensen. Evaluation of the effect of initial texture on the development of deformation texture. *Texture Microstruct.*, 6:231–163, 1986.

Cited on pages 120 and 131.

Lloyd et al. 2005 S. J. Lloyd, A. Castellero, F. Giuliani, Y. Long, K. K. McLaughlin, J. M.Molina-Aldareguia, N. A. Stelmashenko, L. J. Vandeperre, and W. J. Clegg. Observations of nanoindents via cross-sectional transmission electron microscopy: a survey of deformation mechanisms. *Proc. R. Soc. Lond. A*, 461:2521–2543, 2005.

Cited on page 93.

Ma and Roters 2004 A. Ma and F. Roters. A constitutive model for fcc single crystals based on dislocation densities and its application to uniaxial compression of aluminium single crystals. *Acta Mater.*, 52:3603–3612, 2004.

Cited on pages 6, 27, 28, 29, 37, 94, and 96.

Ma et al. 2006a A. Ma, F. Roters, and D. Raabe. A dislocation density based constitutive model for crystal plasticity FEM including geometrically necessary dislocations. *Acta Mater.*, 54:2169–2179, 2006a.

Cited on pages 6, 16, 27, 30, 94, and 196.

Ma et al. 2006b A. Ma, F. Roters, and D. Raabe. On the consideration of interactions between dislocations and grain boundaries in crystal plasticity finite element modeling- theory, experiments, and simulations. *Acta Mater.*, 54:2181–2194, 2006b.

Cited on pages 6, 16, 24, 27, and 32.

Ma et al. 2006c A. Ma, F. Roters, and D. Raabe. Studying the effect of grain boundaries in dislocation density based crystal plasticity finite element simulations. *Int. J. Solids Struct.*, 43:7287–7303, 2006c.

Cited on page 32.

Maaß et al. 2007 R. Maaß, S. Van Petegem, H. Van Swygenhoven, P. M. Derlet, C. A. Volkert, and D. Grolimund. Time resolved Laue diffraction of deforming micropillars. *Phys. Rev. Lett.*, 99:145505, 2007.

Cited on pages 8 and 91.

Maaß et al. 2009 R. Maaß, S. Van Petegem, D. Ma, J. Zimmermann, D. Grolimund, F. Roters, H. Van Swygenhoven, and D. Raabe. Smaller is stronger: The effect of strain hardening. *Acta Mater.*, 57:5996–6005, 2009.

Cited on pages 8, 73, 76, 90, and 91.

Mahajan and Chin 1973 S. Mahajan and G. Y. Chin. Formation of deformation twins in f.c.c. crystals. *Acta Metall.*, 21:1353–1363, 1973.

Cited on pages 152 and 153.

Maniatty et al. 1992 A. M. Maniatty, P. R. Dawson, and Y.-S. Lee. A time integration algorithm for elasto-viscoplastic cubic crystals applied to modelling polychrystalline deformation. *Int. J. Numer. Meth. Eng.*, 35:1565–1588, 1992.

Cited on page 191.

Marketz et al. 2002 W. T. Marketz, F. D. Fischer, F. Kauffmann, G. Dehm, T. Bidlingmaier, A. Wanner, and H. Clemens. On the role of twinning during room temperature deformation of TiAl based alloys. *Mat. Sci. Eng. A*, 329–331:177–183, 2002.

Cited on page 6.

McLaughlin et al. 2005 K. K. McLaughlin, N. A. Stelmashenko, S. J. Lloyd, L. J. Vandeperre, and W. J. Clegg. Measurement of crystal lattice rotations under nanoindents in copper. *Mater. Res. Soc. Symp. Proc.*, 841:3–8, 2005.

Cited on page 93.

Mecking and Kocks 1986 H. Mecking and U. F. Kocks. Kinetics of flow and strain hardening. *Acta Metall.*, 29:1865–1875, 1986.

Cited on pages 19 and 38.

Melchior and Delannay 2006 M. A. Melchior and L. Delannay. A texture discretization technique adapted to polycrystalline aggregates with non-uniform grain size. *Comp. Mater. Sci.*, 37:557–564, 2006.

Cited on pages 16 and 115.

Meng et al. 2007 L. Meng, P. Yang, Q. Xie, H. Ding, and Z. Tang. Dependence of deformation twinning on grain orientation in compressed high manganese steels. *Scripta Mater.*, 56: 931–934, 2007.

Cited on page 157.

Miehe et al. 1999 C. Miehe, J. Schröder, and J. Schotte. Computational homogenization analysis in finite plasticity Simulation of texture development in polycrystalline materials. *Comput. Methods Appl. Mech. Eng.*, 171:387–418, 1999.

Cited on page 133.

Miehe et al. 2002 C. Miehe, J. Schotte, and M. Lambrecht. Homogenization of inelastic solid materials at finite strains based on incremental minimization principles. Application to the texture analysis of polycrystals. *J. Mech. Phys. Solids*, 50:2123–2167, 2002.

Cited on page 133.

Mika and Dawson 1998 D. P. Mika and P. R. Dawson. Effects of grain interaction on deformation in polycrystals. *Mat. Sci. Eng. A*, 257:62–76, 1998.

Cited on page 16.

Molinari et al. 1987 A. Molinari, G. R. Canova, and S. Ahzi. A self-consistent approach of the large deformation polycrystal viscoplasticity. *Acta Metall.*, 35:2983–2994, 1987.

Cited on page 133.

Moulinec and Suquet 1998 H. Moulinec and P. Suquet. A numerical method for computing the overall response of nonlinear composites with complex microstructure. *Comput. Methods Appl. Mech. Eng.*, 157:69–94, 1998.

Cited on pages 133 and 210.

MSC 2010 *MSC.Marc user's manual 2010, User Subroutines and Special Routines, Volume D.* MSC, 2010.

Cited on page 187.

Nakamachi et al. 2001 E. Nakamachi, C. L. Xie, and M. Harimoto. Drawability assessment of BCC steel sheet by using elastic/crystalline viscoplastic finite element analyses. *Int. J. Mech. Sci.*, 43:631–652, 2001.

Cited on page 10.

Nemat-Nasser et al. 1998 S. Nemat-Nasser, L. Ni, and T. Okinaka. A constitutive model for fcc crystals with application to polycrystalline OFHC copper. *Mech. Mater.*, 30:325–341, 1998.

Cited on page 30.

Nix and Gao 1998 W. D. Nix and H. Gao. Indentation size effects in crystalline materials: a law of strain gradient plasticity. *J. Mech. Phys. Solids*, 46:411–425, 1998.

Cited on page 16.

Nix et al. 2007 W. D. Nix, J. R. Greer, G. Feng, and E. T. Lilleodden. Deformation at the nanometer and micrometer length scales: Effects of strain gradients and dislocation starvation. *Thin Solid Films*, 515:3152–3157, 2007.

Cited on page 72.

Nye 1953 J. F. Nye. Some geometrical relations in dislocated crystals. *Acta Metall.*, 1:153–162, 1953.

Cited on pages 8, 24, 30, and 140.

Orowan 1934 E. Orowan. Zur Krsitallplastizität I.–III. *Z. Phys.*, 89:605–659, 1934.

Cited on pages 15 and 27.

Peirce et al. 1982 D. Peirce, R. J. Asaro, and A. Needleman. An analysis of nonuniform and localized deformation in ductile single crystals. *Acta Metall.*, 30:1087–1119, 1982.

Cited on pages 6, 15, and 18.

Peirce et al. 1983 D. Peirce, R. J. Asaro, and A. Needleman. Material rate dependence and localized deformation in crystalline solids. *Acta Metall.*, 31:1951–1976, 1983.

Cited on pages 18 and 191.

Polanyi 1934 M. Polanyi. Über eine Art Gitterstörung, die einen Kristall plastisch machen könnte. *Z. Phys.*, 89:660–664, 1934.

Cited on page 15.

Raabe 1995 D. Raabe. Simulation of rolling textures of bcc metals under consideration of grain interactions and 110, 112 and 123 slip planes. *Mat. Sci. Eng. A*, 197:31–37, 1995.

Cited on page 162.

Raabe and Lücke 1993 D. Raabe and K. Lücke. Textures of ferritic stainless steels. *Mat. Sci. Tech.*, 9:302–312, 1993.

Cited on page 162.

Raabe and Roters 2004 D. Raabe and F. Roters. Using texture components in crystal plasticity finite element simulations. *Int. J. Plasticity*, 20:339–361, 2004.

Cited on pages 8, 16, 160, and 161.

Raabe et al. 2002a D. Raabe, P. Klose, B. Engl, K.-P. Imlau, F. Friedel, and F. Roters. Concepts for integrating plastic anisotropy into metal forming simulations. *Adv. Eng. Mater.*, 4:169–180, 2002a.

Cited on pages 4 and 8.

Raabe et al. 2002b D. Raabe, Z. Zhao, and W. Mao. On the dependence of in-grain subdivision and deformation texture of aluminum on grain interaction. *Acta Mater.*, 50:4379–4394, 2002b.

Cited on page 61.

Raabe et al. 2002c D. Raabe, Z. Zhao, S.-J. Park, and F. Roters. Theory of orientation gradients in plastically strained crystals. *Acta Mater.*, 50:421–440, 2002c.

Cited on pages 75, 76, 82, and 83.

Raabe et al. 2003 D. Raabe, M. Sachtleber, H. Weiland, G. Scheele, and Z. Zhao. Grain-scale micromechanics of polycrystal surfaces during plastic straining. *Acta Mater.*, 51:1539–1560, 2003.

Cited on pages 6 and 10.

Raabe et al. 2004a D. Raabe, F. Roters, F. Barlat, and L.-Q. Chen, editors. *Continuum Scale Simulation of Engineering Materials, Fundamentals - Microstructures - Process Applications*. Wiley-VCH, Weinheim, Germany (ISBN 3-527-30760-5), 2004a.

Cited on page 4.

Raabe et al. 2004b D. Raabe, Z. Zhao, and F. Roters. Study on the orientational stability of cube-oriented FCC crystals under plane strain by use of a texture component crystal plasticity finite element method. *Scripta Mater.*, 50:1085–1090, 2004b.

Cited on pages 76 and 83.

Raabe et al. 2005 D. Raabe, Y. Wang, and F. Roters. Crystal plasticity simulation study on the influence of texture on earing in steel. *Comp. Mater. Sci.*, 34:221–234, 2005.

Cited on pages 10 and 114.

Reuss 1929 A. Reuss. Berechnung der Fließgrenze von Mischkristallen auf Grund der Plastizitätsbeding für Einkristalle. *Z. Angew. Math. Mech.*, 9:49–58, 1929.

Cited on page 132.

Rice 1971 J. R. Rice. Inelastic constitutive relations for solids: an internal variable theory and its application to metal plasticity. *J. Mech. Phys. Solids*, 19:433–455, 1971.

Cited on pages 6 and 18.

Rosenberg and Piehler 1971 J. M. Rosenberg and H. R. Piehler. Calculation of the Taylor factor and lattice rotations for BCC metals deforming by pencil glide. *Metall. Trans.*, 2: 257–259, 1971.

Cited on page 167.

Roters 2003 F. Roters. Application of the Texture Component Crystal Plasticity FEM to Forming Simulation. In *Mat. Sci. Forum*, volume 426–432, pages 3673–3678, Switzerland, 2003. Trans Tech Publications.

Cited on page 160.

Roters 2004 F. Roters. *Continuum Scale Simulation of Engineering Materials*, chapter The Texture Component Crystal Plasticity Finite Element Method, pages 561–572. WILEY-VCH, Weinheim, 2004.

Cited on page 160.

Roters 2005 F. Roters. Application of the crystal plasticity FEM from single crystal to bulk polycrystal. *Comp. Mater. Sci.*, 32:509–517, 2005.

Cited on page 8.

Roters et al. 2000 F. Roters, D. Raabe, and G. Gottstein. Work hardening in heterogeneous alloys - a microstructural approach based on three internal state variables. *Acta Mater.*, 48: 4181–4189, 2000.

Cited on page 27.

Roters et al. 2004 F. Roters, Y. Wang, J.-C. Kuo, and D. Raabe. Comparison of single crystal simple shear deformation experiments with crystal plasticity finite element simulations. *Adv. Eng. Mater.*, 6:653–656, 2004.

Cited on pages 8 and 58.

Roters et al. 2010 F. Roters, P. Eisenlohr, L. Hantcherli, D. D. Tjahjanto, T. R. Bieler, and D. Raabe. Overview of constitutive laws, kinematics, homogenization and multiscale methods in crystal plasticity finite-element modeling: Theory, experiments, applications. *Acta Mater.*, 58:1152–1211, 2010.

Cited on pages 6, 8, and 12.

Sachs 1928 G. Sachs. Zur Ableitung einer Fliessbedingung. *Z. VDI*, 72:734–736, 1928.

Cited on pages 3 and 133.

Sachtleber et al. 2002 M. Sachtleber, Z. Zhao, and D. Raabe. Experimental investigation of plastic grain interaction. *Mat. Sci. Eng. A*, 336:81–87, 2002.

Cited on pages 5, 6, 16, 23, and 58.

Salem et al. 2005 A. A. Salem, S. R. Kalidindi, and S. L. Semiatin. Strain hardening due to deformation twinning in α-titanium: Constitutive relations and crystal-plasticity modeling. *Acta Mater.*, 53:3495–3502, 2005.

Cited on pages 6 and 16.

Sarma and Dawson 1996a G. B. Sarma and P. R. Dawson. Texture predictions using a polycrystal plasticity model incorporating neighbor interactions. *Int. J. Plasticity*, 12:1023–1054, 1996a.

Cited on page 16.

Sarma and Dawson 1996b G. B. Sarma and P. R. Dawson. Effects of interactions among crystals on the inhomogeneous deformations of polycrystals. *Acta Mater.*, 44:1937–1953, 1996b.

Cited on page 114.

Sarma and Zacharia 1999 G. B. Sarma and T. Zacharia. Integration algorithm for modeling the elasto-viscoplastic response of polycrystalline materials. *J. Mech. Phys. Solids*, 47:1219–1238, 1999.

Cited on page 191.

Sarma et al. 1998 G. B. Sarma, B. Radhakrishnan, and T. Zacharia. Finite element simulations of cold deformation at the mesoscale. *Comp. Mater. Sci.*, 12:105–123, 1998.

Cited on pages 16 and 19.

Shen et al. 1986 Z. Shen, R. H. Wagoner, and W. A. T. Clark. Dislocation pile-up and grain boundary interactions in 304 stainless steel. *Scripta Metall.*, 20(6):921–926, 1986.

Cited on page 31.

Smit et al. 1998 R. J. M. Smit, W. A. M. Brekelmans, and H. E. H. Meijer. Prediction of the mechanical behavior of nonlinear heterogeneous systems by multi-level finite element modeling. *Comput. Methods Appl. Mech. Eng.*, 155:181–192, 1998.

Cited on page 133.

Staroselsky and Anand 1998 A. Staroselsky and L. Anand. Inelastic deformation of polycrystalline face centered cubic materials by slip and twinning. *J. Mech. Phys. Solids*, 46:671–696, 1998.

Cited on page 6.

Staroselskya and Anand 2003 A. Staroselskya and L. Anand. A constitutive model for hcp materials deforming by slip and twinning: application to magnesium alloy AZ31B. *Int. J. Plasticity*, 19:1843–1864, 2003.

Cited on page 16.

Suiker and Turteltaub 2005 A. S. J. Suiker and S. Turteltaub. Computational modelling of plasticity induced by martensitic phase transformations. *Int. J. Numer. Meth. Eng.*, 63:1655–1693, 2005.

Cited on page 16.

Svendsen 2002 B. Svendsen. Continuum thermodynamic models for crystal plasticity including the effects of geometrically-necessary dislocations. *J. Mech. Phys. Solids*, 50:1297–1329, 2002.

Cited on page 23.

Tarasiuk and Wierzbanowski 1996 J. Tarasiuk and K. Wierzbanowski. Application of the linear regression method for comparison of crystallographic textures. *Philos. Mag. A*, 73: 1083–1091, 1996.

Cited on pages 124 and 131.

Taylor 1934a G. I. Taylor. The Mechanism of Plastic Deformation of Crystals. Part I.—Theoretical. *Proc. R. Soc. Lond. A*, 145:362–387, 1934a.

Cited on page 15.

Taylor 1934b G. I. Taylor. The Mechanism of Plastic Deformation of Crystals. Part II.—Comparison with Observations. *Proc. R. Soc. Lond. A*, 145:388–404, 1934b.

Cited on page 15.

Taylor 1938 G. I. Taylor. Plastic strain in metals. *J. Inst. Metals*, 62:307–324, 1938.

Cited on pages 3 and 133.

Thamburaja and Anand 2001 P. Thamburaja and L. Anand. Polycrystalline shape-memory materials: effect of crystallographic texture. *J. Mech. Phys. Solids*, 49:709–737, 2001.

Cited on page 6.

Tjahjanto et al. 2007 D. D. Tjahjanto, F. Roters, and P. Eisenlohr. Iso-work-rate weighted-Taylor homogenization scheme for multiphase steels assisted by transformation-induced plasticity effect. *Steel Res. Int.*, 78:777–783, 2007.

Cited on page 135.

Tjahjanto et al. 2008 D. D. Tjahjanto, S. Turteltaub, and A. S. J. Suiker. Crystallographically-based model for transformation-induced plasticity in multiphase carbon steels. *Continuum Mech. Therm.*, 19:399–422, 2008.

Cited on page 6.

Tjahjanto et al. 2010 D. D. Tjahjanto, P. Eisenlohr, and F. Roters. A novel grain cluster-based homogenization scheme. *Modelling Simul. Mater. Sci. Eng.*, 18:015006, 2010.

Cited on page 8.

Tóth and Van Houtte 1992 L. S. Tóth and P. Van Houtte. Discretization techniques for orientation distribution functions. *Texture Microstruct.*, 19:229–244, 1992.

Cited on pages 16, 115, 121, 126, 131, and 132.

Turteltaub and Suiker 2006 S. Turteltaub and A. S. J. Suiker. A multi-scale thermomechanical model for cubic to tetragonal martensitic phase transformations. *Int. J. Solids Struct.*, 43:4509–4545, 2006.

Cited on page 135.

Uchic et al. 2004 M. D. Uchic, D. M. Dimiduk, J. N. Florando, and W. D. Nix. Sample dimensions influence strength and crystal plasticity. *Science*, 305:986–989, 2004.

Cited on page 72.

Van Houtte 1978 P. Van Houtte. Simulation of the rolling and shear texture of brass by the Taylor theory adapted for mechanical twinning. *Acta Metall.*, 26:591–604, 1978.

Cited on page 150.

Van Houtte et al. 1999 P. Van Houtte, L. Delannay, and I. Samajdar. Quantitative prediction of cold rolling textures in low-carbon steel by means of the LAMEL model. *Texture Microstruct.*, 31:109–149, 1999.

Cited on pages 132 and 136.

Van Houtte et al. 2002 P. Van Houtte, L. Delannay, and S. R. Kalidindi. Comparison of two grain interaction models for polycrystal plasticity and deformation texture prediction. *Int. J. Plasticity*, 18:359–377, 2002.

Cited on pages 132 and 136.

Van Houtte et al. 2005 P. Van Houtte, S. Li, M. Seefeldt, and L. Delannay. Deformation texture prediction: from the Taylor model to the advanced Lamel model. *Int. J. Plasticity*, 21:589–624, 2005.

Cited on page 132.

Vegter et al. 2003 H. Vegter, C. ten Horn, Y. An, E. Atzema, H. Pijlman, A. van den Boogaard, and J. Huétink. Characterisation and modelling of the plastic material behaviour and its application in sheet metal forming simulation. In E. Oñate and D. R. J. Owen, editors, *Proceedings of COMPLAS VII, CIMNE*, 2003.

Cited on pages 177, 181, and 182.

Vitek et al. 2004 V. Vitek, M. Mrovec, and J. L. Bassani. Influence of non-glide stresses on plastic flow: From atomistic to continuum modeling. *Mat. Sci. Eng. A*, 365:31–37, 2004.

Cited on page 3.

Voce 1948 E. Voce. The relationship between stress and strain for homogeneous deformation. *J. Inst. Metals*, 74:537–562, 1948.

Cited on page 19.

Voigt 1889 W. Voigt. Über die Beziehung zwischen den beiden Elastizitätskonstanten isotroper Körper. *Wied. Ann.*, 38:573–587, 1889.

Cited on page 132.

Volkert and Lilleodden 2006 C. A. Volkert and E. T. Lilleodden. Size effects in the deformation of submicron Au columns. *Phil. Mag.*, 86:5567–5579, 2006.

Cited on page 72.

Wang et al. 2004 Y. Wang, D. Raabe, C. Klüber, and F. Roters. Orientation dependence of nanoindentation pile-up patterns and of nanoindentation microtextures in copper single crystals. *Acta Mater.*, 52:2229–2238, 2004.

Cited on pages 73 and 97.

Wei and Anand 2004 Y. J. Wei and L. Anand. Grain-boundary sliding and separation in polycrystalline metals: application to nanocrystalline fcc metals. *J. Mech. Phys. Solids*, 52: 2587–2616, 2004.

Cited on page 6.

Wei et al. 2006 Y. J. Wei, C. Su, and L. Anand. A computational study on the mechanical behavior of nanocrystalline fcc metals. *Acta Mater.*, 54:3177–3190, 2006.

Cited on page 6.

Wenk and Van Houtte 2004 H.-R. Wenk and P. Van Houtte. Texture and anisotropy. *Reports on Progress in Physics*, 67:1367–1428, 2004.

Cited on page 113.

Xie and Nakamachi 2002 C. L. Xie and E. Nakamachi. Investigations of the formability of BCC steel sheets by using crystalline plasticity finite element analysis. *Materials & Design*, 23:59–68, 2002.

Cited on pages 10 and 120.

Yang et al. 2004 W. Yang, B. C. Larson, G. M. Pharr, G. E. Ice, J. D. Budai, J. Z. Tischler, and W. Liu. Deformation microstructure under microindents in single-crystal Cu using three-dimensional x-ray structural microscopy. *J. Mater. Res.*, 19:66–72, 2004.

Cited on page 93.

Zaafarani et al. 2006 N. Zaafarani, D. Raabe, R. N. Singh, F. Roters, and S. Zaefferer. Three dimensional investigation of the texture and microstructure below a nanoindent in a Cu single crystal using 3D EBSD and crystal plasticity finite element simulations. *Acta Mater.*, 54:1707–1994, 2006.

Cited on pages 8, 73, 93, 94, 97, 99, and 100.

Zaafarani et al. 2008 N. Zaafarani, D. Raabe, F. Roters, and S. Zaefferer. On the origin of deformation-induced rotation patterns below nanoindents. *Acta Mater.*, 56:31–42, 2008.

Cited on page 8.

Zaefferer et al. 2003 S. Zaefferer, J.-C. Kuo, Z. Zhao, M. Winning, and D. Raabe. On the influence of the grain boundary misorientation on the plastic deformation of aluminum bicrystals. *Acta Mater.*, 51:4719–4735, 2003.

Cited on pages 8 and 58.

Zaefferer et al. 2008 S. Zaefferer, S. I. Wright, and D. Raabe. 3D-orientation microscopy in a FIB SEM: a new dimension of microstructure characterisation. *Metall. Mater. Trans. A*, 39:374–389, 2008.

Cited on page 8.

Zhang et al. 2005 H. Zhang, B. E. Schuster, Q. Wei, and K. T. Ramesh. The design of accurate micro-compression experiments. *Scripta Mater.*, 54:181–186, 2005.

Cited on page 73.

Zhao et al. 2001 Z. Zhao, W. Mao, F. Roters, and D. Raabe. Introduction of a Texture Component Crystal Plasticity Finite Element Method for Anisotropy Simulations. *Adv. Eng. Mater.*, 3:984–990, 2001.

Cited on pages 10 and 16.

Zhao et al. 2004a Z. Zhao, W. Mao, F. Roters, and D. Raabe. A texture optimization study for minimum earing in aluminium by use of a texture component crystal plasticity finite element method. *Acta Mater.*, 52:1003–1012, 2004a.

Cited on pages 3 and 10.

Zhao et al. 2004b Z. Zhao, R. Radovitzky, and A. Cuitiño. A study of surface roughening in fcc metals using direct numerical simulation. *Acta Mater.*, 52:5791–5804, 2004b.

Cited on page 10.

Zhao et al. 2007 Z. Zhao, S. Kuchnicki, R. Radovitzky, and A. Cuitiño. Influence of in-grain mesh resolution on the prediction of deformation textures in fcc polycrystals by crystal plasticity FEM. *Acta Mater.*, 55:2361–2373, 2007.

Cited on page 16.

Zhao et al. 2008 Z. Zhao, M. Ramesh, D. Raabe, A. Cuitiño, and R. Radovitzky. Investigation of Three-Dimensional Aspects of Grain-Scale Plastic Surface Deformation of an Aluminum Oligocrystal. *Int. J. Plasticity*, 24:2278–2297, 2008.

Cited on page 16.

Zienkiewicz 1967 O. C. Zienkiewicz. *The Finite Element Method in Structural and Continuum Mechanics*. McGraw-Hill, New York, 1st edition, 1967.

Cited on pages 3 and 15.

Zienkiewicz and Taylor 2005 O. C. Zienkiewicz and R. L. Taylor. *The Finite Element Method for Solid and Structural Mechanics*. Butterworth-Heinemann, 6th edition, 2005.

Cited on pages 3 and 15.

Zienkiewicz et al. 2005a O. C. Zienkiewicz, R. L. Taylor, and P. Nithiarasu. *The Finite Element Method for Fluid Dynamics*. Butterworth-Heinemann, 6th edition, 2005a.

Cited on pages 3 and 15.

Zienkiewicz et al. 2005b O. C. Zienkiewicz, R. L. Taylor, and J. Z. Zhu. *The Finite Element Method: Its Basis and Fundamentals*. Butterworth-Heinemann, 6th edition, 2005b.

Cited on pages 3 and 15.